frontiers | Research Topics

Challenges in VHEE radiotherapy

Edited by
Luigi Palumbo, Angeles Faus Golfe,
Paola Ballesteros Zebadua and Jiaru Shi

Published in
Frontiers in Physics

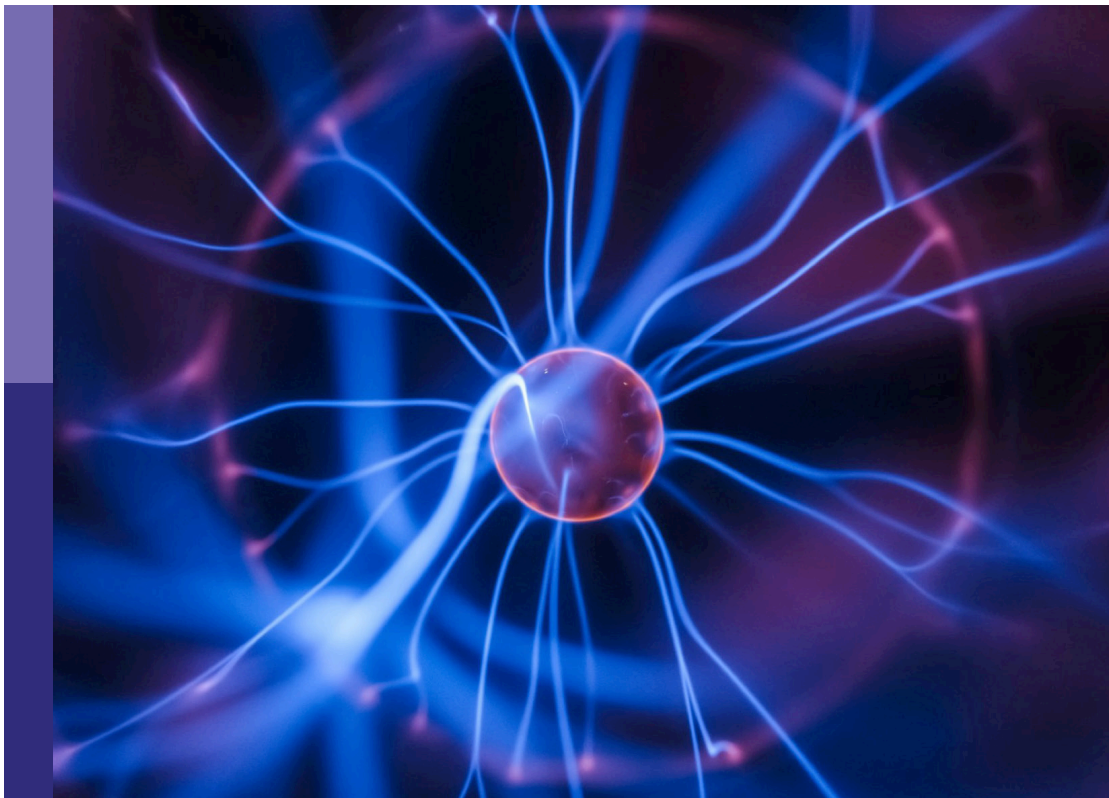

ISSN 1664-8714
ISBN 978-2-8325-7283-2
DOI 10.3389/978-2-8325-7283-2

Generative AI statement
Any alternative text (Alt text) provided alongside figures in the articles in this ebook has been generated by Frontiers with the support of artificial intelligence and reasonable efforts have been made to ensure accuracy, including review by the authors wherever possible. If you identify any issues, please contact us.

About Frontiers

Frontiers is more than just an open access publisher of scholarly articles: it is a pioneering approach to the world of academia, radically improving the way scholarly research is managed. The grand vision of Frontiers is a world where all people have an equal opportunity to seek, share and generate knowledge. Frontiers provides immediate and permanent online open access to all its publications, but this alone is not enough to realize our grand goals.

Frontiers journal series

The Frontiers journal series is a multi-tier and interdisciplinary set of open-access, online journals, promising a paradigm shift from the current review, selection and dissemination processes in academic publishing. All Frontiers journals are driven by researchers for researchers; therefore, they constitute a service to the scholarly community. At the same time, the *Frontiers journal series* operates on a revolutionary invention, the tiered publishing system, initially addressing specific communities of scholars, and gradually climbing up to broader public understanding, thus serving the interests of the lay society, too.

Dedication to quality

Each Frontiers article is a landmark of the highest quality, thanks to genuinely collaborative interactions between authors and review editors, who include some of the world's best academicians. Research must be certified by peers before entering a stream of knowledge that may eventually reach the public - and shape society; therefore, Frontiers only applies the most rigorous and unbiased reviews. Frontiers revolutionizes research publishing by freely delivering the most outstanding research, evaluated with no bias from both the academic and social point of view. By applying the most advanced information technologies, Frontiers is catapulting scholarly publishing into a new generation.

What are Frontiers Research Topics?

Frontiers Research Topics are very popular trademarks of the *Frontiers journals series*: they are collections of at least ten articles, all centered on a particular subject. With their unique mix of varied contributions from Original Research to Review Articles, Frontiers Research Topics unify the most influential researchers, the latest key findings and historical advances in a hot research area.

Find out more on how to host your own Frontiers Research Topic or contribute to one as an author by contacting the Frontiers editorial office: frontiersin.org/about/contact

Challenges in VHEE radiotherapy

Topic editors

Luigi Palumbo — Sapienza University of Rome, Italy

Angeles Faus Golfe — UMR9012 Laboratoire de Physique des 2 infinis Irène Joliot-Curie (IJCLab), France

Paola Ballesteros Zebadua — Manuel Velasco Suárez National Institute of Neurology and Neurosurgery, Mexico

Jiaru Shi — Tsinghua University, China

Citation

Palumbo, L., Golfe, A. F., Zebadua, P. B., Shi, J., eds. (2025). *Challenges in VHEE radiotherapy*. Lausanne: Frontiers Media SA. doi: 10.3389/978-2-8325-7283-2

Table of contents

frontiers | Frontiers in Physics

TYPE Original Research
PUBLISHED 30 July 2024
DOI 10.3389/fphy.2024.1401834

OPEN ACCESS

EDITED BY
Angeles Faus Golfe,
UMR9012 Laboratoire de Physique des 2 infinis Irène Joliot-Curie (IJCLab), France

REVIEWED BY
Lanchun Lu,
The Ohio State University, United States
Claus Andersen,
Technical University of Denmark, Denmark
Itzhak Orion,
Ben-Gurion University of the Negev, Israel

*CORRESPONDENCE
James Cayley,
jcayley@uow.edu.au

RECEIVED 16 March 2024
ACCEPTED 04 July 2024
PUBLISHED 30 July 2024

CITATION
Cayley J, Tan Y-RE, Petasecca M, Cutajar D, Breslin T, Rosenfeld A and Lerch M (2024), MOS*kin* dosimetry for an ultra-high dose-rate, very high-energy electron irradiation environment at PEER.
Front. Phys. 12:1401834.
doi: 10.3389/fphy.2024.1401834

MOS*kin* dosimetry for an ultra-high dose-rate, very high-energy electron irradiation environment at PEER

James Cayley[1]*, Yaw-Ren E. Tan[2], Marco Petasecca[1], Dean Cutajar[1], Thomas Breslin[3], Anatoly Rosenfeld[1] and Michael Lerch[1]

[1]Centre for Medical Radiation Physics, University of Wollongong, Wollongong, NSW, Australia, [2]Australian Synchrotron, ANSTO, Melbourne, VIC, Australia, [3]Department of Oncology, Clinical Sciences, Lund University, Lund, Sweden

FLASH radiotherapy, which refers to the delivery of radiation at ultra-high dose-rates (UHDRs), has been demonstrated with various forms of radiation and is the subject of intense research and development recently, including the use of very high-energy electrons (VHEEs) to treat deep-seated tumors. Delivering FLASH radiotherapy in a clinical setting is expected to place high demands on real-time quality assurance and dosimetry systems. Furthermore, very high-energy electron research currently requires the transformation of existing non-medical accelerators into radiotherapy research environments. Accurate dosimetry is crucial for any such transformation. In this article, we assess the response of the MOS*kin*, developed by the Center for Medical Radiation Physics, which is designed for on-patient, real-time skin dose measurements during radiotherapy, and whether it exhibits dose-rate independence when exposed to 100 MeV electron beams at the Pulsed Energetic Electrons for Research (PEER) end-station. PEER utilizes the electron beam from a 100 MeV linear accelerator when it is not used as the injector for the ANSTO Australian Synchrotron. With the estimated pulse dose-rates ranging from $(7.84 \pm 0.21) \times 10^5$ Gy/s to $(1.28 \pm 0.03) \times 10^7$ Gy/s and an estimated peak bunch dose-rate of $(2.55 \pm 0.06) \times 10^8$ Gy/s, MOS*kin* measurements were verified against a scintillating screen to confirm that the MOS*kin* responds proportionally to the charge delivered and, therefore, exhibits dose-rate independence in this irradiation environment.

KEYWORDS

skin dose, FLASH, dosimetry, very high-energy electrons, MOS*kin*, ultra-high dose-rate, VHEE

1 Introduction

FLASH radiotherapy is an emerging cancer treatment modality that utilises much higher dose-rates than conventional radiotherapy. Recent evidence published indicates that delivering radiation with ultra-high dose-rates (UHDRs) results in a so-called "FLASH effect," whereby healthy tissue is spared and the effects on normal bodily function are reduced while maintaining adequate tumor control [1–5]. The FLASH effect has been demonstrated at average treatment dose-rates ($\dot{D}_t$) above 40 Gy/s (gray; 1 Gy = 1 J/kg) for

various radiation types, including x-rays, protons, and electrons [6, 7]. The use of very high-energy electrons (VHEEs) (above 50 MeV) has been considered for the treatment of deep-seated tumors [8, 9].

Converted medical linear accelerators (linacs) are being used to deliver UHDR electrons. To provide the required dose-rates, the conversion often requires the removal or modification of transmission ion chambers in the head of the linac [10–12] that are used for beam interruption if the radiation delivery diverges from the treatment plan. In the absence of traditional beam interruption systems, there have been advances in fluence monitoring using beam current transformers and pulse delivery optimization systems [13–15]. However, while such advances have been successful and are very important tools for monitoring the delivery of radiation by the linac, these are not forms of dosimetry and so should not be used in isolation for quality assurance. Malfunctioning or mispositioned linac components, such as the jaws or multi-leaf-collimator, installed after the target will cause changes in the dose that are not reflected in the linac beam current.

A critical metric for any external beam radiotherapy modality is the true dose delivered to the patient, often inferred from *in vivo* dosimetry by measuring the dose to the skin, which is itself an important metric [16, 17]. Radiotherapy, of differing types and energies, delivers a dose to the patient's skin that may be high or low relative to the point of maximum dose. When discussing skin dose, the region of interest is the radio-sensitive basal cell layer that resides at the inner-most end of the epidermis at an average depth of 70 μm [16–18]. Although future VHEE treatments may deliver a low skin dose relative to the maximum dose [19–21], the dose should be quantified via *in vivo* measurements and can be used for quality assurance during patient treatment. Current UHDR dosimetry mostly relies upon GafChromic film [11, 22, 23], although other forms of dosimetry such as calorimeters and modified ionization chambers have also been successfully demonstrated as suitable [24, 25]. However, these forms of dosimetry either require complicated setups, lack the near real-time results highly desired in a clinical setting, or are not suitable for evaluating skin dose during treatment delivery. Metal oxide semiconductor field effect transistor (MOSFET) dosimeters offer a promising solution for UHDR environments, which are known for their dose-rates independence, having previously been tested using an electron linac with dose-rates up to 10^7 Gy/s [26]. The Center for Medical Radiation Physics developed MOS*kin* features a design, construction, and packaging distinct from traditional MOSFETs, making them more suitable for clinical dosimetry, especially for the skin [27–29]. With a silicon die approximately 0.168 mm^3 in volume, beam perturbation is negligible at megavoltage and kilovoltage energies [30–33], allowing the device to be attached to the patient for real-time quality assurance during treatment. The sensitive volume is only 0.55 μm thick and can be manufactured in a wide range, from a few micrometers to a few nanometers. Thickness is used to control the sensitivity of the device to ionizing radiation [34, 35]. The MOS*kin* has been validated for on-patient quality assurance skin dose measurements during conventional radiotherapy treatments using x-rays or electrons, where it exhibits a linear response up to 50 Gy [36]. Importantly, for potential UHDR VHEE environments, the MOS*kin* exhibited dose-rate independence in previous studies for clinical use at lower electron energies ranging from 4 MeV to 20 MeV [37, 38], where dose-rates are orders of magnitude lower for medical linacs [39].

Modern medical linacs deliver pulsed electron beams that consist of a sub-structure of electron bunches [40, 41]. Therefore, when discussing dose-rates for medical purposes, not only $\dot{D}_t$ is important, but also the dose-per-pulse (DPP) and dose-per-bunch (DPB) may impact the UHDR radiotherapy effectiveness. DPP and DPB are also expected to impact the response of detectors used for dosimetry. For some commercial detectors, the DPP becomes a limiting factor as it increases above 10 cGy [42]. To increase the DPP, ultra-high pulse dose-rates ($\dot{D}_p$, the dose within the pulse divided by the temporal length of the pulse) are required. As bunches have a non-zero temporal component, the bunch dose-rate ($\dot{D}_b$, the dose within a single bunch, divided by the temporal length of the bunch) must also be considered as it can be multiple orders of magnitude higher than $\dot{D}_t$ and $\dot{D}_p$ and will be "experienced" by a detector as charge generation will occur over these timescales. As medical linacs cannot provide VHEE and are limited in the adjustment of parameters, we take advantage of the new Pulsed Energetic Electrons for Research (PEER), at the heart of which is a custom-built research linac, which has recently become available to selected users when it is not being used as the injector at the ANSTO Australian Synchrotron (AS). The PEER linac accelerates electrons to 100 MeV, in pulses with $\dot{D}_p$ as high as 10^7 Gy/s. As the only linac of its kind available for research in Australia, ongoing transformation to dual-use for synchrotron injection and research will provide previously unavailable capabilities and inform the design choices of future facilities catering to user needs. Dosimetry studies are crucial to characterizing PEER for ongoing medical and VHEE research. In this work, we demonstrate that dose-rate independence exists when the MOS*kin* is exposed to the VHEE beam at PEER.

2 Materials and methods

For an in-depth discussion of the general construction and operation of MOSFET detectors, please refer to [43]. The MOS*kin*s are exposed to the VHEE irradiation field, creating electron–hole pairs in the gate oxide (SiO_2). The gate oxide is biased during irradiation, causing electrons to drift toward the gate electrode, where they are collected. Furthermore, the holes drift toward the substrate and are trapped at the Si/SiO_2 interface defect centers created during the MOS*kin* production process. However, unlike ionization chambers and other solid-state detectors, ionization current is not the response of interest. Instead, the effect of radiation damage via the accumulation of trapped holes causes a quantifiable change in the operating parameters of the device, allowing the dose to be measured. In these p-channel MOS*kin*s, the trapped holes decrease the local hole space-charge density in the p-channel via Coulomb repulsion. This decreased density effectively increases the resistivity of the source-drain p-channel, increasing the measured gate threshold voltage (V_{th}) for a desired source-drain current. The change in V_{th} per unit of the absorbed irradiation dose in the gate oxide is highly reproducible and is also a measure of the sensitivity of the MOS*kin* to the exposing irradiation field environment [43]. Used as a relative dosimeter, the

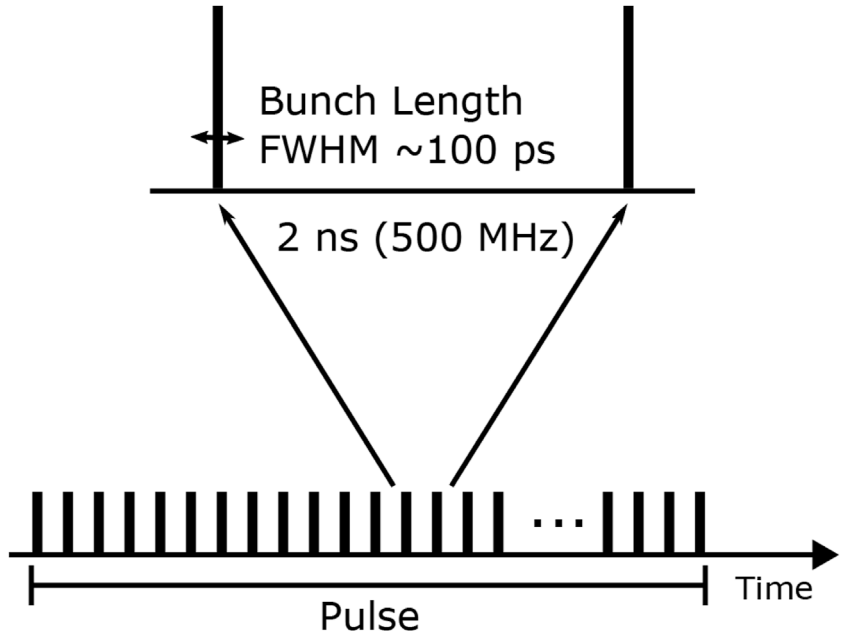

FIGURE 1
Electron linac pulses consist of an underlying bunch structure. PEER parameters are shown.

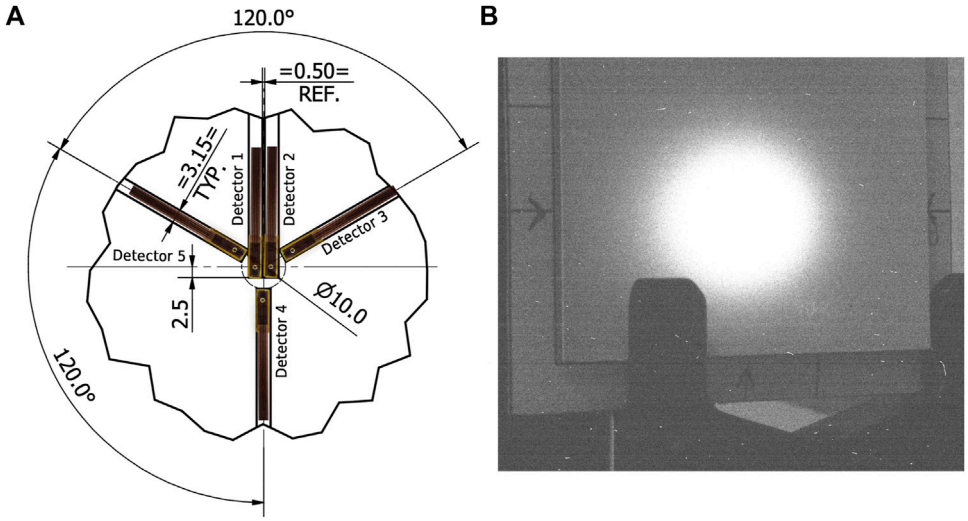

FIGURE 2
(A) Array design with MOS*kin*s overlaid for clarity. Unless otherwise stated, dimensions are in mm. **(B)** Camera image showing scintillating screen with arrows indicating the center of array alignment.

sensitivity is ΔV_{th} / 1 cGy and is used to convert the measured change in V_{th} to the absorbed dose [44].

The VHEE beam at PEER features a custom-built research linac, which is normally used to inject bunched 100 MeV electrons into the AS. The linac is capable of delivering pulses with expected $\dot{D}_p$ of 10^7 Gy/s on nanosecond timescales, and as displayed in Figure 1, it operates with an intra-bunch frequency of 500 MHz and a bunch length of approximately 100 ps. Like medical linacs, a sequence of bunches forms a single pulse [45]. Pulses are delivered at a pulse repetition frequency of 1 Hz (up to 10 Hz will be available in the very near future), with pulse duration ranging from 16 ns to 1000 ns. Electrons exit the linac into air through a 125 μm titanium foil window with a transverse bunch size (sigma) of 1.2 mm in *x* and *y* directions. A fast current transformer (FCT) is used to measure the beam current. As the linac is still undergoing a transformation into a facility for select, by-appointment beamtime, its wide range of capabilities may be restricted to a smaller sub-set where modifications to standard operating conditions are needed.

Two MOS*kin* detectors (Detectors 1 and 2 shown in Figure 2A) were mounted on a 6 mm polymethyl methacrylate frame, positioned on the horizontal axis to measure the dose at the center of the beam. Furthermore, three MOS*kin*s (Detectors 3, 4, and 5 shown in Figure 2A) were positioned around the central axis to detect any undesired beam movement. Any change in the lateral 2D distribution of the beam intensity would be measured as a change in the point dose by the MOS*kin*s. The array was aligned with the VHEE beam using a laser. As an independent measure of beam intensity distribution change, a scintillating screen was positioned behind the MOS*kin*s and imaged using a Mako G-158B PoE camera. These images cannot provide an estimate of the dose, although this technique can be used to verify the relative consistency of fluence between pulses. Although the use of film would appear to be appropriate, with PEER in the early stages of its transformation into a usable research beam, operational and access requirements at the AS facility render it logistically impractical as currently the time required to change film between pulses is in the order of 25–30 minutes.

During the timeframe in which the following experiment was conducted, pulses consisting of 0.300 nC were available. This was a linac constraint at the time to ensure consistent charge per pulse while being able to vary the pulse length. Pulse lengths were on nanosecond timescales, enabling the ultra-high $\dot{D}_p$ necessary for eventual VHEE FLASH radiotherapy. In future experiments, higher DPP will be achieved by increasing the charge within each pulse, delivered over larger timescales. Consequently, $\dot{D}_p$ are expected to remain similar.

Before dosimetry commenced, the VHEE beam was aligned with the center of the scintillator using the arrows visible in Figure 2B, as this was aligned to the array of MOS*kin*s. After beam alignment, single 0.300 nC pulses were delivered across 13 VHEE beam currents, with a requested duration between 20 ns and 400 ns in length. Beam current and, therefore, pulse lengths were varied by adjusting the number of bunches within the pulse, with the intra-bunch spacing fixed at 2 ns. As a result, the charge in each bunch varied, leading to a modified DPB, although the bunch length remained fixed at 100 ps. This method ensured the total charge within a pulse and, therefore, DPP was constant, while $\dot{D}_p$ and $\dot{D}_b$ varied. To calculate the dose, V_{th} must be measured before and after exposure to radiation, and then, a calibration factor representing the sensitivity of the device to a given radiation source is applied to ΔV_{th}. Throughout the experiment, we used a standard MOS*kin* sensitivity of 2.53 ± 0.03mV/cGy, previously calibrated in clinical 6 MV x-ray environments [44], to estimate dose and dose-rates. Further investigation into MOS*kin* sensitivity within VHEE fields is, of course, required. However, this work investigates dose-rate independence, where a consistent response of the MOS*kin* across a range of dose-rates is important rather than absolute dose. To ensure consistency, a script was used to control both the delivery of linac pulses and read the MOS*kin* response before and after each pulse. With nine repeats for each beam current, we report an average with a 95% confidence interval of the MOS*kin* and scintillator responses.

3 Results

An average of $(0.305 +- 0.004)$ nC of charge was delivered in each pulse, as measured by the FCT. The responses of each detector once converted to dose revealed an estimated average DPP of (40.10 ± 0.52) cGy for Detector 1 and (29.32 ± 0.44) cGy for Detector 2, both higher than the 10 cGy limit causing saturation for many commercially available detectors. The responses of the remaining detectors were converted to dose, and then, all readings were normalized to the charge recorded by the FCT for each pulse. These results are shown in Figure 3 and are stable at beam currents above 2 mA, below which a sharp fall off occurs, which was not reflected in the FCT measurements. $\dot{D}_p$ for each pulse was estimated using Detector 1 measurements and range from approximately $(7.84 \pm 0.21) \times 10^5$ Gy/s to $(1.28 \pm 0.03) \times 10^7$ Gy/s, with a peak $\dot{D}_b$ of $(2.55 \pm 0.06) \times 10^8$ Gy/s. $\dot{D}_b$ is calculated as the dose measured within a pulse divided by the number of bunches within the pulse and then divided by the 100 ps temporal length of a bunch. Estimates of $\dot{D}_p$ and $\dot{D}_b$ for each beam current are shown in Table 1.

Using spatial information gained from the array, beam profiles were created from the scintillator data using ImageJ software [46] at the estimated vertical location of Detectors 1 and 2. Typically, a Gaussian distribution would be fitted to beam profiles; however, this was not a good fit for the PEER beam due to high dose gradients in the penumbra region. Instead, a Moffat distribution was used. The Moffat distribution is a modified Lorentzian distribution created to model point-source astronomical objects with steep fall-off gradients [47], which is defined as

$$A\left(1 + \frac{(x - x_0)^2}{\gamma^2}\right)^{-\alpha},$$

where A is the amplitude, x_0 is the center of the distribution, and γ and α are the fitting parameters. Figure 4 demonstrates the difference in beam profile and, therefore, charge delivery between high and low beam currents. The response of Detector 1 remained flat, indicating that its location was within the region of peak amplitude, where gradients are not as steep and the response will be less affected by beam movement. Hence, the value of the Moffat distribution was extracted at x_0, the estimated location of Detector 1.

To assess the behavior of Detector 2, the value was extracted at a fixed point 3.65 mm to the right of x_0 at the highest beam current due to the spacing between the sensitive volumes of detectors 1 and 2 on the array. This was repeated for each pulse to calculate the average response of the scintillator at the estimated locations of detectors 1 and 2 for each beam current. The experimental data used for the beam profiles contain spikes that lie outside the distribution; however, these are radiation-induced noise in the camera images. The results from the scintillator were normalized to 1, which enabled plotting against MOS*kin* data, also normalized to 1, to compare detector response against the charge delivered. Figure 5A displays this comparison for Detector 1, and the same trend is observed in both the MOS*kin* and scintillator responses. The same comparison is found in Figure 5B for Detector 2.

4 Discussion

Due to the design of the array (Figure 2A), the two central detectors should respond equally if the array were aligned perfectly to the beam, and the out-of-field detectors 3, 4, and 5 should also exhibit an equal response due to the Gaussian-like distribution of

10.3389/fphy.2024.1401834

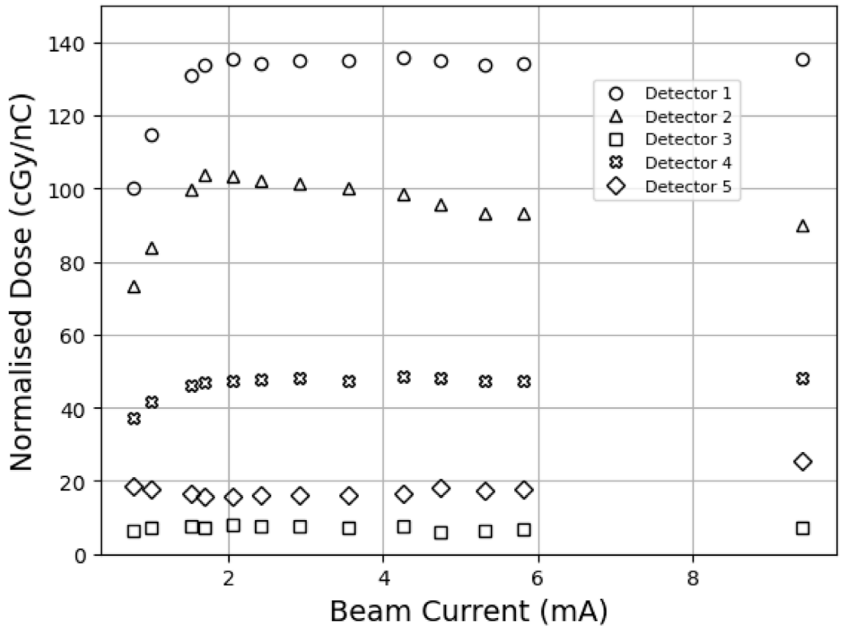

FIGURE 3
MOS*kin* responses converted to dose and normalized to charge as measured by FCT. A 95% confidence interval is within markers. Pulse lengths (nanosecond timescale) are inversely proportional to the beam current. The variation in MOS*kin* response across the symmetrical array allows the assessment of the beam position during the timeframe over which the experiment was conducted.

TABLE 1 Estimated mean $\dot{D}_p$ and $\dot{D}_b$. Bunches have a fixed temporal length of 100 ps. All values have a 95% confidence interval of $\pm$ 2.7% or less.

Pulse length (ns)	Detector 1 (Gy/s)		Detector 2 (Gy/s)	
	Pulse ($\times 10^6$)	Bunch ($\times 10^8$)	Pulse ($\times 10^6$)	Bunch ($\times 10^8$)
32	12.8	2.55	8.48	1.70
52	7.81	1.56	5.43	1.09
58	7.12	1.42	4.95	0.990
64	6.42	1.28	4.54	0.907
72	5.79	1.16	4.21	0.841
86	4.80	0.960	3.55	0.711
106	3.93	0.786	2.95	0.591
128	3.24	0.649	2.47	0.495
148	2.80	0.560	2.13	0.426
178	2.26	0.453	1.76	0.351
208	1.98	0.396	1.51	0.302
314	1.15	0.230	0.841	0.168
414	0.78	0.157	0.575	0.115

electron beams combined with the radial symmetry of the detector positioning on the array. The relative response between detectors, as shown in Figure 3, indicates a misalignment consistent with the position of the array relative to the central beam axis. This misalignment is also shown in Figure 2B, where the arrows marked on the scintillator reflect the vertical and horizontal positioning of the center of the array; the scintillator shows a response consistent with the findings from the relative MOS*kin* responses. Detector 5 responses decreased as the beam current decreased, in contrast to Detector 2, indicating that the beam also shifted horizontally throughout the experiment. Throughout the analysis, x_0, the center of the fitted Moffat distribution was found to shift to the right as the beam current decreased, supporting the indication that the center of the beam shifted as the experiment

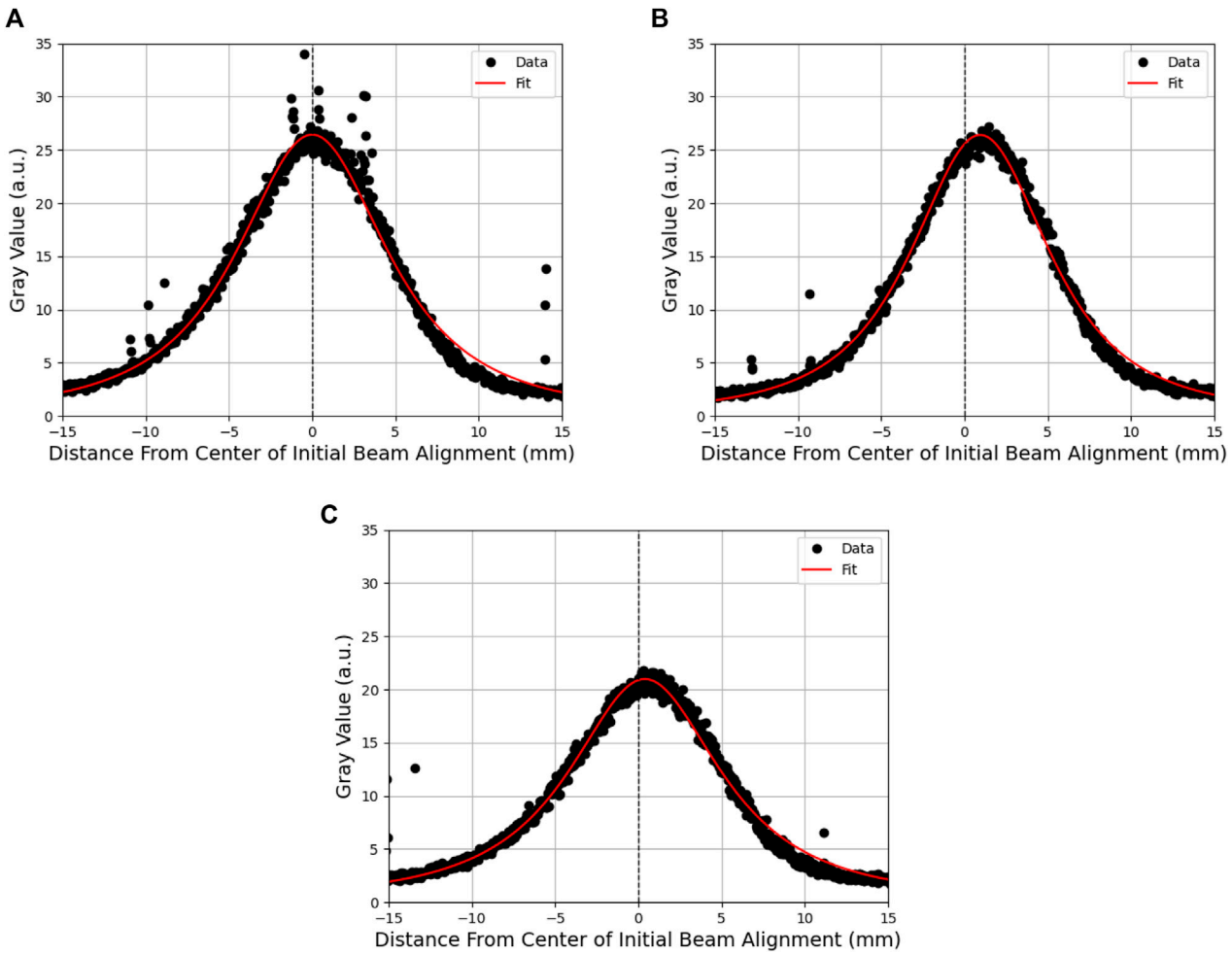

FIGURE 4
Moffat distribution fitted to scintillator beam profiles of a single pulse at a **(A)** high beam current, **(B)** the point at which detector response begins to fall off, and **(C)** low beam current. The difference in intensity between high and low beam currents is visible as a reduction in the magnitude of the profile and the movement of the beam from the initial alignment.

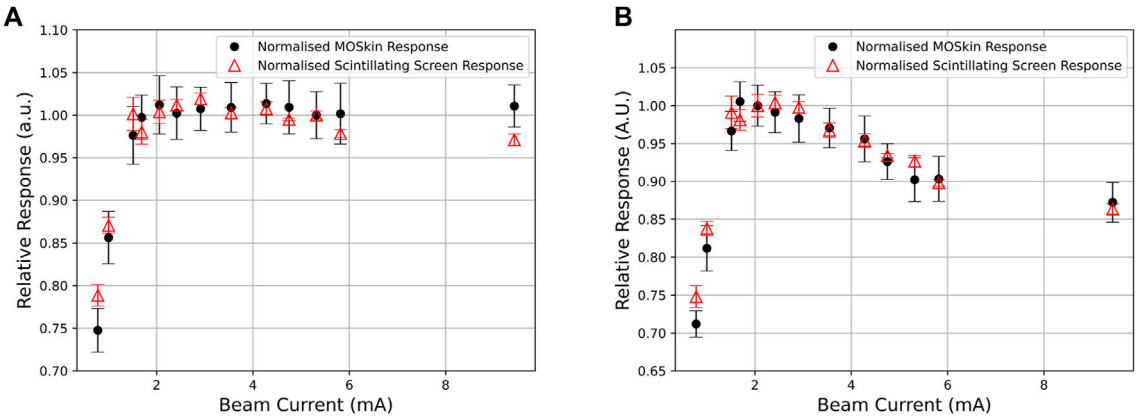

FIGURE 5
(A,B) Relative response of each pulse between the MOS*kin* and scintillating screen for Detector 1 and Detector 2, respectively.

moved from high to low beam current. Detector 2 was positioned 3.65 mm to the right of Detector 1, exposing it to the steep dose gradients, as evident in Figure 4, and, therefore, undesired beam movement caused a large change in the response of the detector at that point. This accounts for the increase in Detector 2 response throughout the experiment. When using the scintillator to verify the consistency of fluence between pulses, it is plausible that it has an intrinsic dependence on beam current/dose-rate. However, detectors 1 and 2 experienced different doses over the same timescales during the experiment and, hence, experienced different dose-rates. If the scintillator possessed a dose-rate dependence equivalent to that of a MOS*kin* detector, it would not be possible to correlate the responses of both detectors 1 and 2 with the scintillator response.

The observed fall-off in the MOS*kin* response below 2 mA indicates either an incorrect response from the MOS*kin*s or an error in charge delivery to the experimental stage. However, after analyzing the scintillator response and comparing the normalized data shown in Figure 5, it is clear that this fall-off is common to both instruments and must be due to a loss of charge from the linac rather than an incorrect reading from the MOS*kin*s. These results indicate that the MOS*kin* responds proportionally to the charge delivered to the experimental stage rather than changing beam current and thus exhibits dose-rate independence when exposed to the VHEE beam at PEER.

Of further importance is the discovery of the limitations of the FCT. Although the PEER FCT was originally commissioned to monitor beam currents during daily AS operation, this work provides important insight into the potential limitations of such devices. With efforts being made to correlate dose delivery to beam current transformers and other fluence monitoring devices on existing and new linacs for UHDR RT, these results suggest a requirement for accurate quality assurance dosimetry in conjunction with online monitoring devices as part of any future UHDR VHEE quality assurance.

5 Conclusion

While being exposed to $\dot{D}_p$ up to $(1.28 \pm 0.03) \times 10^7$ Gy/s, with $\dot{D}_b$ as high as $(2.55 \pm 0.06) \times 10^8$ Gy/s, the MOS*kin*s showed a response consistent with the scintillating screen, hence proportional to the charge delivered. This explains the observed trends in the MOS*kin* response and indicates dose-rate independence. FCT measurements were found to be an unreliable diagnostic for verifying dose delivery; however, this study instills confidence in the use of MOS*kin* for eventual UHDR VHEE quality assurance and skin dosimetry and justifies further work toward realization.

Data availability statement

The raw data supporting the conclusions of this article will be made available by the authors, without undue reservation.

Author contributions

JC: conceptualization, formal analysis, investigation, methodology, visualization, writing–original draft, and writing–review and editing. Y-RT: conceptualization, data curation, investigation, methodology, resources, software, supervision, and writing–review and editing. MP: conceptualization, investigation, methodology, and writing–review and editing. DC: conceptualization, investigation, methodology, and writing–review and editing. TB: conceptualization, investigation, methodology, and writing–review and editing. AR: conceptualization, funding acquisition, investigation, methodology, resources, supervision, and writing–review and editing. ML: conceptualization, funding acquisition, investigation, methodology, resources, supervision, and writing–review and editing.

Funding

The authors declare that financial support was received for the research, authorship, and/or publication of this article. JC received Australian Government RTP scholarship APP505948.

Acknowledgments

This research was undertaken on the PEER beamline, Australian Synchrotron, part of ANSTO. The authors would like to thank Khonraed Gill for the creation of engineering drawings and STEP files.

Conflict of interest

ML, AR, MP, and DC declare consulting with Electrogenics Laboratories Ltd., which is commercializing the MOSkin detector.

The remaining authors declare that the research was conducted in the absence of any commercial or financial relationships that could be construed as a potential conflict of interest.

The authors declared that they were an editorial board member of Frontiers, at the time of submission. This had no impact on the peer review process and the final decision.

Publisher's note

References

1. Favaudon V, Caplier L, Monceau V, Pouzoulet F, Sayarath M, Fouillade C, et al. Ultrahigh dose-rate FLASH irradiation increases the differential response between normal and tumor tissue in mice. *Sci Translational Med* (2014) 6:245ra93. doi:10.1126/scitranslmed.3008973

2. Montay-Gruel P, Acharya MM, Gonçalves Jorge P, Petit B, Petridis IG, Fuchs P, et al. Hypofractionated FLASH-RT as an effective treatment against glioblastoma that reduces neurocognitive side effects in mice. *Clin Cancer Res* (2021) 27:775–84. doi:10.1158/1078-0432.CCR-20-0894

3. Chabi S, To THV, Leavitt R, Poglio S, Jorge PG, Jaccard M, et al. Ultra-high-dose-rate FLASH and conventional-dose-rate irradiation differentially affect human acute lymphoblastic leukemia and normal hematopoiesis. *Int J Radiat Oncol - Biol - Phys* (2021) 109:819–29. doi:10.1016/j.ijrobp.2020.10.012

4. Simmons DA, Lartey FM, Schüler E, Rafat M, King G, Kim A, et al. Reduced cognitive deficits after FLASH irradiation of whole mouse brain are associated with less hippocampal dendritic spine loss and neuroinflammation. *FLASH Radiother Int Workshop* (2019) 139:4–10. doi:10.1016/j.radonc.2019.06.006

5. Vozenin MC, De Fornel P, Petersson K, Favaudon V, Jaccard M, Germond JF, et al. The advantage of FLASH radiotherapy confirmed in mini-pig and cat-cancer patients. *Clin Cancer Res* (2019) 25:35–42. doi:10.1158/1078-0432.CCR-17-3375

6. Lin B, Gao F, Yang Y, Wu D, Zhang Y, Feng G, et al. FLASH radiotherapy: history and future. *Front Oncol* (2021) 11:644400. doi:10.3389/fonc.2021.644400

7. Atkinson J, Bezak E, Le H, Kempson I. The current status of FLASH particle therapy: a systematic review. *Phys Eng Sci Med* (2023) 46:529–60. doi:10.1007/s13246-023-01266-z

8. Sarti A, De Maria P, Battistoni G, De Simoni M, Di Felice C, Dong Y, et al. Deep seated tumour treatments with electrons of high energy delivered at FLASH rates: the example of prostate cancer. *Front Oncol* (2021) 11:777852. doi:10.3389/fonc.2021.777852

9. Böhlen TT, Germond JF, Traneus E, Bourhis J, Vozenin MC, Bailat C, et al. Characteristics of very high-energy electron beams for the irradiation of deep-seated targets. *Med Phys* (2021) 48:3958–67. doi:10.1002/mp.14891

10. Giuliano L, Franciosini G, Palumbo L, Aggar L, Dutreix M, Faillace L, et al. Characterization of ultra-high-dose rate electron beams with ElectronFlash linac. *Appl Sci* (2023) 13:631. doi:10.3390/app13010631

11. Lempart M, Blad B, Adrian G, Bäck S, Knöös T, Ceberg C, et al. Modifying a clinical linear accelerator for delivery of ultra-high dose rate irradiation. *Radiother Oncol* (2019) 139:40–5. doi:10.1016/j.radonc.2019.01.031

12. Rahman M, Ashraf MR, Zhang R, Bruza P, Dexter CA, Thompson L, et al. Electron FLASH delivery at treatment room isocenter for efficient reversible conversion of a clinical LINAC. *Int J Radiat Oncol - Biol - Phys* (2021) 110:872–82. doi:10.1016/j.ijrobp.2021.01.011

13. Gonçalves Jorge P, Grilj V, Bourhis J, Vozenin MC, Germond JF, Bochud F, et al. Technical note: validation of an ultrahigh dose rate pulsed electron beam monitoring system using a current transformer for FLASH preclinical studies. *Med Phys* (2022) 49:1831–8. doi:10.1002/mp.15474

14. Jain S, Cetnar A, Woollard J, Gupta N, Blakaj D, Chakravarti A, et al. Pulse parameter optimizer: an efficient tool for achieving prescribed dose and dose rate with electron FLASH platforms. *Phys Med Biol* (2023) 68:19NT01. doi:10.1088/1361-6560/acf63e

15. Vignati A, Giordanengo S, Fausti F, Martì Villarreal OA, Mas Milian F, Mazza G, et al. Beam monitors for tomorrow: the challenges of electron and photon FLASH RT. *Front Phys* (2020) 8. doi:10.3389/fphy.2020.00375

16. Qi ZY, Deng XW, Huang SM, Zhang L, He ZC, Allen Li X, et al. *In vivo* verification of superficial dose for head and neck treatments using intensity-modulated techniques. *Med Phys* (2009) 36:59–70. doi:10.1118/1.3030951

17. McDermott PN. Surface dose and acute skin reactions in external beam breast radiotherapy. *Med Dosimetry* (2020) 45:153–8. doi:10.1016/j.meddos.2019.09.001

18. Valentin J. Basic anatomical and physiological data for use in radiological protection: reference values: ICRP Publication 89: approved by the Commission in September 2001. *Ann ICRP* (2002) 32:1–277. doi:10.1016/S0146-6453(03)00002-2

19. Ronga MG, Cavallone M, Patriarca A, Leite AM, Loap P, Favaudon V, et al. Back to the future: very high-energy electrons (VHEEs) and their potential application in radiation therapy. *Cancers* (2021) 13:4942. doi:10.3390/cancers13194942

20. DesRosiers C, Moskvin V, Bielajew AF, Papiez L. 150-250 MeV electron beams in radiation therapy. *Phys Med Biol* (2000) 45:1781–805. doi:10.1088/0031-9155/45/7/306

21. Papiez L, DesRosiers C, Moskvin V. Very high energy electrons (50-250 MeV) and radiation therapy. *Technol Cancer Res Treat* (2002) 1:105–10. doi:10.1177/153303460200100202

22. Szpala S, Huang V, Zhao Y, Kyle A, Minchinton A, Karan T, et al. Dosimetry with a clinical linac adapted to FLASH electron beams. *J Appl Clin Med Phys* (2021) 22:50–9. doi:10.1002/acm2.13270

23. Jaccard M, Durán MT, Petersson K, Germond JF, Liger P, Vozenin MC, et al. High dose-per-pulse electron beam dosimetry: commissioning of the Oriatron eRT6 prototype linear accelerator for preclinical use. *Med Phys* (2018) 45:863–74. doi:10.1002/mp.12713

24. Gómez F, Gonzalez-Castaño DM, Fernández NG, Pardo-Montero J, Schüller A, Gasparini A, et al. Development of an ultra-thin parallel plate ionization chamber for dosimetry in FLASH radiotherapy. *Med Phys* (2022) 49:4705–14. doi:10.1002/mp.15668

25. Bass GA, Shipley DR, Flynn SF, Thomas RAS. A prototype low-cost secondary standard calorimeter for reference dosimetry with ultra-high pulse dose rates. *Br J Radiol* (2023) 96:20220638. doi:10.1259/bjr.20220638

26. Fleetwood D, Winokur P, Schwank J. Using laboratory X-ray and cobalt-60 irradiations to predict CMOS device response in strategic and space environments. *IEEE Trans Nucl Sci* (1988) 35:1497–505. doi:10.1109/23.25487

27. Kwan I, Rosenfeld A, Qi Z, Wilkinson D, Lerch M, Cutajar D, et al. Skin dosimetry with new MOSFET detectors. *Radiat Measurements* (2008) 43:929–32. doi:10.1016/j.radmeas.2007.12.052

28. Patterson E, Stokes P, Cutajar D, Rosenfeld A, Baines J, Metcalfe P, et al. High-resolution entry and exit surface dosimetry in a 1.5 T MR-linac. *Phys Eng Sci Med* (2023) 46:787–800. doi:10.1007/s13246-023-01251-6

29. Tai M, Patterson E, Metcalfe PE, Rosenfeld A, Oborn BM. Skin dose modeling and measurement in a high field in-line MRI-linac system. *Front Phys* (2022) 10. doi:10.3389/fphy.2022.902744

30. Thorpe NK, Cutajar D, Lian C, Pitney M, Friedman D, Perevertaylo V, et al. A comparison of entrance skin dose delivered by clinical angiographic c-arms using the real-time dosimeter: the MOSkin. *Australas Phys Eng Sci Med* (2016) 39:423–30. doi:10.1007/s13246-016-0435-0

31. Alnawaf H, Butson M, Yu PKN. Measurement and effects of MOSKIN detectors on skin dose during high energy radiotherapy treatment. *Australas Phys Eng Sci Med* (2012) 35:321–8. doi:10.1007/s13246-012-0153-1

32. Souris JS, Cheng SH, Pelizzari C, Chen NT, La Riviere P, Chen CT, et al. Radioluminescence characterization of *in situ* x-ray nanodosimeters: potential real-time monitors and modulators of external beam radiation therapy. *Appl Phys Lett* (2014) 105:203110. doi:10.1063/1.4900962

33. Jornet N, Carrasco P, Jurado D, Ruiz A, Eudaldo T, Ribas M. Comparison study of MOSFET detectors and diodes for entrance *in vivo* dosimetry in 18 MV x-ray beams. *Med Phys* (2004) 31:2534–42. doi:10.1118/1.1785452

34. Fleetwood DM. Perspective on radiation effects in nanoscale metal–oxide–semiconductor devices. *Appl Phys Lett* (2022) 121:070503. doi:10.1063/5.0105173

35. Rosenfeld AB. MOSFET dosimetry on modern radiation oncology modalities. *Radiat Prot Dosimetry* (2002) 101:393–8. doi:10.1093/oxfordjournals.rpd.a006009

36. Qi ZY, Deng XW, Huang SM, Lu J, Lerch M, Cutajar D, et al. Verification of the plan dosimetry for high dose rate brachytherapy using metal–oxide–semiconductor field effect transistor detectors. *Med Phys* (2007) 34:2007–13. doi:10.1118/1.2736288

37. Jong W, Ung N, Tiong A, Rosenfeld A, Wong J. Characterisation of a MOSFET-based detector for dose measurement under megavoltage electron beam radiotherapy. *Radiat Phys Chem* (2018) 144:76–84. doi:10.1016/j.radphyschem.2017.11.021

38. Choi JH, Cutajar D, Metcalfe P, Downes S. Application of MOSkin detector for *in vivo* dosimetry on total skin electron therapy (TSET). *Biomed Phys Eng Express* (2018) 4:024002. doi:10.1088/2057-1976/aaac61

39. Shepard AJ, Matrosic CK, Radtke JL, Jupitz SA, Culberson WS, Bednarz BP. Technical Note: characterization of clinical linear accelerator triggering latency for motion management system development. *Med Phys* (2018) 45:4816–21. doi:10.1002/mp.13191

40. Metcalfe P, Kron T, Hoban P, Cutajar D, Hardcastle N. *The Physics of radiotherapy X-rays and electrons*. 3rd ed. Madison, WI: Medical Physics Publishing (2023).

41. Romano F, Bailat C, Jorge PG, Lerch MLF, Darafsheh A. Ultra-high dose rate dosimetry: challenges and opportunities for FLASH radiation therapy. *Med Phys* (2022) 49:4912–32. doi:10.1002/mp.15649

42. Di Martino F, Barca P, Barone S, Bortoli E, Borgheresi R, De Stefano S, et al. FLASH radiotherapy with electrons: issues related to the production, monitoring, and dosimetric characterization of the beam. *Front Phys* (2020) 8. doi:10.3389/fphy.2020.570697

43. Oldham TR. Ionizing radiation effects in MOS oxides. In: *International series on advances in solid state electronics and technology*. World Scientific (2000). doi:10.1142/3655

44. Jong WL, Wong J, Ung NM, Ng KH, Ho G, Cutajar D, et al. Characterization of MOSkin detector for *in vivo* skin dose measurement during megavoltage radiotherapy. *J Appl Clin Med Phys/Am Coll Med Phys* (2014) 15:120–32. doi:10.1120/jacmp.v15i5.4869

45. Meier E, Dowd R, LeBlanc G. Characterization of the Australian synchrotron linac. *Nucl Instr Methods Phys Res Section A: Acc Spectrometers, Detectors Associated Equipment* (2008) 589:157–66. doi:10.1016/j.nima.2008.02.009

46. Schneider CA, Rasband WS, Eliceiri KW. NIH Image to ImageJ: 25 years of image analysis. *Nat Methods* (2012) 9:671–5. doi:10.1038/nmeth.2089

47. Moffat AFJ. A theoretical investigation of focal stellar images in the photographic emulsion and application to photographic photometry. *Astron Astrophysics* (1969) 3:455.

frontiers | Frontiers in Physics

TYPE Original Research
PUBLISHED 01 October 2024
DOI 10.3389/fphy.2024.1448025

OPEN ACCESS

EDITED BY
Luigi Palumbo,
Sapienza University of Rome, Italy

REVIEWED BY
Andrea Mostacci,
Sapienza University of Rome, Italy
Wania Wolff,
Federal University of Rio de Janeiro, Brazil

*CORRESPONDENCE
James Cayley,
jcayley@uow.edu.au

RECEIVED 12 June 2024
ACCEPTED 11 September 2024
PUBLISHED 01 October 2024

CITATION
Cayley J, Paino J, Guatelli S, Rosenfeld A, Lerch M and Tan Y-RE (2024) Simulation and commissioning of a Faraday cup for absolute charge measurements of very high-energy electrons in-air at PEER.
Front. Phys. 12:1448025.
doi: 10.3389/fphy.2024.1448025

Simulation and commissioning of a Faraday cup for absolute charge measurements of very high-energy electrons in-air at PEER

James Cayley[1]*, Jason Paino[1], Susanna Guatelli[1], Anatoly Rosenfeld[1], Michael Lerch[1] and Yaw-Ren E. Tan[2]

[1]Centre for Medical Radiation Physics, University of Wollongong, Wollongong, NSW, Australia, [2]Australian Synchrotron, ANSTO, Melbourne, VIC, Australia

The Pulsed Energetic Electrons for Research (PEER) beamline at the ANSTO Australian Synchrotron comprises a 100 MeV linac injector that is currently being developed for ultra-high dose-rate, very high-energy electron radiotherapy research. Previously, dosimetry studies discovered a lack of reliable charge measurement to the in-air end station, though no change in response was recorded in fast current transformer measurements, the only available diagnostic device for measuring charge. This work describes the process of simulating and then commissioning a purpose-built Faraday cup to ascertain absolute in-air charge measurements at PEER. By combining simulation data with experimental results, the PEER Faraday cup is shown to possess a primary electron capture efficiency of (99.22 $\pm$ 0.10)%, with a net capture efficiency due to secondary electron emission of (97.87 $\pm$ 0.24)%. These results show the PEER Faraday cup performs as intended and, when scaled against simulations, will be suitable for measuring absolute charge at PEER.

KEYWORDS

Faraday cup, very high-energy electrons, radiotherapy, FLASH, absolute charge, beam diagnostics, GEANT4

1 Introduction

The ANSTO Australian Synchrotron is a third-generation light source with a 100 MeV electron linac injector. During machine development periods, the Pulsed Energetic Electrons for Research (PEER) end-station can use the linac for very high-energy electron (VHEE, electrons with energy greater than 50 MeV) research. The linac is believed to be capable of delivering average dose-rates many orders of magnitude greater than 40 Gy/s, making it suitable for research into FLASH radiotherapy, an emerging cancer treatment modality that utilizes ultra-high dose-rate (UHDR) radiation due to its tissue-sparing qualities [1–3].

Of increasing interest is the combination of UHDR with VHEE to treat deep-seated tumors [4–6]. To investigate the combination of UHDR and VHEE for novel radiotherapy treatments, preliminary dosimetric investigations have been performed at PEER to begin characterizing the beam delivered to the end-station. Previously, while using a fixed pulse charge across a range of beam currents from 0.78 mA to 9.42 mA, Cayley et al. [7] showed

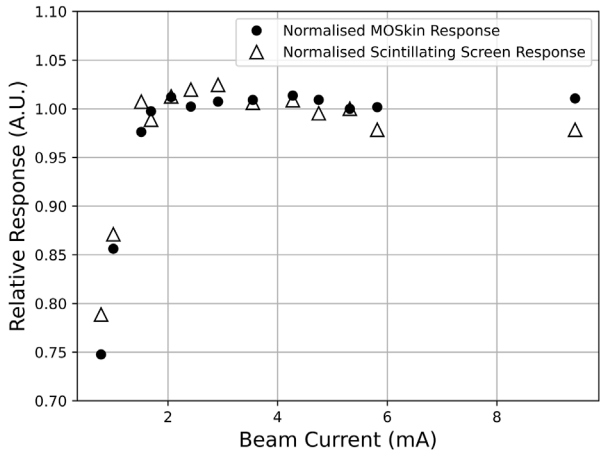

FIGURE 1
The loss of charge to the experimental stage at PEER for beam currents below 2 mA is observed in both MOS*kin* and scintillating screen data. The CT measurements were consistent across all beam currents. Figure from Cayley et al. [7], reproduced with permission.

that at beam currents below 2 mA, the responses of a Centre for Medical Radiation Physics-designed MOS*kin* detector [8–12] array and scintillating screen simultaneously revealed a loss of charge at the in-air experimental stage, as evident in Figure 1. This loss of charge was not reflected in measurements from an in-vacuum fast current transformer (CT), demonstrating a lack of reliable charge measurement over a range of different beam delivery parameters. Hence, quantifying the absolute charge delivered to the PEER end-station is a critical requirement for further dosimetry studies and overall beamline development. With known charge values, simulations can be created to predict dose, and accurate measurements will also enable the quantification of relative differences in charge delivery between consecutive irradiations during experiments. Although the preliminary investigations uncovered issues with the currently available diagnostics, PEER is considered suitable for further VHEE radiotherapy research and presents capabilities previously unavailable in Australia. To continue developing the PEER beamline, further diagnostics, in particular, in-air charge measurements, are critical to the advancement of the beamline and future user research.

A Faraday cup (FC) is a device that measures charge in the form of electrons, protons, or heavy ions. Many facilities globally have designed and built devices suited to their needs, with FC use during radiotherapy research documented over 40 years ago during proton therapy [13]. Recently, the advancement of UHDR research has led to the requirement for dose-rate independent diagnostics. FC devices are considered dose-rate independent and, hence, are often used to characterize other diagnostic devices [14–18].

In its most basic form, an FC is a block of conductive material insulated from an external housing of a sufficient size and density to absorb all of the energetically charged primary particles incident upon it, ideally retaining the secondary particles generated within [19, 20]. Although most often used in-vacuum, vacuumless designs have been found to provide sufficiently accurate measurements comparable to more complex, in-vacuum designs [20]. When designing an FC, an important consideration is the energy and type of the incident particles, as this will directly influence the physical size of the device [21]. Electric and magnetic fields are often used to filter and confine particles, especially in the case of proton beams [22], but the device may also be used passively for electrons if sized appropriately for the beam energy.

When charged particles are incident upon the conductive absorber of an FC, an electric current is generated within the FC. This current creates a signal that can be measured, for instance, with an oscilloscope or electrometer, allowing the charge incident upon the FC to be quantified. When measuring charge, the creation of secondary electrons with energies sufficient to leave the conductive absorber cannot be ignored. Those that are generated and stopped within the absorber will have no contribution to the measurable signal. However, those that leave will contribute to a loss in signal proportional to their quantity relative to the number of incident primary particles. Many FC designs use a high voltage ring at the beam entrance in order to repel secondary electrons created prior to the FC while suppressing those that are backscattered after being produced within the conductive absorber [16]. Another method is to add a second conductive material of lower density at the FC entrance, allowing primary particles to pass through to the absorber while collecting backscattered secondary electrons [19, 23]. In the case of the latter, the FC may be used without an external voltage applied, which would require less complicated readout systems, less electrical infrastructure, and would be considerably safer when used in close proximity to personnel conducting experiments. Regardless, the proportion of escaping secondaries must be known; if the proportion is large relative to the number of particles within the incident beam, the measurements will be inaccurate and not wholly reflect the charge being delivered.

To quantify the charge delivered by VHEE to the in-air end station at PEER, an FC was designed using locally available, off-the-shelf materials. As the PEER beamline is in the early stages of development, the FC should be a simple, portable, and cost-effective device. It is intended to be used passively to allow for simplified measurements and increased personnel safety while still allowing the application of an external voltage for commissioning purposes. The FC will be located in a small experimental area 900 mm downstream of the exit foil of the PEER linac, shown in Figure 2. In order to estimate absolute charge, a larger FC will minimize any scaling factors required, as all the incident charge will be absorbed, and any secondary particles will be retained. However, the limited space at PEER concedes the opportunity to simply oversize the components in excess of what is required, so a Monte Carlo simulation was used to assess the primary electron-stopping efficiency and secondary electron escape. Once built, the electrical readout was optimized for use with an external voltage source for commissioning and comparison against simulations. Within this paper, we show that the PEER FC performs as expected when unbiased and, therefore, is suitable for in-air measurements of 100 MeV electrons delivered to the end-station at PEER.

2 Methods

2.1 Initial design

To be suitable for the in-air end station at PEER, the most critical design metric of the FC was physical size limitation due to the

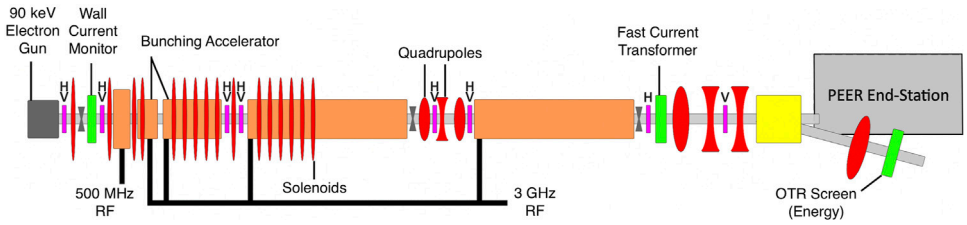

FIGURE 2
PEER beamline design. The Faraday cup will be situated in the small experimental area after the exit foil of the linac, immediately adjacent to the quadrupole and OTR screen that make up the first section of the booster ring transition. The physical size limitations of the FC are critical as extra space cannot currently be created in this area.

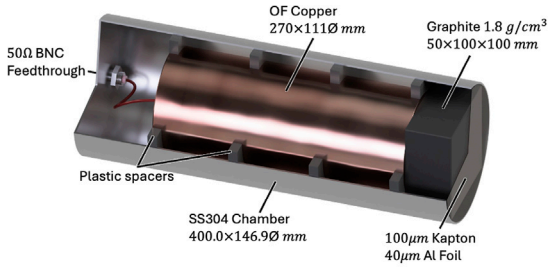

FIGURE 3
PEER FC dimensions and material choices. The graphite and copper may be left unbiased, or a DC voltage can be applied, if necessary, via the 50 Ω BNC feedthrough.

limited available space at PEER while remaining capable of stopping 100 MeV electrons and retaining secondary electrons generated by the incident beam. Detailed in Figure 3, a cylinder of oxygen-free copper with a length of 270 mm and diameter of 111 mm was used for the conductive absorber, with a block of graphite measuring 100 mm × 100 mm × 50 mm placed in front at the beam entrance to act as a secondary conductive absorber for backscattered electrons. These dimensions were maximized within the size constraints. The absorbers are supported by 3D-printed spacers made from polylactic acid (PLA), a common plastic used in additive manufacturing that also provides electrical insulation from the stainless-steel housing. A 100 μm thick Kapton entrance foil was used to seal the front of the housing, with the addition of 40 μm thick aluminum foil to isolate the FC from electrical noise present in the linac tunnel. An electrical connection is provided by a 50 Ω BNC feedthrough at the rear of the cup. The FC is positioned 900 mm downstream of the linac exit foil, centered upon the beam's central axis, a position which will place it behind future VHEE radiotherapy experiments conducted at PEER.

2.2 Monte Carlo simulation

A Monte Carlo simulation was used to assess the design. The Geant4 toolkit (Version 11.00p03, with the G4EmStandardPhysics_option4 physics list) was chosen as it is a robust and reliable software package validated in many fields of physics [24, 25]. The simulation consists of a 100 MeV electron beam generated within a vacuum tube, with a 125 μm exit foil to replicate the conditions at PEER. Beam parameters advised by Australian Synchrotron staff include an energy distribution of σ equal to 0.7 MeV, with estimates of lateral distribution and beam divergence determined experimentally using beam profiles extracted from scintillating screen measurements. To replicate the experimental setup, the entrance of the FC is placed at a distance of 900 mm from the linac exit foil, centered upon the beam axis. Using a range cut of 0.05 mm, the simulation is aimed to calculate the number of primary electrons that stop in the FC and the position where they are stopped. The positions of the origin and, eventually, the absorption of secondary electrons are also scored in the simulation.

Geant4, however, cannot be used to predict the electrical output signal of a device. Hence, the information provided by the simulation will be analyzed in the context of the expected contribution to the electrical signal. For instance, if an electron is generated and stopped within the same volume, there will be no contribution to the signal. However, if the generation and stopping volumes are different, a loss or accumulation of secondary electrons within the copper and graphite absorbers will contribute to the signal and render it unrepresentative of the incident electron beam. Increasing levels of charge may affect the FC response due to space-charge effects, which cannot be studied with Geant4. However, due to the large physical dimensions of the conductive absorbers, it is expected that the FC should respond linearly and that the Geant4 simulations will remain representative of the physical device.

Within the simulation, the kinetic energy of any secondaries escaping the absorbers was also scored to assess whether, experimentally, they can be retained with the application of an external DC voltage to bias the FC. With 3×10^5 histories representing 3×10^5 primary electrons per simulation, five repeats were used to calculate a mean, with a standard deviation of less than 0.5%.

2.3 Experimental commissioning

2.3.1 Unbiased operation

For unbiased readout, the FC is connected to an oscilloscope using a triaxial cable connected to the 50 Ω BNC feed, as shown in Figure 3. The circuit schematic is shown in Figure 4. A LeCroy Waverunner 8404 M oscilloscope with a 50 Ω input was used with a sample rate of 40 GS/s. Prior to measurements, the oscilloscope input impedance was confirmed to be accurate to within 0.24% by using a Keithley 6220 Precision Current Source and measuring the

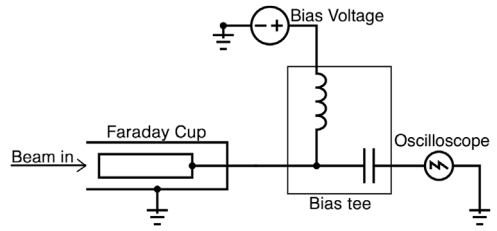

FIGURE 4
The FC is connected to the oscilloscope via a bias tee to allow the application of an external DC voltage during measurements. For passive, unbiased use, the power supply and bias tee are removed, and the FC is connected directly to the oscilloscope.

voltage generated across the input. Included in this value is the manufacturer's stated uncertainty for the Keithley current source. To convert the measured voltage generated by the FC to charge, the oscilloscope traces for each pulse were integrated over time for any data below a value corresponding to the largest point within the baseline signal prior to pulse arrival. The integration returns a value in units of Weber (volt-seconds), which can then be divided by the oscilloscope input impedance to calculate current-seconds, equivalent to the charge contained within the pulse, as seen in Equations 1 and 2.

$$\int_0^t V(t)\,dt = Vs \tag{1}$$

$$\frac{Vs}{R} = Is = q \tag{2}$$

During any testing or commissioning at PEER, the standard practice is to deliver charge in a single pulse (also known as a bunch-train) consisting of 75 bunches, corresponding to a pulse length of approximately 150 ns, although satellite bunches at the head and tail will increase this value. The PEER bunch length is 100 ps with a 2 ns bunch spacing. To increase the level of charge within a pulse, the radio frequency (RF) power is increased in finite steps while holding all other parameters constant. The CT was used to measure in-vacuum charge prior to the final set of magnets, before the electrons pass through the exit foil, for comparison with FC measurements. The CT at PEER has not been calibrated for absolute charge and is, therefore, only a measure of relative charge. It should not be forgotten, however, that CT measurements have previously been shown to become uncorrelated with dose measurements at the in-air end station [7], so any deviation from linearity may not be a failure of the FC. Rather, any such deviations are further justification as to why an FC is required as part of a greater diagnostics suite for future experiments.

2.3.2 Externally biased operation

If enough low-energy secondary electrons escape the FC, it may be possible to use an external DC voltage to bias the FC and retain those secondary electrons. In order to determine this and compare it to the Geant4 simulation, increasing positive bias can be applied to the conductive absorber until the relative response between different voltages is flat. At this point, it can be assumed that either all the secondaries have been retained or that no further improvements are possible. A measurement of this level of accuracy would be suitable for the intended use of the FC during future VHEE radiotherapy experiments at PEER.

A Pulse Labs 5550B-104 bias tee was used to facilitate the application of an external DC voltage to the FC while isolating the oscilloscope. A bias tee is a device consisting of an inductor and a capacitor, connected as shown in Figure 4. Commonly used to prevent AC signals from passing the inductor on one leg of the tee to the power supply while allowing the passage of DC, the reverse is true via the other leg containing a capacitor for the connection to the oscilloscope. However, in the case of the FC measurement, power supply and oscilloscope protection are required while measuring the incident pulse of electrons, which is essentially a transient DC signal. As a preliminary experiment, the FC was tested unbiased, as well as with a bias of −50 V, 0 V (bias circuit connected with power supply set to 0 V), 50 V, and 102 V. The negative bias is used to confirm the circuit is wired correctly and behaves as expected by producing a signal less than that of the unbiased circuit. This preliminary experiment produced results that did not improve with the addition of positive external bias, which was at odds with expectations. Inspection of oscilloscope traces revealed what appeared to be a mismatch of the resistor-capacitor (RC) time constant of the circuit with the pulse length of the linac due to a constantly diminishing signal during the pulse and a significantly positive tail. Although convention states that capacitors allow AC currents while blocking DC, any transient currents will pass the capacitor for a short period of time, proportional to the RC time constant. Hence, when measuring a DC signal with a bias tee circuit, the value of the capacitor in the bias tee will cause signal decay according to $e^{\frac{-t}{RC}}$ and can even reduce the initial signal significantly if the RC time constant is low enough. A custom-built bias tee (CBT) of increased capacitance (and inductance, to maintain 50 Ω impedance) was designed to reduce signal decay over the pulse length of 150 ns to less than 0.5%. When integrating over the length of the pulse, a decrease of this magnitude will have a negligible effect on the result of the integral.

With the biased FC signal corrected, the experiment was repeated with a wider range of charge values. For voltages of −50 V, 0 V, +25 V, +50 V, +75 V, and +100 V, as well as unbiased, RF power was again increased in finite steps to increase the charge contained within a pulse. Measurements were also made with 0 RF power at the beginning of each iteration of the experiment to quantify signal due to background noise, which was subsequently subtracted from both the CT and FC measurements. At each level of RF power, 10 measurements were recorded to allow a mean and standard deviation to be calculated. During the period in which the experiments were conducted, the linac suffered from a minor vacuum leak, producing fluctuations that could not be immediately rectified due to operational requirements at the Australian Synchrotron. This led to different levels of charge being produced for a given RF power over the course of a shift. However, charge production was constant for each data point during the short time frame in which a series of measurements were made for a given bias. Results were plotted, with a linear trend line fitted to each dataset, to assess any change in signal during biased measurements by comparing the slope of the line. Increased electron stopping efficiency due to a positive bias on the FC absorber should lead to a proportional increase in signal and can be compared to the expected losses predicted by Geant4 when unbiased to assess the FC performance.

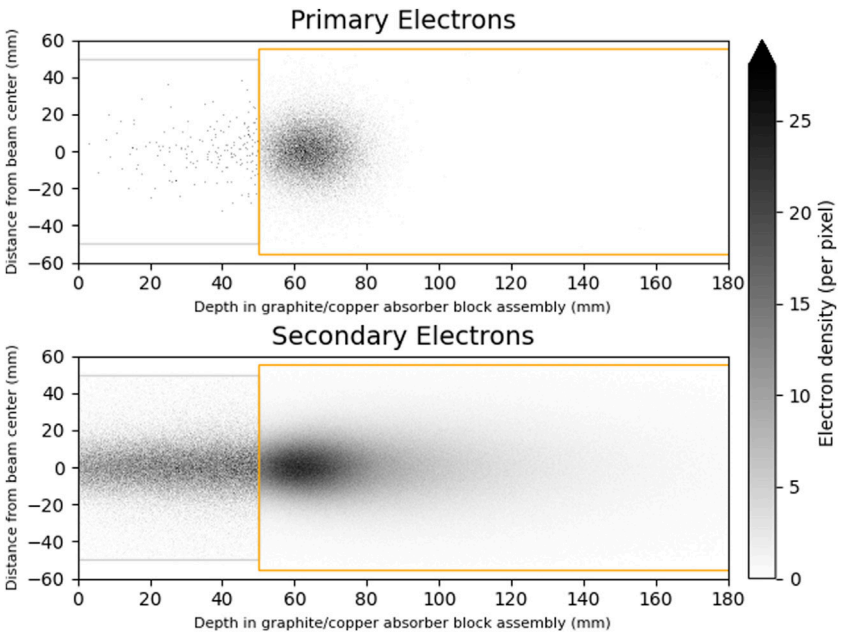

FIGURE 5
Geant4 simulation result of 3×10^5 histories scoring the positions at which primary and secondary electrons stop within the graphite and copper blocks (shown as gray and orange rectangles, respectively) of the PEER FC. Transverse coordinates have been collapsed into a single dimension on the vertical axis. The heatmap reflects the number of electrons stopped at that location.

3 Results

Figure 5 shows the simulated positions of stopped primary and secondary electrons for 3×10^5 generated histories within the simulation. In an unbiased circuit, the primary electron stopping efficiency is predicted to be as high as (99.22 ± 0.10)% including (1.38 ± 0.02)% that are backscattered from the copper toward the graphite. Of the secondaries created in the copper and graphite, relative to the generated primary electrons, only (2.49 ± 0.04)% are expected to escape. However, secondary electrons created elsewhere, both within and from outside the FC may stop in the conductive absorbers, as well as the stainless-steel housing. Secondary electrons are also created in the stainless steel housing, of which some leave.

Table 1 collates the results of these scenarios and expresses their quantities, the primary electron capture efficiency, and net capture efficiency due to escaping secondaries, and the expected electrical signal loss relative to the 3×10^5 primary electrons generated in the Geant4 simulation. Electrons leaving or stopping in the conductive absorbers and stainless-steel housing, as well as primary electrons that did not stop in the conductive absorbers, will contribute to the expected electrical signal, the magnitude of which has also been expressed in Table 1. The energy of secondary electrons escaping the conductive absorbers in the simulation has been plotted in Figure 6 to gain a further understanding of the FC performance and to aid in the analysis of experimental measurements.

Figure 7 shows the first results of the PEER FC. Initially, an unbiased measurement was made, followed by the addition of a Pulse Labs bias tee to the measuring circuit to allow a DC voltage to be applied to the copper conducting block. Voltages of −50 V, 0 V, 50 V, and 102 V were tested. Applying −50 V yielded a lower stopping efficiency, as expected. However, applying a bias of 0 V, 50 V, and 102 V also resulted in a lower stopping efficiency relative to unbiased measurements. The introduction of the Pulse Labs bias tee caused a large signal loss, irrespective of the applied voltage. Figure 8B displays a sample oscilloscope trace when using the Pulse Labs bias tee to

TABLE 1 Numerical results of five repeats of the Geant4 simulation, scoring the quantity of particles stopped in a volume that did not originate within or leaving a volume after originating within. The net capture efficiency is relative to the generated primary electrons. It is calculated by summing the expected contributions to the signal with a negative term for those contributions that will lead to a decreased current in the FC measuring circuit. Stated uncertainties are sample standard deviations.

	Percentage
Primary stopped in absorbers	99.22 ± 0.10
Primary stopped in housing	0.19 ± 0.01
Primary never stopped	0.61 ± 0.02
Secondary stopped in absorbers	1.3 ± 0.02
Secondary leaving absorbers	2.49 ± 0.04
Secondary stopped in housing	1.83 ± 0.02
Secondary leaving housing	2.47 ± 0.03
Backscattered from copper to graphite	1.38 ± 0.02
Primary electron capture efficiency	99.22 ± 0.10
Net capture efficiency	97.87 ± 0.24
Expected electrical signal loss	2.13 ± 0.24

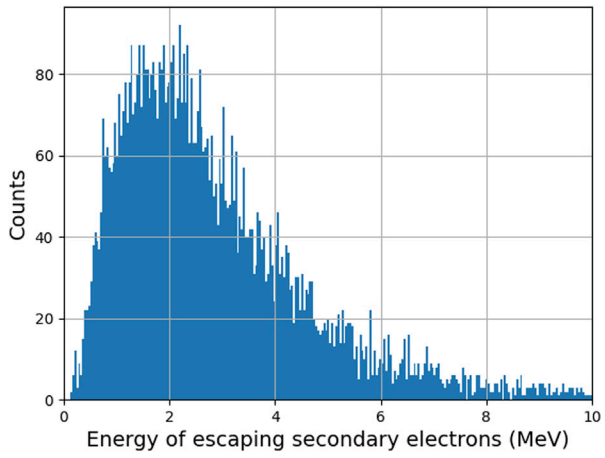

FIGURE 6
Simulated energy spectrum of secondary electrons as they leave the copper and graphite absorbers. The minimum energy is 0.12 MeV.

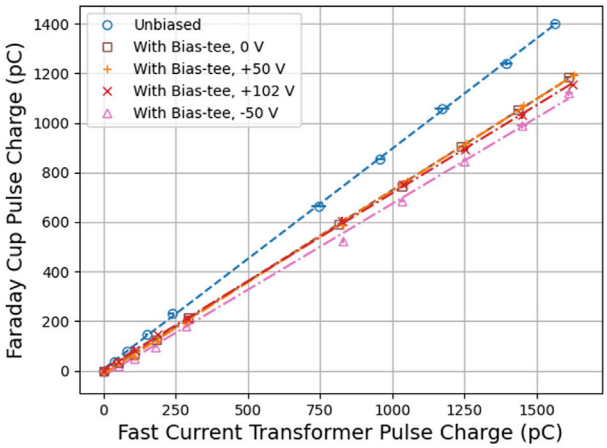

FIGURE 7
Charge measurements for the PEER FC, plotted against the CT with a Pulse Labs 5550B-104 bias tee in the measurement circuit. Measurements have been offset by the baseline measurement with no RF power to the linac. Measurements with a positive DC voltage applied to the FC yield a lower stopping efficiency than the unbiased measurements, indicating an issue with the readout system as a lower efficiency is not in agreement with theory. Uncertainties, if not visible, are within markers.

facilitate the external bias, compared to the unbiased trace shown in Figure 8A. Clearly, the shape of the pulse has been affected by introducing the bias tee into the measurement circuit. The diminishing signal during the pulse, coupled with the non-negligible positive tail, indicated a CBT with a larger RC time constant was required.

By constructing a CBT with the capacitance raised by more than an order of magnitude, the FC signal returned to a shape that was visually comparable to an unbiased signal, and a sample trace is shown in Figure 9A. It should be noted that this sample trace is included only to demonstrate the shape of the pulse, and the magnitude should not be compared to previous results in Figure 8, as the measurements were performed over a month later under different operating parameters due to operational conditions at the Australian Synchrotron. As VHEE accelerators are at the frontier of what is possible for maximizing charge within a pulse while minimizing the temporal profile, possible changes in operating conditions are to be expected and further highlight the requirement for custom diagnostic solutions to perform radiotherapy research.

After testing the CBT and ensuring the shape of the oscilloscope trace was as expected, the FC was used to measure the charge delivered by the linac, with and without the CBT, again including a measurement at 0 RF power to assess any electrical noise present in the linac tunnel and subtract it from the results. The data presented in Figure 9B compare unbiased measurements to those including the CBT with the power supply set to 0 V and demonstrate that within uncertainty, the CBT has no significant impact upon the resulting measurements.

With the CBT allowing unhindered measurement of the FC signal, the remaining external bias voltages were applied. Figure 10A presents a comparison of −25 V, unbiased, and +100 V, the largest positive voltage used. Linear fits for all positive external voltages used, as well as unbiased, are found in Figure 10B, with markers removed to aid readability. The results for external voltages of 25 V through to 100 V do not display a trend proportional to the magnitude of the voltage with an average improvement in the signal of (3.90 ± 0.04)%. Hence, it can be assumed that at 25 V or greater, all missing primaries and secondaries contributing to signal loss are retained or that no further retention is possible within the scope of the device, and any improvement may be due to collecting an ionization current produced in the air surrounding the conducting absorbers.

4 Discussion

The Geant4 simulation predicted that the FC would retain (99.22 ± 0.10)% of the primary electrons generated by the linac when placed 900 mm from the exit foil of the linac. However, losses due to secondary electrons result in an expected net efficiency of (97.87 ± 0.24)%. The simulation also predicted that the minimum energy of the secondary electrons leaving the copper and graphite absorbers would be 0.12 MeV. With this minimum energy, it will not be possible to retain any of the secondary electrons that leave the conductive absorbers by adding an external bias within a range that is practically possible.

The experimental results, while linear, may suggest the FC is not collecting all the charge as the magnitude of measurements is always lower than the CT. The CT that is currently installed, however, is an in-vacuum device located prior to the final magnets on the PEER linac that are normally used for shaping the electron beam and steering it into the booster ring of the Australian Synchrotron. This position can be seen in Figure 2. Uncalibrated and used only for relative measurements, the CT is not a measure of absolute charge, although it can still be used to compare the performance of the FC across different levels of RF power and, hence, the charge contained within a pulse.

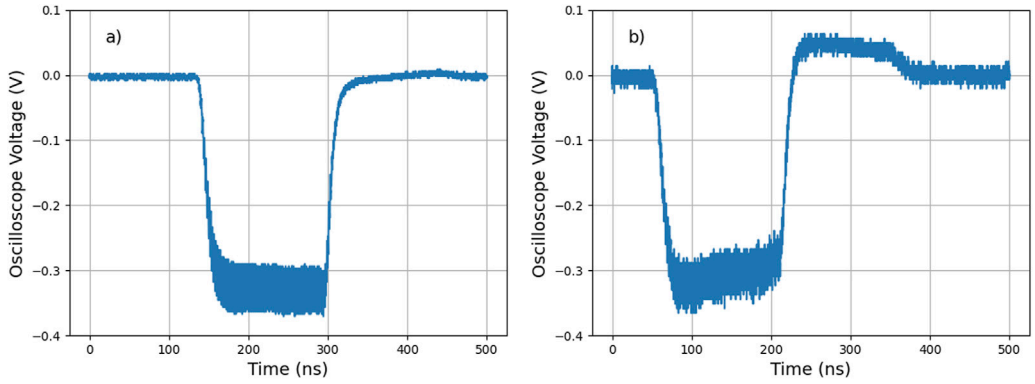

FIGURE 8
The oscilloscope trace recorded from unbiased FC measurements and when using a Pulse Labs 5550B-104 bias tee to facilitate the application of an external DC voltage to bias the FC are shown above in **(A, B)**, respectively. The shape of the biased trace is indicative of an RC constant that is too low to allow measurement of the transient signal produced during the pulse of the linac.

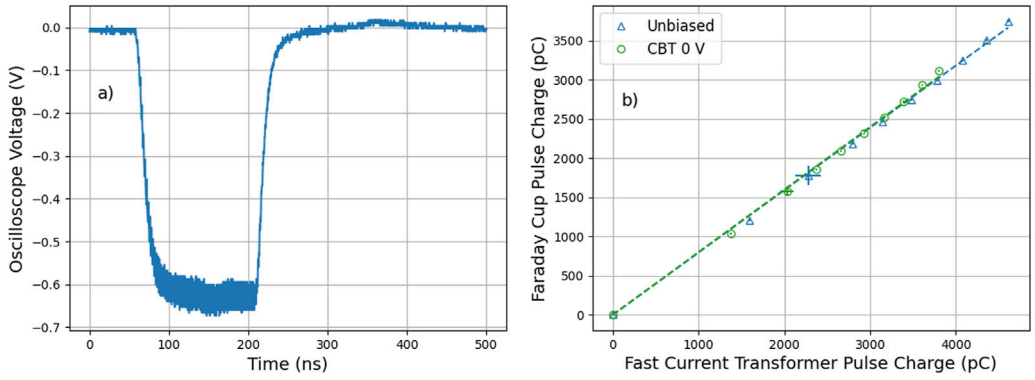

FIGURE 9
(A) Oscilloscope trace recorded when using the CBT to facilitate the application of an external DC voltage to bias the FC. The shape of the trace is what is expected from a linac pulse. **(B)** Results of the FC at 0 V via the CBT and unbiased with direct connection to the oscilloscope to investigate any impact on the signal due to the inclusion of the CBT. The slopes of the fitted lines are the same, with a slope of 0.795 $\pm$ 0.004 for measurements with a direct connection between the FC and oscilloscope and 0.799 $\pm$ 0.005 for the measurements with the CBT included in the circuit. The CBT has no impact on the measurements. Uncertainties, if not visible, are within markers.

Initially, including a commercial bias tee in the measurement circuit to facilitate the application of an external DC voltage resulted in measurements of lower magnitude than those without external bias. Further work led to the build of a CBT for this application, the inclusion of which resulted in no change to the electrical signal, as shown in Figure 9B. With this improvement to the measurement circuit, the experiment produced results in which the application of a negative voltage produced a decreased signal compared to the unbiased circuit, while positive voltages showed no correlation to an improved signal, leading to an average increase in signal of (3.9 $\pm$ 0.04)%.

During the design phase of the FC, the ability to apply an external bias to the FC was incorporated with the intent of retaining all secondaries created within the copper and graphite absorbers. However, as discussed above and shown in Figure 6, the Geant4 simulation reveals that the energies of escaping secondaries are orders of magnitude too great to be retained with the application of 100 V. Hence, retaining these secondary electrons with an external bias is not possible as a voltage of the required magnitude, on the order of 10^6 V, simply cannot be applied to the FC. These secondaries must undergo minimal interaction within the copper and graphite, retaining most of the energy imparted to them, and would be likely to leave even if the size of the copper and graphite absorbers were to be marginally increased. Hence, any effort to retain these secondaries would require significant changes to the physical size of the FC, which would not be possible due to the space limitations at PEER.

The improvement in signal did not trend proportionally to the magnitude of the applied voltage. A plausible explanation is that the increase in signal is due to the collection of a small ionization current in the air surrounding the absorbers. To briefly investigate this,

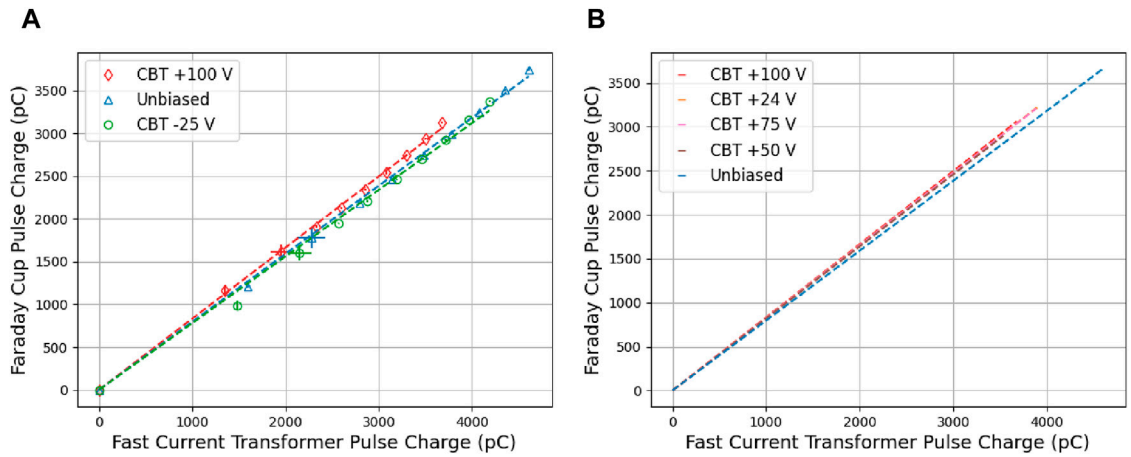

FIGURE 10
(A) FC results for both unbiased and with the CBT in the measurement circuit. Data for −25 V, unbiased, and +100 V only are included in this figure for clarity. The negatively biased measurements result in a lower stopping efficiency, as expected. Uncertainties, if not visible, are within markers. **(B)** Results for all measurements with a positive bias applied *versus* the unbiased measurement. Markers have been removed to facilitate a clearer presentation of data. The linear fits show the improvement in FC stopping efficiency is not correlated with increasing positive bias. The average slope of the measurements with external voltage applied is 0.826 ± 0.005, an increase of 3.90 ± 0.04% relative to the unbiased measurements with a slope of 0.795 ± 0.004.

consider that applying an external bias of 25 V–100 V produces an electric field between the copper absorber (the dominant absorber by surface area) and outer housing in the radial direction of 13.93 V cm^{-1} to 55.71 V cm^{-1}. These values can be used to calculate the electron drift velocity in-air using the Magboltz code (version 11.19) [26], a Monte Carlo simulation for solving the Boltzmann transport equations for electrons in gas mixtures. For a simple mixture of 78% oxygen and 22% nitrogen at 20°C and 101.3 kPa, the Magboltz code calculates an electron drift velocity of 1.84 μm ns^{-1} to 3.45 μm ns^{-1}. Within this range of drift velocities, the maximum distance an electron escaping recombination in-air can travel during the FC measurement is estimated to be 0.52 mm. This suggests any ionization current collected must have originated within very close proximity to the conductive absorbers. If all the electrons created in the void between the conductive absorbers and outer shell due to ionization of the air were collected, the expected increase in the signal would be orders of magnitude larger. This explanation could be investigated further by designing the FC to be operated under a vacuum, as there would no longer be any ionization of air. In this scenario, any operation of the FC with an external bias would require a vacuum. However, the operation of the FC under vacuum, without the application of an external bias, would not produce any benefits. Given the strong performance of the FC without an external bias, the increased complexity of evacuating the FC will create a situation whereby diminishing returns will quickly render further pursuits of marginal gains unpractical.

As the increase in electrical signal cannot be due to the retention of the secondary electrons created within the copper and graphite, the improved results should be discarded as they do not reflect the charge within the linac pulse that is incident upon the FC. Without the application of an external voltage, oscilloscope isolation is not required, reducing measurement complexities. Additionally, this renders the PEER environment safer for future users working in close proximity to the FC by removing any risk of contact with an external voltage.

5 Conclusion

The results of this work demonstrate that the PEER FC is believed to accurately represent the charge incident upon it for the intended use of informing future dosimetry simulations at PEER and relative measurements of charge between pulses during experiments. To calculate the charge traversing the exit foil for different experimental settings, we recommend that the PEER FC be used unbiased with the application of a scaling factor determined by Geant4 simulation on a case-by-case basis dictated by user requirements.

The designed and built Faraday cup is suitable for determining in-air, the total charge delivered by 100 MeV electrons to the PEER end-station, and will, therefore, form a valuable part of the expanding suite of diagnostic tools for future UHDR VHEE radiotherapy research.

Data availability statement

The raw data supporting the conclusions of this article will be made available by the authors, without undue reservation.

Author contributions

JC: conceptualization, data curation, formal analysis, investigation, methodology, visualization, writing–original draft, and writing–review and editing. JP: formal analysis and writing–review and editing. SG: software, supervision, and writing–review and editing. AR: funding acquisition, resources, supervision, and writing–review and editing. ML:

funding acquisition, resources, supervision, and writing–review and editing. Y-RT: conceptualization, data curation, funding acquisition, investigation, resources, software, supervision, and writing–review and editing.

Funding

The author(s) declare that financial support was received for the research, authorship, and/or publication of this article. JC receives the Australian Government RTP scholarship APP505948.

Acknowledgments

This research was undertaken on the PEER beamline, Australian Synchrotron, which is part of ANSTO.

Conflict of interest

The authors declare that the research was conducted in the absence of any commercial or financial relationships that could be construed as a potential conflict of interest.

The author(s) declared that they were an editorial board member of Frontiers, at the time of submission. This had no impact on the peer review process and the final decision.

Publisher's note

References

1. Schüler E, Acharya M, Montay-Gruel P, Loo JBW, Vozenin MC, Maxim PG. Ultra-high dose rate electron beams and the FLASH effect: from preclinical evidence to a new radiotherapy paradigm. *Med phys*, 49 (2022) 2082–95. doi:10.1002/mp.15442John Wiley and Sons, Ltd

2. Favaudon V, Caplier L, Monceau V, Pouzoulet F, Sayarath M, Fouillade C, et al. Ultrahigh dose-rate FLASH irradiation increases the differential response between normal and tumor tissue in mice. *Sci Translational Med* (2014) 6:245ra93. doi:10.1126/scitranslmed.3008973

3. Montay-Gruel P, Acharya MM, Gonçalves Jorge P, Petit B, Petridis IG, Fuchs P, et al. Hypofractionated FLASH-RT as an effective treatment against glioblastoma that reduces neurocognitive side effects in mice. *Clin Cancer Res official J Am Assoc Cancer Res* (2021) 27:775–84. doi:10.1158/1078-0432.CCR-20-0894

4. Sarti A, De Maria P, Battistoni G, De Simoni M, Di Felice C, Dong Y, et al. Deep seated tumour treatments with electrons of high energy delivered at FLASH rates: the example of prostate cancer. *Front Oncol* (2021) 11:777852. doi:10.3389/fonc.2021.777852

5. Ronga MG, Cavallone M, Patriarca A, Leite AM, Loap P, Favaudon V, et al. Back to the future: very high-energy electrons (VHEEs) and their potential application in radiation therapy. *Cancers* (2021) 13:4942. doi:10.3390/cancers13194942

6. DesRosiers C, Moskvin V, Bielajew AF, Papiez L. 150-250 MeV electron beams in radiation therapy. *Phys Med and Biol* (2000) 45:1781–805. doi:10.1088/0031-9155/45/7/306

7. Cayley J, Tan YRE, Petasecca M, Cutajar D, Breslin T, Rosenfeld A, et al. MOSkin dosimetry for an ultra-high dose-rate, very high-energy electron irradiation environment at PEER. *Front Phys* (2024) 12. doi:10.3389/fphy.2024.1401834

8. Kwan I, Rosenfeld A, Qi Z, Wilkinson D, Lerch M, Cutajar D, et al. Skin dosimetry with new MOSFET detectors. *Proc 15th Solid State Dosimetry (Ssd15)* (2008) 43:929–32. doi:10.1016/j.radmeas.2007.12.052

9. Tai M, Patterson E, Metcalfe PE, Rosenfeld A, Oborn BM. Skin dose modeling and measurement in a high field in-line MRI-linac system. *Front Phys* (2022) 10. doi:10.3389/fphy.2022.902744

10. Patterson E, Stokes P, Cutajar D, Rosenfeld A, Baines J, Metcalfe P, et al. High-resolution entry and exit surface dosimetry in a 1.5 T MR-linac. *Phys Eng Sci Med* (2023) 46:787–800. doi:10.1007/s13246-023-01251-6

11. Biasi G, Su FY, Al Sudani T, Corde S, Petasecca M, Lerch MLF, et al. On the combined effect of silicon oxide thickness and boron implantation under the gate in MOSFET dosimeters. *IEEE Trans Nucl Sci* (2020) 67:534–40. Conference Name: IEEE Transactions on Nuclear Science. doi:10.1109/TNS.2020.2971977

12. Su FY, Biasi G, Tran LT, Pan V, Hill D, Lielkajis M, et al. Characterization of MOSFET dosimeters for alpha particle therapy. *IEEE Trans Nucl Sci* (2022) 69:925–31. Conference Name: IEEE Transactions on Nuclear Science. doi:10.1109/TNS.2022.3153697

13. Verhey LJ, Koehler AM, McDonald JC, Goitein M, Ma I-C, Schneider RJ, et al. The determination of absorbed dose in a proton beam for purposes of charged-particle radiation therapy. *Radiat Res* (1979) 79:34–54. Publisher: Radiation Research Society. doi:10.2307/3575020

14. Diffenderfer ES, Verginadis II, Kim MM, Shoniyozov K, Velalopoulou A, Goia D, et al. Design, implementation, and *in vivo* validation of a novel proton FLASH radiation therapy system. *Int J Radiat Oncol Biol Phys* (2020) 106:440–8. doi:10.1016/j.ijrobp.2019.10.049

15. Darafsheh A, Hao Y, Zwart T, Wagner M, Catanzano D, Williamson JF, et al. Feasibility of proton FLASH irradiation using a synchrocyclotron for preclinical studies. *Med Phys* (2020) 47:4348–55. United States. doi:10.1002/mp.14253

16. Schoenauen L, Coos R, Colaux JL, Heuskin AC. Design and optimization of a dedicated Faraday cup for UHDR proton dosimetry: implementation in a UHDR irradiation station. *Nucl Instr Methods Phys Res Section A: Acc Spectrometers, Detectors Associated Equipment* (2024) 1064:169411. doi:10.1016/j.nima.2024.169411

17. Giuliano L, Franciosini G, Palumbo L, Aggar L, Dutreix M, Faillace L, et al. Characterization of ultra-high-dose rate electron beams with ElectronFlash linac. *Appl Sci* (2023) 13:631. doi:10.3390/app13010631

18. Richter C, Karsch L, Dammene Y, Kraft SD, Metzkes J, Schramm U, et al. A dosimetric system for quantitative cell irradiation experiments with laser-accelerated protons. *Phys Med Biol* (2011) 56:1529–43. doi:10.1088/0031-9155/56/6/002

19. Johnston R, Bernauer J, Cooke C, Corliss R, Epstein C, Fisher P, et al. Realization of a large-acceptance Faraday cup for 3MeV electrons. *Nucl Instr Methods Phys Res Section A: Acc Spectrometers, Detectors Associated Equipment* (2019) 922:157–60. doi:10.1016/j.nima.2018.12.080

20. Cascio EW, Gottschalk B. A simplified vacuumless Faraday cup for the experimental beamline at the francis H. Burr proton therapy center. In: Journal Abbreviation: 2009 IEEE Radiation Effects Data Workshop (2009). p. 161–5. doi:10.1109/REDW.2009.5336294*IEEE Radiat Effects Data Workshop*

21. Brown KL, Tautfest GW. Faraday-cup monitors for high-energy electron beams. *Rev Scientific Instr* (1956) 27:696–702. doi:10.1063/1.1715674

22. Winterhalter C, Togno M, Nesteruk KP, Emert F, Psoroulas S, Vidal M, et al. Faraday cup for commissioning and quality assurance for proton pencil beam scanning beams at conventional and ultra-high dose rates. *Phys med biol*, 66 (2021) 124001. doi:10.1088/1361-6560/abfbf2IOP Publishing

23. Morgan A. Design of the Faraday cups in diamond. In: *Proceedings of DIPAC 2005* (2005).

24. Agostinelli S, Allison J, Amako K, Apostolakis J, Araujo H, Arce P, et al. Geant4—a simulation toolkit. *Nucl Instr Methods Phys Res Section A: Acc Spectrometers, Detectors Associated Equipment* (2003) 506:250–303. doi:10.1016/S0168-9002(03)01368-8

25. Arce P, Bolst D, Bordage MC, Brown JMC, Cirrone P, Cortés-Giraldo MA, et al. Report on G4-med, a Geant4 benchmarking system for medical physics applications developed by the Geant4 medical simulation benchmarking group. *Med. Phys.* 48 (2021) 19–56. doi:10.1002/mp.14226John Wiley and Sons, Ltd

26. Biagi S. Monte Carlo simulation of electron drift and diffusion in counting gases under the influence of electric and magnetic fields. *Nucl Instr Methods Phys Res Section A: Acc Spectrometers, Detectors Associated Equipment* (1999) 421:234–40. doi:10.1016/S0168-9002(98)01233-9

frontiers | Frontiers in Physics

TYPE Original Research
PUBLISHED 05 November 2024
DOI 10.3389/fphy.2024.1454854

OPEN ACCESS

EDITED BY
Paola Ballesteros Zebadua,
Manuel Velasco Suárez National Institute of Neurology and Neurosurgery, Mexico

REVIEWED BY
Antonio Gilardi,
Stanford University, United States
Markus Kuster,
European X-Ray Free Electron Laser, Germany

*CORRESPONDENCE
Paul Schütze,
paul.schuetze@desy.de

RECEIVED 25 June 2024
ACCEPTED 25 September 2024
PUBLISHED 05 November 2024

CITATION
Schütze P, Abel A, Burkart F, de Silva LMS, Dinter H, Dojan K, Herkert A, Jaster-Merz S, Kellermeier MJ, Kuropka W, Mayet F, Ruiz Daza S, Spannagel S, Vinatier T and Wennlöf H (2024) electronCT - an imaging technique using very-high energy electrons. *Front. Phys.* 12:1454854. doi: 10.3389/fphy.2024.1454854

electronCT - an imaging technique using very-high energy electrons

Paul Schütze[1]*, Aenne Abel[1,2], Florian Burkart[1], L. Malinda S. de Silva[1], Hannes Dinter[1], Kevin Dojan[3], Adrian Herkert[1], Sonja Jaster-Merz[1], Max Joseph Kellermeier[1], Willi Kuropka[1], Frank Mayet[1], Sara Ruiz Daza[1,3], Simon Spannagel[1], Thomas Vinatier[1] and Håkan Wennlöf[1]

[1]Deutsches Elektronen-Synchrotron DESY, Hamburg, Germany, [2]Institut für Experimentalphysik, University of Hamburg, Hamburg, Germany, [3]Physikalischen Institut, University of Bonn, Bonn, Germany

The electronCT technique is an imaging method based on the multiple Coulomb scattering of relativistic electrons and has potential applications in medical and industrial imaging. It utilizes a pencil beam of electrons in the very high energy electron (VHEE, 50–250 MeV) range and a single detection layer for the determination of the beam profile. The technique constitutes a projectional, two-dimensional imaging method and thus also qualifies for the tomographic reconstruction of samples. Given the simplicity of the technical setup and its location behind the sample, the electronCT technique has potential synergies with VHEE radiotherapy, making use of the same electron source for both treatment and diagnostics and thus being a candidate for *in situ* imaging and patient localization. At the same time, several technical challenges arise from the measurement technique when applied for the imaging of living beings. Measurements performed at the ARES linear particle accelerator at an electron energy of 155 MeV using a mouse phantom and a Timepix3 silicon pixel detector assembly demonstrate the feasibility of this technique. Both projectional and tomographic reconstructions are presented and the potential and limits of the technology are discussed.

KEYWORDS

electronCT, medical imaging, multiple scattering, ARES, VHEE, Timepix3, radiation therapy

1 Introduction

In the past years, the field of radiation therapy has seen fast developments, driven by particle accelerator technologies that leverage the use of the very high energy electron (VHEE) regime, which typically refers to electrons in the energy range of 50 MeV–250 MeV, and the advancements in FLASH radiotherapy [1]; [2]; [3]; [4]. In order to achieve a safe and effective treatment in radiation therapy, reliable imaging strategies are inevitable. The application of imaging techniques in the planning and performance of radiation therapy is condensed in the term of image guided radiation therapy (IGRT). A large number of imaging methods can be and are applied in the context of IGRT, such as X-ray imaging and CT, magnetic resonance imaging (MRI), positron emission tomography (PET), ultrasound imaging and camera-based imaging [5]. While a good accuracy of a few millimeters can be achieved in aligning the treatment beam with an image using separate devices for these

tasks, a unification of the treatment and an imaging device could improve this accuracy significantly and has been achieved for photon therapy [6].

We present an alternative imaging technique called electron computed tomography (electronCT), that is based on highly energetic charged particles such as VHEE and their interaction with matter, in particular the multiple Coulomb scattering of the particles traversing the patient. This measurement technique enables the use of the same accelerating structure for both treatment and diagnostics in the context of radiotherapy with VHEE and thus naturally creates a common coordinate system and does not require any alteration of the instrumentation around the patient. This makes electronCT a candidate for an IGRT imaging technique in VHEE radiotherapy, for example, for the *in situ* localization of tumors or as an input for the alignment of high-resolution X-ray, CT or MRI images with the coordinate system applied for the treatment.

This article presents the concepts of the electronCT technique and shows proof-of-concept measurements. Furthermore, the potential and limits of this method are discussed.

2 The electronCT technique

The technique of electronCT relies on the multiple Coulomb scattering of highly energetic particles in matter. When traversing matter, charged particles, typically of momenta in the order of few hundreds of MeV, are stochastically deflected by the electrostatic force of the material's nuclei, leading to an effective deflection when traversing an object. The effective deflection depends on the radiation length X_0 and the thickness l of the material, as well as on the charge and momentum p of the incident particle. This scattering process and with it the effective deflection angle distribution are theoretically described by Molière's theory [7]; [8]. The central part of this distribution of deflection angles can be described by a Gaussian distribution centered around zero. The width θ_0 of this distribution is commonly approximated via a formula introduced by Highland [9], with the parameters revised by Lynch and Dahl [10]:

$$\theta_0 = \frac{13.6\,\mathrm{MeV}}{\beta c p} z \sqrt{\frac{l}{X_0}} \left(1 + 0.038 \ln\left(\frac{l}{X_0}\right)\right), \tag{1}$$

with β as the velocity in fractions of the speed of light c and z the charge number of the incident particle. The width of the distribution depends on the radiation length of the material traversed, increases with the thickness of the material and is reduced for higher momenta.

In the electronCT technique, the amount of material traversed by a beam is measured by determining the opening angle of a collimated beam of particles after traversing a sample. The amount of material is defined as the material's thickness normalized to its radiation length, $\epsilon = l/X_0$, and often referred to as the material budget. This measurement can be accomplished by detecting the transverse beam profile using a single detection layer downstream of the sample, employing position sensitive radiation detectors. Assuming an incident beam of charged particles with low transverse size and low divergence, the width of the transverse beam profile at a given distance behind the sample is thus a measure for the material budget along the path of the particles.

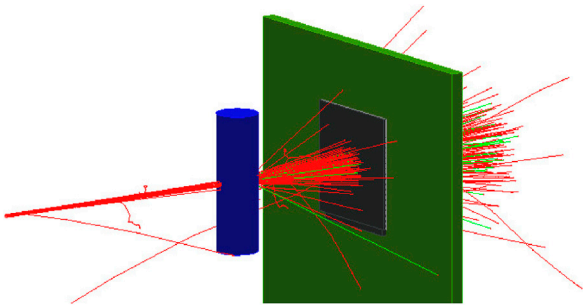

FIGURE 1
Visualisation of the simulation corresponding to the acquisition of a single data point acquired via the electronCT technique. A beam consisting of one hundred electrons with a width of 100 µm (red lines) is scattered at a sample (blue) and consecutively passes through a silicon detector (grey). Along the electron trajectories, a small number of Bremsstrahlung photons is generated (light green).

While many types of radiation detectors are applicable and should be chosen depending on the expected size and intensity of the beam delivered by the particle accelerator, this publication presents the use of silicon pixel detectors which are typically applied in high energy physics. Silicon detectors measure the amount of energy deposited in a sensitive volume via ionisation processes and a segmentation of the sensor in pixels allows for the retrieval of two-dimensional information on a particle's traversal position [11]. They are typically optimized for the tracking of individual particles through a multi-detector setup, thus their dynamic range is optimized for a small number of particles per readout cell. In this case, silicon pixel detectors come with the benefit of less signal per readout channel and thus a lower required dynamic range compared to sensors segmented in strips.

Figure 1 shows the visualisation of the simulated acquisition of a single data point with this technique, performed via the semiconductor detector simulation framework Allpix^2 [12], which utilizes the software toolkit Geant4 [13] for the simulation of the interaction of particles with matter. The incident beam, of which the individual particle trajectories are shown in red, is scattered at the sample (blue) before it is detected in the silicon detector (grey). In addition, a small number of Bremsstrahlung photons is generated (light green). The sample in this case consists of two nested cylinders with radii in the range of small medical samples and radiation lengths in the range of tissues. Figure 2 shows two examples for simulated beam profiles, with (right) and without sample present (left). Both beam profiles are displayed as the charge collected in the sensor, in units of kiloelectrons, as a function of the impact pixel coordinates and can clearly be distinguished from each other. Gaussian distributions are fitted to the projections of the beam profiles onto the x- and the y-axes and the corresponding beam sizes are determined as widths of the fitted distributions in units of pixels. The means of these widths, $\sigma_b = (\sigma_x + \sigma_y)/2$, are indicated in the corresponding graphs in Figure 2. The simulation demonstrates that a measurement of the beam profile of an initially collimated electron beam via a pixelated silicon sensor is sensitive to the traversal through a sample prior to the detection. In addition, this simulation was applied for designing the experimental layout. For this simulation, Allpix Squared version 3.0.3 [14], compiled with Geant4 version 11.2.1, has been used to

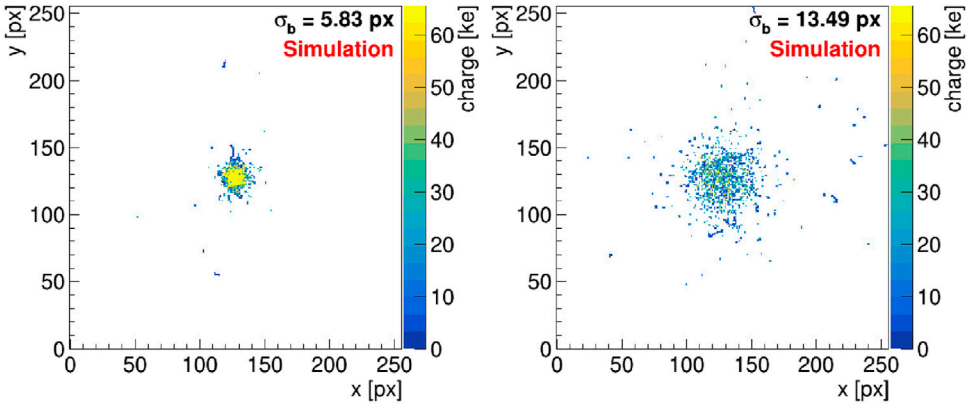

FIGURE 2
Simulation of beam profiles as detected by the silicon pixel detector in a simulation such as shown in Figure 1 for the beam not passing through the sample (left) and traversing the center of the sample (right). Shown is the collected charge in units of kiloelectrons as a function of the impact pixel coordinates.

simulate the interaction of a beam containing 1,000 primary electrons with the sample and the detector, applying a Geant4 physics list with the electromagnetic constructor *Livermore*. It should be noted that for the visualisation in Figure 1A beam of only one hundred electrons has been simulated for a better visibility.

Two-dimensional or projectional imaging can be achieved by the bunched particle beam rastering the sample or by moving the sample across a fixed beam, such that each electron bunch and thus each measured width of a bunch profile can be attributed to a certain impact position on a virtual transverse plane through the sample.

Three-dimensional imaging is enabled by recording projections at different impact angles. This can be achieved by either rotating the sample or, similarly to X-ray based computed tomography (CT) measurements, the rotation of the particle source, here the accelerating structure, and detector around the sample. The rotation of the particle accelerator around the sample or patient is technologically available in a few modern radiation treatment facilities [15]; [16].

Consequently, the experimental setup comprises an accelerating structure delivering a beam with momenta of a few hundreds of MeV and a beam size in the order of a few 100 µm, and a silicon pixel detector capable of coping with a high data rate.

A similar technique, also based on multiple Coulomb scattering but applying the measurement of individual electron trajectories of GeV-electrons in a large beam, has proven to provide 3D imaging with resolutions in the order of 100 µm and good contrast-to-noise ratios for a wide range of material densities, at the downside of a low particle rate and thus extensive measurement times [17]. The development of scanning the sample with a pencil beam brings the opportunity to drastically decrease the measurement time. In addition, it has the potential to reduce the complexity of both the setup and the analysis by omitting the need to reconstruct individual particle trajectories and thus to reduce the time required for the reconstruction of an image.

3 Experimental setup

The measurements shown in this work were performed at the Accelerator Research Experiment at SINBAD (ARES) [18] at DESY, Hamburg, using a Timepix3 silicon pixel detector assembly [19]. A medical phantom resembling a mouse was placed between the electron extraction window of the accelerator and the detector. The individual components were positioned as closely together as possible while assuring a clearance of the motion stages with respect to further components, leading to distances between the beam window and the phantom of 68 mm and between the beam window and the silicon detector of 134 mm. A picture of the main experimental setup can be seen in Figure 3.

The measurements presented herein use a sample mounted to a 4D positioning system which rasters the sample across a fixed beam.

3.1 ARES

The ARES accelerator is a linear electron accelerator delivering ultra-short bunches with a charge of up to few hundreds of picocoulombs [18]. It is designed for a kinetic energy of up to 155 MeV [18] and a bunch repetition rate of between 1 Hz and 50 Hz. For this experiment a repetition rate of 10 Hz was applied and significantly lower bunch charges, estimated to be in the order of 1 fC and less, were achieved via the use of the dark current, a current generated by field emission in the accelerating structure [20]. The beam was transversely focussed onto the sample using the last quadrupole magnets of the accelerator beamline. With this, a symmetric beam spot with an RMS size of around 320 µm was reached at the position of the sample and of about 360 µm at the detection plane, as will be presented below. The transverse beam size was observed to be dominated by the scattering at the beam exit window, consisting of a titanium (Ti Grade 5) foil of 50 (5) µm thickness.

3.2 Timepix3 silicon pixel detector

The choice of the detector is a crucial parameter for the electronCT method. For the presented application, a large readout buffer and a large dynamic range are two main demands

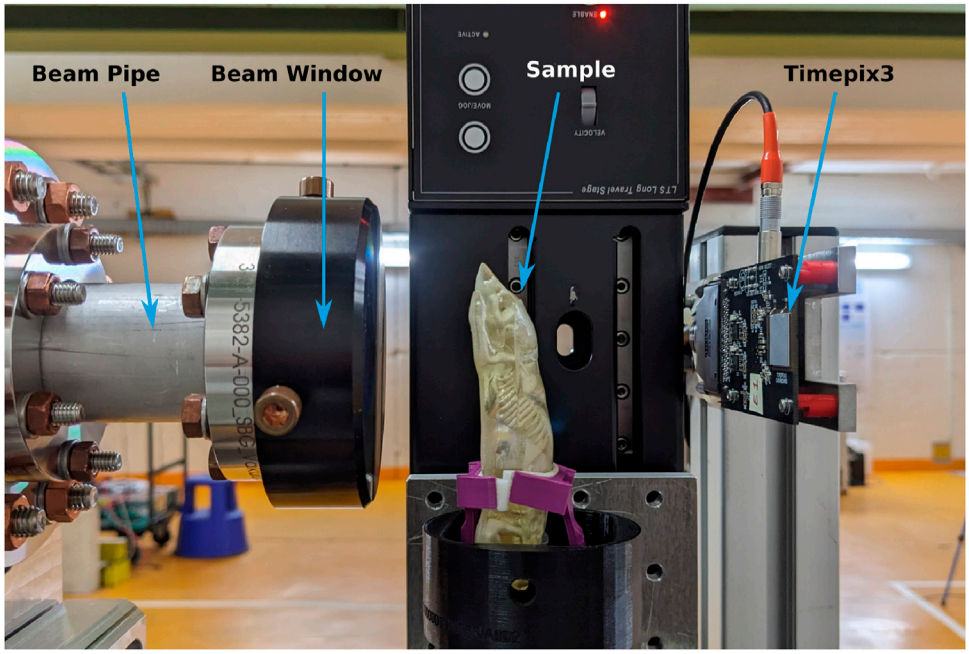

FIGURE 3
Picture of the electronCT setup at the ARES accelerator facility. The mouse phantom is mounted on a positioning stage and located in the center of the experiment. The beam exit window, secured by a black metallic cover, is to the left and the detector on the right hand side.

on the detection layer. The former is motivated by the fact, that at the traversal of a single bunch a large area of the detector and thus a large quantity of pixels is hit within a small amount of time, and all buffered data has to be read out before the arrival of the succeeding bunch to avoid potential dead times. The requirement for a large dynamic range arises from the fact, that the number of incident electrons remains constant, while the width of the beam profile strongly changes depending on the traversed material. In this experiment, both large peaks and long tails in the beam profile need to remain resolvable.

One type of detectors that fulfil these requirements are assemblies based on the Timepix3 or Medipix3 readout chips, which are already used in several medical applications [21]; [22]. Timepix3 readout chips feature an array of 256 × 256 pixels with a pitch of 55 µm × 55 µm and provide charge information via Time-over-threshold (ToT) detection with a TDC resolution of 10 bit, as well as a time-of-arrival (ToA) measurement. The assembly used herein consists of a Timepix3 readout chip bump-bonded to a silicon sensor with a thickness of 100 µm. The sensor was operated at a bias voltage of −21V to ensure full depletion [23] and read out using a Katherine readout system [24] controlled via the TrackLab software framework [25].

3.3 Phantom and positioning

The phantom represents a mouse body with the tissue additively manufactured from resin, a skeleton made from a water-gypsum mixture and organs formed from agarose [26]. These materials have been chosen due to their manufacturing properties, low costs and their X-ray attenuation coefficients close to those of a real mouse. It should be noted that the radiation length, as the underlying material parameter for electronCT measurements, does not scale linearly with the X-ray attenuation coefficient, but both strongly depend on the atomic number. However, the X-ray attenuation coefficient also exhibits a dependency on the particle energy, which is not the case for the radiation length. Hence, although the materials contained in the sample are not expected to reproduce the exact multiple Coulomb scattering behaviour of a biological sample, it is expected to provide a good benchmark for electronCT measurements.

Linear translation stages of the type LTS300 by Thorlabs [27]. were utilized for scanning the phantom across the beam in the two transverse dimensions, while the beam was kept at a constant position and the detector mounted on a fixed stand. The stages feature an accuracy of about 2 µm. The sample can also be moved along the beam axis, but the range of motion in this dimension is severely restricted as the experiment setup is optimized for minimum distances along the beam axis. The sample is furthermore mounted to a rotational stage of the type PRM1/MZ8 by Thorlabs [28]. with a vertical rotation axis, featuring a sub-degree rotational precision. This allows for an illumination from different angles and thus a tomographic measurement.

4 Methodology

4.1 Scan sequence

For two-dimensional measurements, the sample is moved across the x-y-plane, with the x-axis as the horizontal, and the y-axis as the vertical axis. The scans have been conducted using a continuous

motion along the x-axis at discrete steps along the y-axis, forming a serpentine path. In this schematic, the minimum achievable resolution of the resulting images is given by the velocity of the motion stage along x and the bunch repetition rate of 10 Hz, and the step size along y. With a motion velocity of e.g., 5 mm s^{-1}, the bunches sample the phantom with a spacing of $\Delta x = 0.5$ mm.

Three-dimensional, tomographic measurements via electronCT require a rotation of the sample, which is achieved by a rotation around the y-axis with the angle denoted as φ. For these studies, the motion system was set up to perform two-dimensional scans as mentioned above for a configurable number of rotation angles consecutively.

An alternative sequence has been defined as a scan in the x-φ-space at a fixed y-position, representing a single horizontal line for several rotation angles, which allows for the tomographic reconstruction of a single slice of the sample through the x-z-plane. The advantage of this measurement in comparison with a full three-dimensional scan is the potential to study the tomographic reconstruction potential and performance at a drastically reduced measurement time.

It should be noted that for all scan types the sequence of data points taken is not relevant for the data analysis and can be optimized e.g., for reducing the measurement time.

4.2 Data acquisition

For electronCT measurements, the electron bunch is focused at the detector, such that in most cases several electrons contribute to the signals of individual pixels. The time structure of the bunch does not allow for a separate detection of the individual primary particles and hence the summed deposited charge below each pixel is measured. As a consequence, a high bunch charge focused onto a small number of pixels would lead to a saturation of the detector front-end dynamic range and should thus be avoided.

The Timepix3 chip was configured with a threshold of about four kiloelectrons. It should be noted that the unit kiloelectrons (ke^-) here denotes the number of charge carriers collected per pixel and not the number of primary electrons contributing to the signal. The threshold corresponds to about 40% of the signal induced by a single electron and is thus sufficient for the detection of individual beam particles.

The readout chip performs a zero-suppression, i.e., only pixels detecting a signal larger than the configured threshold are registered, and can be operated in two modes, the so-called *sequential* (often called *frame-based*) readout mode or the *data-driven* mode. In the frame-based mode a readout frame is defined by an external signal and the data from all pixels that registered a signal above the configurable threshold within this frame is read out after the frame has ended. The Katherine readout system allows to delay the frame start with respect to an external signal and to set a configurable frame duration. In this readout mode the system can be configured, such that each frame represents the signals from an individual bunch. The data-driven readout mode represents a continuous detector readout, leading to a data set of all signals exceeding the threshold, containing the corresponding pixel addresses including timestamps. In this mode, the timestamps of the signals can be used to group them into signals arising from individual bunches during the post-processing of the data.

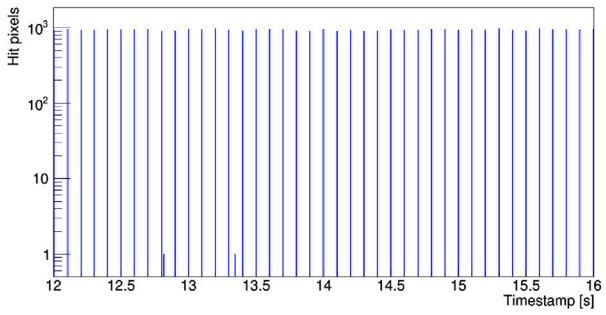

FIGURE 4
Time structure of the beam generated by ARES as recorded by the Timepix3 detector assembly, represented as the number of hit pixels as a function of time.

In case of the frame-based readout, frames have been triggered via the accelerator machine clock, with the delay manually adjusted, such that bunches arrive within the first microsecond of a frame. The frames were configured to feature a width of 10 µs The data contain the coordinates and ToT values of all pixels registering a signal above the threshold per readout frame as well as their ToA within the frame.

In the data-driven readout mode, the data contain the coordinates and ToT values of all signals above the threshold as well as each signal's ToA within the data stream. While the global timestamp of the readout chip itself features a range of 409.6 µs, the Katherine DAQ system is capable of extending the timestamp to a range of more than 20 days and is hence sufficient for all measurements performed.

4.3 Data analysis

4.3.1 Data processing

The data were converted and every frame was interpreted using the software framework Corryvreckan [29]. To interpret data recorded with the Katherine readout system via this framework, a module for reading data recorded by TrackLab was added. In the case of measurements applying the data-driven readout mode, no inherent frame structure is available that would allow to assign the detector data to a given state of the motion system. Instead, a continuous array containing all pixels with a signal above the threshold with the corresponding ToA is obtained. An example of the time structure of the recorded data is shown in Figure 4 by means of the number of hits as a function of their corresponding time stamps. The time structure shows a clear, regular pattern caused by the ARES bunch structure leading to large numbers of hit pixels in a vanishingly small time frame with a distance of 100 ms as expected from the bunch repetition rate of 10 Hz. Infrequent signals are recorded in between the arrivals of two bunches as seen at the positions of 12.8 s and 13.3 s and can be caused by noise or uncorrelated radiation.

The ToA information of each signal was used to group them into frames, where every frame represents the data induced by a single bunch. This was achieved with a minimal bias on the actual event separation by an algorithm splitting the data stream at positions where no significant group of signals has been recorded.

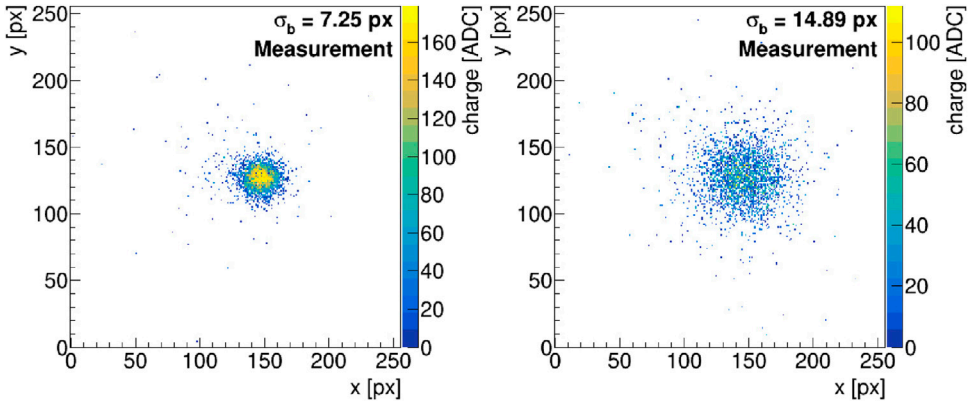

FIGURE 5
Charge map of the detector signal from two individual bunches, one not traversing the sample (left) and one traversing it (right).

Figure 5 shows two charge maps for individual frames, representing a mapping of all hits to their pixel coordinates with the ToT as color scale, one corresponding to a frame in which the beam does not pass through the sample (left) and one to a frame for which the sample was traversed by the beam (right). It is readily visible that the multiple scattering of the beam particles at the object enlarges the beam laterally at the position of the sensor. The sensor front-end saturates in case of large amounts of particles impinging in individual pixels, leading to a plateau visible in Figure 5 (left).

For the analysis of this data, a dedicated module in the Corryvreckan data analysis framework projects these maps onto the x- and the y-axes and performs a fit of a Gaussian distribution to each projection, retrieving the widths of the fitted distributions, σ_x and σ_y. Previous measurements showed that the scattering angles of individual particles along two orthogonal axes are uncorrelated, while the means of the distributions strongly correlate [17]. This suggests that σ_x and σ_y represent the same quantity and hence the measurements of the beam size along x and y can be treated as two independent measurements in order to reduce uncertainties. This procedure is mathematically equivalent to the generation of two images from the individual widths and averaging the image content. In the following, the beam size per frame is determined as the mean of the standard deviations retrieved from both fits, $\sigma_b = (\sigma_x + \sigma_y)/2$.

4.3.2 Image generation

The beam size per frame, as the measured quantity of interest, is attributed to the positions of the linear motion stages and, in case of tomographic measurements, the rotation stage. For this, the current stage positions are queried at a 10 Hz frequency and stored with their corresponding UNIX time stamps. As this process is not synchronized to the DAQ system, a synchronisation has to be performed in the post-processing and is implemented as follows: In a first step, the position of an absorber with a sharp edge, located next to the sample, is determined. This is achieved by means of a slow, manually controlled motion of the stage, in which the beam samples the edge of the absorber, and the simultaneous observation of a change in the charge maps recorded by the detector. Subsequently, before the beginning of each two- or three-dimensional scan, the absorber is moved into and out of the beam path as a part of the automated scan sequence. With the position of the absorber edge known, the exact time of the edge transition can be located both in the data stream of stage positions and in the beam profile data, as the latter exhibits a drastic increase in deposited charge at the time of this transition. The two data streams are then correlated using their individual time stamps corrected by the determined offset. No significant drift between the time stamps has been observed. This synchronization strategy requires stable beam conditions in terms of intensity and beam position, which was measured to be satisfied with relative intensity fluctuations in the order 5% and variations of the beam position of less than 20 µm at the position of the detection plane.

With the synchronized data streams of stage positions and beam profile data, each reconstructed beam size value can be attributed to a certain point in the x-y (2D), x-y-φ (3D) or x-φ (Single Slice) scan range. Equally spaced image cells within the scan range can be defined such, that either a single value is obtained per image cell, or the average of multiple values falling into a cell's range is determined. The former enables a better image resolution, while the latter has the potential to improve the image contrast.

In case of three-dimensional measurements, the beam size obtained by a measurement as discussed above is corrected by subtracting a background value, determined as the mean observed beam width within a region where the beam did not pass through the sample. This correction compensates for the finite width of the beam after traversing the beam window and takes into account the effect of multiple Coulomb scattering in air.

Subsequently, the data set is structured in sinograms, which are representations of the corrected beam size as a function of the x- and φ-positions for individual steps along the y-axis, using the assignment of beam size values to the x-y-φ phase space of the motion system. From these sinograms, slices of the material through the x-z-plane are obtained via inverse Radon transforms [30], computed individually for every step along y. For the measurements presented here, the open source software framework scikit-image [31]; [32] was used to perform a filtered back-projection applying a ramp filter for the reconstruction of individual slices. Subsequently, a wavelet denoising algorithm included in the framework following [33] is applied on the final images for an improvement of the image quality.

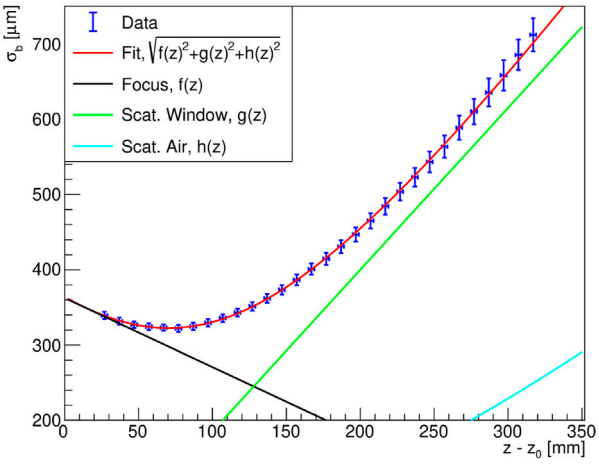

FIGURE 6
Measurement of the beam width σ_b as a function of the detector distance from the beam exit window. A fit to the data represents a quadratic superposition of a focusing and two scattering contributions from the beam exit window and air.

4.4 Beam characterization

The lateral size of the electron beam generated by the ARES linear accelerator was characterized in terms of a measurement as a function of the longitudinal distance from the beam exit window. For this measurement, the Timepix3 detector assembly, read out via the data acquisition system described above, was mounted to the three-dimensional x-y-z linear motion stage system and a scan along the beam axis was performed covering a distance range from the beam exit window of 27 mm $< z <$ 317 mm with a step size of 10 mm. The minimum distance was limited by mechanical constraints and the maximum distance given by the range of the motion stage. Per step, the stage positions were kept constant for 60 s.

The beam size was evaluated on a per-bunch basis and the mean beam size per step is displayed in Figure 6, with the error bars representing the RMS of the beam sizes per step.

The beam features a focal point at a distance of about 71 mm from the beam exit window with a beam size of 322 µm as a result of focusing the beam onto the sample. The trend as a function of the longitudinal distance can qualitatively be described via three terms added quadratically: the contributions represent a focusing of the beam via the quadrupoles ($f(z)$), the scattering at the beam window ($g(z)$) (both polynomials of first degree) and a contribution describing scattering in air ($h(z)$). The latter applies Equation 1 for computing the RMS lateral displacement after Equation (34.20) of [34]. This is indicated by a fit to the function

$$h(z) = \sqrt{f(z)^2 + g(z)^2 + h(z)^2} = \sqrt{\left(b_f + m_f x\right)^2 + \left(b_g + m_g x\right)^2 + \frac{a}{\sqrt{3}} z\theta_0(z)}$$

with the free parameters $b_{f,g}$, $m_{f,g}$ and a. The individual contributions are displayed in black, green and cyan. A quantitative analysis was not performed due to systematic effects such as a saturation of the detector for small beam sizes and the limited data range.

The data shows that the beam is focused at the position of the sample and the rotation axis, located at a distance of 68 mm from the beam exit window, which enables an optimal image resolution. The detection plane was positioned as close as possible, at a position of 134 mm with a beam size of 360 µm.

5 Results

5.1 Projectional measurements

In the following results, the beam size is displayed as a function of the sample position. This beam size serves as an estimator for the traversed material budget, hence a two-dimensional measurement qualitatively represents a two-dimensional projection of the material budget onto the image plane.

Figure 7 shows the result of a measurement performed in the frame-based readout mode with a scan velocity of 0.5 mm/s along the x-axis and 520 steps of 0.1 mm each along the y-axis. The measurement time amounted to 620 min.

The data were evaluated with image cell sizes of 0.05 mm × 0.1 mm (left) and 0.5 mm × 0.5 mm (right). Both images reveal many details of the sample: the skeleton can clearly be distinguished from the tissue and is resolved to a good level of detail, exhibiting the spine, the ribs, the arms and the skull. The tissue can be well distinguished from the background. The smallest features resolved in these images are the ribs with a thickness of about 0.5 mm, which provides an upper limit for the achieved resolution.

It is readily visible, that while achieving a better resolution in Figure 7 (left), Figure 7 (right) exhibits less noise and thus a higher contrast. The contrast-to-noise ratios (CNR) are determined by

$$\mathrm{CNR} = \frac{\mu_{\mathrm{sig}} - \mu_{\mathrm{bg}}}{\sqrt{\sigma_{\mathrm{sig}}^2 + \sigma_{\mathrm{bg}}^2}} \quad (2)$$

with μ and σ as the mean and standard deviation of values defined in a signal and a noise area. As a signal region, a homogeneous region in the shoulder of the sample representing tissue, and as a noise region, an equally sized region outside the sample have been used and are indicated as orange boxes. The CNRs result in 18.8 for the left image in Figure 7 and 34.7 for the right image in Figure 7.

5.2 Tomographic measurements

Two types of tomographic measurements have been performed using the presented phantom:

1. x-y-φ scan for a three-dimensional tomographic reconstruction.
2. x-φ scan for the tomographic reconstruction of a single slice in the x-z-plane.

For measurement 1, a scan velocity of 1.5 mm/s along the x-axis and 50 steps of 1 mm along the y-axis have been selected, with 37 projections recorded for a half turn, resulting in angular steps of 5°. The measurements were performed using the Katherine readout system in the data-driven readout mode, recording a continuous data stream for around 18 h.

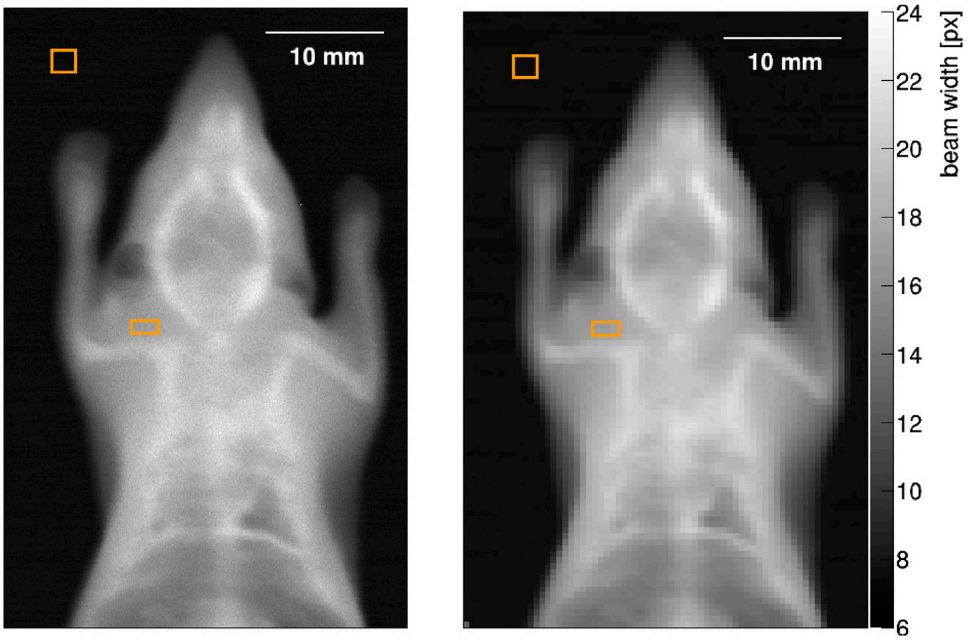

FIGURE 7
Two-dimensional electronCT measurements of a mouse phantom, evaluated with image cell sizes of 0.05 mm × 0.1 mm (left) and 0.5 mm × 0.5 mm (right). Orange boxes indicate the regions used for the determination of the image contrast.

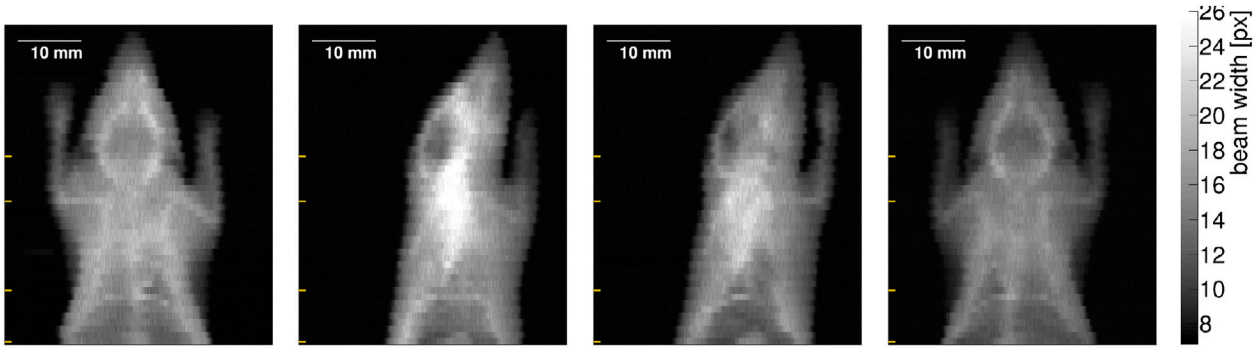

FIGURE 8
Two-dimensional projections of the phantom recorded for a tomographic measurement at rotation angles of $\varphi = \{ 0^{\circ}, 60^{\circ}, 120^{\circ}, 175^{\circ} \}$ (f.l.t.r.). Orange ticks on the left side of the images indicate the vertical positions for which reconstructions are presented.

From the three-dimensional scan, two-dimensional projection images can be generated for different rotation angles of the sample. Figure 8 shows four such projections for rotation angles of $\varphi = \{ 0^{\circ}, 60^{\circ}, 120^{\circ}, 175^{\circ} \}$ with image cell sizes of 0.15 mm × 1 mm. Due to the higher scan velocity and larger step size along y with respect to the images presented in Figure 7, the resolution is inferior to these. The projections acquired at rotation angles of 0° (left) and 175° (right) show similar features, but a reduced contrast can be observed in the latter. The reason for this is the positioning of the sample slightly off the rotation axis and thus the sample having different distances from the detector, which comes with an impact on the measured beam size.

Sinograms are generated for each horizontal line, hence for every scan step along the y-axis, combining the data of all rotation steps. An example is shown in Figure 9, displaying the beam size as a function of x and φ for a vertical position inside the head region of the phantom.

Inverse Radon transforms are performed separately for each position along the y-axis, resulting in horizontal cuts, or slices, through the sample. Figure 10 shows four such slices for the vertical positions indicated via orange ticks on the left hand sides of the images shown in Figure 8. They comprise regions of the abdomen including the spine (left), the lung including the spine and a cavity for an insertable heart (center-left), the upper arm and the shoulder (center-right) and the head including the skull and the arms (right). The latter corresponds to the sinogram shown in Figure 9. Despite a larger noise contribution compared to the two-dimensional scans, the features of the phantom can be recognized and a differentiation between air, tissue-like and bone-like material is possible.

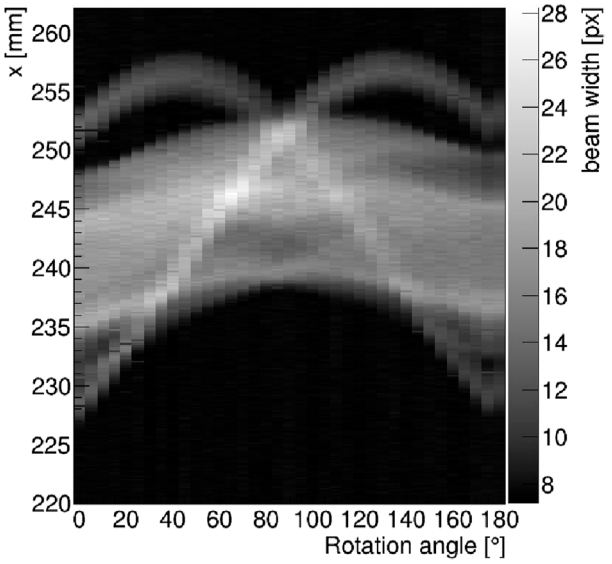

FIGURE 9
Sinogram generated from two-dimensional projections, such as shown in Figure 8 for a vertical position representing the head of the phantom.

Measurement 2 was performed at a lower scan velocity of 0.7 mm/s along the x-axis, with 101 rotations covering a half turn. This measurement is performed at a constant y-position within the head (cf. Figures 9, 10 (right)) and thus yields a single horizontal cut through the sample. The measurement time was 101 min.

The result is presented in Figure 11 (right) and compared to a reconstruction slice at the same position from measurement 1 (left), both with image cell sizes of 0.15 mm × 0.15 mm. A clear improvement from (left) to (right) is visible in terms of contrast and resolution, as well as a reduction of artefacts. The CNRs, calculated from signal and background regions indicated via orange boxes and determined via Equation 2, amount to 1.96 (Figure 11, left) and 4.62 (right). These improvements are achieved by an increase in statistics: while Figure 11 (left) contains the information of 10,360 frames, (right) contains information of 57,700 frames due to the reduced stage velocity and the increased number of projections. Differences caused by a variation in the scanning procedure are neither expected nor observed.

It should be noted that the reconstruction via an inverse Radon transform assumes a linear dependency of the measured observable, here the beam width, on the quantity to be reconstructed, here the material budget density. While Equation 1 suggests a dependency of the opening angle and thus the beam width on the square root of the material budget, it has been found that using the detected beam width with a background subtraction as an input to the filtered backprojection, yields reasonable results with minor artefacts. Further corrections mitigating non-linearities are expected to improve the image quality and are subject to current studies.

6 Potential and limitations

The presented measurements demonstrate the technological feasibility of the electronCT imaging technique and show reasonable resolution and contrast for macroscopic objects of sizes in the order of a few tens of millimeters, resolving details such as the skeleton of a mouse. In the following, the potential and the limitations of this technology are discussed.

6.1 Scanning strategy

For the measurements presented above, a constant transverse position was chosen for the electron beam, while the phantom was moved across the transverse plane. For the studies on phantoms such a strategy is applicable whereas it would be unfeasible for imaging in medical scenarios.

Instead, dipole magnets used for steering the transverse beam trajectory could be used to move the beam relatively to a static sample. This however comes with the necessity to either move the detector synchronously with the center of the electron beam or to use a much larger detector that would be required to cover the full scan range of incident beam positions, and with the requirement of a small energy spread to avoid dispersion effects.

6.2 Spatial resolution

The achievable resolution for the electronCT technique depends on several parameters:

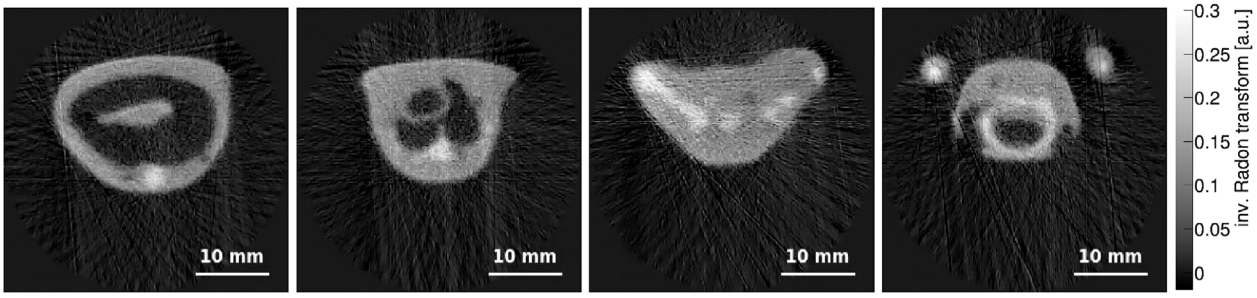

FIGURE 10
Three-dimensional electronCT measurement of a mouse phantom with an image cell size of 0.15 mm × 0.15 mm, evaluated at four positions along the vertical axis representing different anatomical regions of the phantom.

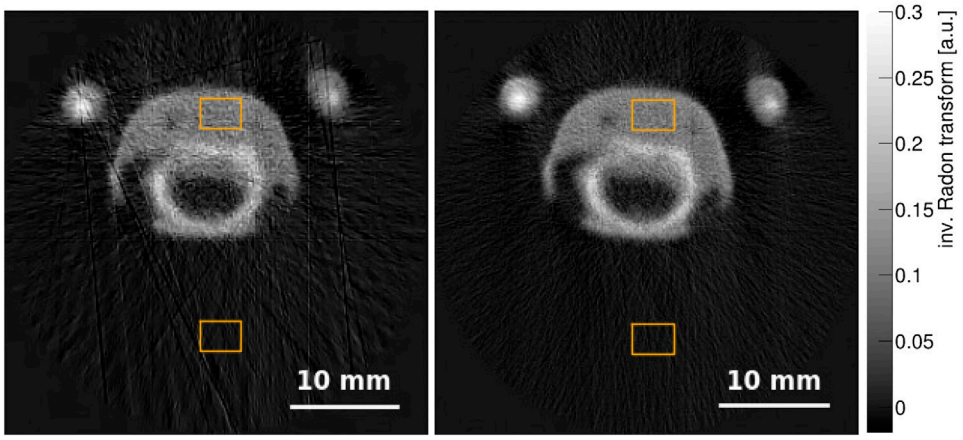

FIGURE 11
Comparison of two tomographic reconstructions of the sample, both acquired and evaluated at the same vertical position and displayed with image cell sizes of 0.15 mm × 0.15 mm (left) shows the enlarged result of an x-y-φ scan shown in Figure 10 (right) shows the result of an x-φ-scan with increased amount of data. Orange boxes indicate regions used for the determination of the image contrast.

- Step size: naturally the resolution of an image depends on the pitch of the individual image cells, which for this technique is limited by the distance between the impact positions of consecutive bunches or the step size along discretely scanned axes. This parameter also has a direct impact on the measurement time.
- Beam size: the transverse size of the beam can pose a limit on the spatial resolution of the obtained image, as individual electrons are scattered at different positions at the sample. This property is limited by the accelerator performance and the geometry of the experiment.
- Beam widening: already while traversing the sample, the beam size increases due to multiple Coulomb scattering. Hence, the spatial resolution suffers in the case of samples with a large thickness and high material budget.
- Beam stability: shot-to-shot fluctuations or long-term drifts of the beam position and intensity at the sample can affect the spatial resolution but could partially be recovered by correcting individual image points for the center of the detected beam profile.

For the measurements shown above, the limits on the spatial resolution were posed by the RMS beam size of around 320 µm for some of the measurements, while others were dominated by the step size. The phantom was chosen sufficiently small to not expect dominating effects from a beam widening inside the sample and the position of the beam center was found to be stable within less than 20 µm.

6.3 Measurement time

A great challenge for this imaging technique lies in the measurement time. The measurements presented above range from 101 min to 18 h and are thus unacceptable for medical imaging of living beings. The measurement time however strongly depends on, and is in these studies limited by, the repetition rate of the accelerator in use. Using higher repetition rates directly decreases the measurement time, such that images such as the ones shown in Figure 7 with a repetition rate of e.g., 1 kHz could be performed within less than 10 min. For the detector in use, the readout bandwidth is limited to 85 MHits/s, such that with less than 2,000 hit pixels per frame (see Figure 4), even repetition rates of up to 42 kHz and thus measurement times of less than a minute would be theoretically possible. However, at very high rates, the synchronisation of the data acquisition with the scan of the beam position across the sample via dipole magnets requires a high precision for a proper image reconstruction.

At the same time, the requirement on the spatial resolution of an image depends on its purpose and could thus be much looser than the resolution achieved with the above studies. As the resolution impacts the number of data points and thus the total number of electron bunches required for an image, imaging could be performed much faster by adapting the target resolution.

7 Conclusion and outlook

The feasibility of the imaging technique electronCT has been demonstrated by means of two- and three-dimensional measurements. The method is based on the determination of the beam profile of a low-charge electron beam with energies in the range of few hundreds of MeV after the traversal of a phantom. Projectional images as well as tomographic reconstructions of a medical mouse phantom have been acquired using the ARES linear accelerator for beam generation and a Timepix3 detector assembly as the detection layer. The images exhibit many details of the phantom and show good resolution and contrast. This proof of concept enables studies toward an application in the context of radiation treatment with VHEE, where this method could create synergies in applying the same accelerating structure for treatment and imaging.

The presented studies expose limitations and technical challenges of the technique in the prospect of medical imaging,

which lie in the measurement time and with it artifacts arising from the motion of living beings, and the spatial resolution when applied to larger objects. Hence, further studies on this technique are required to gain an understanding on the improvement potential of the measurement time, but also for an estimation of the dose delivered to a sample or patient in various imaging scenarios to explore its potential as imaging modality in a medical context. In summary, electronCT represents a candidate for *in situ* imaging in the context of VHEE radiotherapy and could contribute to IGRT, among others for the patient and tumor localization, under the premise of overcoming and gaining a further understanding of the aforementioned challenges.

Additional future studies serve the optimisation of this technique and comprise detailed simulations using the semiconductor detector simulation framework Allpix^2, which is capable of simulating the effects of multiple Coulomb scattering in a phantom as well as the detector response to the particle beam. Such simulations can serve as a guidance for an optimized measurement setup and strategy and provide insight into resolution limits and potential artefacts. These limits will be studied via the imaging of more generic, geometric samples such as a Derenzo phantom [35].

As indicated above, the linearity of the input to the reconstruction on the material budget is essential for an artefact-free three-dimensional imaging. To overcome this, calibration measurements applying materials of different, known properties in terms of radiation length and thickness, can furthermore be performed and applied.

Data availability statement

The raw data supporting the conclusions of this article will be made available by the authors, without undue reservation.

Author contributions

PS: Conceptualization, Formal Analysis, Funding acquisition, Investigation, Methodology, Project administration, Software, Supervision, Visualization, Writing–original draft. AA: Writing–review and editing. FB: Methodology, Resources, Writing–review and editing. Ld: Formal Analysis, Investigation, Writing–review and editing. HD: Investigation, Software, Writing–review and editing. KD: Formal Analysis, Investigation, Writing–review and editing. AH: Investigation, Writing–review and editing. SJ-M: Investigation, Writing–review and editing. MK: Investigation, Software, Writing–review and editing. WK: Investigation, Writing–review and editing. FM: Investigation, Software, Writing–review and editing. SR: Investigation, Writing–review and editing. SS: Conceptualization, Formal Analysis, Investigation, Methodology, Software, Writing–review and editing. TV: Investigation, Writing–review and editing. HW: Methodology, Supervision, Writing–review and editing.

Funding

The author(s) declare financial support was received for the research, authorship, and/or publication of this article. This project received funding via the DESY Generator Program.

Acknowledgments

The phantom has been obtained from *Universitätsklinikum Hamburg-Eppendorf*. The authors acknowledge support from DESY (Hamburg, Germany), a member of the Helmholtz Association HGF, and thank all the technical groups at DESY for their work and support in the ARES implementation, maintenance and operation.

Conflict of interest

The authors declare that the research was conducted in the absence of any commercial or financial relationships that could be construed as a potential conflict of interest.

Publisher's note

References

1. Ronga MG, Cavallone M, Patriarca A, Leite AM, Loap P, Favaudon V, et al. Back to the future: very high-energy electrons (vhees) and their potential application in radiation therapy. *Cancers* (2021) 13:4942. doi:10.3390/cancers13194942

2. Farr JB, Parodi K, Carlson DJ. Flash: current status and the transition to clinical use. *Med Phys* (2022) 49:1972–3. doi:10.1002/mp.15401

3. Vozenin MC, Bourhis J, Durante M. Towards clinical translation of flash radiotherapy. *Nat Rev Clin Oncol* (2022) 19:791–803. doi:10.1038/s41571-022-00697-z

4. Lin B, Gao F, Yang Y, Wu D, Zhang Y, Feng G, et al. Flash radiotherapy: history and future. *Front Oncol* (2021) 11. doi:10.3389/fonc.2021.644400

5. De Los Santos J, Popple R, Agazaryan N, Bayouth JE, Bissonnette JP, Bucci MK, et al. Image guided radiation therapy (igrt) technologies for radiation therapy localization and delivery. *Int J Radiat Oncology*Biology*Physics* (2013) 87:33–45. doi:10.1016/j.ijrobp.2013.02.021

6. Ruchala KJ, Olivera GH, Schloesser EA, Mackie TR. Megavoltage CT on a tomotherapy system. *Phys Med and Biol* (1999) 44:2597–621. doi:10.1088/0031-9155/44/10/316

7. Molière G. Theorie der Streuung schneller geladener Teilchen II - Mehrfach- und Vielfachstreuung. *Z Naturforsch Teil* (1948) A(3):78–97. doi:10.1515/zna-1948-0203

8. Bethe HA. Molière's theory of multiple scattering. *Phys Rev* (1953) 89:1256–66. doi:10.1103/PhysRev.89.1256

9. Highland VL. Some practical remarks on multiple scattering. *Nucl Instrum Meth* (1975) 129:497–9. doi:10.1016/0029-554X(75)90743-0

10. Lynch GR, Dahl OI. Approximations to multiple coulomb scattering. *Nucl Instrum Meth B* (1991) 58:6–10. doi:10.1016/0168-583X(91)95671-Y

11. Lutz G. *Semiconductor radiation detectors*. Verlag Berlin Heidelberg: Springer (1999).

12. Spannagel S, Wolters K, Hynds D, Tehrani NA, Benoit M, Dannheim D, et al. Allpix^2: A modular simulation framework for silicon detectors. *Nucl Instrum Meth A* (2018) 901:164–72. doi:10.1016/j.nima.2018.06.020

13. Agostinelli S, Allison J, Amako K, Apostolakis J, Araujo H, Arce P, et al. GEANT4 - a simulation toolkit. *Nucl Instrum Meth A* (2003) 506:250–303. doi:10.1016/S0168-9002(03)01368-8

14. Spannagel S, Wennlöf H, Schütze P. Allpix squared - generic pixel detector simulation framework (2023). doi:10.5281/zenodo.8171803

15. Weinrich U, Fuchs R, Sust E. Assembly of the carbon beam gantry at the heidelberg ion therapy (HIT) accelerator. *Conf Proc C* (2008).

16. Chinniah S, Deisher AJ, Herman MG, Johnson JE, Mahajan A, Foote RL. Rotating gantries provide individualized beam arrangements for charged particle therapy. *Cancers* (2023) 15:2044. doi:10.3390/cancers15072044

17. Jansen H, Schütze P. Feasibility of track-based multiple scattering tomography. *Appl Phys Lett* (2018) 112:144101. doi:10.1063/1.5005503

18. Burkart F, Aßmann R, Dinter H, Jaster-Merz S, Kuropka W, Mayet F, et al. The ARES linac at DESY. In: Proc. LINAC'22 International Linear Accelerator Conference; Liverpool, UK. Geneva, Switzerland: JACoW Publishing (2022). p. 691–4.

19. Poikela T, Plosila J, Westerlund T, Campbell M, Gaspari MD, Llopart X, et al. Timepix3: a 65k channel hybrid pixel readout chip with simultaneous toa/tot and sparse readout. *J Instrumentation* (2014) 9:C05013. doi:10.1088/1748-0221/9/05/C05013

20. Bienvenu G. Dark current in high-gradient accelerator. *IEEE Trans Electr Insul* (1989) 24:1037–9. doi:10.1109/14.46334

21. Dudak J. High-resolution x-ray imaging applications of hybrid-pixel photon counting detectors timepix. *Radiat Measurements* (2020) 137:106409. doi:10.1016/j.radmeas.2020.106409

22. Turecek D, Jakubek J, Trojanova E, Sefc L, Kolarova V. Application of timepix3 based cdte spectral sensitive photon counting detector for pet imaging. *Nucl Instr Methods Phys Res Section A: Acc Spectrometers, Detectors Associated Equipment* (2018) 895:84–9. doi:10.1016/j.nima.2018.04.007

23. Pitters FM, Alipour Tehrani N, Dannheim D, Fiergolski A, Hynds D, Klempt W, et al. Time and energy calibration of Timepix3 assemblies with thin silicon sensors. *CLICdp-Note-2018-008* (2018).

24. Burian P, Broulím P, Jára M, Georgiev V, Bergmann B. Katherine: ethernet embedded readout interface for timepix3. *J Instrumentation* (2017) 12:C11001. doi:10.1088/1748-0221/12/11/C11001

25. Mánek P, Burian P, David-Bosne E, Smolyanskiy P, Bergmann B. Track Lab: extensible data acquisition software for fast pixel detectors, online analysis and automation (2023).

26. Wegner M, Frenzel T, Krause D, Gargioni E. Development and characterization of modular mouse phantoms for end-to-end testing and training in radiobiology experiments. *Phys Med and Biol* (2023) 68:085009. doi:10.1088/1361-6560/acc566

27. Thorlabs Inc. 300 mm linear translation stage with integrated controller, stepper motor (2024). Available from: https://www.thorlabs.com/newgrouppage9.cfm?objectgroup_id=7652&pn=LTS300/M (Accessed June 10, 2024).

28. Thorlabs Inc. PRM1/MZ8 - Ø1 motorized precision rotation stage (metric) (2024). Available from: https://www.thorlabs.com/thorproduct.cfm?partnumber=PRM1/MZ8 (Accessed June 10, 2024).

29. Dannheim D, Dort K, Huth L, Hynds D, Kremastiotis I, Kröger J, et al. Corryvreckan: a modular 4d track reconstruction and analysis software for test beam data. *J Instrumentation* (2021) 16:P03008. doi:10.1088/1748-0221/16/03/P03008

30. Deans S. The Radon transform and some of its applications. In: *Dover books on mathematics series*. Dover Publications (2007).

31. scikit-image development team. scikit-image (2024). Available from: http://scikit-image.org/ (Accessed June 10, 2024).

32. van der Walt S, Schönberger JL, Nunez-Iglesias J, Boulogne F, Warner JD, Yager N, et al. scikit-image: image processing in Python. *PeerJ* (2014) 2:e453. doi:10.7717/peerj.453

33. Chang S, Yu B, Vetterli M. Adaptive wavelet thresholding for image denoising and compression. *IEEE Trans Image Process* (2000) 9:1532–46. doi:10.1109/83.862633

34. Workman RL, Burkert VD, Crede V, Klempt E, Thoma U, Tiator L, et al. Review of particle physics. *PTEP 2022* (2022) 2022:083C01. doi:10.1093/ptep/ptac097

35. Derenzo SE, Budinger TF, Cahoon JL, Huesman RH, Jackson HG. High resolution computed tomography of positron emitters. *IEEE Trans Nucl Sci* (1977) 24:544–58. doi:10.1109/tns.1977.4328738

frontiers | Frontiers in Physics

TYPE Original Research
PUBLISHED 20 November 2024
DOI 10.3389/fphy.2024.1443306

OPEN ACCESS

EDITED BY
Angeles Faus Golfe,
UMR9012 Laboratoire de Physique des 2 infinis Irène Joliot-Curie (IJCLab), France

REVIEWED BY
Antonio Gilardi,
Stanford University, United States
Lanchun Lu,
The Ohio State University, United States

*CORRESPONDENCE
Francesca Nicolanti,
francesca.nicolanti@uniroma1.it

RECEIVED 03 June 2024
ACCEPTED 14 October 2024
PUBLISHED 20 November 2024

CITATION
Arsini L, Caccia B, Ciardiello A, De Gregorio A, Franciosini G, Giagu S, Guatelli S, Muscato A, Nicolanti F, Paino J, Schiavi A and Mancini-Terracciano C (2024) Fast and precise dose estimation for very high energy electron radiotherapy with graph neural networks. *Front. Phys.* 12:1443306. doi: 10.3389/fphy.2024.1443306

Fast and precise dose estimation for very high energy electron radiotherapy with graph neural networks

Lorenzo Arsini[1,2], Barbara Caccia[3], Andrea Ciardiello[1,2], Angelica De Gregorio[1,2], Gaia Franciosini[2,4], Stefano Giagu[1,2], Susanna Guatelli[5,6], Annalisa Muscato[2,4], Francesca Nicolanti[1,2]*, Jason Paino[5,7], Angelo Schiavi[4] and Carlo Mancini-Terracciano[1,2]

[1]Department of Physics, Sapienza University of Rome, Rome, Italy, [2]INFN Section of Rome, Rome, Italy, [3]National Centre for Radiation Protection and Computational Physics, Istituto Superiore di Sanità, Rome, Italy, [4]Department of Basic and Applied Sciences for Engineering, Sapienza University of Rome, Rome, Italy, [5]Illawarra Health and Medical Research Institute, University of Wollongong, Wollongong, NSW, Australia, [6]School of Computing and Information Technology, University of Wollongong, Wollongong, NSW, Australia, [7]Centre for Medical Radiation Physics, University of Wollongong, Wollongong, NSW, Australia

Introduction: External beam radiotherapy (RT) is one of the most common treatments against cancer, with photon-based RT and particle therapy being commonly employed modalities. Very high energy electrons (VHEE) have emerged as promising candidates for novel treatments, particularly in exploiting the FLASH effect, offering potential advantages over traditional modalities.

Methods: This paper introduces a Deep Learning model based on graph convolutional networks to determine dose distributions of therapeutic VHEE beams in patient tissues. The model emulates Monte Carlo (MC) simulated doses within a cylindrical volume around the beam, enabling high spatial resolution dose calculation along the beamline while managing memory constraints.

Results: Trained on diverse beam orientations and energies, the model exhibits strong generalization to unseen configurations, achieving high accuracy metrics, including a δ-index 3% passing rate of 99.8% and average relative error <1% in integrated dose profiles compared to MC simulations.

Discussion: Notably, the model offers three to six orders of magnitude increased speed over full MC simulations and fast MC codes, generating dose distributions in milliseconds on a single GPU. This speed could enable direct integration into treatment planning optimization algorithms and leverage the model's differentiability for exact gradient computation.

KEYWORDS

VHEE, radiotherapy, dose engine, deep learning, flash, very high energy electrons, Monte Carlo

1 Introduction

In the treatment of cancer for deep-seated tumors, external beam radiotherapy (RT) is recognized as one of the most effective and commonly employed therapies [1]. Various types of radiation have been explored, with X-ray radiotherapy being the most commonly used, while a smaller portion of patients undergo particle therapy (PT) utilizing protons or heavier ions. Electrons, due to their unique interaction properties with matter, offer potential advantages over photon RT and PT, especially for specific irradiation modalities [2, 3]. For example, electrons possess an advantageous attribute since they can be easily stirred by a magnetic field, providing great flexibility in selecting the entry angles of the radiation beams. Very high-energy electrons (VHEE) in the 60–120 MeV range have been investigated for treating deep-seated tumors, demonstrating comparable performance to volumetric modulated arc therapy (VMAT) [4] and proton irradiation, albeit with complexities and cost considerations [5, 6]. Technological advances, such as compact and cost-effective C-band accelerating structures, now enable the feasible production of high-energy electron fields, potentially making VHEE therapy more accessible for clinical use [7].

Finally, there has been growing interest in the exploration of high-dose-rate therapies, with electron FLASH therapy standing out as a possible revolutionary treatment [8]. FLASH-RT is a novel approach that promises an ultra-fast delivery of radiation (less than 200 milliseconds per treatment) with pulses featuring an ultra-high dose rate (> 40 Gy/s). This makes FLASH-RT approximately 400 times faster than traditional radiotherapy, with a dose rate several orders of magnitude higher than the traditional rate (approximately 0.5 Gy/min). FLASH-RT derives its name from the "FLASH effect" a biological phenomenon where irradiation at ultra-high dose rates exhibits a superior ability to spare healthy tissues while maintaining its effectiveness against tumors [9–11].

The prime candidates for fully exploiting the potential of this effect are believed to be electrons, specifically VHEE, for the treatment of deep-seated tumors [2, 12]. Currently, a treatment planning (TP) algorithm exploiting the electron beam possibilities is needed. The first step for a TP system is the estimation of the dose as a function of the beam parameters. The ongoing research in the field of TP for VHEE RT and electron FLASH-RT predominantly relies on Monte Carlo (MC) simulations or the development of fast MC simulations, such as FRED (Fast paRticle thErapy Dose evaluator) [12–14].

In this context, deep learning (DL) algorithms are a promising alternative to overcome current limitations, offering a dual benefit of speed and precision in dose estimation. These algorithms can be trained to replicate the output of MC simulations, enabling the fast generation of dose distribution maps with a precision comparable to MC. Moreover, the speed of DL models in generating these dose distributions and the differentiability of their output enable the development of a TP system based on them. Such a TP system could integrate them into the merit function and exploit gradient-based optimization algorithms for plan optimization.

Recently, an increasing number of studies on the application of DL techniques to dose estimation and treatment planning has emerged [15]. The majority of these studies concentrate on clinically established treatments for which extensive datasets from past patients are readily available. Moreover, only a limited number address the DL emulation of dose distributions for individual beams or fields [16, 17], while the majority of these efforts aim to replicate entire treatment plans based on historical records [18, 19]. Although it has been shown that DL models can effectively reproduce the dose distributions, it is important to note that the accuracy of DL models is intrinsically constrained by the precision of the algorithms that they are trained to emulate. However, these are often the deterministic algorithms used in the optimization of most current treatment plans [18, 19]. Conversely, we propose that the true advantage of employing DL lies in emulating MC simulations, which, although substantially more accurate than deterministic algorithms, are currently too slow for practical clinical use. This approach can potentially enhance both treatment efficiency and quality.

Few studies have explored the feasibility of reproducing MC-simulated dose distributions [20, 21], and these are primarily focused on novel radiotherapy treatments where deterministic algorithms are not applicable. Finally, no DL-based solution has yet been developed or applied for VHEE RT dose estimation.

We thus introduce a DL model designed to replicate MC-simulated dose distributions for therapeutic VHEE beams in patient tissues. Our strategy involves considering a voxelized cylindrical volume around the beam, enabling us to predict the dose at varying spatial resolutions. This approach minimizes the model's memory requirements while maintaining high accuracy in the most relevant regions. The model is trained to take as input the beam's energy and the densities of organs inside the cylinder around the beam and delivers an accurate and ultra-fast (0.02 s on CPU) estimate of the dose distribution within the cylinder.

This paper is organized as follows. Section 2 describes in detail the MC simulations used to build the dataset to train our DL model along with the description of the model itself. Section 3 presents the metrics used to evaluate our model and summarize the main results of our work. Finally, Section 4 is dedicated to final discussion and conclusions.

2 Materials and methods

The proposed DL model is trained to estimate the dose distribution in a cylindrical volume with the symmetry axis aligned with the beam. It outputs a 3D cylindrical dose map which uses as input the densities in such a cylinder and the beam energy.

2.1 Dataset

2.1.1 Monte Carlo simulation

The dataset used to train, validate, and test the proposed DL model was built running a set of MC simulations using the Geant4 toolkit (version 11.1.1) [22–24]. Geant4 is the most used toolkit for developing radiation matter MC simulations, being regularly validated also for medical applications [25]. Each element of the dataset is a different simulation in which an electron beam of varying energy and orientation simulates an incident on a patient's head and neck CT scan.

TABLE 1 Materials' table. Left column: list of materials used in the MC simulation, based on that used in [27]. Right column: upper bound of the material binning is reported so that all voxels with HU less than −820 are assigned to the material "Air", all voxels with HU between −820 and 39 are assigned the material "Soft Tissue", and so on.

Material	HU upper bound
Air	−820
SoftTissue	39
BrainTissue	84
SpinalDisc	115
TrabecularBone_HEAD	242
CorticalBone	1,208
ToothDentin	1,540
ToothEnamel	3,071

TABLE 2 Calibration curve which rules the conversion between HU and density, for the patient M1 [14]. The calibration curve was used to assign each voxel of the CT scan a nominal density value.

HU	Density [g/cm^3]
−1,024	0.0
−820	0.205
−531	0.507
−89	0.96
−43	0.99
19	1.
22	1.06
42	1.070
187	1.160
850	1.530
1,302	1.820
4,000	3.551

The CT scan used in this study contains the head of a patient with a meningioma (hereafter M1) treated at the Trento Particle Therapy Center. We decided to use the M1 patient CT scan because it has been used in a recent publication to compare treatment plans delivered with VHEE FLASH RT, IMRT, and Proton therapy [14]. In future, we plan to compare a DL generated treatment plan with that produced by currently available techniques. The CT scan was composed of 260 slices 1 mm thick. Each slice was composed of 512 × 512 pixels with a side length of 0.6015626 mm. The CT scan was imported as the detector geometry in a Geant4 simulation based on the ICRP110 Human Phantoms Advanced Example [26].

Each voxel was assigned a material and a nominal density based on its Hounsfield unit (HU) value. Firstly, depending on the binning on HU values reported in Table 1, materials were assigned to each voxel. In particular, on the right side of Table 1 the upper bounds of the material binning were reported so that voxels with HUs −820 were assigned to the material "Air", voxels with HU between −820 and 39 were assigned the material "Soft Tissue", and so on. The material list is that used for the Geant4 DICOM Digital Head in the DICOM example [27]. HU boundary values between different organs were computed based on the data in [27] where HU mean and standard deviation values were reported for each tissue. Boundaries are computed as the intersection points between the Gaussian distributions with those mean and standard deviation values. The upper bound for the air was set manually to −820. In Geant4, a material is defined by an atomic composition and a density value. To avoid the definition of a large number of materials (one for each density value), we created a sub-binning for each material with bin width equal to 50 HU. Using the calibration curve used for the treatment planning of M1 [14] (reported in Table 2), a nominal density was then assigned to each voxel. Finally, nominal densities were averaged, so that each voxel of a certain material's sub-bin had the average density of the voxels assigned to that sub-bin. As a result, there was univocal correspondence between HU sub-bin ranges, materials, and densities.

Using this geometry setting, therapeutic very high energy electron (VHEE) beams were directed towards the center of the CT scan. Each beam was modeled as a Gaussian pencil-beam with a full width at half maximum (FWHM) of 0.5 cm whose source lies on a 30-cm-radius sphere centered in the CT scan center. To collect dose data, we used a cylindrical scorer with the z axis aligned with the beam. The scorer comprised 100 voxels of 4 mm length along the z axis, 20 voxels of 4 mm length along the r axis, and 25 voxels along the theta axis, so that the inner voxels had an angular length of ~ 1 mm, while the outer ones had an angular length of ~ 2 cm.

Using a cylindrical scorer has two main advantages. The first is that it is more precise near the beam line, where most of the dose is deposited. The second advantage regards the exemplification of the DL emulation problem. We required the DL model to reproduce the dose in the cylinder around the beam so that we did not have to account for a direct dependence on the beam orientation. Because the beam distribution was fixed, the dose only depended on the beam energy and the densities of the tissues in the cylindrical region around the beam. On the left of Figure 1, we present a two-dimensional schematic representation of cylindrical voxels superimposed on a regular grid. Depending on the grid spacing and cylinder voxelization, the cylindrical scorer can have an increased resolution near the beamline. In the same figure, the central and right panels show front and lateral slices of the CT scan, respectively. The blue regions correspond to the intersection with a cylinder whose axis is represented by the light blue line in the right panel.

It is worth noting that the actual tracing in the simulation was done considering the CT voxels, and only the scoring was done in the cylindrical voxels.

Using this setting, we generated a dataset of 10.000 examples with low statistics (10.000 primaries per beam, average 20% statistical uncertainty) to train, validate, and test the DL model. Each example contained the dose of a monochromatic electron beam inside the cylindrical scorer. The beam energy was uniformly sampled between 70 and 130 MeV. The two angular values defining the orientation of the beams θ and ϕ were sampled uniformly as integers respectively of 0–180° and 0–360°.

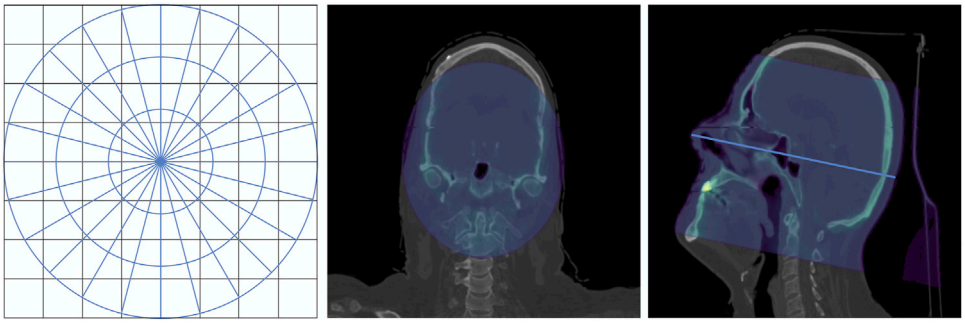

FIGURE 1
Cylindrical approximation. Left: 2D schematic drawing of cylindrical voxels superimposed on a regular grid. Center and right panels: front and lateral sections of the CT scan. The intersection between the CT scan and a cylinder is highlighted in blue. Right panel: the cylinder axis, which coincides with the beam line, is displayed as a light blue line.

Our dataset was built to simulate conventional VHEE beams, and our DL model was trained to reproduce such simulations. It is possible to account for the FLASH effect after the conventional dose calculation using the FLASH modifying factor (FMF), as in [14]. The FMF, defined in [28], is the ratio of doses that need to be administered at conventional and ultra-high dose rates to achieve the same effect for a given biological system. Thus, by multiplying the simulated absorbed dose by the FMF, it is possible to account for the organs at risk induced by the FLASH effect [14]. Such a computation was performed after the treatment plan optimization and thus was not an object of this study.

2.1.2 Density interpolation

As already mentioned, we sought to train the DL algorithm to produce the dose map in a density map with the same mesh of the input.

Therefore, for each example, we computed the density values in the cylindrical voxels interpolating the densities we assigned to the CT scan voxels. To obtain a reliable estimate of the density, we sampled N random 3D points inside each cylindrical voxel. We then computed the fraction of such points that fall in each of the CT voxels, to which we refer as N_i, $i \in \{1, N_{CTvox}\}$. The density associated with a cylindrical voxel j ρ^j is then the average of the density in the CT voxels weighted by the values $\{N_i\}$ (Equation 1):

$$\rho^j = \frac{\sum_i N_i \, \rho_i}{N}. \tag{1}$$

For large N, this expression converges to the average weighted with intersection volumes (Equation 2):

$$\rho^j = \frac{\sum_i v_i^j \, \rho_i}{V_j}, \tag{2}$$

where V_j is the volume of the cylindrical voxel j, while v_i^j is the volume of the intersection between the cylindrical voxel j and the CT voxel i. We chose N to be equal to 100 in order to obtain a satisfactory estimate in a contained computing time. The study we performed for choosing the most suitable number of sampling points can be found in the Supplementary Material.

The cylindrical density maps represent the input to our DL model, along with the information about the beam energy.

2.2 Deep learning model

The DL model developed in this work is based on graph neural networks and has a U-net structure. A U-net [29] is a two-dimensional fully convolutional neural network that is widely used in medical applications. Its encoder–decoder architecture, combined with skip connections, enables efficient modeling of hierarchical features while mitigating the issue of vanishing gradients. To account for the geometric structure of our data, we replaced traditional with graph convolutions. Such a model represents an improvement over the already published recursive nearest neighbors (ReNN) graph variational auto encoder [30], which we proved to be effective in predicting dose distributions in homogeneous and simple in-homogeneous materials. Finally, we compared such a model to a 3D U-net on a dose prediction task on standard grid-like data presented in [21], finding comparable or superior performance [31].

The model is composed of three modules: the encoder, the embedder, and the decoder. The encoder takes input from the density cylindrical graphs ρ, each with 50.000 nodes. Data are processed through six *GraphConv* layers with an increasing number of output channels: 32, 64, 128, 256, 256, 256 followed by rectified linear unit activation (*ReLu*) functions. In the *GraphConv* layer, the new node features x' are a linear combination between their old features x and a weighted mean of their neighbors' features (Equation 3):

$$x_i' = ReLu\left(W_1 x_i + W_2 \frac{1}{|N(i)|} \sum_{j \in N(i)} e_{ij} x_j \right). \tag{3}$$

The edge features e_{ij} represent the weight of the link between nodes i and j; in our model, they are learnable parameters of the network. Between the convolutive layers, we used ReNN-Pool [30]. This pooling technique allows the graph to reduce dimensionality, dropping a consistent number of nodes but always assuring a unique connected graph, creating new links between far nodes regularly and efficiently. After five pooling operations, the output of the encoder consisted of a small connected graph with 33 nodes.

The embedder is a two-layer multilayer perceptron which takes input from the energy of the beam E and outputs a feature map with the dimensionality of the number of nodes in the smallest graph

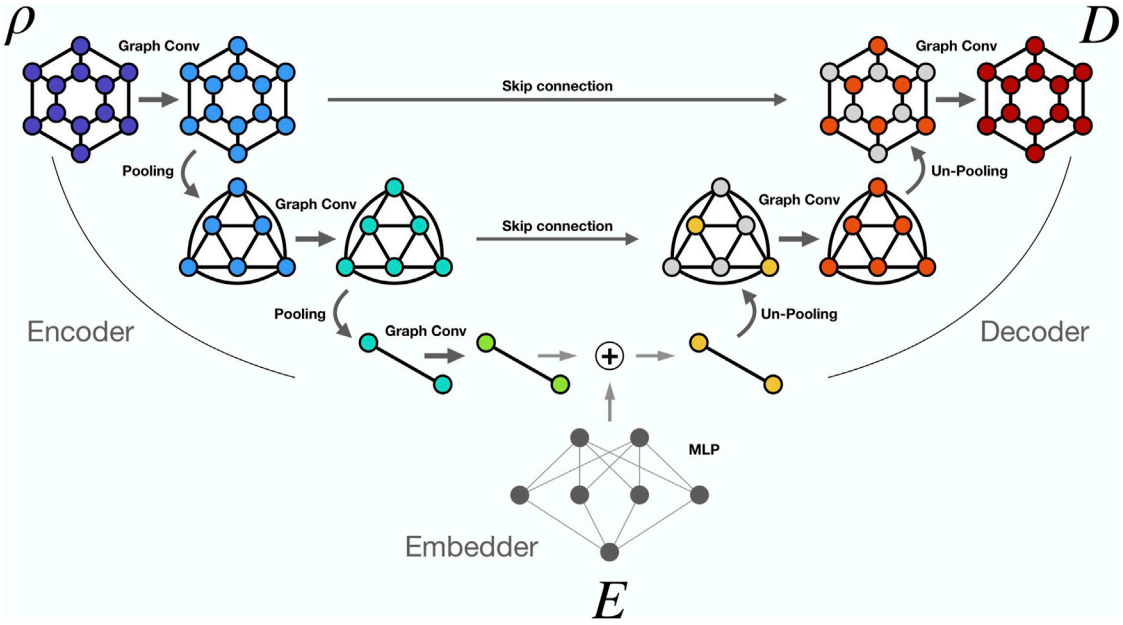

FIGURE 2
ReNN GU-Net. Simplified scheme of the ReNN GU-Net with two pooling layers. Density information ρ in the form of a 3D graph is processed by the model through the encoder. The energy of the beam E is processed by the embedder and then added to the encoder output. The resulting graph is processed by the decoder to retrieve the original graph dimensionality and to predict the dose distribution D.

representation—33 nodes. The output of the encoder and the embedder are then summed.

The decoder applies five GraphConv layers with a decreasing number of output channels: 256, 128, 64, 32, 1. Each GrapConv layer is followed by a ReLu activation except the last, which is followed by a sigmoid activation function. Before each convolutive layer, ReNN-UnPool is applied to retrieve the original graph dimensionality and to allow skip connection between the encoder and the decoder. Indeed, each decoder layer takes as input the sum of the unpooled output of the previous layer and the partial output from the skip connection coming from the encoder.

Figure 2 presents a schematic representation of the model architecture, including only two pooling layers for simplicity.

3 Results and discussion

We divided our 10.000 example dataset between train, validation, and test sets. The examples selected for the test set are 275 and satisfy these conditions:

- Beam energy $E \in [60, 70] \cup [80, 90]$ MeV,
- Angle $\theta \in [45, 75] \cup [105, 135]$ degree,
- Angle $\phi \in [75, 105] \cup [165, 195] \cup [255, 285]$ degree.

The rest of the dataset was split between train and validation sets with a 1/10 ratio, so that the training set contained 8,752 examples while the validation set contained 973. We chose this arrangement for the test set in order to put ReNN GU-Net under a strict test, testing its ability to interpolate between samples and generalize to unseen configurations from both the point of view of patient anatomy and the beam's energy.

We also generated ten high statistical examples, whose Geant4 simulations were run using one million primaries per beam ($\times$ 100 more particles than in train, validation, and test sets) with an average statistical uncertainty of 2%. These samples, whose energies and orientations lie in the ranges of the test set, were used for the final evaluation and plots.

After an extensive hyper-parameter optimization of the learning rate, convolutional filters, and model depth, we trained our final model with a learning rate of 0.005 and a batch dimension of 16, with the learning rate scheduler ReduceOnPlateau with a patience of 20 epochs. The model was trained using Binary Cross-Entropy loss. We stopped the training at the convergence of the validation loss after 104 epochs. The training was conducted on a Tesla V100 GPU and lasted approximately 4 h. The complete information about the hyper-parameter optimization can be found in the Supplementary Material.

In order to evaluate the results of our model, we considered four different metrics:

- Mean absolute error (MAE): voxel-wise mean absolute error between MC and DL dose.
- δ-index: introduced by Mentzel [20] and inspired by the clinical γ-index [32]. It quantifies the voxel-wise absolute error difference between MC and DL doses normalized by the maximum dose. This measure gives less importance to regions in which the dose is low and thus are therapeutically less important. In particular, we consider the δ-index 3% passing rate, which accounts for the percentage of voxels in which the δ-index if less than 3%.

TABLE 3 Dose results: we report the results for all metrics for training, validation, testing, and high-statistics evaluation set. Note that the best agreement is found for the evaluation set because, by construction, DL models produce a smooth approximation of the learned function.

	MAE [μGy]	$\delta < 3\%$ [%]	MRE z [%]	MRE r [%]	MRE E [%]
Train	1.1 ± 0.1	98.7 ± 0.2	1.2 ± 0.3	2.0 ± 0.4	0.2 ± 0.2
Validation	1.2 ± 0.1	98.7 ± 0.2	1.4 ± 0.5	2.1 ± 0.5	0.3 ± 0.4
Test	1.2 ± 0.1	98.6 ± 0.3	1.6 ± 0.7	2.2 ± 0.4	0.4 ± 0.4
Eval	0.29 ± 0.07	99.8 ± 0.2	0.9 ± 0.9	0.5 ± 0.2	0.3 ± 0.3

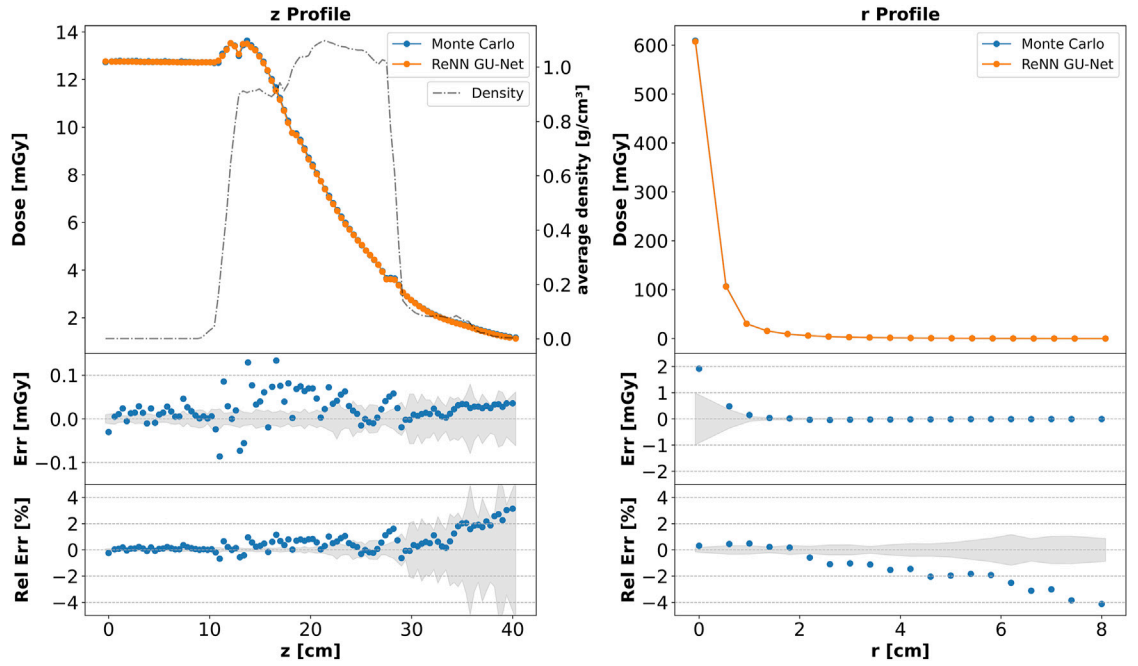

FIGURE 3
Integrated dose profiles. Top: comparison of dose profiles along the z and r axes of the cylinder, computed through MC simulation (blue) and our DL model (orange), showcasing an example from the high-statistics evaluation set. The average CT scan density, calculated from HU using a calibration curve, is indicated by a gray dashed line. Bottom: absolute error and percentage relative error between the dose profiles computed by MC and DL methods (blue dots) along with the MC standard deviation (gray band).

- Mean relative error (MRE) on dose profiles. We compute the integrated dose profiles along the two cylindrical axes z and r and compute the MRE between the MC and DL predictions. We refer to these metrics as MRE z and MRE r.
- MRE on total dose. MRE computed on the full integral of the dose, which represents the total dose, computed with MC and DL. We refer to this measure as MRE E

We present the results for all metrics in Table 3 for the training, validation, testing, and evaluation sets. The MAE, expressed in micrograys (μGy), is calculated considering the dose as deposited by a beam of 10^6 electrons.

The best agreement is observed on the high statistics examples of the evaluation set. Increasing the statistics in an MC simulation yields a reduction of the fluctuations with a consequent better estimate of the dose distribution. DL models, by construction, learn to interpolate smooth functions between the training samples. Models based on convolutional layers are particularly known for their smoothing effect on outputs. This effect is leveraged in de-noising tasks, also performed on MC simulations for radiation therapy [33], where a model is trained to suppress fluctuations in noisy images or distributions. We took advantage of this effect by training our DL model on low-statistics samples, which can be produced more quickly, testing it on clinically valid high-statistics MC samples. As shown in the results, the model learns to ignore the fluctuation and predict a good estimate of the dose distribution, comparable with the one generated by high statistics MC simulations.

All the metrics show good agreement between the MC simulated dose and the DL emulated one, with 99.8% of the voxels of the evaluation set examples exhibiting a δ-index inferior to 3%.

In the top plots of Figure 3, we show the integrated dose profiles along the z and r axes of the cylinder for an example drawn from the high-statistics evaluation set with beam orientation defined by $\theta = 122^\circ$ and $\phi = 178^\circ$, and beam energy $E = 82.44$ MeV. The dose profiles predicted by our ReNN GU-Net (in orange) agree with the

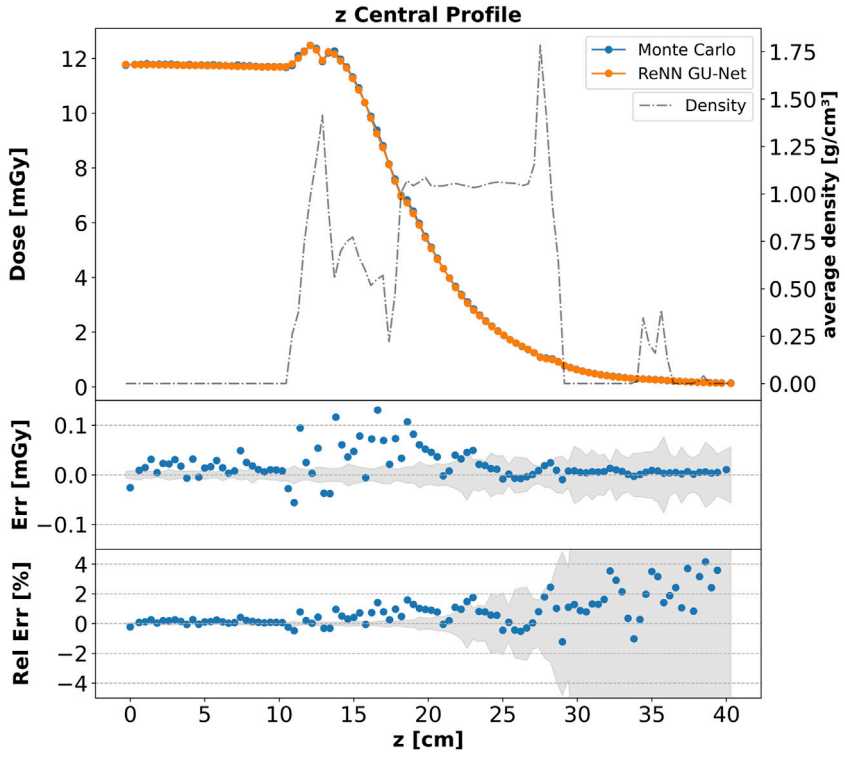

FIGURE 4
Core dose profile. Top: comparison of the dose z profile computed for the core cylinder around the beam (with $r < 4$ mm), using MC simulation (blue) and our DL model (orange), for an example from the high-statistics evaluation set. The average CT scan density, calculated from HU using a calibration curve, is indicated by a gray dashed line. Bottom: absolute error and percentage relative error between the dose profiles computed by MC and DL methods (blue dots) along with the MC standard deviation (gray band).

MC simulated profiles (in blue), even on the boundaries between tissues with very different densities. The average density in g/cm^3 computed from the CT scan using a calibration curve, as explained in Section 2.2, is also shown for reference as a dashed gray line. The agreement between the two profiles is quantified in the bottom plots, where we report respectively the absolute difference between the profiles (Err) and the percentage relative error between the profiles (Rel Err) in blue dots. In both plots we also report the standard deviation of the MC simulation (gray band). The percentage relative error is computed directly between the two integrated profiles as follows (Equation 4):

$$RE\ [\%] = \frac{D^{prof}_{MC} - D^{prof}_{DL}}{D^{prof}_{MC}} \times 100, \tag{4}$$

where D^{prof}_{MC} and D^{prof}_{DL} are respectively the dose profiles computed with a MC simulation and with our DL model. The relative error is mostly inferior to 2% except from the tails of the distributions, where a lower amount of dose is deposited. These regions are typically those in which the standard deviation of the MC simulation is also higher due to the low statistics. Indeed, as is evident from the middle and bottom plots, the errors appear to be correlated with the MC standard deviation, and the absolute error rarely exceeds 0.1 mGy. It is worth noting that the tails of the dose distribution are subject to a large amount of uncertainty in the low-statistics training examples of over 50%. Therefore, a larger error in the DL prediction, but still coherent with the MC uncertainty, is expected.

The agreement is not limited to the integrated profiles but also extends locally. In Figure 4, we present a plot similar to that in Figure 3, depicting the dose profiles along the z-axis. This computation is specifically for the central voxels, considering only one voxel along the r-axis and marginalizing over θ. This accounts for the region in the highest proximity to the beam line with $r < 4$ mm, where a large amount of dose is deposited—around 75% of the total. Such a plot shows that the agreement between MC and DL dose profiles persists, also restricting our analysis in the core of the cylinder. Looking at the bottom plots, it is worth noting that the relative error is also clearly correlated in this case with the standard deviation of the MC simulation, and that DL and the MC curves are mostly consistent within a standard deviation.

To show our model's ability to generalize to different unseen beam energies and orientations, Figure 5 compares DL and MC computed core dose profiles for four additional examples from the evaluation set. Each panel's title reports the two angles, θ and ϕ, that define the beam orientation, as well as the beam energy for the respective example. In all cases, discrepancies between DL and MC are mostly within the range of MC uncertainty.

In Figure 6 we show a visual comparison between the CT scan (in the left panel), the MC simulated dose (central panel), and the DL emulated dose (right panel). These panels were extracted from our cylindrical structures considering two opposite sets of voxels in the θ dimension. In other words, these represent a horizontal slice taken from the cylinder, slicing it in one of the z-r planes.

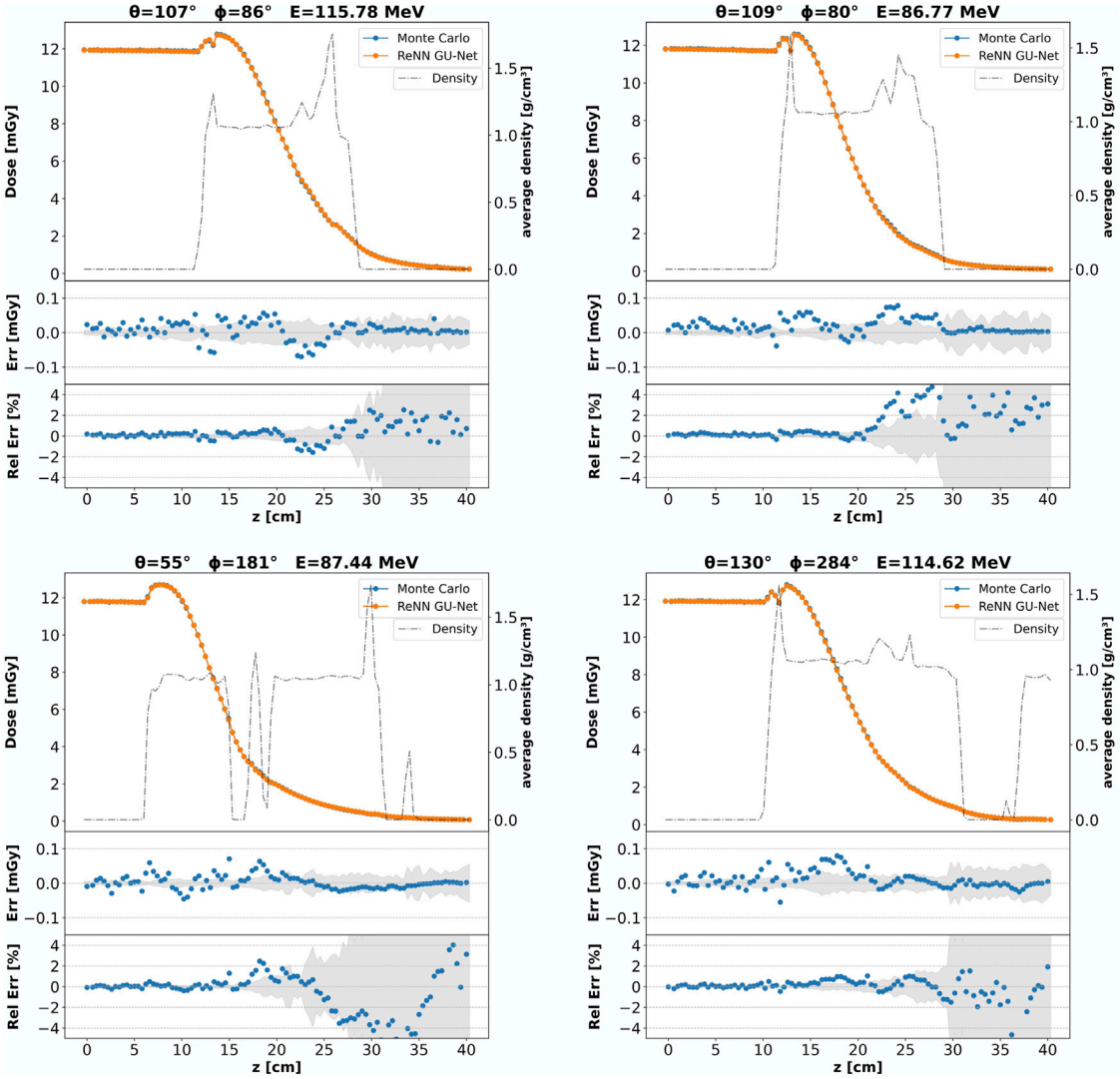

FIGURE 5
Core dose profiles: different beam configurations. Each panel corresponds to a different example from the evaluation set, featuring varying beam energies and orientations as indicated by the panel titles. For each panel, a comparison of the core dose z-profile computed using MC simulation (blue) and our DL model (orange) is shown, along with the average CT scan density represented by a gray dashed line. Below each profile: the absolute error and the percentage relative error between the dose profiles computed by the MC and DL methods (blue dots) are displayed, along with the MC standard deviation (gray band).

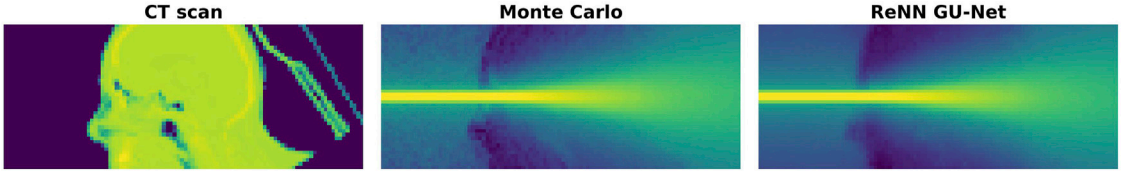

FIGURE 6
CT, Monte Carlo, and ReNN GU-Net. Image representation of a horizontal slice taken from the considered cylindrical volume around the beam. On the left panel is shown the CT scan, which is the input to our DL model. The MC simulated and DL predicted dose distributions are reported, respectively, on the central and right panels.

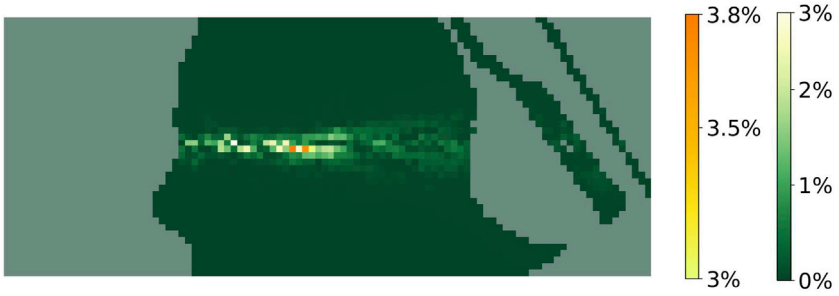

FIGURE 7
δ-index. Distribution of the δ-index computed on the voxels of a slice of the cylinder around the beam. The green-to-yellow scale indicates values below 3%; yellow-to-red scale indicates higher values.

Moreover, we show in Figure 7 the δ-index computed on the cylinder slice shown in Figure 6. δ-index values are reported for all but the voxels which contain air. On a green-to-yellow scale, we report all the δ-index values below 3%, while on a yellow-to-red scale the higher values (up to 3.8%) are drawn.

Finally, our DL model can significantly enhance speed in generating dose distributions. Currently, the available methods to compute VHEE dose maps are full MC simulations and fast MC codes such as FRED, which run on GPU. Our DL algorithm produces a dose map in approximately 0.02 s on a 16-core CPU (HP Z2 Tower G5 Workstation). A full MC simulation with Geant4 takes five orders of magnitude more time on the same machine. Moreover, running the DL model on GPU devices can further reduce the execution time. Generating a single example on a Nvidia Tesla V100 32G GPU takes approximately 7 milliseconds. If generating in batches, the execution time can be further reduced: generating a batch of 64 samples takes approximately 0.15 s, bringing the generation time of a single sample down to 2.3 milliseconds—roughly three orders of magnitude faster than FRED.

Although the DL dose engine presented shows promise in balancing accuracy and speed in dose computation, it is important to note some limitations. This study aims to demonstrate the feasibility and effectiveness of the cylindrical scoring method combined with an innovative GNN-based DL model for dose predictions. Although nearly 100% of the dose predictions achieve a δ-index passing rate of 3% inspired by the clinical global γ-index, the current cylindrical voxel dimensions along z and r do not permit comparison at the required clinical spatial resolution. This comparison will be conducted in subsequent research, in which we plan to increase the cylinder's resolution to meet, and even over-sample, in the core of the cylinder the clinically required spatial resolution. A larger cohort of patients will then be considered to test the model's generalization ability. Given that the execution time of graph convolutional layers scales linearly with the number of nodes, reducing the resolution to 2 mm—increasing the nodes by a factor of 4—would still keep the total execution time below 10 ms.

4 Conclusion

The current study proposes a DL model to compute the dose distribution of a therapeutic VHEE beam in patient tissues. The model, based on graph convolutional networks, is trained to emulate the MC simulated dose inside a cylindrical volume around the beam. This approach allows us to compute the dose with high spatial resolution on the beamline, where most of the dose is deposited, while containing the model's memory footprint. The model was trained on a set of examples comprising different beam orientations and energies, and it was tested on a different set. The test set has been realized using couples of beam orientation and energy not used to produce the train set to test model's generalization capability. The model's accuracy was measured using MAE and MRE on integrated dose profiles, and δ-index. The results show that the model can generate dose distributions with a δ-index 3% passing rate of 99.8%. Moreover, integrated dose profiles agree with MC simulations, with an average relative error less than 1%.

With respect to other current methods for calculating VHEE dose distributions—full MC simulations and FRED—our model provides an acceleration of several orders of magnitude. Indeed, it can generate dose distribution in milliseconds on a single GPU. The dose calculation is so fast that the DL model could be directly integrated into the merit function of an optimization algorithm for treatment planning. Moreover, taking advantage of the fact that the output of a DL model is differentiable with respect to the input, it would be possible to build a treatment planning optimization strategy based on exact gradient computation.

We plan to explore this possibility in future research aiming to build a treatment plan optimization algorithm which can fully exploit the benefits of DL dose generation.

Data availability statement

The raw data supporting the conclusions of this article will be made available by the authors, without undue reservation.

Ethics statement

Ethical approval was not required for the studies involving humans because this study uses the same patient data on a previously published paper in *Frontiers in Physics*: https://doi.org/10.3389/fphy.2023.1185598. As stated there: "Ethical review and

approval was not required for the study on human participants, and written informed consent for participation was obtained."

Author contributions

LA: conceptualization, data curation, formal analysis, investigation, methodology, resources, software, validation, visualization, writing–original draft, and writing–review and editing. BC: funding acquisition, supervision, writing–original draft, and writing–review and editing. AC: software, validation, writing–original draft, and writing–review and editing. AD: writing–original draft and writing–review and editing. GF: writing–original draft and writing–review and editing. StG: funding acquisition, resources, supervision, writing–original draft, and writing–review and editing. SuG: writing–review and editing, supervision, and writing–original draft. AM: data curation, writing–original draft, and writing–review and editing. FN: writing–original draft and writing–review and editing. JP: software, writing–original draft, and writing–review and editing. AS: funding acquisition, supervision, writing–original draft, and writing–review and editing. CM-T: conceptualization, formal analysis, funding acquisition, investigation, methodology, project administration, resources, software, supervision, validation, writing–original draft, and writing–review and editing.

Funding

The authors declare that financial support was received for the research, authorship, and/or publication of this article. This research was partially supported by PNRR MUR project PE0000013-FAIR. This research was partially funded by INFN National Scientific Committee 5 project FRIDA (Flash Radiotherapy with hIgh Dose-rate particle beAms).

Acknowledgments

The authors acknowledge the CINECA award under the ISCRA initiative for the availability of high-performance computing resources and support.

Conflict of interest

The authors declare that the research was conducted in the absence of any commercial or financial relationships that could be construed as a potential conflict of interest.

Publisher's note

Supplementary material

The Supplementary Material for this article can be found online at: https://www.frontiersin.org/articles/10.3389/fphy.2024.1443306/full#supplementary-material

References

1. Delaney G, Jacob S, Featherstone C, Barton M. The role of radiotherapy in cancer treatment: estimating optimal utilization from a review of evidence-based clinical guidelines. *Cancer* (2005) 104:1129–37. doi:10.1002/cncr.21324

2. Schüler E, Eriksson K, Hynning E, Hancock SL, Hiniker SM, Bazalova-Carter M, et al. Very high-energy electron (VHEE) beams in radiation therapy; Treatment plan comparison between VHEE, VMAT, and PPBS. *Med Phys* (2017) 44:2544–55. doi:10.1002/mp.12233

3. Krim DE, Rrhioua A, Zerfaoui M, Bakari D. Monte Carlo modeling of focused very high energy electron beams as an innovative modality for radiotherapy application. *Nucl Instrum Methods Phys Res A* (2023) 1047:167785. doi:10.1016/j.nima.2022.167785

4. Otto K. Volumetric modulated arc therapy: IMRT in a single gantry arc. *Med Phys* (2008) 35:310–7. doi:10.1118/1.2818738

5. Ronga MG, Cavallone M, Patriarca A, Leite AM, Loap P, Favaudon V, et al. Back to the future: very high-energy electrons (vhees) and their potential application in radiation therapy. *Cancers* (2021) 13:4942. doi:10.3390/cancers13194942

6. Maxim PG, Tantawi SG, Loo BW, Jr. PHASER: a platform for clinical translation of FLASH cancer radiotherapy. *Radiother Oncol* (2019) 139:28–33. doi:10.1016/j.radonc.2019.05.005

7. Giuliano L, Alesini D, Behtouei M, Bosco F, Carillo M, Cuttone G, et al. *Preliminary studies of a compact VHEE linear accelerator system for FLASH radiotherapy*. Geneva, Switzerland: JACOW Publishing (2021). 1229–32.

8. Lin B, Gao F, Yang Y, Wu D, Zhang Y, Feng G, et al. FLASH radiotherapy: history and future. *Front Oncol* (2021) 11:644400. doi:10.3389/fonc.2021.644400

9. Favaudon V, Caplier L, Monceau V, Pouzoulet F, Sayarath M, Fouillade C, et al. Ultrahigh dose-rate FLASH irradiation increases the differential response between normal and tumor tissue in mice. *Sci Transl Med* (2014) 6:245ra93. doi:10.1126/scitranslmed.3008973

10. Vozenin MC, De Fornel P, Petersson K, Favaudon V, Jaccard M, Germond JF, et al. The advantage of FLASH radiotherapy confirmed in mini-pig and cat-cancer patients. *Clin Cancer Res* (2019) 25:35–42. doi:10.1158/1078-0432.ccr-17-3375

11. Bourhis J, Sozzi WJ, Jorge PG, Gaide O, Bailat C, Duclos F, et al. Treatment of a first patient with FLASH-radiotherapy. *Radiother Oncol* (2019) 139:18–22. doi:10.1016/j.radonc.2019.06.019

12. Sarti A, De Maria P, Battistoni G, De Simoni M, Di Felice C, Dong Y, et al. Deep seated tumour treatments with electrons of high energy delivered at FLASH rates: the example of prostate cancer. *Front Oncol* (2021) 11:777852. doi:10.3389/fonc.2021.777852

13. Schiavi A, Senzacqua M, Pioli S, Mairani A, Magro G, Molinelli S, et al. Fred: a GPU-accelerated fast-Monte Carlo code for rapid treatment plan recalculation in ion beam therapy. *Phys Med Biol* (2017) 62:7482–504. doi:10.1088/1361-6560/aa8134

14. Muscato A, Arsini L, Battistoni G, Campana L, Carlotti D, De Felice F, et al. Treatment planning of intracranial lesions with VHEE: comparing conventional and FLASH irradiation potential with state-of-the-art photon and proton radiotherapy. *Front Phys* (2023) 11. doi:10.3389/fphy.2023.1185598

15. Wang M, Zhang Q, Lam S, Cai J, Yang R. A review on application of deep learning algorithms in external beam radiotherapy automated treatment planning. *Front Oncol* (2020) 10:580919. doi:10.3389/fonc.2020.580919

16. Zhang X, Hu Z, Zhang G, Zhuang Y, Wang Y, Peng H. Dose calculation in proton therapy using a discovery cross-domain generative adversarial network (DiscoGAN). *Med Phys* (2021) 48:2646–60. doi:10.1002/mp.14781

17. Kontaxis C, Bol GH, Lagendijk JJW, Raaymakers BW. DeepDose: towards a fast dose calculation engine for radiation therapy using deep learning. *Phys Med Biol* (2020) 65:075013. doi:10.1088/1361-6560/ab7630

18. Kearney V, Chan JW, Wang T, Perry A, Descovich M, Morin O, et al. DoseGAN: a generative adversarial network for synthetic dose prediction using attention-gated discrimination and generation. *Sci Rep* (2020) 10:11073. doi:10.1038/s41598-020-68062-7

19. Jensen PJ, Zhang J, Koontz BF, Wu QJ. A novel machine learning model for dose prediction in prostate volumetric modulated arc therapy using output initialization and optimization priorities. *Front Artif Intell* (2021) 4:624038. doi:10.3389/frai.2021.624038

20. Mentzel F, Kröninger K, Lerch M, Nackenhorst O, Paino J, Rosenfeld A, et al. Fast and accurate dose predictions for novel radiotherapy treatments in heterogeneous phantoms using conditional 3D-UNet generative adversarial networks. *Med Phys* (2022) 49:3389–404. doi:10.1002/mp.15555

21. Mentzel F, Paino J, Barnes M, Cameron M, Corde S, Engels E, et al. Accurate and fast deep learning dose prediction for a preclinical microbeam radiation therapy study using Low-Statistics Monte Carlo simulations. *Cancers* (2023) 15:2137. doi:10.3390/cancers15072137

22. Agostinelli S, Allison J, Amako K, Apostolakis J, Araujo H, Arce P, et al. Geant4—a simulation toolkit. *Nucl Instrum Methods Phys Res A* (2003) 506:250–303. doi:10.1016/s0168-9002(03)01368-8

23. Allison J, Amako K, Apostolakis J, Araujo H, Arce Dubois P, Asai M, et al. Geant4 developments and applications. *IEEE Trans Nucl Sci* (2006) 53:270–8. doi:10.1109/tns.2006.869826

24. Allison J, Amako K, Apostolakis J, Arce P, Asai M, Aso T, et al. Recent developments in geant4. *Nucl Instrum Methods Phys Res A* (2016) 835:186–225. doi:10.1016/j.nima.2016.06.125

25. Arce P, Bolst D, Bordage MC, Brown JMC, Cirrone P, Cortés-Giraldo MA, et al. Report on G4-Med, a geant4 benchmarking system for medical physics applications developed by the geant4 medical simulation benchmarking group. *Med Phys* (2021) 48:19–56. doi:10.1002/mp.14226

26. Large MJ, Malaroda A, Petasecca M, Rosenfeld AB, Guatelli S. Modelling ICRP110 adult reference voxel phantoms for dosimetric applications: development of a new geant4 advanced example. *J Phys Conf Ser* (2020) 1662:012021. doi:10.1088/1742-6596/1662/1/012021

27. Giacometti V, Guatelli S, Bazalova-Carter M, Rosenfeld AB, Schulte RW. Development of a high resolution voxelised head phantom for medical physics applications. *Phys Med* (2017) 33:182–8. doi:10.1016/j.ejmp.2017.01.007

28. Böhlen TT, Germond JF, Bourhis J, Vozenin MC, Ozsahin EM, Bochud F, et al. Normal tissue sparing by FLASH as a function of Single-Fraction dose: a quantitative analysis. *Int J Radiat Oncol Biol Phys* (2022) 114:1032–44. doi:10.1016/j.ijrobp.2022.05.038

29. Ronneberger O, Fischer P, Brox T. U-Net: convolutional networks for biomedical image segmentation, 234, 41. doi:10.1007/978-3-319-24574-4_282015).

30. Arsini L, Caccia B, Ciardiello A, Giagu S, Mancini Terracciano C. Nearest neighbours graph variational AutoEncoder. *Algorithms* (2023) 16:143. doi:10.3390/a16030143

31. Arsini L, Humphreys J, White C, Mentzel F, Paino J, Bolst D, et al. Comparison of deep learning models for fast and accurate dose map prediction in microbeam radiation therapy. *Submitted Physica Med* (2024).

32. Low DA, Harms WB, Mutic S, Purdy JA. A technique for the quantitative evaluation of dose distributions. *Med Phys* (1998) 25:656–61. doi:10.1118/1.598248

33. Javaid U, Souris K, Dasnoy D, Huang S, Lee JA. Mitigating inherent noise in Monte Carlo dose distributions using dilated U-Net. *Med Phys* (2019) 46:5790–8. doi:10.1002/mp.13856

frontiers | Frontiers in Physics

TYPE Original Research
PUBLISHED 11 December 2024
DOI 10.3389/fphy.2024.1496850

OPEN ACCESS

EDITED BY
Luigi Palumbo,
Sapienza University of Rome, Italy

REVIEWED BY
Jiaru Shi,
Tsinghua University, China
Mauro Migliorati,
Sapienza University of Rome, Italy

*CORRESPONDENCE
Deepa Angal-Kalinin,
deepa.angal-kalinin@stfc.ac.uk

RECEIVED 15 September 2024
ACCEPTED 12 November 2024
PUBLISHED 11 December 2024

CITATION
Angal-Kalinin D, Boogert S and Jones JK (2024) Potential of the CLARA test facility for VHEE radiotherapy research.
Front. Phys. 12:1496850.
doi: 10.3389/fphy.2024.1496850

Potential of the CLARA test facility for VHEE radiotherapy research

Deepa Angal-Kalinin[1,2,3]*, Stewart Boogert[2,3] and James Kevin Jones[1,3]

[1]ASTeC, United Kingdom Research and Innovation, Science and Technology Facilities Council (UKRI STFC) Daresbury Laboratory, Sci-Tech Daresbury, Warrington, United Kingdom, [2]Department of Physics and Astronomy, The University of Manchester, Manchester, United Kingdom, [3]The Cockcroft Institute, Sci-Tech Daresbury, Warrington, United Kingdom

The Compact Linear Accelerator for Research and Applications (CLARA) is a test facility at the STFC Daresbury Laboratory, which is capable of delivering ultra-bright electron bunches of up to 250 MeV beam energy. A new beam line has been designed to maximise the exploitation of the CLARA facility in a variety of scientific fields, including novel acceleration and new modalities of radiotherapy. In this paper, we present the specification and design of this beam line to explore the possibilities of pursuing R&D in very high-energy electron (VHEE) radiotherapy and VHEE with FLASH radiotherapy. We describe the beam line design, including the flexibility of the beam optics to focus the beam in a range of locations and present results from preliminary start-to-end simulations using Monte Carlo tracking codes. We highlight advantages of this beam line, including rapid access to the shielded experimental hutch and the possibilities for the installation of different experimental setups in two dedicated chambers. The beam line includes focussing magnets, extensive diagnostics, and allows in-air installation within the experimental beam line. The facility will allow an experimental programme towards addressing many outstanding issues related to this new radiotherapy modality. We also describe the available flexibility in beam parameters for both conventional dose rates and those entering into the FLASH regime. The possibility of both living cells and treatment planning studies is anticipated to be conducted at this world-class facility.

KEYWORDS

ultra-bright electron source, beam energy, bunch charge, repetition rate, shielded hutch, very high-energy radiotherapy, flash dose rate

1 Introduction

The Compact Linear Accelerator for Research and Applications (CLARA) is an ultra-bright electron beam test facility at the STFC Daresbury Laboratory in the UK. The facility was originally created to test advanced free-electron laser (FEL) schemes that could be implemented on existing and future short-wavelength FEL facilities [1]. The facility is divided into three phases: Phase 1, front end of CLARA includes an S-band photoinjector, a 2-m-long S-band linac, a collimator, focussing and spectrometer magnets, and diagnostics. The front end, which produced 50-MeV, 250-pC electron bunches from a 10-Hz S-band photoinjector gun and linac, was successfully commissioned in 2018

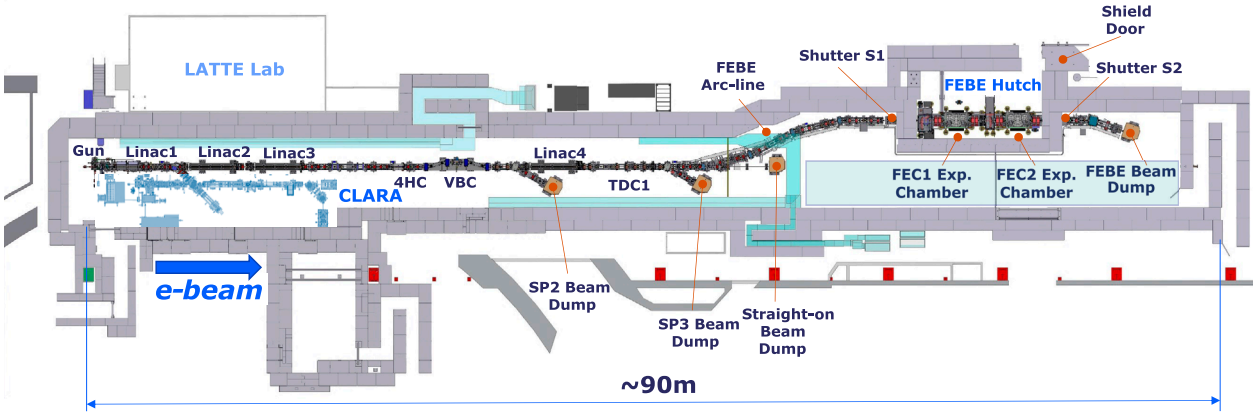

FIGURE 1
Schematic representation of the CLARA linear accelerator test facility, including the FEBE beam line, shielded FEBE hutch, and space reserved for potential future applications (shaded light blue area). The major components of the accelerator are highlighted, including the two shutters and the shield door used to allow rapid access to the hutch. The 100-TW laser system (not shown) is situated above the FEBE Hutch.

[2]. Phase 2 includes additional accelerator modules that increase the beam energy to 250 MeV. The front end photoinjector gun has also been replaced with a novel 100-Hz high-repetition rate gun (HRRG) [3], which was previously commissioned on an adjacent beam line. The Phase 2 accelerator consists of a front end with the new high-repetition rate injector, three 4-m-long S-band (2,998.5 MHz) linacs, an X-band (11.994 GHz) fourth-harmonic cavity (4HC) phase-space linearliser, a variable magnetic bunch compressor (VBC), a dielectric dechirper, and a dedicated diagnostics line including a transverse deflecting cavity (TDC) for 6D phase-space characterisation. Focussing magnets and spectrometer beam lines are incorporated into the beam line for beam optics control and energy and energy spread measurements. Although Phase 3, which includes the installation of the FEL, has not yet been funded, the space has been reserved for possible future applications.

Access to the electron beam from the low-energy Phase 1 CLARA front end was made available from the beginning of 2018 to users from both academia and industry. This allowed for experiments to be carried out in a wide range of disciplines to test new concepts and ideas, such as the development of advanced accelerator technology [4], medicinal applications [5], and novel particle beam acceleration concepts [6–8]. For most experiments, a beam energy of 35 MeV with 100 pC charge was delivered, with beam energy of 20 – 40 MeV available for medical applications. Based on increasing user demand for experimental access, it was decided to design and build an additional dedicated beam line for user experiments at the maximum CLARA beam energy of 250 MeV, which is available in Phase 2. As shown in Figure 1, the beam line for full energy beam exploitation (FEBE) is installed parallel to the space originally allocated for the FEL and will enable an expanded range of experiments with all new experimental chambers and a high-powered 100-TW laser system.

CLARA is one of only a few of test facilities worldwide that can provide user access to mid-energy range (less than 300 MeV), high-brightness electron beams to test proof-of-principle novel applications. A survey of beam dynamics challenges of such mid-energy high-brightness facilities in Europe was recently carried out and presented at IPAC'23 [9]. In addition to CLARA, there are three other comparable facilities in Europe: CLEAR@CERN [10, 11], ARES@DESY [12, 13], and SPARC_LAB@INFN [14].

In contrast to most other medium-energy facilities, the FEBE beam line is relatively unique in providing a dedicated shielded experimental hutch. This arrangement allows on-demand user access to the experimental area without fully switching off the accelerator, reducing disruption, improving machine stability, and allowing experiments to resume promptly after access periods. This is achieved by interlocking the FEBE dipoles to the accelerator personal safety system, allowing the continued operation of the RF systems and electron beam in the main CLARA accelerator while users have free access to the hutch. Upon completion of user access, the hutch is searched and locked, and the FEBE dipoles are re-energised to provide beam into the FEC chambers with minimal downtime and with minimal change to the electron beam properties from the CLARA accelerator. Such rapid experimental access is currently not possible at similar facilities in Europe, although CLEAR has developed robotic systems to reduce user access requirements during some types of experiments.

The detailed design of the FEBE beam line for the delivery of high-brightness beams for novel acceleration and other applications was recently published [15]. In this article, our focus is on the specification and design of the FEBE beam line and its suitability to explore VHEE and VHEE with FLASH in detail. The article is structured as follows: the layout of the machine and beam specification is presented in Section 2. Section 3 discusses previous studies on VHEE utilising the CLARA front end. Section 4 presents the results of beam dynamics simulations conducted from the CLARA photoinjector through the FEBE experiment chamber, where VHEE water phantom and other irradiation samples (such as plasmids and cells) will be installed. Section 5 details the dosage calculations performed using BDSIM/GEANT4 for different beam parameters at the predicted location of the experiment that will support future user exploitation. Section 6 describes future work.

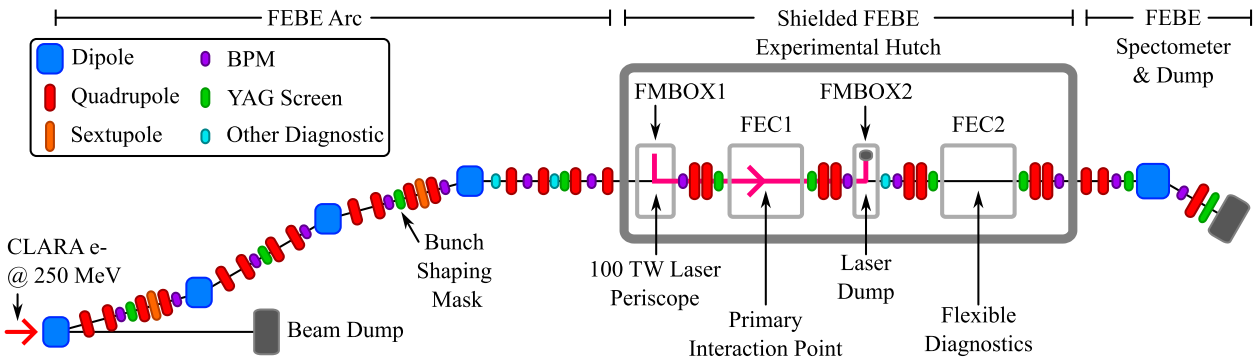

FIGURE 2
Schematic representation of the full energy beam exploitation (FEBE) beam line, including arc (connecting to the upstream CLARA main beam line, Figure 1), experiment hutch, and post-hutch beam dump with energy and emittance diagnostics.

The article concludes with the current status of the facility in Section 7 and summary in Section 8.

2 Layout and beam specification

FEBE is designed to support a variety of experiments in the fields of accelerator applications and accelerator technology. A user survey performed in 2018 established a particular interest in R&D related to the new modality of VHEE and FLASH radiotherapy, as well as novel acceleration R&D. As a result, we separate the beam parameter specification provided for general FEBE operation from that for novel acceleration experiments, which frequently prioritises longitudinal peak-current and ultra-short bunch lengths. On the contrary, requirements for VHEE with bunch lengths in the multiple *ps*-range and negligible longitudinal chirp require minimal longitudinal beam manipulation. Variable bunch charges (10 – 250 pC) and energies (50 – 250 MeV) should be relatively simple to implement in this operating mode. In this regime, collective effects (particularly coherent synchrotron radiation (CSR)) are insignificant, resulting in the delivery of close to the designed normalised emittances from the photoinjector.

A schematic representation of the beam line is shown in Figure 2. The FEBE layout is divided into three sections, namely, an arc and matching section connected to the main CLARA beam line; the FEBE experimental hutch, which brings the electron beam to a focus at two possible interaction points (IPs); and the post-hutch transport line and beam dump. The FEBE experimental hutch is a $10 \times 5.4 \times 3$-m^3 dedicated area for users to perform beam experiments utilising electron beams.

The hutch is transversely offset from the main CLARA beam line, with a quadrupole FODO structure providing a horizontal $-I$ transform between two 14° dipoles and optimised to reduce emittance growth due to CSR [16]. This solution leads to a strong focussing, achromatic, and non-isochronous arc with large natural second-order longitudinal dispersion, which requires correction using sextupole magnets at positions of high dispersion. Six quadrupole families allow matching the main beam line for a range of electron beam configurations. The arc has a nominal R_{56} value of +7.7 mm, with no residual dispersion. The longitudinal bunch compression of the electron beam at the hutch can be achieved using a combination of the FEBE arc and the upstream VBC. Although current requirements from the VHEE community do not require this mode of operation, in case dependence of the VHEE dose rate on the electron bunch length will be of interest in future R&D, we mention this possibility.

The beam transport within the hutch is notionally designed to deliver a strong focus to two possible IPs (IP1/2), each of which is located within a large-volume (~2 m^3) experimental chamber known as the FEBE experiment chamber (FEC1/2), as shown schematically in Figure 3. The internal dimensions of each chamber are 1.8 m × 1.0 m × 0.93 m, and the beam height is 0.4 m from the bottom of the chamber. The double-IP design provides flexibility in the experiment design and implementation, as well as allows the installation of multiple independent experiments in FEC1 and FEC2, when compatible, minimising the downtime required for the experimental setup. The beam parameters in the two modes of operations at the IP1/2 *in vacuo* are given in Table 1; the general category covers a broad range from highly longitudinally compressed bunches (as required for the wakefield category of novel acceleration experiments) to longer bunches where there is no such demand for high peak currents.

VHEE experiments will be conducted in air. To enable this, a beryllium window will be installed at the entrance and exit of the relevant experimental chamber (FEC1 or FEC2). In previous CLARA front end VHEE experiments, a 500-μm-thick beryllium window with a 25-mm-diameter aperture was installed on the vacuum pipe at the end of the CLARA front end beam line, and a similar window is planned to be installed in the FEBE beam line. The window flange has a vent facility for local pump-down and release of the small interspace volume between the window and the gate valve. When in-air experiments are completed, vacuum gate valves on either side of the chamber are closed off, and the inter-space between the gate valve and window is decreased. The window is then removed, and the chamber pumped down to vacuum for in-vacuum experiments. The simulations presented in Section 5 for dose calculations take this window thickness and material into account.

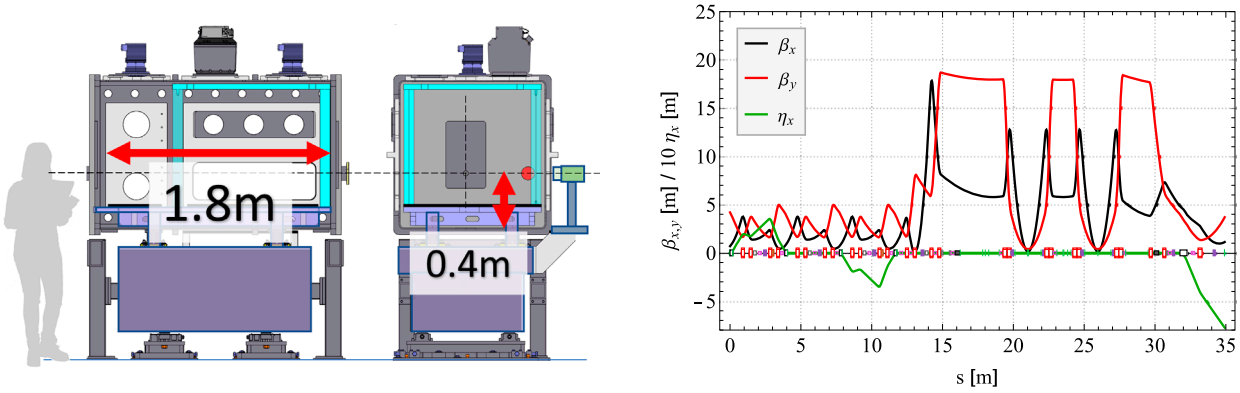

FIGURE 3
Left: schematic representation of the FEBE experimental chambers FEC [1/2]. The dotted line shows the electron beam height. Right: Twiss parameters for the FEBE beam line shown in Figure 2. The dotted lines indicate the locations of IP1/2 in FEC1/2, respectively.

TABLE 1 Design beam parameters at the FEC1 and FEC2 interaction points.

Parameter (*in vacuo*)	FEBE (general)	FEBE (VHEE)
Energy	50–250 MeV	50–250 MeV
Charge (max)	250 pC	250 pC
Repetition rate	100 Hz (5 Hz with laser)	100 Hz
RMS bunch length σ_t	50 fs–10 ps	1–10 ps
RMS energy spread σ_E	<5%	<0.5%
Normalised horizontal beam emittance $\epsilon_{N,x}$	<5 μm-rad	<1 μm-rad
Normalised vertical beam emittance $\epsilon_{N,y}$	<2 μm-rad	<1 μm-rad

Access to the hutch with the accelerator running is made possible via an interlock of the FEBE arc dipoles to the machine personal safety system. Radiation shutters on either side of the enclosure (in the CLARA accelerator hall) are used to shield the hutch from the radiation generated from the main CLARA accelerator.

3 Previous studies on the CLARA front end

As noted, access to the 35-MeV, 100-pC electron beam from the CLARA front end was used for major experimental runs. Experimental setups were custom built at CLARA, and experiments at higher energies were carried out at CLEAR. During each of these experimental runs, VHEE irradiation experiments were performed in collaboration with the Manchester group, including studies on dosimetric inhomogeneities on beam dose profiles in water phantoms at various energies [17, 18], plasmid irradiation studies quantifying characteristics of VHEE relative biological effectiveness (RBE) [5, 19], and comparisons between radiotherapy modalities using DNA plasmids [20].

These experimental runs were vital for developing experience and the technical knowledge in running high-throughput irradiation experiments for both wet and dry VHEE biological experiments. A simple, yet robust and repeatable, system of stages and sample holders was developed to allow multiple samples to be irradiated sequentially with the whole system automated from the CLARA control room. Although relatively simple in comparison to other facilities' advanced commercial robotic sample preparation systems, the rapid experimental access available at the CLARA front end and designed into the FEBE beam line mitigate some of these disadvantages. The system is also intrinsically flexible due to its simplicity and can accommodate a variety of irradiation targets.

4 Beam dynamics simulations

4.1 Start-to-end simulations on CLARA/FEBE

Particle tracking simulations were carried out using ASTRA [21] and ELEGANT [22], accounting for the non-linear effects

(both longitudinal and transverse) of space charge and CSR. A Python-based framework (Simframe) developed at the STFC Daresbury Laboratory, which allows a single human-readable lattice file to be deployed consistently across several codes, was used throughout. ASTRA was used to simulate the CLARA injector at low energy (below 35 MeV), where transverse and longitudinal space charge forces are the dominant emittance-diluting processes. ELEGANT was used above 35 MeV due to its processing speed and the inclusion of CSR effects in the bunch compressor and FEBE arc.

The main optimisation actuators for the FEBE beam are found in the preceding CLARA beam line, as shown in Figure 1. The first 2-m S-band injector linac (Linac 1) can act as either a standard low-energy accelerating structure or a longitudinal bunching structure for a short single-spike operation. The remaining three 4-m-long S-band linacs (Linacs 2–4) provide acceleration up to a nominal beam energy of 250 MeV. A chicane-type VBC is located between Linac3 and Linac4, with X-band 4HC immediately before the VBC to compensate for longitudinal phase-space curvatures. The VBC is located at a nominal energy of ~ 180 MeV to maximise its effectiveness for the moderate compression required for the original CLARA FEL concept.

4.2 Start-to-end simulations for VHEE

Start-to-end simulations were performed to evaluate and optimise the electron beam properties at the FEC1 IP, although operation at FEC2 IP is similar. Simulations targeted expected requirements for VHEE operation as shown in Table 1: high charge (250 pC), high energy (250 MeV), long pulse length (>2ps), and low momentum spread (<0.5%).

The machine settings for the optimised VHEE mode are set to provide a mild amount of compression, following the variable bunch compressor (~2 ps RMS) with Linacs 1, 2, and 3 at moderate off-crest phases (+5°) and the 4HC cavity at the nominal phase of −180°. Linac4 is set to reduce the longitudinal chirp at −45°. These settings, including the required photoinjector laser pulse length for ~2-ps bunch lengths, are compatible with machine requirements for other expected operation modes on CLARA. For ultra-compressed modes, we only need to modify the linac off-crest phases to increase the longitudinal compression in the VBC and FEBE arcs and *vice versa* for the VHEE operation.

The relaxed longitudinal emittance required for VHEE studies (as compared to other experiments planned on FEBE) reduces the impact of collective effects (such as CSR) in the bunch compressor and FEBE arc sections, allowing for significantly lower nominal transverse emittance at the FEBE IP (<1 μm-rad, normalised). Transverse matching of the FEBE beam line was performed for two scenarios: a large diameter pencil beam with a half-width of 10 mm ($\sigma \approx 3.5$ mm) and a focused beam with a large divergence of >1 m-rad in both transverse planes at the IP. These two scenarios adequately demonstrate the extreme range of possible VHEE beams required in most experiments. The relevant transverse beam sizes and Twiss parameters for both scenarios are shown in Figure 4. In both scenarios, we do not modify the FEBE arc optics and utilise only the quadrupole magnets in the post-arc matching section and within the FEBE hutch. The quadrupoles on either side of the FEC1 chamber are large-bore (74 *mm* aperture), high-strength magnets (maximum integrated gradient of 4.5 *T*, with a magnetic length of 0.225 *m*) designed to allow the FEBE high-power (100 TW) laser to pass. These quadrupoles are identical to the four other quadrupoles located on either side of the FEC2 chamber, and they are designed to operate at up to 600 MeV to allow for the potential acceleration in the experimental chambers (for instance, via acceleration in a dielectric wakefield structure or through plasma wakefield acceleration processes). This scenario does not apply to VHEE beams, but the large quadrupole apertures allow stronger focussing. Similar optics setup can be delivered to IP2 if experiments are conducted in FEC2.

Variation in the focus position is also possible within the chamber, providing a variable dose-depth profile and a spread-out-electron-peak (SOEP). The results for such a variation are shown in Figure 5 in vacuum, ignoring scattering from the beryllium window or for air or water. Focussing close to the chamber entrance is difficult, but variation in the focus position between 0.5 m and 1.5 m of the chamber shows a very flat distribution. The beam transverse angular divergence achievable for a flat SOEP, 250 μrad, is smaller than the optimised case shown in Figure 4, left, which reaches approximately 1.5 mrad angular divergence, 250 μrad vs 1.5 mrad.

5 BDSIM/Geant4 dose calculations

The dose delivered to IP1/2 in FEBE was calculated using Beam Delivery Simulation (BDSIM) [23]. BDSIM is a Geant4-based code, which simulates the passage of particles through accelerator components. BDSIM has already extensively been used to simulate a wide range of facilities from proton beam therapy systems to high-energy particle physics colliders. Inside the vacuum of common accelerator components, such as quadrupoles, accelerator style tracking is used. As particles pass through matter and/or complex field regions Geant4 style tracking is employed. A BDSIM model of the FEBE beam line was created by converting the optical configurations, as shown in Figure 4. The physical (mass) geometry of the accelerator uses generic BDSIM accelerator components but with magnetic fields consistent with the accelerator optics. Electrons with the same phase space characteristics were tracked through the BDSIM magnetic fields, and beam sizes were computed after each element. The BDSIM-computed beam size agrees with that presented in Figure 4, confirming that the BDSIM model accurately represented the FEBE magnetic lattice.

The drift space around the FEC1 focus is replaced in the BDSIM model with a 500-μm-thick beryllium window, followed by 80.4 cm of air, 30 cm of water, and by 73.7 cm of air and another 500-μm window. An indicative visualisation of 100 incident electrons in BDSIM/Geant4 is shown in Figure 6. An all-particle dose-scoring mesh is placed at the nominal focus location of FEC1. The dose scoring mesh is 5 cm × 5 cm × 30 cm, and the number of bins is $100 \times 100 \times 100$, providing a mesh cell size of $500\,\mu\text{m} \times 500\,\mu\text{m} \times 3\,\text{mm}$. For each different material or beam optics configuration, 2×10^6 primary particles (histories) were simulated. The Geant4 physics lists used for the simulations were *em* for electromagnetic

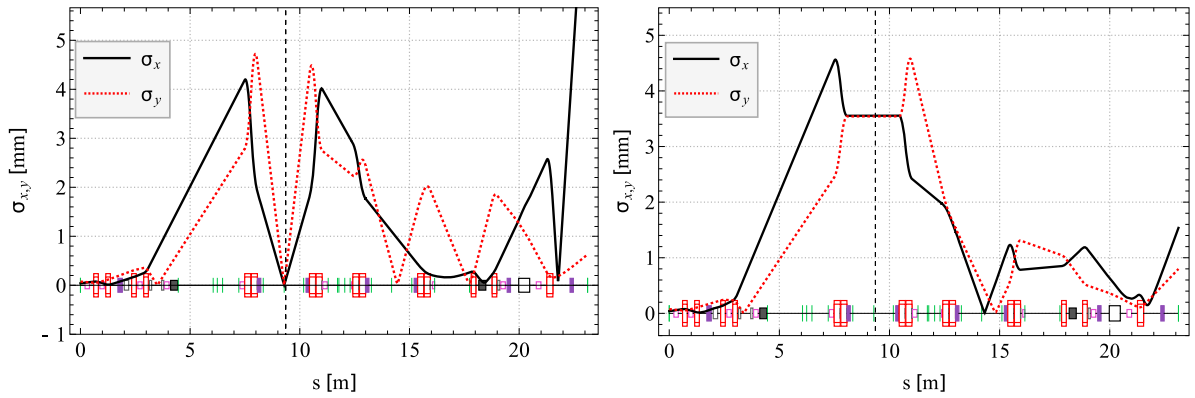

FIGURE 4
Left: transverse beam sizes for a focused beam at IP1 in FEC1. Right: transverse beam sizes for a pencil beam at IP1 in FEC1, both *in vacuo*.

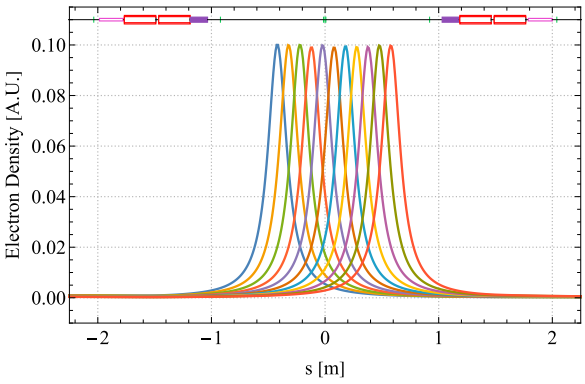

FIGURE 5
Variation in the electron focus position inside the FEC1 chamber shown using electron density plots. All results are *in vacuo* and do not include the effects of the beryllium window or scattering in air/water.

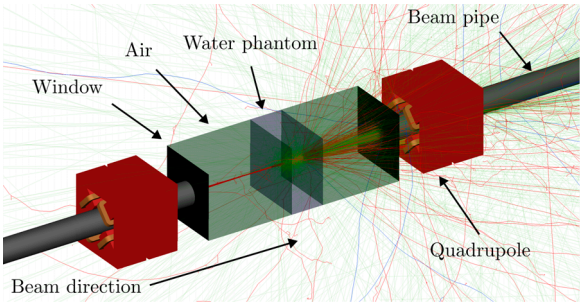

FIGURE 6
BDSIM/Geant4 visualisation region around the water phantom, including the quadrupoles before and after the experimental FEC1 chamber. Overlaid includes 100 primary electrons and the interaction products.

processes and *qgsp_bic* for hadronic. A range cut[1] of 1 mm was used for all BDSIM/Geant4 simulations. The final simulated dose-scoring mesh data are scaled by $N_{\text{bunch}}f/N_{\text{histories}}$, where N_{bunch} is the bunch population, $N_{\text{histories}}$ is the number of initial electrons simulated, and f is the machine frequency, to provide a dose rate in Gy/s.

The Geant4 computed doses are shown in Figures 7, 8 for the focused and pencil electron optics, respectively. In both optics configurations, FLASH dose rates (>40 Gy/s) are achievable at FEBE. For a focused beam with a realistic material budget (window, air, and target), the maximum dose rate is 238.5 Gy/s and transversely Gaussian-distributed with a full width at half maximum of 3.9 mm. For the pencil beam with a realistic material budget (window, air, and target), the maximum dose rate is 102.6 Gy/s and transversely Gaussian-distributed with a full width at half maximum of 6.1 mm. The target-only dose curves shown in Figures 7, 8 represent the absolute maximum dose deliverable at FEBE. Reducing the air length by a factor of two and using a thinner 250-μm window will increase the dose rates to approximately 500 Gy/s and 125 Gy/s for the focused and pencil beams, respectively.

Achieving a large dose uniformly over a large volume will either require a focus spot scanning system or a scattering system. Given the dose rates presented in this paper, a single or multiple scattering system at CLARA/FEBE is likely to reduce dose rates below those that are required for FLASH. Although the scanning system is technically possible, questions about the spatio-temporal dose rate distribution remain unexplored. From the perspective of accelerator beam delivery, both these questions can be studied using ELEGANT and BDSIM/Geant4 models of FEBE developed for this paper. The utility of VHEE FLASH via spot scanning also requires radiobiological experiments, which are likely to be performed at CLARA/FEBE.

1 A range cut is the minimum distance to consider physical processes in a Geant4 simulation. The distance range cut is converted to an energy minimum for each material used in the simulation. Particles which then fall below the energy are not then simulated further. Typically range cuts need to be smaller than the distances in a Geant4 simulation.

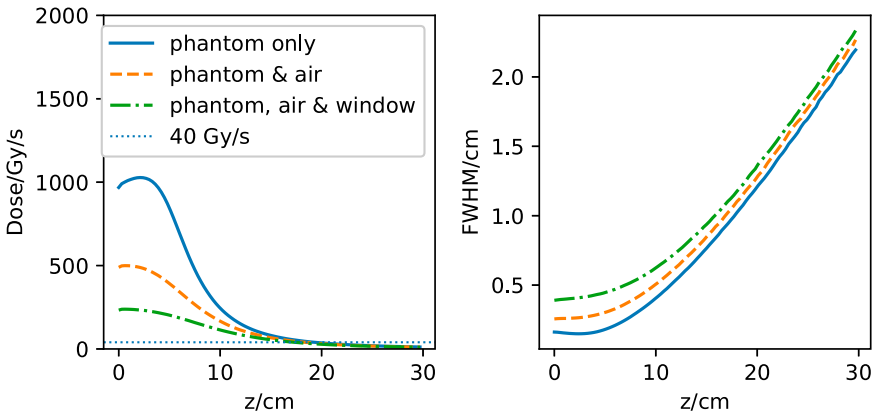

FIGURE 7
Left: axial dose distribution for the focused electron beam distribution as a function of depth in the water phantom. The horizontal dashed line at 40 Gy/s indicates the nominal FLASH dose rate. Right: full width at half maximum of the focused electron beam dose distribution as a function of depth in the water phantom. The solid line is just for the water phantom target, the dashed line is for air and target, and the dot-dash line is for the window, air, and target.

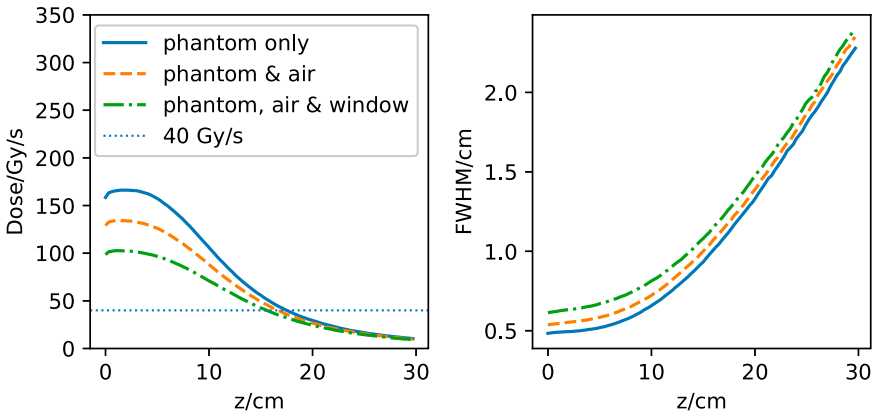

FIGURE 8
Left: axial dose distribution for the pencil electron beam distribution as a function of depth in the water phantom. The horizontal dashed line at 40 Gy/s, indicating the nominal FLASH dose rate. Right: full width at half maximum of the pencil electron beam dose distribution as a function of depth in the water phantom. The solid line is just for the water phantom target, the dashed line is for air and target, and the dot-dash line is for the window, air, and target.

6 Further work

The VHEE working group within the Cockcroft Institute at STFC Daresbury Laboratory is bringing together interested groups from universities and STFC to develop a long-term plan for VHEE studies on CLARA, as well as other relevant facilities. The primary focus for the near term is VHEE focussing on studies and their applicability for FLASH radiotherapy. Simulation work will prioritise improved focussing models and enhancements to enable more rapid optimisation of other potential operating modes for VHEE and FLASH operations. Experimental work on FEBE will prioritise electron focussing and spread-out electron peak (SOEP) research in water phantoms alongside tissue and cell biological studies, particularly those investigating previously unavailable FLASH modalities at CLARA. Exact details of conducting in-air VHEE experiments in FEBE experimental chambers will be worked out with the experimental groups in the near future.

7 Current status of the facility

As of this writing, CLARA installation in the accelerator hall is almost complete, and installation of the FEBE beam line into the hutch is expected to be completed by the end of 2024. RF conditioning of the gun and linacs is currently ongoing. It is expected that the RF conditioning of gun, linacs, 4HC, and TDC will be progressed sufficiently in the next few months for first beam threading, allowing for the completion of technical systems commissioning with the beam. This is followed by beam commissioning, characterisation, and setup to experimentally confirm beam parameters in the hutch; the installation and

commissioning of the 100-TW laser transport in the hutch will then take place, with completion scheduled for mid-2025. An open call to the community is expected to be issued in early 2025 for beam time in Autumn 2025, depending on the results of beam commissioning.

8 Summary

A new beam line for full energy beam exploitation (FEBE) has been designed and is currently undergoing installation on the CLARA test facility at the STFC Daresbury Laboratory. The goal of this beam line is to support a wide variety of user-driven experiments utilising 250-MeV ultra-bright electron bunches of 250-pC bunch charge delivered at repetition rates of up to 100 Hz. The beam line incorporates two large-volume experiment chambers with a shielded user hutch for easy user access and flexibility when setting up of in-air VHEE and VHEE with FLASH experiments. Initial simulations of the viability of the beam line for VHEE studies have demonstrated the potential for FLASH dose rates, alongside the use of beam focussing and spread-out electron peak studies.

The planned studies at the CLARA/FEBE facility will further extend the work done on the CLARA front end at lower energy levels, pushing the facility into a new era of high-energy, high-charge FLASH modalities.

Data availability statement

The original contributions presented in the study are publicly available. This data can be found here: https://edata.stfc.ac.uk/handle/edata/962

Author contributions

DA-K: conceptualisation, investigation, methodology, writing–original draft, and writing–review and editing. SB: formal analysis, investigation, methodology, software, validation, and writing–review and editing. JJ: data curation, formal analysis, investigation, methodology, software, validation, and writing–review and editing.

Funding

The author(s) declare that financial support was received for the research, authorship, and/or publication of this article. This work was supported by the Science and Technology Facilities Council under the Cockcroft Institute core grant ST/V001612/1.

Acknowledgments

The authors would like to thank members of the CLARA team at Daresbury Laboratory for help and support with various aspects of the design, simulation, and experimental studies on CLARA front end. In particular, they would also like to thank Barry Fell and George Marshall from Technology Division for useful discussions and advice on in-air experiments in FEBE chambers and Roger Jones and Kristina Small from the University of Manchester and the Cockcroft Institute for useful discussions.

Conflict of interest

The authors declare that the research was conducted in the absence of any commercial or financial relationships that could be construed as a potential conflict of interest.

Publisher's note

References

1. Clarke J, Angal-Kalinin D, Bliss N, Buckley R, Buckley S, Cash R, et al. Clara conceptual design report. *J Instrumentation.* (2014) 9:T05001. doi:10.1088/1748-0221/9/05/t05001

2. Angal-Kalinin D, Bainbridge A, Brynes A, Buckley R, Buckley S, Burt G, et al. Design, specifications, and first beam measurements of the compact linear accelerator for research and applications front end. *Phys Rev Acc Beams* (2020) 23:044801. doi:10.1103/physrevaccelbeams.23.044801

3. McKenzie J, Goudket P, Jones T, Militsyn B, Cowie L, Burt G, et al. High repetition rate s-band photoinjector design for the clara fel. In: *Proceedings of FEL'14*. Basel, Switzerland (2014).014801.

4. Pacey T, Saveliev Y, Healy A, Huggard P, Alderman B, Karataev P, et al. Continuously tunable narrow-band terahertz generation with a dielectric lined waveguide driven by short electron bunches. *Phys Rev Acc Beams* (2019) 22:091302. doi:10.1103/physrevaccelbeams.22.091302

5. Small K, Henthorn N, Angal-Kalinin D, Chadwick A, Santina E, Aitkenhead A, et al. Evaluating very high energy electron rbe from nanodosimetric pbr322 plasmid dna damage. *Scientific Rep* (2021) 11:3341. doi:10.1038/s41598-021-82772-6

6. Hibberd M, Healy AL, Lake DS, Georgiadis V, Smith EJH, Finlay OJ, et al. Acceleration of relativistic beams using laser-generated terahertz pulses. *Nat Photon* (2020) 14:755–9. doi:10.1038/s41566-020-0674-1

7. Saveliev YM, Pacey TH, Jones JK, Xia G. First dielectric wakefield experiments at daresbury laboratory. *J Phys Conf Ser* (2020) 1596:012015. doi:10.1088/1742-6596/1596/1/012015

8. Saveliev Y, Overton TJ, Pacey TH, Joshi N, Mathisen S, Muratori BD, et al. Experimental study of transverse effects in planar dielectric wakefield accelerating structures with elliptical beams. *Phys Rev Accel Beams* (2022) 25:081302. doi:10.1103/PhysRevAccelBeams.25.081302

9. Angal-Kalinin D, Jones JK, Pacey T, Corsini R, Burkart F, Pompili R, et al. Electron beam test facilities for novel applications. In: *Proceedings of IPAC'23*. Venice, Italy (2023).

10. CERN. CERN linear electron accelerator for research (2024). Available from: http://clear.cern/ (Accessed October 22, 2024).

11. Corsini R, Farabolini W, Malyzhenkov A, Dyks A, Korysko P, Sjobak K, et al. Status of the clear user facility at cern and its experiments. In: *Proceedings of LINAC'22, liverpool, United Kingdom (JaCoW, Geneva, Switzerland)* (2022).

12. DESY. Accelerator research experiment at SINBAD (2024). Available from: https://ares.desy.de/ (Accessed October 22, 2024).

13. Burkart F, Assmann R, Dinter H, Jaster-Merz S, Kuropka W, Mayet F, et al. The ares linac at desy. In: *Proceedings of LINAC'22*. Liverpool, United Kingdom (2022).

14. SPARC_LAB. Sources for plasma accelerators and radiation compton with laser and beam (2024). Available from: https://sparclab.lnf.infn.it/ (Accessed October 22, 2024).

15. Snedden EW, Angal-Kalinin D, Bainbridge AR, Brynes AD, Buckley SR, Dunning DJ, et al. Specification and design for full energy beam exploitation of the compact linear accelerator for research and applications. *Phys Rev Accel Beams* (2024) 27:041602. doi:10.1103/PhysRevAccelBeams.27.041602

16. Di Mitri S, Cornacchia M, Spampinati S. Cancellation of coherent synchrotron radiation kicks with optics balance. *Phys Rev Lett* (2013) 110:014801. doi:10.1103/PhysRevLett.110.014801

17. Lagzda A. *VHEE radiatherapy studies at CLARA and CLEAR facilities*. Manchester, UK: University of Manchetser (2019) PhD dissertation.

18. Lagzda A, Angal-Kalinin D, Jones J, Aitkenhead A, Kirkby KJ, MacKay R, et al. Influence of heterogeneous media on very high energy electron (vhee)dose penetration and a Monte Carlo-based comparison with existing radiotherapy modalities. *Nucl Instr Methods Phys Res B* (2020) 482:70–81. doi:10.1016/j.nimb.2020.09.008

19. Small K. *Nanodosimetric properties of very high energy electrons through pBR322 plasmid DNA studies*. Manchester, UK: University of Manchester (2020) PhD dissertation.

20. Wanstall HC, Henthorn NT, Jones J, Santina E, Chadwick AL, Angal-Kalinin D, et al. Quantification of damage to plasmid dna from 35 MeV electrons, 228 MeV protons and 300 kVp x-rays in varying hydroxyl radical scavenging environments. *J Radiat Res* (2023) 64:547–57. doi:10.1093/jrr/rrad032

21. Floetmann K. ASTRA. (2024) 1, doi:10.1145/3641231.3649151

22. Borland M. Elegant: a flexible sdds-compliant code for accelerator simulation. In: *Proceedings of ICAP'00*. Darmstadt, Germany: Darmstadt University of Technology (2000).

23. Nevay L, Boogert S, Snuverink J, Abramov A, Deacon L, Garcia-Morales H, et al. Bdsim: an accelerator tracking code with particle–matter interactions. *Computer Phys Commun* (2020) 252:107200. doi:10.1016/j.cpc.2020.107200

frontiers | Frontiers in Physics

TYPE Original Research
PUBLISHED 11 December 2024
DOI 10.3389/fphy.2024.1472759

OPEN ACCESS

EDITED BY
Luigi Palumbo,
Sapienza University of Rome, Italy

REVIEWED BY
Lanchun Lu,
The Ohio State University, United States
Imran Iqbal,
New York University, United States
Luca Serafini,
National Institute of Nuclear Physics of Milan, Italy

*CORRESPONDENCE
Christopher P. J. Barty,
cbarty@uci.edu

RECEIVED 30 July 2024
ACCEPTED 01 November 2024
PUBLISHED 11 December 2024

CITATION
Barty CPJ, Algots JM, Amador AJ, Barty JCR, Betts SM, Castañeda MA, Chu MM, Daley ME, De Luna Lopez RA, Diviak DA, Effarah HH, Feliciano R, Garcia A, Grabiel KJ, Griffin AS, Hartemann FV, Heid L, Hwang Y, Imeshev G, Jentschel M, Johnson CA, Kinosian KW, Lagzda A, Lochrie RJ, May MW, Molina E, Nagel CL, Nagel HJ, Peirce KR, Peirce ZR, Quiñonez ME, Raksi F, Ranganath K, Reutershan T, Salazar J, Schneider ME, Seggebruch MWL, Yang JY, Yeung NH, Zapata CB, Zapata LE, Zepeda EJ and Zhang J (2024) Design, construction, and test of compact, distributed-charge, X-band accelerator systems that enable image-guided, VHEE FLASH radiotherapy. *Front. Phys.* 12:1472759. doi: 10.3389/fphy.2024.1472759

Design, construction, and test of compact, distributed-charge, X-band accelerator systems that enable image-guided, VHEE FLASH radiotherapy

Christopher P. J. Barty[1,2,3]*, J. Martin Algots[1], Alexander J. Amador[1], James C. R. Barty[1], Shawn M. Betts[1], Marcelo A. Castañeda[1], Matthew M. Chu[1], Michael E. Daley[1], Ricardo A. De Luna Lopez[1], Derek A. Diviak[1], Haytham H. Effarah[1,2,3], Roberto Feliciano[1], Adan Garcia[1], Keith J. Grabiel[1], Alex S. Griffin[1], Frederic V. Hartemann[1], Leslie Heid[1,2], Yoonwoo Hwang[1], Gennady Imeshev[1], Michael Jentschel[1], Christopher A. Johnson[1], Kenneth W. Kinosian[1], Agnese Lagzda[1], Russell J. Lochrie[1], Michael W. May[1], Everardo Molina[1], Christopher L. Nagel[1], Henry J. Nagel[1], Kyle R. Peirce[1], Zachary R. Peirce[1], Mauricio E. Quiñonez[1], Ferenc Raksi[1], Kelanu Ranganath[1], Trevor Reutershan[1,2,3], Jimmie Salazar[1], Mitchell E. Schneider[1], Michael W. L. Seggebruch[1,2], Joy Y. Yang[1], Nathan H. Yeung[1], Collette B. Zapata[1], Luis E. Zapata[1], Eric J. Zepeda[1] and Jingyuan Zhang[1]

[1]Lumitron Technologies, Inc., Irvine, CA, United States, [2]Physics and Astronomy Department, University of California, Irvine, Irvine, CA, United States, [3]Beckman Laser Institute and Medical Clinic, University of California, Irvine, Irvine, CA, United States

The design and optimization of laser-Compton x-ray systems based on compact distributed charge accelerator structures can enable micron-scale imaging of disease and the concomitant production of beams of Very High Energy Electrons (VHEEs) capable of producing FLASH-relevant dose rates (~ 10 Gy in less than 100 ns). The physics of laser-Compton x-ray scattering ensures that the x-rays produced by this process follow exactly the trajectory of the electrons from which the x-rays were produced, thus providing a route to not only compact VHEE radiotherapy but also image-guided, VHEE FLASH radiotherapy. This manuscript will review the compact accelerator architecture considerations that simultaneously optimize the production of laser-Compton x-rays from the collision of energetic laser pulses with high energy electrons and the production of high-bunch-charge VHEEs. The primary keys to this optimization are use of X-band RF accelerator structures which have been demonstrated to operate with over 100 MeV/m acceleration gradients. The operation of these structures in a distributed charge mode in which each radiofrequency (RF) cycle of the drive RF pulse is filled with a low-charge, high-brightness electron bunch is

enabled by the illumination of a high-brightness photogun with a train of UV laser pulses synchronized to the frequency of the underlying accelerator system. The UV pulse trains are created by a patented pulse synthesis approach which utilizes the RF clock of the accelerator to phase and amplitude modulate a narrow band continuous wave (CW) seed laser. In this way it is possible to produce up to 10 μA of average beam current from the accelerator. Such high current from a compact accelerator enables production of sufficient x rays via laser-Compton scattering for clinical imaging and does so from a machine of "clinical" footprint. At the same time, the production of 1,000 or greater individual micro-bunches per RF pulse enables > 10 nC of charge to be produced in a macrobunch of < 100 ns. The design, construction, and test of the 100-MeV class prototype system in Irvine, CA is also presented.

KEYWORDS

lasers, x-rays, laser-Compton scattering, accelerators, X-band, flash, high-resolution radiography, VHEE

1 Introduction

The Distributed Charge Compton Source (DCCS) [1] architecture and its underlying electron accelerator system are a solution for compact, image-guided, ultra-high dose rate (UHDR), very high energy electron (VHEE) radiation therapy systems. VHEEs (electron energy > 50 MeV) have been identified as a promising ionizing radiation modality, but the current clinical applicability of VHEE technology is limited [2, 3]. An ideal clinical VHEE source would be compact, capable of UHDR operation to potentially leverage the FLASH effect [4] (dose-rate dependent sparing of healthy tissue with dose-rate independent tumor kill), and administered with reliable image guidance [5–7]. An ideal clinical x-ray imaging source based on laser-Compton scattering (LCS), sometimes known as inverse Compton scattering (ICS) [8], would also be compact, have a micron-scale effective source size for high-resolution imaging, and able to produce sufficient x-ray flux for clinically relevant phase contrast and/or spectral contrast imaging. We argue here that the linear electron accelerator (LINAC) required for these two applications is optimized by a distributed charge architecture.

"Distributed charge" is a strategy to increase the average current of a linear accelerator by distributing electrons over many bunches separated by a single radiofrequency (RF) period instead of maximizing the number of electrons in a single bunch. In compact RF accelerators with high operation frequencies into the X band (8–12 GHz), the total number of electrons that can be effectively accelerated in a single bunch decreases, especially when trying to preserve electron beam quality [9]. A distributed charge architecture allows the production of enough electrons for both LCS and VHEE applications while maintaining a compact accelerator footprint. Figure 1 is a CAD model of the currently operational DCCS at Lumitron Technologies, Inc. with primary systems labeled. Figure 2A is a photograph of inside of the radiation safety enclosure of the compact MeV-class laser-Compton light source and VHEE system at Lumitron Technologies, Inc. in Irvine, CA. Figure 2B is a close-up of the compact VHEE accelerator of the DCCS at Lumitron Technologies (item four in Figure 1). This accelerator is designed to produce electrons with energies up to 100 MeV with sufficient charge for UHDR operation. For a detailed animated fly-through of the DCCS electron acceleration and laser-electron interaction process, see Ref. [10].

In this work, we describe the distributed charge architecture and discuss its advantages as a laser-Compton x-ray source for clinically relevant x rays capable of high-resolution, narrow-bandwidth imaging and its advantages as a radiotherapy source of VHEEs for applications in clinically relevant UHDR operations. The results of systems integration tests of the DCCS in Irvine, CA with respect to production of both x rays and FLASH-relevant electron beams are presented. To conclude, the potential for the DCCS architecture to serve as a framework for x-ray image-guided VHEE FLASH radiotherapy is discussed.

2 Motivation

2.1 Laser-Compton X-Ray sources

Compact laser-Compton light sources are capable of creating quasi-monoenergetic, tunable, x rays and γ rays with outputs that are similar to those of much larger, km-scale, international synchrotron facilities [11, 12]. Synchrotron facilities have demonstrated the potential for clinically-relevant imaging techniques that leverage narrow spectral bandwidths for K-edge subtraction imaging [13] and small effective x-ray source sizes for phase contrast imaging [14, 15]. Although synchrotrons are capable of imaging modalities currently unfeasible for conventional x-ray tube technologies, the cost and size of synchrotron facilities is prohibitive for widespread clinical use. Since the first conceptions of a laser-Compton x-ray source in 1963 [16, 17], just 3 years after the first experimental demonstration of the laser [18], and the first demonstrations of laser-Compton scattering [19–21], a rich field has developed with many differing strategies for optimizing laser-Compton x-ray sources for various applications and different energy regimes [8].

Briefly, the laser-Compton interaction can be described as the interaction of short-duration, energetic laser pulses with bright,

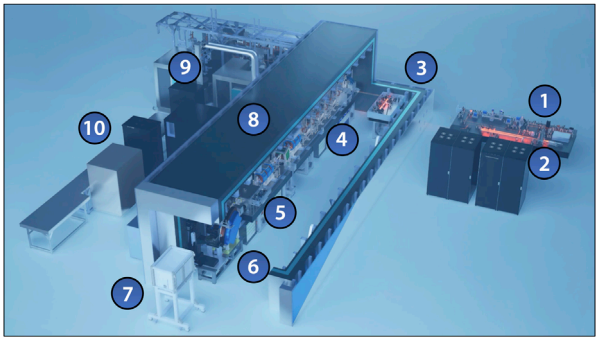

FIGURE 1
CAD model of the Distributed Charge Compton Source (DCCS) at Lumitron Technologies, Inc. in Irvine, CA. (1) Multi-GHz Interaction Laser System (ILS), (2) multi-GHz Photogun Laser System (PGL), (3) multi-pass cell, (4) X-band accelerator beamline, (5) laser-Compton interaction chamber, (6) electron beam dump, (7) X-ray and γ-ray imaging systems, (8) 9.6-m long custom radiation enclosure, (9) X-band radiofrequency power systems, (10) control station. For a detailed animated fly-through of the DCCS electron acceleration and laser-electron interaction process, see Ref. [10].

monoenergetic, relativistic electrons. This interaction induces a transverse motion on the electron bunch, which in turn radiates as an electric dipole and produces Doppler-upshifted x rays and/or γ rays in the laboratory frame of reference. In effect, the laser-Compton interaction performs a similar function to that of the periodic array of magnets of a synchrotron wiggler [22]. In the laboratory frame, the Compton "scattered" photons appear to be higher energy than incident photons and as such this process is sometimes referred to as "inverse" Compton scattering [23]. The laboratory-frame formula to describe the energy of Compton-scattered x rays in a head-on collision of counter-propagating photons and electrons can be described as

$$E_{ph} = \frac{4\gamma^2}{1+\gamma^2\theta^2+4\gamma k_0 \lambda} E_L, \tag{1}$$

where E_{ph} is the scattered-photon energy, E_L is the incident laser photon energy, γ is the electron relativistic factor, θ is a small observation angle relative to the electron propagation axis, k_0 is the incident laser photon angular wavenumber, and $\bar{\lambda}$ is the reduced Compton wavelength of the electron. However, in the rest frame of the moving electron, the Doppler effect leads to the incident photon appearing to be higher frequency. In the rest frame of the electron, the scattered photon is lower frequency, just as in traditional Compton scattering [24]. To remove any confusion, we refer to the relativistic x-ray generation process as laser-Compton scattering.

The primary advantage of using a laser's electric field to induce periodic motion in relativistic electrons is that the induced oscillations can occur at much higher spatial frequencies than what are achievable by a periodic magnet array. This rapid laser-induced oscillation drastically reduces the energy requirements of the interacting electron beam, which has enabled the production of x rays and γ rays from 6 keV to 1 GeV using many different architectural designs [8, 25–27].

The primary limitation of laser-Compton sources is the small Thomson cross section (6×10^{-25} cm^2) for laser-scattering from the relativistic electrons. To overcome this limitation, the most efficient laser-Compton systems operate in a co-focused geometry in which both the electron bunch and laser pulses are brought to a common focus and are synchronized so that both entities arrive at that focus at the same time. While laser-Compton scattering can be configured for any angle of incidence between the electron and the laser pulses, the head-on or 180-degree configuration yields the highest on-axis Doppler upshift and provides the most tolerance with respect to errors in arrival timing between the electron bunch and laser pulse. Ideally, the duration of the laser pulses and electron bunches are both on the order of the transit time of the focal region or less. Tuning of the x-ray energy can be accomplished by changing the energy of the laser photons [28], changing the laser-electron interaction angle [29], or changing the energy of the electron bunch. In the DCCS architecture described here, changing the energy of the electron bunch is the most practical approach.

By conservation of energy and momentum, the spectrum of a laser-Compton source is angle-correlated (Equation 1). The spectrum of a 180-degree incidence configuration ranges from about $4\gamma^2E_L$ in the direction of the electron bunch to half that value for photons scattered at 90°relative to the electron trajectory. By placing an aperture in the generated beam path, the integrated bandwidth of the transmitted beam may be reduced until such point that the energy and angle variations of the electrons and photons involved in the Compton scattering process dominate the effect on the bandwidth. At this point, reducing the aperture size simply reduces the total flux without changing the bandwidth. Laser-Compton sources have typically achieved on-axis bandwidths of between 3% and 12% [26, 30–36]. However, an optimized laser-Compton source based on high-brightness, monoenergetic electron bunches and high-beam-quality, picosecond laser pulses, can theoretically produce a minimum, on-axis bandwidth of 0.1% full width at half maximum (FWHM). The first experimental confirmation of a laser-Compton source design with exceptionally narrow on-axis x-ray bandwidth was demonstrated using the compact Energy Recovery Linac (cERL) at KEK with a measured on-axis x-ray bandwidth of 0.4% operating at 6.95 keV [37]. The cERL approach to producing high-brightness, monoenergetic electron bunches was to use superconducting accelerators. While this approach provides small on-axis energy bandwidths with demonstrated imaging capabilities [38], albeit at sub-clinical x-ray energies (<20 keV), the widespread adoption of superconducting accelerator architectures is prohibited by the cost, size, and complexity of the required infrastructure.

There are two generic approaches to production of clinically-relevant x rays via laser-Compton scattering. These approaches can be separated by the underlying accelerator architecture which is either that of an electron storage ring or that of a linear accelerator (LINAC).

2.1.1 Storage ring laser-Compton systems

In the storage ring approach, an energetic electron bunch is injected into a closed-loop magnetic lattice and "stored" for a number of round trips. On each round trip the bunch interacts with a synchronized laser pulse to produce Compton x rays. Due

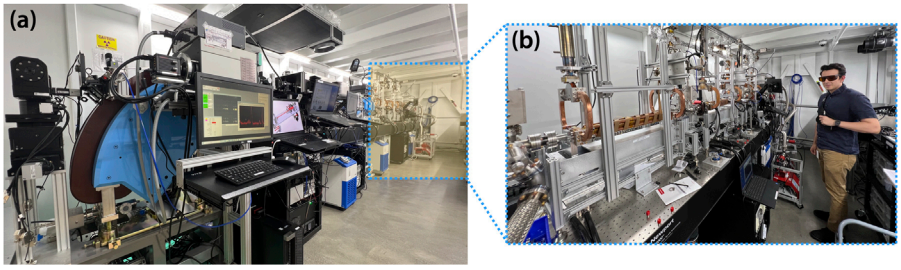

FIGURE 2
(A) Photograph of the Distributed Charge Compton Source (DCCS) at Lumitron Technologies, Inc. in Irvine CA inside the radiation safety enclosure (bunker). The total length of the bunker is 9.6 m. Highlighted in yellow with a dotted outline is the portion of the beamline dedicated to electron acceleration. **(B)** A close up of the installed and operational DCCS accelerator. The total length of accelerator sections capable of producing VHEEs is approximately 3 m.

to synchrotron losses and imperfections in the lattice, the electron bunch quality will decay over time. At some point, the circulating electrons are ejected from the cavity and a new bunch is injected. The advantage of a storage ring approach is that the electron beam average current can be high thus, in principle, increasing the laser-Compton x-ray flux from the machine. The disadvantages of storage ring approaches are; a) the electron bunches cannot be focused to a tight spot without destroying the electron beam quality which limits the potential output flux, b) the laser average power required to achieve high flux cannot be readily obtained without the use highly-sensitive, resonant enhancement cavities, c) the electron beam characteristics (emittance, energy, and energy spread) change over the course of its lifetime within the storage ring, d) the synchronization of the laser and electron bunch timing at the interaction region is non-trivial, e) the tuning of the x-ray energy via changes in the electron beam energy is limited by the speed with which modifications of the magnetic lattice and the electron beam injector can be made, and f) the charge of the stored electron bunch is not sufficient to be of practical use as an UHDR clinical electron irradiation source.

Nonetheless, storage ring-based laser-Compton systems have produced beams with clinically relevant x-ray energy (MuCLS [39] and ThomX [12]) and above (HIγS [26]). Pre-clinical studies at the Munich Compact Light Source (MuCLS) have demonstrated spectral contrast imaging and phase contrast imaging applications that are much more difficult or impossible to perform with conventional x-ray tube sources with reported x-ray fluxes up to 4.5×10^{10} photons per second at energies up to 35 keV [40]. The main limitations of the MuCLS are its upper energy limit (electrons: 45 MeV; x rays: 35 keV) and its 50-μm x-ray root-mean-square (RMS) source radius. The ThomX collaboration, which recently demonstrated first x-ray production [34], also uses a storage ring architecture. Although improvements in their system are expected to increase x-ray energy to up to 90 keV, their minimum effective x-ray source size is currently no less than 65 μm RMS based on their interaction laser spot size.

2.1.2 LINAC laser-Compton systems

In the LINAC based approaches to laser-Compton sources, a new electron bunch is generated from a laser-driven photogun for each laser-Compton interaction, i.e., the electrons are used once and discarded. Doing so allows the electrons be focused to much smaller spot sizes than possible in storage ring based systems. This increases the output flux of the system per electron and enhances the imaging capabilities of the device. Tuning of the system from one x-ray energy to another can be done rapidly (seconds to minutes) by changing the RF power to the accelerator sections of the LINAC. The electrons produced by the system can have sufficient charge and pulse structure to enable VHEE and VHEE FLASH radiotherapy. Traditionally, LINAC-based systems have operated with one electron bunch per RF pulse driving the accelerator. The downsides of this LINAC based approach are: a) average beam current is limited by the repetition rate of the RF power system and the charge that may be stably accelerated by the system, b) the photogun laser system which produces the initial electrons must be timed precisely with respect to the phase of the RF driving the accelerator, and c) the interaction laser system which creates the laser pulses that interact with the focused electron bunches to produce Compton x rays must be timed precisely with respect to the electrons. The above disadvantages are eliminated via a distributed charge Compton source architecture [1] that uses RF pulse synthesis to create the photogun and interaction laser pulse trains.

The exceptional electron beam quality afforded by the DCCS architecture enables the production of an x-ray beam with an RMS source radius below 5 μm, and a total x-ray flux greater than 10^{12} photons/second (see Section 3.1). The current upper energy limits of the DCCS also expand the flexibility of its applications with electron energies up to 100 MeV and x-rays energies up to 360 keV, enabling both the investigation of VHEE irradiation and nuclear-based x-ray imaging techniques.

Using compact, normal-conducting, RF accelerator technology is necessary for the eventual clinical translation of laser-Compton technology. To produce x rays with the most exquisite quality to leverage the spectral and phase-based imaging modalities developed at synchrotron facilities, high-brightness electron beams must be used to minimize the on-axis x-ray bandwidth and effective x-ray source size. The quality (brightness) of an electron beam is most readily achieved with relatively little charge in each electron bunch, especially in high-frequency RF accelerators (Section 3.2). Counteracting this charge limitation to obtain a clinically relevant x-ray flux requires a distribution of charge across long, consecutive

trains of electron bunches (Section 3.4). We argue here that the DCCS architecture is the solution for clinically translatable laser-Compton x-ray sources that enable spectral and phase-based imaging techniques.

2.2 Very high energy electron (VHEE) sources

There is urgent need for transformative technologies in compact, high-gradient accelerator architectures that enable both VHEE and FLASH capabilities [2]. Compared to photon or proton radiation sources, electron sources are most readily capable of achieving ultra-high dose rates [41, 42] and, in the VHEE regime, will have appropriate penetration to treat deep-seated tumors in humans [43–45]. One of the tightest bottlenecks in investigating the FLASH effect is simply the lack of availability of appropriate ionizing radiation sources [42]. More VHEE sources are being designed and commissioned to address this need [46–51] with varying strategies regarding accelerator design.

VHEE research opportunities and clinical translatability are both fundamentally limited by facility size requirements. The first reported VHEE dosimetry experiments were performed at the Oak Ridge electron linear accelerator (ORELA) [43], at the Sources for Plasma Accelerators and Radiation Compton with Lasers and Beams (SPARC) S-band beamline [52] and at the Next Linear Collider Test Accelerator (NLCTA) S-band/X-band beamline [53]. Recent VHEE experiments at the CERN Linear Electron Accelerator Research (CLEAR) facility continue to garner interest in VHEE, especially with potential for UHDR operation, through investigating VHEE dosimetry [54, 55], VHEE insensitivity to tissue inhomogeneity [56], VHEE beam focusing [57, 58], and techniques for UHDR VHEE dose monitoring [59, 60]. Even with promising VHEE results from the CLEAR facility, the total beamline length of 41 m (25 m injector +16 m beamline, [46]) limits the practicality of widespread clinical adoption. Another VHEE collaboration, the FLASHlab@PITZ, is being commissioned to further investigate VHEE with charge-per-pulse values deep into UHDR regime, but at the cost of a clinically impractical footprint using L-band accelerators (1.4 GHz) [48]. The FLASHlab@PITZ requires the existing 22-m photoinjector to reach 22 MeV and an additional 20 m of planned accelerators to reach 250 MeV. SAFEST, a recently announced collaboration between Sapienza University and Istituto Nazionale di Fisica Nucleare (INFN), is seeking to address the VHEE facility size problem by operating at C-band (5.712 GHz), with an anticipated final beamline length of around 5 m to reach up to 130 MeV [49, 50]. Finally, a research team at Tsinghua University has also proposed a compact VHEE accelerator design to reach up to 100 MeV electrons using X-band (11.424 GHz) accelerators with an anticipated total beamline length of less than 2 m [51]. The proposed Tsinghua approach is similar to that used by Lumitron. In this regime, the accelerator hardware is small compared to the underlying RF power components and thus is no longer the limiting factor with respect to reducing machine footprint.

While both the SAFEST and Tsinghua designs seek to address the compactness problem for clinical translation of VHEE technology, both designs rely on the use of a high-voltage direct current (DC) thermionic electron gun to produce a large electron current. This strategy increases the available charge for UHDR operation at the expense of fundamentally limiting the quality of the electron beam. Comparing the SAFEST and Tsinghua DC gun normalized transverse electron emittance (10 mm-mrad expected, and 7.26 mm-mrad measured, respectively) to the LLNL/SLAC electron gun design (0.3 mm-mrad measured) (See Section 3.2) emphasizes that the DCCS architecture retains the ability to efficiently produce a high quality diagnostic x-ray beam through laser-Compton scattering while producing sufficient electron current for UHDR VHEE operation. The DCCS architecture is designed to produce 10 μA of average current when operating at with 1,000 microbunches at 400 Hz and at energies up to 100 MeV. To date, the prototype DCCS accelerator at Lumitron Technologies in Irvine, CA has demonstrated the production of 49 MeV electrons at 14 nC in 86.6 ns at 100 Hz, which corresponds to a an average current of 1.4 μA. Even though the DCCS accelerator bunch charge is limited by the laser fluence on a photocathode and is thus more challenging to produce current than a DC gun, distributing the charge over long trains of closely spaced bunches overcomes this limitation. Additionally, variable illumination of the photogun enables precise control of the total electron charge delivered to a patient.

For these reasons, we posit that the DCCS architecture is not only the solution for clinically relevant laser-Compton x-ray imaging, but also the solution for a clinically-translatable, FLASH-capable, VHEE source. The potential to rapidly switch between these modes of operation to enable laser-Compton x-ray image-guided VHEE FLASH radiation therapy will be discussed in Section 6.

3 Distributed charge compton source architecture

The Distributed Charge Compton Source (DCCS) architecture is founded on research and development efforts surrounding laser-Compton scattering (LCS) activities at the Lawrence Livermore National Laboratory (LLNL) [61–64], as well as new innovations and systems integration studies that have occurred at Lumitron Technologies, Inc. in Irvine, California. The DCCS is a patented architecture [1, 65] that involves the repeated interaction of trains of electron bunches with trains of laser pulses each of which being spaced at exactly the repetition period of the compact, high-gradient, X-band RF accelerator. This architecture enables bright electron beams and reduces requirements on the interaction laser. Extensions of the currently operational DCCS prototype at Lumitron Technologies could produce tunable, 30-keV to 3-MeV, x-ray bursts at an effective 400-kHz repetition rate with a total flux of greater than 10^{12} photons/sec and an on-axis bandwidth as low as 0.1% [66].

The large x-ray flux and narrow x-ray energy bandwidth of the DCCS are enabled by three core technologies: high-gradient X-band (11.424 GHz) photoguns and LINACs, RF laser-pulse synthesis of 11.424 GHz pulse trains, and diode-pumped infrared (IR) laser technology.

TABLE 1 Simulation parameters used to model the production of 975-keV γ-rays with an on-axis RMS energy bandwidth of 1% and a total flux of 2.3×10^{12} photons/second through laser-Compton scattering of directly counter-propagating beams. These parameters are based on DCCS design specifications for the DARPA Gamma Ray Inspection Technology (GRIT) program. Both the laser and electron beam are modeled to be radially symmetric about their propagation axes. σ_i refers to the standard (RMS) deviation of the underlying distribution. $\varepsilon_{n,rms}$ is the transverse normalized RMS emittance of the electron beam. FTL = Fourier transform limit.

Interaction Laser		Electron Beam	
Wavelength	354.67 nm	Beam energy	137 MeV
Micropulse energy	10 mJ	Bunch charge	25 pC
M^2	1	$\varepsilon_{n,rms}$	0.3 mm-mrad
FTL bandwidth	93 pm	Energy spread (σ_E/E)	0.05%
Pulse train length	100	Bunch train length	1000 microbunches
Recirculation efficiency	10	Duration (σ_t)	0.59 ps
FWHM duration	2.0 ps	Duration (σ_θ)	2.4265°
Temporal shape	Gaussian	Temporal shape	Gaussian
FWHM diameter	3.46 μm	Radius ($\sigma_{x,y}$)	1.5 μm
Focal shape	Gaussian	Focal shape	Gaussian
Pulse spacing	87.535 ps	X-band frequency	11.424 GHz
Repetition rate	400 Hz	Repetition rate	400 Hz

3.1 Numerical modeling of the DCCS

In this section, we will describe a representative numerical modeling study that outlines the ideal laser-electron interaction specifications to maximize output flux at 10^{12} photons per second with a Distributed Charge Compton source (DCCS) architecture at a fixed interaction laser pulse energy. A summary of these specifications is presented in Table 1. If one desired to minimize bandwidth, it is possible to do so by increasing the interaction spot size at the expense of output flux, unless the laser pulse energy is increased accordingly.

The X-band electron accelerator system for the DCCS under development at Lumitron Technologies, Inc. is commissioned to produce low-emittance electron beams with energies up to 137 MeV as part of the DARPA Gamma Ray Inspection Technology (GRIT) program. Based on previous work at Lawrence Livermore National Laboratory (LLNL), the SLAC National Accelerator Laboratory, and further developments to the X-band accelerator systems at Lumitron Technologies (details in Sections 3.2 and 3.3), normalized electron beam transverse emittance values of 0.3 mm-mrad are expected. The beamline at Lumitron Technologies, Inc. is designed to focus such an electron beam to an RMS-radius focal spot of 1.5 μm with an RMS bunch length of 0.59 ps.

In the numerical analysis presented here, we consider a UV interaction laser with a central wavelength of 345.67 nm and a FWHM pulse length of 2.0 ps produced through third-harmonic generation from a 1064-nm Nd:YAG laser. Though the experimental results presented later in this work use a 532-nm interaction laser (Sections 4, 5), the simulation results presented here are still valid with the consideration that the final laser-Compton scattered energy is linearly proportional with the frequency of the interaction photons. With these values set, we leave the transverse focal size of the interaction laser as a free parameter to solve for the size that maximizes total Compton-scattered photon flux.

The hallmark of the DCCS architecture is the distribution of electron bunch charge and laser pulse energy over long pulse trains (macrobunches) that are produced at high repetition rates. The commissioning goals of the DCCS at Lumitron are to produce electron macrobunches and laser macropulses with bunch-train lengths of 1,000 bunches and 100 pulses respectively. This mismatch will ultimately be overcome by using a laser recirculation strategy based on previously described work first pioneered at LLNL [64], in which a 10x enhancement in effective laser/electron overlap is expected. With this recirculation cavity in place and with both the electron beam and interaction laser systems operating at 400 Hz, an expected 400,000 interactions are expected to occur each second. This scaling factor of 4×10^5 is included in the flux calculations shown in Figure 3.

Using a previously described numerical model [67], a three-dimensional diffracting Gaussian laser pulse is overlapped with a relativistic electron beam considering its full six-dimensional phase space. This model also accounts for electron recoil and potential nonlinear effects induced by the ponderomotive force during interaction while calculating the resulting spectrum of Compton-scattered photons. The simulation inputs are based on the parameters summarized in Table 1. Assuming a counter-propagating laser-electron geometry, a 3.46-μm FWHM diameter was found to be the optimum focal spot size for the interaction laser, with a total expected output flux of 2.3×10^{12} photons per second (Figure 3A), a peak on-axis energy of 975 keV, and an on-axis RMS energy bandwidth of 1% (Figure 3B).

This numerical model provides the theoretical foundation of the DCCS architecture and its suitability for producing both narrow bandwidth x rays (or γ rays) and VHEE beams. In the systems integration results reported in Section 4, the working interaction laser and electron beam specifications are summarized in Table 2. The operational conditions of the electron beam during the results reported in Section 5 are also summarized in Table 2. Both electron and interaction laser systems were operating at 100 Hz, with a typical electron bunch charge of 5 pC and an interaction laser pulse energy of 2.5 mJ and electron energies around 40 MeV. Typical normalized emittance values measured were below 0.5 mm-mrad, with electron bunch lengths indirectly measured to be 1.1 ps RMS based on streak camera measurements of the photoinjector laser after conversion to UV. Interaction laser pulse lengths were measured to be 7 ps FWHM. Additionally, since no recirculation cavity was installed at the time of the presented experiments, the electron bunch train lengths were set to 100 to match those of the interaction laser. In the results presented in Section 5, the electron beam was set to produce 1000-bunch trains at 100 Hz. Finally, while the interaction laser was focused to a 5-μm FWHM spot, the electron beam was only focused

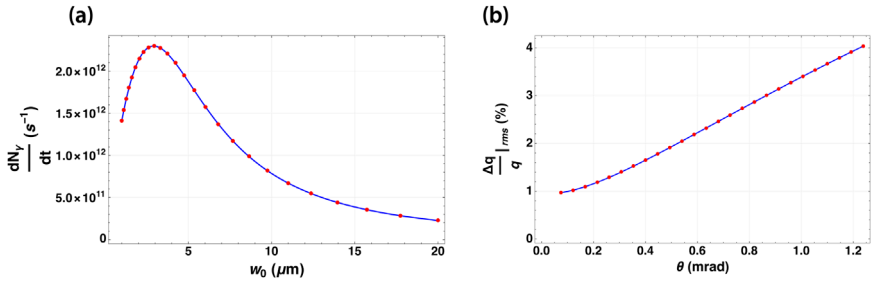

FIGURE 3
(A) Calculation of Compton-scattered photons produced per second from counter-propagating electron and laser pulse trains following the parameters summarized in Table 1 as a function of the $1/e^2$-radius of the focused interaction laser (w_0). 2.94 μm (3.46 μm FWHM) is identified as maximizing the total flux of the interaction at 2.3×10^{12} photons per second. **(B)** Corresponding relative bandwidth of the resulting Compton-scattered γ-ray beam as a function of integrated solid angle about the central beam axis.

TABLE 2 Measured interaction laser and electron beam parameters used to produce the experimental results presented in this work. For the electron beam parameters, numbers in parentheses indicate values that were measured for Section 5. Parameters without corresponding parenthetical values were not measured during those Section 5 experiments.* Here, these values refer to the effective values when considering the entire 100-bunch train (macrobunch) of electrons. †The interaction laser FWHM bandwidth was only directly measured in the IR (260 pm) before frequency conversion. The listed value is the FTL FWHM bandwidth assuming an underlying Gaussian spectrum. It can serve as a lower bound on the bandwidth based on the measured 532-nm FWHM pulse duration. FTL = Fourier transform limit.

Interaction laser		Electron beam	
Wavelength	532 nm	Beam energy	38 (49.4) MeV
Micropulse energy	2.5 mJ	Bunch charge	5 (14) pC
M^2	~1.6	$\varepsilon_{n,rms}$*	< 0.5 mm-mrad
FTL bandwidth†	60 pm	Energy spread*(σ_E/E)	0.2%
Pulse train length	100	Bunch train length	100 (1,000)
Recirculation efficiency	N/A	Duration (σ_t)	1.1 ps
FWHM duration	7 ps	Duration (σ_θ)	4.52°
FWHM diameter	5 μm	Radius σ_x, σ_y	17 μm, 19 μm
Pulse spacing	87.535 ps	X-band frequency	11.424 (11.424) GHz
Repetition rate	100 Hz	Repetition rate	100 (100) Hz

to a 17-μm RMS spot (41-μm FWHM) to facilitate alignment during this first experimental campaign.

3.2 High-current, high-brightness photoguns

The minimum on-axis bandwidth from a laser-Compton system depends strongly on emittance of the accelerated electron bunches [68–70]. The production of low-emittance electron beams (ϵ_n = 0.35 mm-mrad at 20 pC/bunch and ϵ_n = 0.8 mm-mrad at 100 pC/bunch) has previously been demonstrated using a 5.5 cell X-band photogun (Mark 0) [71], based on a design by LLNL and SLAC [72]. Later, the Mark 1 version of this X-band photogun (5.59 cells) demonstrated significantly improved beam emittance relative to Mark 0 at substantial charge per bunch (ϵ_n = 0.3 mm-mrad at 80 pC/bunch) [73]. This LLNL/SLAC X-band photogun concept was originally designed to operate in a single bunch mode, with a nominally 250-pC bunch charge. At LLNL, the feasibility of using the LLNL/SLAC X-band photogun with distributed charge operation was supported by initial modeling studies [72, 74], and was demonstrated experimentally with 11.424-GHz bunch trains using up to 4 [75] and then up to 16 consecutive electron bunches [76]. These initial demonstrations of 11.424 GHz distributed charge operation did not use pulse synthesis, but rather, a hyper-Michelson interferometer to space the photogun drive laser pulses by 87.5 ps [77]. Additionally, in the first demonstrations of multi-bunch operation, the photogun drive laser operated at 10 Hz [75, 76]. The integration of pulse synthesis (Section 3.4) in the DCCS architecture potentially extends these results to 1,000 consecutive electron bunches with repetition rates up to 400 Hz.

This extension to long pulse trains and high repetition rates presents two fundamental challenges. The first challenge is the uniform acceleration of all 1,000 bunches during one RF pulse, and the second challenge is controlling the thermal loading and distortions that accompany the higher repetition rate. The former requires precision shaping of the RF pulses that drive the gun and accelerator sections and is further complicated by the use of RF pulse compression on the output of each klystron/modulator unit. Low power tests to date using shaped RF seed pulses provide encouragement that the required RF pulse shapes and stability can be achieved at high power. Thermal models for operation of the gun at 400 Hz indicate that mechanical distortions of the gun cells would be significant enough to impact performance if not compensated. To alleviate this issue, a custom cooling jacket has been designed and constructed for the next-generation of X-band photoguns to handle high repetition rate operation. These novel X-band photoguns rated for high repetition rate operation are fabricated from oxygen-free copper. Parts were machined to 1-μm accuracy, diffusion bonded,

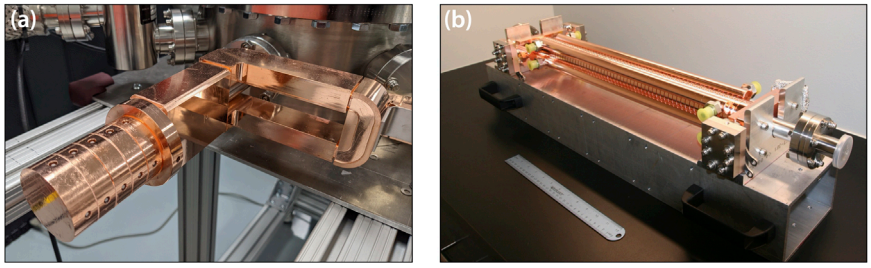

FIGURE 4
(A) X-band photogun designed, fabricated, and tuned at Lumitron Technologies, Inc. **(B)** T53VG3 X-band accelerator section fabricated and tuned by Lumitron Technologies, Inc.

brazed, RF tuned, and prepared for ultra-high vacuum (UHV) installation at Lumitron Technologies (Figure 4A).

3.3 High-gradient X-band LINACs

In the DCCS, high-gradient, X-band (11.424 GHz) LINACs are operated in a distributed charge mode with average beam currents of up to 10 μA. The baseline specification is 25 pC per microbunch with 1,000 microbunches per macrobunch and a macrobunch repetition rate of 100 Hz (2.5 μA) with potential operation up to 3,000 microbunches and 400 Hz (30 μA). This baseline configuration represents an extension of X-band multi-bunch operation from 16 microbunches per macrobunch demonstrated at LLNL [76] up to 3,000. In this work, we demonstrate successful multi-bunch operation with electron beam quality high enough to produce Compton-scattered x rays using 100-bunch trains at 100 Hz (Section 4). The T53VG3 accelerator design was chosen because of its technological maturity, its demonstration of exceptional acceleration gradients greater than 100 MeV/m [78], and its use of a traveling wave accelerating field, making it less susceptible to electron beam-induced electromagnetic wake fields.

Regarding the accelerator sections, the primary concerns with this approach are variations in microbunch energy and emittance within the bunch train and overall bunch train pointing stability due to electron-induced wakes. Modeling to date suggests that the electron bunch wakes should be minimal from 1,000 bunch, multi-bunch operation at 25 pC per microbunch. Further modeling has also informed the exact RF pulse shapes that will be required to drive both the photogun and the LINAC sections so that all bunches emerge from the system with the same energy ± 0.1%. The chosen X-band photogun and high-gradient accelerator technologies are higher beam current extensions of the X-band (11.424 GHz) designs previously demonstrated both at the Lawrence Livermore National Laboratory and the SLAC National Accelerator Laboratory. These higher-current systems have increased thermal loading and require the addition of precision thermal management. The T53VG3 LINAC sections in this work were fabricated from oxygen-free copper. Parts were machined to 2.5-μm accuracy, RF tuned, and prepared for UHV installation at Lumitron Technologies (Figure 4B).

3.4 RF laser-pulse synthesis and amplification of 11.424 GHz pulse trains

An inherent challenge for any laser-Compton source is the synchronization of the arrival of the electrons and laser photons at a common focus. In all existing systems, the accelerator RF (3–12 GHz) is significantly greater than the natural repetition rate of short-duration, mode-locked lasers (80–100 MHz) that seed the photogun and interaction laser systems. Even specialized systems used at CLEAR that use a 1.4-GHz mode-locked laser still need to utilize an interferometer scheme to maximally distribute charge over a train of consecutive bunches at 3 GHz [79]. Timing synchronization is usually accomplished via locking of the laser repetition rate to a sub-multiple of the accelerator RF via precision movement of an intra-cavity, piezoelectric-actuated element. The whole system is then controlled by one or more phase locked loops. The DCCS architecture takes a fundamentally different approach to the synchronization problem by synthesizing the drive laser pulses using the accelerator RF. In this patented approach [65] that has been previously demonstrated at 11 GHz [80], a stable, narrow-bandwidth seed laser is phase and amplitude modulated using standard, 40-GHz bandwidth, telecommunications-quality fiber optic components to produce trains of approximately 50-ps duration, chirped, IR laser pulses that then seed both the photogun laser system (PGL) and the interaction laser system (ILS). This section will, as an example, focus on the pulse synthesis (Figure 5A) and pre-amplification (Figure 5B) stages of the PGL.

The output of a continuous wave (CW) laser diode is first amplitude modulated using a 5.712 GHz signal with a null bias, resulting in an 11.424 GHz laser output. This initial amplitude modulation defines the structure of the laser micropulses, and is performed using the same RF input that is used as a seed for the RF power systems that drive the accelerator system. An 800 kHz signal then amplitude modulates the signal to carve the macropulse structure. For the laser-Compton x-ray results presented here, the width of this signal was 8.75 ns, corresponding to 100 micropulses per macropulse. For the electron beam results presented here, the width of this signal was adjusted to 87.5 ns, corresponding to 1,000 micropulses per macropulse. Finally, an 11.424 GHz RF signal is used to phase modulate, and thus spectrally broaden, the laser micropulse trains. Critically, the RF input to the phase and amplitude modulators is the same RF that is used as a seed for the RF power

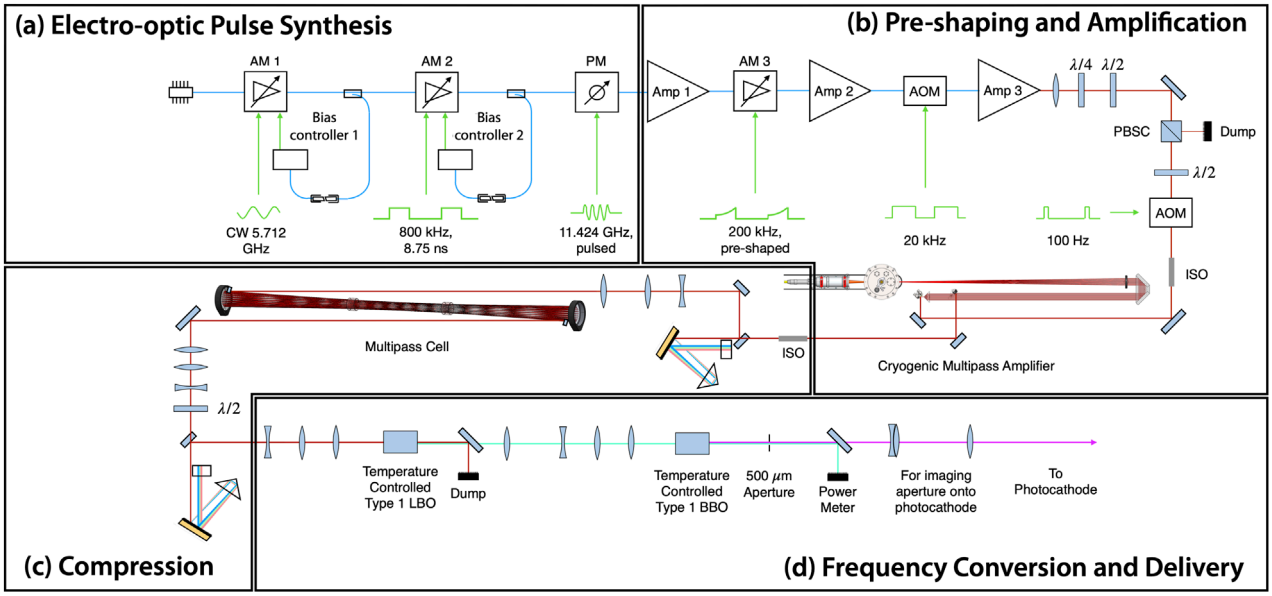

FIGURE 5
Diagram of the photogun laser system (PGL) used at Lumitron Technologies, Inc. for the results presented in this work. **(A)** Pulse synthesis approach used to generate 11.424 GHz micropulse trains from a 995.2 nm CW seed laser. A CW laser is first amplitude modulated (AM 1) with a 5.712 GHz sinusoidal signal. The resulting 11.424 GHz optical signal is then partitioned into macropulses with an 800-kHz signal from a bit pattern generator (AM 2). Finally, the micropulse bandwidth is broadened with a comb line structure after sinusoidal phase modulation (PM). **(B)** The micropulse trains are amplified (Amp 1), preshaped and reduced in repetition rate to 200 kHz (AM 3), amplified again (Amp 2), reduced to 20 kHz using an AOM, then sent through a final fiber amplifier (Amp 3) before being sent through a final AOM to reduce repetition rate to 100 Hz. The pulse trains are then sent through a multi-pass bulk amplifier system. **(C)** The fully amplified pulse trains are sent through a grating compressor, spectrally broadened through a multi-pass cell, and compressed again through a second grating compressor. **(D)** The pulse trains are frequency converted to the fourth harmonic (249 nm) before being imaged from a 500 μm aperture onto the photocathode for electron production. CW = continuous wave, AM = amplitude modulator, PM = phase modulator, Amp = amplifier, AOM = acousto-optic modulator, PBSC = polarizing beam splitter cube, ISO = optical isolator, LBO = lithium triborate, BBO = barium borate.

systems that drive the accelerator system. In this way it is possible to create a train of laser pulses whose repetition rate matches exactly to the bunch repetition rate of the accelerator system. Any phase instability in the seed RF is transferred automatically to both systems identically. Thus, the Compton interaction timing problem is reduced to establishing a simple optical or electronic delay for the laser pulses illuminating the photocathode and used in Compton x-ray generation.

Experimental verification of the production of 11.424 GHz micropulse trains is presented in Figure 6. The right portion of this figure shows a raw streak camera trace of 59 micropulses taken from the PGL system captured within a 5.2 ns window. On the left side of the figure is a profile view of the streak trace integrated over the horizontal dimension. The 5.2 ns window was chosen to maximize the number of micropulses that could be seen while maintaining enough resolution to visualize the individual macropulses. For the experimental results presented in Section 4, micropulse durations were measured to be 2.5 ps FWHM.

The initial amplification of the PGL and ILS also occur in fiber, going through three amplification stages as the macropulse repetition rate is eventually decreased to 20 kHz (PGL) or 200 kHz (ILS). Before entering the bulk amplification stage, which will be discussed in Section 3.5, the repetition rate is reduced to its final operational value using acousto-optic modulators. For the results presented here, this final operational value was 100 Hz.

3.5 Diode-pumped infrared laser technology

Two laser amplification systems are used to produce the results discussed in this work (Sections 4, 5), both of which are based on diode-pumped IR laser technologies. The laser amplifier system used to produce the ILS that is ultimately focused and collided with a counter-propagating electron beam is a Nd:YAG regenerative amplifier and multipass bulk amplifier system that amplifies a highly structured seed pulse (see Section 3.4) at 1,064 nm. A schematic of the ILS is shown in Figure 7. In the systems integration results for the production of laser-Compton x rays reported here, the ILS is frequency converted to produced 532 nm macropulses at 100 Hz (Table 2). Each macropulse consisted of 100 micropulses spaced at 87.5 ps, corresponding to the 11.424 GHz LINAC operating frequency. These highly structured pulses were generated through electro-optic pulse synthesis (Figure 7A), fiber amplification (Figure 7B), and subsequent repetition rate reduction to 100 Hz after passing through an acousto-optic modulator (AOM) in free space. The ILS micropulses were then amplified through a diode-pumped Nd:YAG (4-mm diameter) regenerative amplifier (Figure 7C). After 30 passes, the macropulse is dumped from the regenerative amplifier cavity using a Pockels cell. In the final stages of amplification, the ILS pulses were double-passed through two 7-mm diameter diode-pumped Nd:YAG

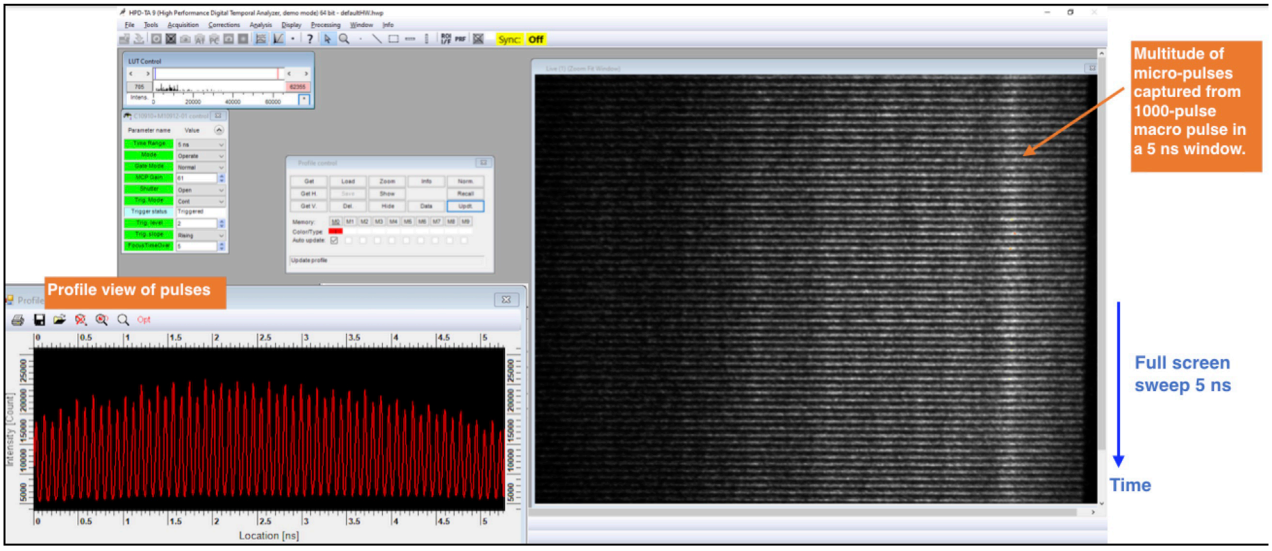

FIGURE 6
Streak camera recording of evenly-spaced micropulses within a single laser macropulse used to produce electron bunches at the DCCS photocathode. 59 micropulses are present within the illustrated streak camera exposure window of 5.2 ns. This is consistent with a micropulse spacing of 87.5 ps which is in turn set by the master clock operating frequency of 11.424 GHz. Illustrated at the left is an integration over the horizontal dimension of the raw streak camera image.

rods and single-passed through two 12-mm diode-pumped Nd:YAG rods (Figure 7D). During the final amplification stages, the pulses were sent through three Keplerian vacuum telescopes with spatial filters labeled T1, T2, and T3 in Figure 7D. After the ILS pulses were fully amplified, they were image relayed to a grating compressor where the pulses were temporally compressed before second harmonic frequency conversion. After second harmonic conversion to 532 nm, 25 W of average power was available for the laser-Compton interaction. Considering 100 micropulses per macropulse at a 100-Hz macropulse repetition rate, this corresponded to an average micropulse energy of 2.5 mJ.

Assuming a copper photocathode quantum efficiency of 10^{-5} and 1,000 microbunches, an average IR power of nominally 10 W would be needed for VHEE FLASH operation. Thus, Yb:YLF was chosen as an initial photogun laser (PGL) amplifier system (Figure 5B) using a previously reported cryogenic Yb:YAG multi-pass amplifier design [81]. The multi-pass amplifier system from Zapata, et al. (2023) [81] was modified to operate with Yb:YLF at the 995.2 nm emission line [82]. Operation at 995.2 nm decreases the quantum defect when pumping with high-power 960 nm diodes, and enables the potential to operate at greater than 10 W of average power by decreasing cooling requirements on the crystal. One limitation of this PGL design is that the 995.2 nm emission line is narrower than the emission band near 1,020 nm. To overcome gain narrowing and reach sufficiently short pulses to maintain electron beam quality, a multi-pass nonlinear compression scheme was implemented to spectrally broaden the pulse (Figure 5C). This allowed for subsequent grating compression to pulse widths as low as 2.5 ps before fourth harmonic frequency conversion and incidence onto the photocathode surface (Figure 5D). This nonlinear compression scheme employed during production of laser-Compton x rays (see Section 4) was an in-air multi-pass cell optimized for low pulse energies and capable of compressing pulses with initial pulse widths as long as 14 ps [83]. To maximize charge production at the photocathode, the multi-pass cell was bypassed, resulting in degraded electron beam quality during the electron beam studies in Section 5.

It should be noted that Lumitron's patented DCCS architecture distributes the energy of the laser macropulse over 100 micropulses and as such reduces the peak intensity of laser pulses transmitted through optical windows, lenses, and nonlinear crystals by two orders of magnitude relative to laser-Compton architectures based on a single high-energy, short duration interaction laser pulse. This eliminates the potential for optical damage from nonlinear self-focusing and significantly expands the design possibilities for the optics within the overall system. For example, this architecture enables the use of lenses (as opposed to curved mirrors) for beam focusing and beam transport which would otherwise not be possible for higher peak intensity pulses.

4 Laser-Compton X-ray results

As part of the DCCS systems integration test reported here, the laser-Compton x-ray beam produced using the DCCS architecture was tested for feasibility of precision imaging. Figure 8 provides a detailed look at the imaging setup used in the systems integration test. After laser-Compton x rays are produced in the laser-electron interaction chamber, the x rays leave vacuum and pass through an experimental bay dedicated to holding sample objects for imaging. After passing through objects of interest, the imaging x-rays propagate out of the radiation safety bunker, through a modular set of beam tubes, and finally onto an x-ray imaging

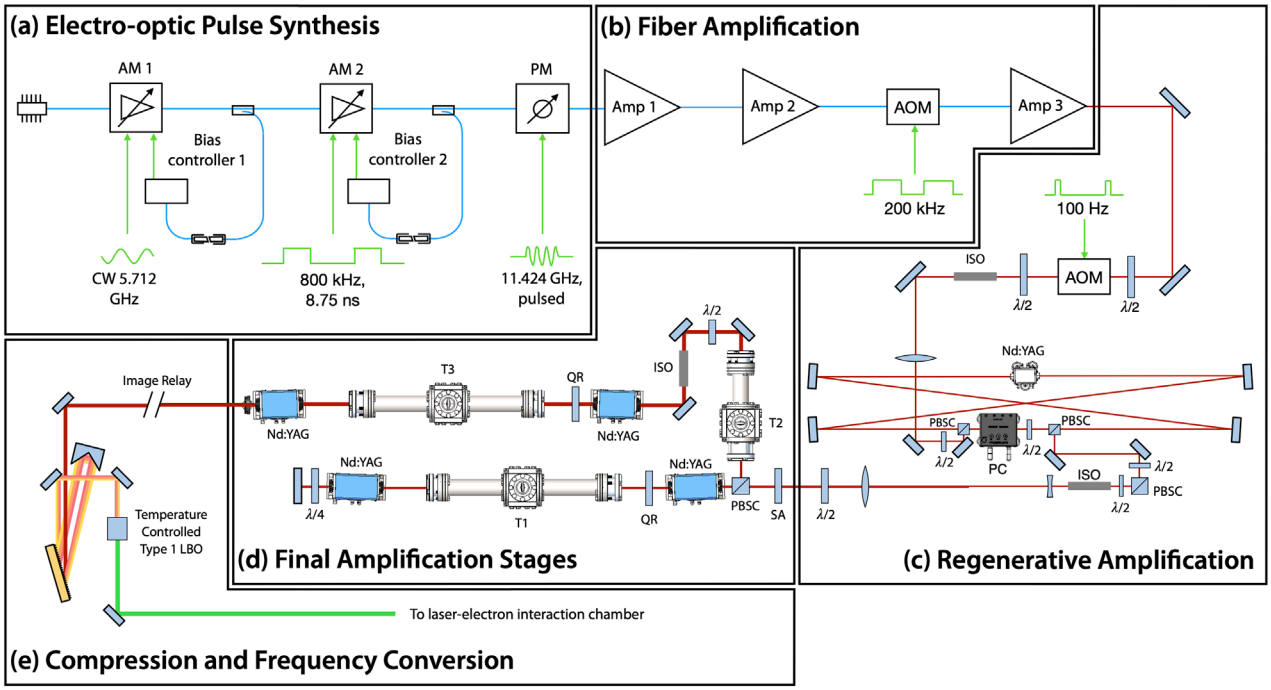

FIGURE 7
Diagram of the interaction laser system (ILS) used at Lumitron Technologies, Inc. for the results presented in this work. **(A)** Pulse synthesis approach used to generate 11.424 GHz micropulse trains from a 1,064 nm CW seed laser. A CW laser is first amplitude modulated (AM 1) with a 5.712 GHz sinusoidal signal. The resulting 11.424 GHz optical signal is then partitioned into macropulses with an 800-kHz signal from a bit pattern generator (AM 2). Finally, the micropulse bandwidth is broadened with a comb line structure after sinusoidal phase modulation (PM). **(B)** The micropulse trains are amplified twice (Amp 1 and Amp 2) before being reduced in repetition rate to 200 kHz (AM 3), and amplified again (Amp 3). **(C)** The free-space macropulse repetition rate is reduced to 100 Hz with an AOM before being sent into a Nd:YAG regenerative amplifier. The PC switches the polarization of the pulse train after about 30 passes. **(D)** The amplified and stretched pulse train is then double-passed through two 7-mm diameter Nd:YAG crystals and single-passed through two 12-mm diameter Nd:YAG crystals as the final amplification stages. **(E)** The pulse trains are temporally compressed with partial spatial overlap, frequency converted to the second harmonic (532 nm), and finally delivered to the laser-electron interaction chamber. CW = continuous wave, AM = amplitude modulator, PM = phase modulator, Amp = amplifier, AOM = acousto-optic modulator, PBSC = polarizing beam splitter cube, PC = Pockels cell, Nd:YAG = neodymium-doped yttrium aluminum garnet, ISO = optical isolator, QR = 90°quartz rotator, SA = serrated aperture, T1-3 = vacuum telescopes with spatial filters, LBO = lithium triborate.

detector. For the results presented in this work, a flat panel x-ray detector was used (Varex, 1512 CMOS), with a pixel pitch of 74.8 μm, a field-of-view of 15 cm by 12 cm, and 200 μm of CsI as the scintillation material.

Laser-Compton x-ray beam profiles were imaged with peak on-axis energies ranging from 30 keV to 140 keV. During these experiments, the x-ray source volume was predominantly determined by the ILS spot size when focused at the interaction point. While the beam quality (M^2) was not measured directly, the measured focal spot is consistent with an equivalent-diameter eighth-order super-Gaussian assuming a flat spatial phase at the input to the lens. To facilitate alignment for these first imaging demonstrations, the electron beam was focused to a 17-μm RMS spot (41-μm FWHM) at the interaction point. The interaction laser was operated at 25 W of average power while producing trains of 100 micropulses at 100 Hz. This corresponds to 2.5 mJ per micropulse.

The interaction of a 532 nm (2.33 eV) laser pulse train with an 38.5 MeV electron beam was used to produce laser-Compton scattered x-ray photons with a peak on-axis energy of 54 keV shown in Figure 9A. The image shown is the accumulation of 10^{10} x rays. Figure 9B is a simulated x-ray beam using the same expected interaction parameters. In order to demonstrate the angle-correlated spectrum and determine the on-axis bandwidth of the laser-Compton x rays, a 100-μm-thick Gd foil was placed in the beamline and the peak on-axis was tuned to 51.8 keV by changing the electron energy to 37.4 MeV (Figure 10A). X rays with energies just above the K-edge of Gd will be highly attenuated compared to energies just below the K-edge. Since the K-shell absorption edge of Gd is 50.2 keV, and since the spectrum of a laser-Compton source produced using a low-emittance electron beam is highly angle-correlated, an attenuation "hole" will appear where the mean energy of the angle-correlated energy spectrum is above the K-edge near the center of the beam. Previous work has demonstrated that the sharpness of this hole is related to the divergence and energy spread of the electron beam [70]. The electron beam parameters that corresponded with the simulated x-ray beam profile that best matched the experimental x-ray spectrum were consistent with the measured electron beam energy spread of 0.2% and expected divergence of around 0.12 mrad (Figure 10B). Based on this approach, the best-fit simulated x-ray spectrum corresponds to an on-axis RMS energy bandwidth of 0.41%. This is consistent with a relatively large electron beam that is not focused as sharply as that used to produce the simulated

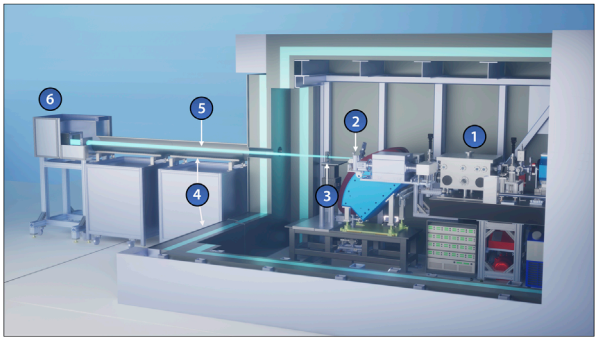

FIGURE 8
Laser-Compton x-ray imaging setup at Lumitron Technologies, Inc. (1) Laser-Compton interaction chamber where laser pulses scatter off of counter-propagating electron bunches to produce a pulsed, laser-Compton x-ray beam. (2) X-ray output window where x rays exit vacuum and begin propagating through air. (3) Object to be imaged is placed on a translation stage system to align with the x-ray beam. (4) Radiation shielding is used to house the accelerator and beam dump in the bunker enclosure in addition to a Pb-lined beam tube that surrounds the x-ray beam as it leaves the bunker. (5) The Laser-Compton x-ray beam. (6) A high resolution detector system is placed in a shielded hutch to detect LCS x rays.

results in Figure 3. To our knowledge, this is the narrowest on-axis bandwidth ever produced from a normal-conducting laser-Compton source.

To demonstrate feasibility of high-resolution imaging using the DCCS architecture, a set of test objects was imaged at 50 keV (Figure 11). A bean pod, a dried anchovy, and a chili pepper were acquired at a local grocery store, bound with adhesive tape, and mounted onto the x-ray sample stage. A photograph of the bound objects is shown in Figure 11A. A composite image produced with 3.2×10^{10} x-ray photons is shown with a vignette to isolate the region of interest in Figure 11B with an inset scale bar. Considering a source-to-sample distance of 1.55 m and a source-to-detector distance of 5.66 m, there is a geometric magnification factor of 3.65. This results in an effective detector pixel size of 20.5 μm. The width of the anchovy spine was measured to be 320 μm, and even smaller features are evident in the image. Since the lower bound on the focused laser spot size is 5 μm, this sets a lower bound on the potential imaging resolution of the laser-Compton x-ray source. With that in mind, the resolution of the image in Figure 11B is detector-limited. It is also worth noting that although this imaging set-up was not optimized for phase-based imaging applications, there is evidence of edge enhancement in Figure 11B. Edge enhancement effects are most obvious around the seeds inside of the chili pepper.

5 FLASH-relevant electron beam results

To demonstrate the feasibility of operating the DCCS architecture with 1,000 electron microbunches per macrobunch at 100 Hz, temporary modifications were made to the photogun laser system. Using the pulse synthesis scheme in Figure 5A, the bit pattern generator was programmed to produce trains of 1,000 microbunches at 800 kHz and subsequent amplification and repetition rate reduction steps were adjusted accordingly. Although the currently operating DCCS prototype at Lumitron Technologies is not fully configured to optimally run at 1,000 microbunches, this adjustment was made for an initial demonstration study. The multi-pass cell typically used to spectrally broaden the photogun laser (PGL) pulses before final compression [83] was bypassed to maximize micropulse energy before frequency conversion to the UV. Without extra spectral broadening and subsequent compression, the amplified PGL pulse width increased to about 14 ps, which was not ideal for low-emittance electron beam operation. For this initial demonstration of high-charge electron beam operation, the goal was to evaluate the feasibility of 1000-bunch operation at high charge and moderate electron energy, to understand beam stability under those operating conditions, and to evaluate the structural integrity of a custom diamond exit window assembly for electron irradiation.

The electron beam was successfully accelerated to 49.4 MeV using Lumitron's built-in-house X-band photogun and three T53VG3 sections operating at 100 Hz. The photogun and each accelerating structure were fed RF power from separate klystron/modulator units each capable of operation up to 400 Hz. For this demonstration, all RF power was delivered at 100 Hz. The first section received 10 MW of peak RF power, the second accelerator section received 5.7 MW of peak RF power, and the third accelerator section received 19 MW of peak RF power. The RF power to the sections was tuned so that the mean electron energy would be near 50 MeV as measured by a 35° dipole magnet spectrometer available in the beamline. Beam quality degradation was noted with a 1% tail on the electron beam spectrum that otherwise reflected a symmetric energy spread of 0.2%. Figure 12 illustrates the measured traces from two separate Bergoz integrating current transformers (ICTs) with custom 5-ns output pulse widths. The total charge in each electron macrobunch could be measured just after the photogun (cyan) and just before the laser-electron interaction chamber (purple) near the vacuum exit window. More charge loss than usual was noted through the accelerator line, most likely because of the large electron energy spread and deteriorated beam quality due to the relatively long PGL micropulses. After accumulating statistics over 172 electron macrobunches, an integrated signal (white) over the downstream ICT trace (magenta) measured 69.62 ± 9.87 nWb as a typical macrobunch signal. Dividing this by the manufacturer-reported ICT conversation factor of 5 V/A yields a measured macrobunch charge of 13.85 ± 1.97 nC.

Figure 13A shows the 100-μm-thick mounted diamond exit window assembly at the end of the beam pipe that was used during this electron beam demonstration. Larger aperture window assemblies optimized for both x-ray and electron beam operation are currently being developed for future experiments. A Ce:YAG imaging system was placed just downstream of the exit window to measure the scintillation signal of the electron beam. When the electron beam was fully aligned to the window, the camera was saturated when set to operate with an exposure time of 10 ms to capture the contributions of a single macrobunch. Although the image in Figure 13B cannot provide a quantitative measure of electrons leaving vacuum, it confirms successful operation

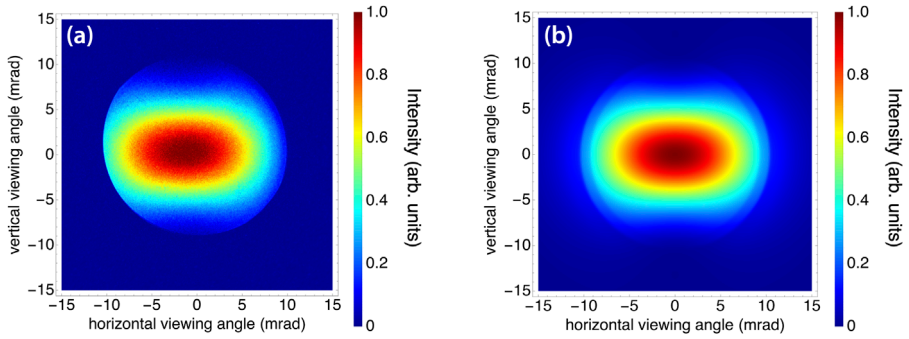

FIGURE 9
(A) An x-ray image produced using 10^{10} photons and **(B)** the corresponding simulation for laser-Compton x-ray beam tuned to a peak on-axis energy of 54 keV. The shape of the x-ray intensity distribution is consistent with a dipole radiation pattern resulting from a vertically polarized interaction laser. The apparent cutoff in the distribution pattern in **(A)** is due to beam offset relative to the vacuum window aperture.

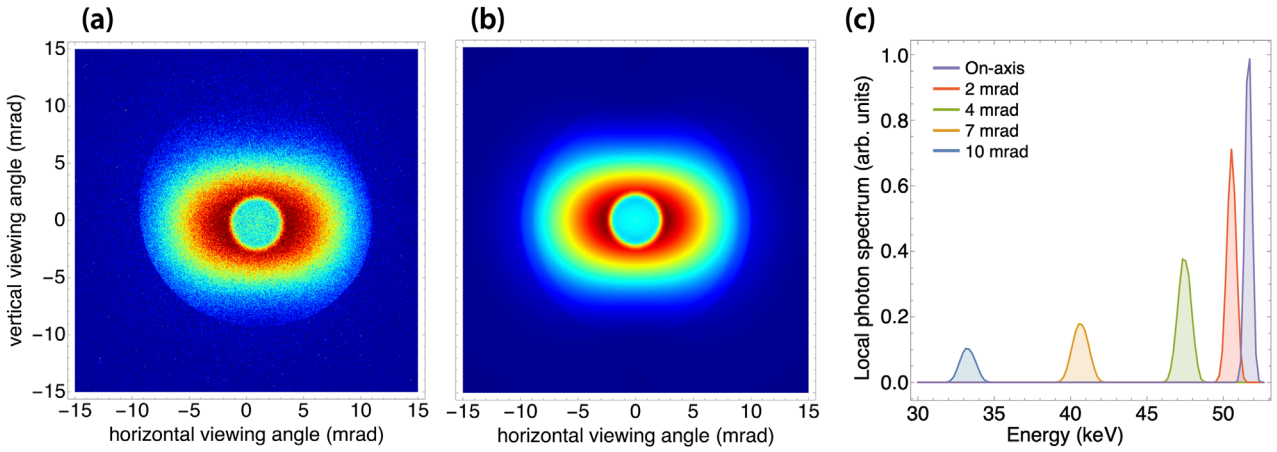

FIGURE 10
(A) An x-ray image and **(B)** corresponding simulation for laser-Compton x-ray beam tuned to a peak on-axis energy of 51.8 keV. The beam is sent through a 100-μm-thick Gd foil before reaching the detector, demonstrating the angle-correlated energy spectrum of the laser-Compton x rays. **(C)** Numerically reconstructed local energy spectra of the best-fit simulation, which used the measured electron beam energy spread of 0.2% to predict an on-axis x-ray RMS bandwidth of 0.41%.

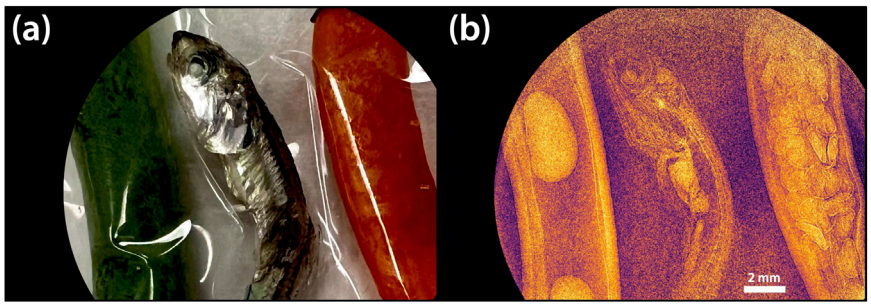

FIGURE 11
(A) Photograph of, from left to right, a bean pod, a dried anchovy, and a chili pepper. The image is vignetted to match the field of view of the corresponding x-ray image. **(B)** Laser-Compton x-ray image of the photographed objects using a total of 3.2×10^{10} x-ray photons with a peak on-axis energy of 50 keV. Phase-based edge enhancement is visible on various structures, including the seeds inside the chili pepper. The width of the anchovy spine is 320 μm.

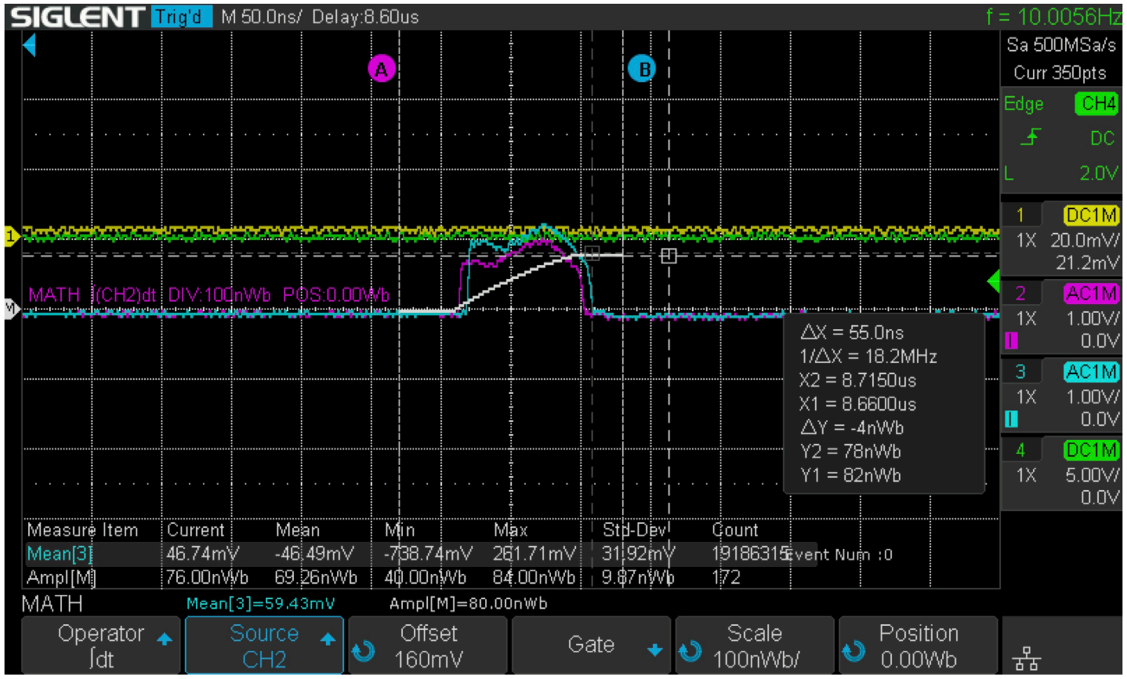

FIGURE 12
Screenshot of two ICT traces taken on a Siglent oscilloscope. The pulse widths of the ICT traces are consistent with the expected 86.6 ns length of a train of 1,000 electron microbunches spaced at 87.5 ps. CH3 (cyan) is the ICT signal just after the photogun while CH2 (magenta) is the signal from the ICT after all accelerator sections just after the laser-electron interaction chamber. An integration of CH2 (white) is carried out to calculate the total charge in the macrobunch. From the "Ampl[M]" Measure Item on the bottom of the screen, an integrated signal of 69.62 ± 9.87 nWb was measured over 172 macrobunches. This corresponds to a macrobunch charge of 13.85 ± 1.97 nC.

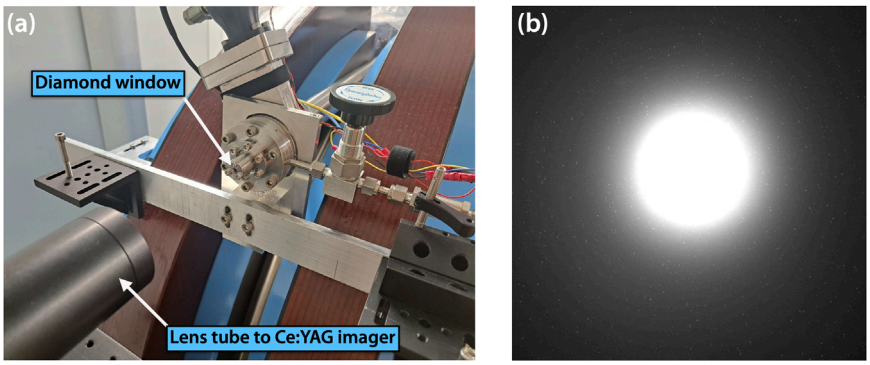

FIGURE 13
(A) Installed diamond window assembly at the end of vacuum beamline is pictured in center. In the bottom left foreground is a lens tube holding a Ce:YAG scintillator screen that is imaged onto a camera sensor. **(B)** Measured Ce:YAG scintillation signal indicating a highly collimated output from the diamond exit window and successful transport of electrons into air.

of the diamond exit window assembly and the presence of a collimated ionizing beam. An in-air ICT is currently being deployed just downstream of the exit window to directly measure the electron charge.

While these initial electron beam results were performed at 49.4 MeV, the DCCS accelerator has produced up to 70 MeV electron beams to date, and is configured to produce 100 MeV in its current state. Upgrades are planned for 137 MeV operation in the next 12 months from the time of writing this manuscript for advanced high-energy imaging applications of relevance to industrial nondestructive tests. The current 100 MeV setup is sufficient for *in vivo* animal irradiation studies planned in the near term. While 14 nC was initially generated per macrobunch in this demonstration, upwards of 50 nC per macrobunch are readily possible by extending the bunch train to 3,000 microbunches. Extending bunch train length further is limited by the temporal length of the compressed RF pulses that drive the accelerator sections.

6 A vision for image-guided VHEE radiation therapy

The concomitant, inherently colinear production of high-brightness x rays through laser-Compton scattering and VHEEs provides a unique opportunity for in-line image-guided radiation therapy using a single device. The notion that a Compton-scattered x-ray beam could be used for image guidance for an underlying VHEE source was, to the best of our knowledge, first suggested by DesRosiers, et al. [84] in the context of laser-plasma VHEE sources. Although DesRosiers, et al. [84] pointed to the potential benefits in x-ray quality, comparing laser-Compton x rays to those produced by synchrotron facilities, there have not been, to the best of our knowledge, any discussions on the feasibility of a laser-Compton x-ray image-guided VHEE radiation therapy system. In this section, we aim to outline the challenges and propose solutions for implementing such a system.

Fundamentally, this concept requires the rapid switching between the production of laser-Compton x rays to the delivery of a VHEE beam. The most straightforward implementation of this switching, considering the DCCS architecture, would be to shutter both ILS and PGL lasers, turn off the final electron bending magnet, and then release bursts of PGL pulses based on the prescribed radiation treatment. In this operation mode, the minimum time between imaging and therapy is the time required to operate laser shutters and the decay time of the bending magnet, which may be on the order of seconds. For this approach to work, the electron energy used to produce LCS x rays must also be of an energy relevant for the radiation treatment. For the DCCS architecture presented here, producing a 70 keV imaging beam, which has been previously identified as an energy of interest for minimizing dose during phase contrast imaging applications [66], requires 45 MeV electrons. Recent treatment planning simulation studies have suggested that this energy range may be of interest, especially when operated at FLASH-relevant dose rates, for treating pediatric brain tumors [85]. However, 45 MeV electrons are insufficient for use in deep-seated tumors in adult humans, and simply increasing the electron energy will correspond with an x-ray beam whose energy is too high for practical clinical imaging applications. One of the appeals of producing x rays or γ rays through laser-Compton scattering is to minimize the energy requirements on the electron beam, thus enabling the use of compact accelerator architectures, especially when compared to the required synchrotron facility requirements to produce the same x-ray or γ-ray energy. Additionally, counter-propagating electron and laser beams uses the *least* energetic electrons possible for a given scattered x-ray energy.

If one could quickly adjust the electron beam energy after x-ray imaging, then the combinations of imaging x-ray energies and therapeutic electron beam energies increases dramatically. In this operation mode on the DCCS, imaging could be performed using an optimal laser-Compton spectrum for either minimizing dose, maximizing contrast, or any combination of metrics for the specific imaging task. Then, after tuning the electron beam energy by changing the amount of RF power delivered to the accelerating sections, an electron beam could be delivered for image-guided radiation therapy. Activities at Lumitron have demonstrated the ability to manually tune the system from one energy to the next with better than 1% accuracy in less than 10 min without relying on any preset values for RF power and steering magnets. In principle, with appropriate preset values established, electron beam energy can be adjusted on the timescale of seconds.

Another consideration for image-guided VHEE FLASH radiation therapy is identifying appropriate combinations of x-ray and electron beam transverse sizes for imaging and therapy respectively. For example, the 38-MeV electron beam considered in the manuscript in Section 4 resulted in a usable x-ray imaging field of about 8 cm at a distance of 5.66 m from the laser-electron interaction point. Although this field-of-view is smaller than what is used with current clinical x-ray sources, a benefit of using a low-divergence beam is that the detector can be placed further away from the patient while preserving the x-ray image. Scattered x rays from the patient are naturally filtered away, improving the image quality on the detector. Additionally, placing the detector further away from the patient enables phase-based image techniques, which can improve the differentiation of soft tissue for increased diagnostic potential. For the electron beam, preclinical small-animal studies are a primary short-term objective to demonstrate the feasibility of UHDR electron beam irradiation using the DCCS. Beams of this type can be constructed using natural beam expansion from the exit window and simple collimators and scattering foils [86]. For clinical applications, VHEE pencil-beam scanning is a potential modality, and a proposed magnet kicker system has recently been discussed [48]. However, pencil-beam scanning would result in an "image-informed" as opposed to a strictly "image-guided" modality in which the laser-Compton x-ray image can define the extent of the scan, but is no longer inherently colinear with the electron beam since the electron beam path is modified by a steering magnet. In general, as long as any electron beam shaping does not modify the central trajectory of the electron beam, the potential for x-ray image guidance is preserved.

Previously presented work has investigated the feasibility of using the free propagating x-ray and electron beams after passing through a common vacuum exit window, and has identified operating conditions of 37 MeV electrons and 51 keV Compton-scattered x rays to potentially image and subsequently irradiate a target the size of a mouse skull [87]. 51 keV was chosen as the imaging energy to utilize a Gd foil to produce a K-edge hole that can be used as an image-guidance crosshair to more accurately identify the central propagation axis of the electron beam (see Figure 10). To fully explore the parameter space available, the incorporation of electron beam optics, x-ray optics, and considerations of different laser-electron interaction geometries should be considered, and will be explored further in future work.

7 Conclusion

Very high energy electrons (VHEEs) have been identified as a promising ionizing radiation modality, especially in the context of eliciting the FLASH effect, but VHEE source size and access to high-fidelity image guidance limit clinical implementation. In this work, we described the Distributed Charge Compton Source (DCCS) as a uniquely suited architecture for image-guided VHEE FLASH radiation therapy. Through maximally distributing electron

charge in long, low-charge trains of microbunches at 11.424 GHz (X-band), large currents can be accelerated without compromising the quality of the electron beam. This conservation of electron beam quality enables the electron beam to be used not only directly as an ionizing radiation source, but also as a generator of secondary x rays through the head-on collision with a counter-propagating train of laser pulses through the process of laser-Compton scattering. Since the laser micropulses and electron microbunches are generated using the same RF master lock, the pulse/bunch trains are inherently synchronized up to a simple phase delay. As a systems integration test, the DCCS has demonstrated the production of laser-Compton x rays with narrow energy bandwidths (54 keV with 0.41% on-axis RMS bandwidth presented here) and the production of electron macrobunches with FLASH-relevant charge densities (14 nC in 86.6 ns at 100 Hz). As the underlying systems are continued to be commissioned, a primary milestone is to use the same electron beam for both the production of inherently colinear laser-Compton x-rays and electron irradiation in a single experimental session, thus demonstrating the feasibility of using the DCCS architecture for x-ray image-guided VHEE FLASH radiation therapy.

Data availability statement

The raw data supporting the conclusions of this article will be made available by the authors, without undue reservation.

Ethics statement

Ethical approval was not required for the study involving animals in accordance with the local legislation and institutional requirements because the animal product (dried anchovy) used for imaging tests was purchased at a grocery store. Written informed consent was obtained from the individual(s) for the publication of any identifiable images or data included in this article.

Author contributions

CB: Conceptualization, Investigation, Project administration, Software, Supervision, Visualization, Writing–original draft, Writing–review and editing. JA: Conceptualization, Project administration, Software, Visualization, Writing–review and editing. AA: Investigation, Software, Writing–review and editing. JB: Investigation, Software, Writing–review and editing. SB: Investigation, Visualization, Writing–review and editing. MCa: Resources, Writing–review and editing. MCh: Investigation, Writing–review and editing. MD: Resources, Writing–review and editing. RD: Investigation, Writing–review and editing. DD: Resources, Writing–review and editing. HE: Conceptualization, Formal Analysis, Investigation, Software, Visualization, Writing–original draft, Writing–review and editing. RF: Project administration, Writing–review and editing. AG: Investigation, Writing–review and editing. KG: Project administration, Writing–review and editing. AG: Resources, Writing–review and editing. FH: Conceptualization, Investigation, Project administration, Software, Writing–review and editing. LH: Investigation, Software, Writing–review and editing. YH: Conceptualization, Formal Analysis, Investigation, Software, Visualization, Writing–review and editing. GI: Writing–review and editing, Conceptualization, Investigation, Project administration. MJ: Investigation, Writing–review and editing. CJ: Resources, Writing–review and editing. KK: Resources, Writing–review and editing. AL: Formal Analysis, Investigation, Software, Visualization, Writing–review and editing. RL: Investigation, Writing–review and editing. MM: Visualization, Writing–review and editing. EM: Investigation, Writing–review and editing. CN: Resources, Writing–review and editing. HN: Resources, Writing–review and editing. KP: Investigation, Visualization, Writing–review and editing. ZP: Visualization, Writing–review and editing. MQ: Investigation, Software, Writing–review and editing. FR: Conceptualization, Investigation, Project administration, Visualization, Writing–review and editing. KR: Resources, Writing–review and editing, Investigation. TR: Formal Analysis, Investigation, Software, Visualization, Writing–review and editing. JS: Software, Visualization, Writing–review and editing. MSc: Investigation, Writing–review and editing. MSe: Investigation, Visualization, Writing–review and editing. JY: Visualization, Writing–review and editing. NY: Visualization, Writing–review and editing. CZ: Resources, Writing–review and editing. LZ: Conceptualization, Investigation, Project administration, Writing–review and editing. EZ: Resources, Writing–review and editing. JZ: Investigation, Writing–review and editing.

Funding

The authors declare that financial support was received for the research, authorship, and/or publication of this article. This work was supported by funds from Lumitron Technologies, Inc and in part by the DARPA GRIT program under Contract Number HR00112090059. HHE and TR received partial training funding through the NIH T32GM008620.

Acknowledgments

The authors wish to acknowledge the following individuals for their varied contributions to the establishment of prior configurations of the hardware described in this document and/or the creation of relevant machine-related infrastructure: Ted Andreas, Lisset Ayala, Sam Chu, Mackenzie E. Drobny, Jake Ewing, Derek Fietz, Christopher Fluxa, Daniel Gitlin, Albert Herrero Parareda, Jason Holtkamp, Salma Idrus, Patrick Lancuba, Mealaud Mokhtarzad, Eric C. Nelson, Christine V. Nguyen, Milan N. Nguyen, Colin Sledge, Ahmed Srass, Vy Tran, Alexandra Valanis, Gabriella Vass, Kinga Vassne, Daniel Vega, and Li Yi-Ning.

Conflict of interest

Authors CB, JA, AA, JB, SB, MCa, MCh, MD, RD, DD, HE, RF, AG, KG, AG, FH, LH, YH, GI, MJ, CJ, KK, AL, RL, MM, EM, CN,

HN, KP, ZP, MQ, FR, KR, TR, JS, MSc, MSe, JY, NY, CZ, LZ, EZ, and JZ were employed by Lumitron Technologies, Inc.

The authors declare that this study received funding from Lumitron Technologies, Inc. The funder had the following involvement in the study: manufacturing of machine hardware, test of subsystem hardware, assembly of full system hardware, machine operations, and machine and experiment safety.

Publisher's note

References

1. Barty CPJ. Modulated method for efficient, narrow-bandwidth, laser Compton X-ray and gamma-ray sources. United States patent US 9706631B2 (2017).

2. Ronga MG, Cavallone M, Patriarca A, Leite AM, Loap P, Favaudon V, et al. Back to the future: very high-energy electrons (VHEEs) and their potential application in radiation therapy. *Cancers (Basel)* (2021) 13:4942. doi:10.3390/cancers13194942

3. Vozenin MC, Bourhis J, Durante M. Towards clinical translation of FLASH radiotherapy. *Nat Rev Clin Oncol* (2022) 19:791–803. doi:10.1038/s41571-022-00697-z

4. Favaudon V, Caplier L, Monceau V, Pouzoulet F, Sayarath M, Fouillade C, et al. Ultrahigh dose-rate FLASH irradiation increases the differential response between normal and tumor tissue in mice. *Sci Translational Med* (2014) 6:245ra93. doi:10.1126/scitranslmed.3008973

5. El Naqa I, Pogue BW, Zhang R, Oraiqat I, Parodi K. Image guidance for FLASH radiotherapy. *Med Phys* (2022) 49:4109–22. doi:10.1002/mp.15662

6. Taylor PA, Moran JM, Jaffray DA, Buchsbaum JC. A roadmap to clinical trials for FLASH. *Med Phys* (2022) 49:4099–108. doi:10.1002/mp.15623

7. Garibaldi C, Beddar S, Bizzocchi N, Böhlen TT, Iliaskou C, Moeckli R, et al. Minimum and optimal requirements for a safe clinical implementation of ultra-high dose rate radiotherapy: a focus on patient's safety and radiation protection. *Radiother Oncol* (2024) 196:110291. doi:10.1016/j.radonc.2024.110291

8. Günther BS. Overview on inverse Compton x-ray sources (2023) *Storage ring-based inverse Compton X-ray sources: cavity design, beamline development and X-ray applications*. Cham: Springer International Publishing. p. 117–47. doi:10.1007/978-3-031-17742-2_6

9. Rosenzweig J, Colby E. Charge and wavelength scaling of RF photoinjector designs. *AIP Conf Proc* (1995) 335:724–37. doi:10.1063/1.48260

10. Yang J, Barty CPJ. Producing electrons and laser-Compton x-rays with a distributed charge Compton source (2024). doi:10.6084/m9.figshare.26108956

11. Hartemann FV, Brown WJ, Gibson DJ, Anderson SG, Tremaine AM, Springer PT, et al. High-energy scaling of Compton scattering light sources. *Phys Rev Acc Beams* (2005) 8:100702. doi:10.1103/PhysRevSTAB.8.100702

12. Jacquet M. Potential of compact Compton sources in the medical field. *Phys Med* (2016) 32:1790–4. doi:10.1016/j.ejmp.2016.11.003

13. Thomlinson W, Elleaume H, Porra L, Suortti P. K-edge subtraction synchrotron x-ray imaging in bio-medical research. *Phys Med* (2018) 49:58–76. doi:10.1016/j.ejmp.2018.04.389

14. Liu Y, Nelson J, Holzner C, Andrews JC, Pianetta P. Recent advances in synchrotron-based hard x-ray phase contrast imaging. *J Phys D: Appl Phys* (2013) 46:494001. doi:10.1088/0022-3727/46/49/494001

15. Walsh CL, Tafforeau P, Wagner WL, Jafree DJ, Bellier A, Werlein C, et al. Imaging intact human organs with local resolution of cellular structures using hierarchical phase-contrast tomography. *Nat Methods* (2021) 18:1532–41. doi:10.1038/s41592-021-01317-x

16. Milburn RH. Electron scattering by an intense polarized photon field. *Phys Rev Lett* (1963) 10:75–7. doi:10.1103/PhysRevLett.10.75

17. Arutyunian FR, Tumanian VA. The Compton effect on relativistic electrons and the possibility of obtaining high energy beams. *Phys Lett* (1963) 4:176–8. doi:10.1016/0031-9163(63)90351-2

18. Maiman TH. Stimulated optical radiation in ruby. *Nature* (1960) 187:493–4. doi:10.1038/187493a0

19. Fiocco G, Thompson E. Thomson scattering of optical radiation from an electron beam. *Phys Rev Lett* (1963) 10:89–91. doi:10.1103/PhysRevLett.10.89

20. Kulikov OF, Telnov YY, Filippov EI, Yakimenko MN. Compton effect on moving electrons. *Phys Lett* (1964) 13:344–6. doi:10.1016/0031-9163(64)90040-X

21. Bemporad C, Milburn RH, Tanaka N, Fotino M. High-energy photons from Compton scattering of light on 6.0-gev electrons. *Phys Rev* (1965) 138:B1546–9. doi:10.1103/PhysRev.138.B1546

22. Brown G, Halbach K, Harris J, Winick H. Wiggler and undulator magnets — a review. *Nucl Instr Methods Phys Res* (1983) 208:65–77. doi:10.1016/0167-5087(83)91105-5

23. Jones FC. Inverse Compton scattering of cosmic-ray electrons. *Phys Rev* (1965) 137:B1306–11. doi:10.1103/PhysRev.137.B1306

24. Compton AH. A quantum theory of the scattering of x-rays by light elements. *Phys Rev* (1923) 21:483–502. doi:10.1103/PhysRev.21.483

25. Gibson DJ. A high-energy, uiltrashort-pulse X-ray system for the dynamic study of heavy, dense materials (2004). Dissertation. University of California, Davis.

26. Weller HR, Ahmed MW, Gao H, Tornow W, Wu YK, Gai M, et al. Research opportunities at the upgraded HIS facility. *Prog Part Nucl Phys* (2009) 62:257–303. doi:10.1016/j.ppnp.2008.07.001

27. Barty C, Hartemann F. T-REX: Thomson-radiated extreme x-rays moving x-ray science into the "nuclear" applications space with thompson scattered photons. *Tech. rep.* (2004). Livermore, CA: Lawrence Livermore National Lab LLNL.

28. Drebot I, Petrillo V, Serafini L. Two-colour x-gamma ray inverse Compton back-scattering source. *EPL* (2017) 120:14002. doi:10.1209/0295-5075/120/14002

29. Suerra E, Giannotti D, Canella F, Drebot I, Capra S, Cipriani D, et al. A new method for spatial mode shifting of stabilized optical cavities for the generation of dual-color x-rays. *Nucl Instr Methods Phys Res Section A: Acc Spectrometers, Detectors Associated Equipment* (2021) 1019:165852. doi:10.1016/j.nima.2021.165852

30. Schoenlein RW, Leemans WP, Chin AH, Volfbeyn P, Glover TE, Balling P, et al. Femtosecond X-ray pulses at 0.4 Å generated by 90° Thomson scattering: a tool for probing the structural dynamics of materials. *Science* (1996) 274:236–8. doi:10.1126/science.274.5285.236

31. Hartemann FV, Tremaine AM, Anderson SG, Barty CPJ, Betts SM, Booth R, et al. Characterization of a bright, tunable, ultrafast Compton scattering x-ray source. *Laser Part Beams* (2004) 22:221–44. doi:10.1017/S0263034604223059

32. Albert F, Anderson SG, Gibson DJ, Hagmann CA, Johnson MS, Messerly M, et al. Characterization and applications of a tunable, laser-based, MeV-class Compton-scattering γ-ray source. *Phys Rev Spec Top - Acc Beams* (2010) 13:070704. doi:10.1103/PhysRevSTAB.13.070704

33. Gibson DJ, Albert F, Anderson SG, Betts SM, Messerly MJ, Phan HH, et al. Design and operation of a tunable MeV-level Compton-scattering-based γ-ray source. *Phys Rev ST Accel Beams* (2010) 13:070703. doi:10.1103/PhysRevSTAB.13.070703

34. Jacquet M, Alexandre P, Alkadi M, Alves M, Amer M, Amoudry L, et al. First production of x-rays at the ThomX high-intensity Compton source. *The Eur Phys J Plus* (2024) 139:459. doi:10.1140/epjp/s13360-024-05186-z

35. Tilton S, Eckrosh K, Larsen R, Ros E, Lee HS, Valentin D, et al. (2024) Laser systems and diagnostics for the ASU compact x-ray source. Optica Publishing Group. doi:10.1364/EUVXRAY.2024.ETu2A.2

36. Sakai Y, Babzien M, Fedurin M, Kusche K, Williams O, Fukasawa A, et al. Hard x-ray inverse Compton scattering at photon energy of 87.5 keV. *Sci Rep* (2024) 14:18467. doi:10.1038/s41598-024-68170-8

37. Akagi T, Kosuge A, Araki S, Hajima R, Honda Y, Miyajima T, et al. Narrow-band photon beam via laser Compton scattering in an energy recovery linac. *Phys Rev Acc Beams* (2016) 19:114701. doi:10.1103/PhysRevAccelBeams.19.114701

38. Kosuge A, Akagi T, Honda Y, Araki S, Urakawa J, Terunuma N, et al. (2018) ERL-based laser-Compton scattering x-ray source for x-ray imaging. In: T Kawachi, SV Bulanov, H Daido, Y Kato, editors. *X-ray lasers 2016*. Cham: Springer International Publishing, p. 261–4.

39. Eggl E, Dierolf M, Achterhold K, Jud C, Günther B, Braig E, et al. The Munich Compact Light Source: initial performance measures. *J Synchrotron Radiat* (2016) 23:1137–42. doi:10.1107/s160057751600967x

40. Günther B, Gradl R, Jud C, Eggl E, Huang J, Kulpe S, et al. The versatile x-ray beamline of the Munich Compact Light Source: design, instrumentation and applications. *J Synchrotron Radiat* (2020) 27:1395–414. doi:10.1107/s1600577520008309

41. Dunning CAS, Bazalova-Carter M. X-ray fluorescence computed tomography induced by photon, electron, and proton beams. *IEEE Trans Med Imaging* (2019) 38:2735–43. doi:10.1109/TMI.2019.2912137

42. Giannini N, Gadducci G, Fuentes T, Gonnelli A, Di Martino F, Puccini P, et al. Electron FLASH radiotherapy *in vivo* studies. a systematic review. *Front Oncol* (2024) 14:1373453. doi:10.3389/fonc.2024.1373453

43. DesRosiers C, Moskvin V, Bielajew AF, Papiez L. 150-250 MeV electron beams in radiation therapy. *Phys Med and Biol* (2000) 45:1781–805. doi:10.1088/0031-9155/45/7/306

44. Sarti A, De Maria P, Battistoni G, De Simoni M, Di Felice C, Dong Y, et al. Deep seated tumour treatments with electrons of high energy delivered at FLASH rates: the example of prostate cancer. *Front Oncol* (2021) 11:777852. doi:10.3389/fonc.2021.777852

45. Böhlen TT, Germond JF, Desorgher L, Veres I, Bratel A, Landström E, et al. Very high-energy electron therapy as light-particle alternative to transmission proton FLASH therapy - an evaluation of dosimetric performances. *Radiother Oncol* (2024) 194:110177. doi:10.1016/j.radonc.2024.110177

46. Gamba D, Corsini R, Curt S, Doebert S, Farabolini W, McMonagle G, et al. The CLEAR user facility at CERN. *Nucl Instr Methods Phys Res Section A: Acc Spectrometers, Detectors Associated Equipment* (2018) 909:480–3. doi:10.1016/j.nima.2017.11.080

47. Maxim PG, Tantawi SG, Loo J, Billy W. PHASER: a platform for clinical translation of FLASH cancer radiotherapy. *Radiother Oncol* (2019) 139:28–33. doi:10.1016/j.radonc.2019.05.005

48. Stephan F, Gross M, Grebinyk A, Aboulbanine Z, Amirkhanyan Z, Budach V, et al. FLASHlab@PITZ: new R&D platform with unique capabilities for electron FLASH and VHEE radiation therapy and radiation biology under preparation at PITZ. *Phys Med* (2022) 104:174–87. doi:10.1016/j.ejmp.2022.10.026

49. Faillace L, Alesini D, Bisogni G, Bosco F, Carillo M, Cirrone P, et al. Perspectives in linear accelerator for FLASH VHEE: study of a compact C-band system. *Phys Med* (2022) 104:149–59. doi:10.1016/j.ejmp.2022.10.018

50. Palumbo L, Sarti A, Mostacci A, De Gregorio A, De Arcangelis D, Francescone D, et al. (2023) SAFEST. A compact C-band linear accelerator for VHEE-FLASH radiotherapy. In: *Proc IPAC'23*. JACoW Publishing. p. 5079–82. doi:10.18429/JACoW-IPAC2023-THPM087

51. Lin XC, Zha H, Shi JR, Gao Q, Hu FJ, Li QZ, et al. A compact X-band backward traveling-wave accelerating structure. *Nucl Sci Tech* (2024) 35:40. doi:10.1007/s41365-024-01403-7

52. Subiel A, Moskvin V, Welsh GH, Cipiccia S, Reboredo D, Evans P, et al. Dosimetry of very high energy electrons (VHEE) for radiotherapy applications: using radiochromic film measurements and Monte Carlo simulations. *Phys Med Biol* (2014) 59:5811–29. doi:10.1088/0031-9155/59/19/5811

53. Bazalova-Carter M, Liu M, Palma B, Dunning M, McCormick D, Hemsing E, et al. Comparison of film measurements and Monte Carlo simulations of dose delivered with very high-energy electron beams in a polystyrene phantom. *Med Phys* (2015) 42:1606–13. doi:10.1118/1.4914371

54. Poppinga D, Kranzer R, Farabolini W, Gilardi A, Corsini R, Wyrwoll V, et al. VHEE beam dosimetry at cern linear electron accelerator for research under ultra-high dose rate conditions. *Biomed Phys Eng Express* (2020) 7:015012. doi:10.1088/2057-1976/abcae5

55. Small KL, Henthorn NT, Angal-Kalinin D, Chadwick AL, Santina E, Aitkenhead A, et al. Evaluating very high energy electron RBE from nanodosimetric pBR322 plasmid DNA damage. *Sci Rep* (2021) 11:3341. doi:10.1038/s41598-021-82772-6

56. Lagzda A, Angal-Kalinin D, Jones J, Aitkenhead A, Kirkby KJ, MacKay R, et al. Influence of heterogeneous media on very high energy electron (VHEE) dose penetration and a Monte Carlo-based comparison with existing radiotherapy modalities. *Nucl Instr Methods Phys Res Section B: Beam Interactions Mater Atoms* (2020) 482:70–81. doi:10.1016/j.nimb.2020.09.008

57. Kokurewicz K, Brunetti E, Curcio A, Gamba D, Garolfi L, Gilardi A, et al. An experimental study of focused very high energy electron beams for radiotherapy. *Commun Phys* (2021) 4:33. doi:10.1038/s42005-021-00536-0

58. Whitmore L, Mackay RI, van Herk M, Korysko P, Farabolini W, Malyzhenkov A, et al. CERN-based experiments and monte-carlo studies on focused dose delivery with very high energy electron (VHEE) beams for radiotherapy applications. *Sci Rep* (2024) 14:11120. doi:10.1038/s41598-024-60997-5

59. Bateman JJ, Buchanan E, Corsini R, Farabolini W, Korysko P, Garbrecht Larsen R, et al. Development of a novel fibre optic beam profile and dose monitor for very high energy electron radiotherapy at ultrahigh dose rates. *Phys Med Biol* (2024) 69:085006. doi:10.1088/1361-6560/ad33a0

60. Hart A, Giguere C, Bateman J, Korysko P, Farabolini W, Rieker V, et al. Plastic scintillator dosimetry of ultrahigh dose-rate 200 MeV electrons at CLEAR. *IEEE Sens J* (2024) 24:14229–37. doi:10.1109/JSEN.2024.3353190

61. Anderson SG, Barty CPJ, Betts SM, Brown WJ, Crane JK, Cross RR, et al. Short-pulse, high-brightness x-ray production with the PLEIADES Thomson-scattering source. *Appl Phys B: Lasers Opt* (2004) 78:891–4. doi:10.1007/s00340-004-1455-0

62. Gibson DJ, Anderson SG, Barty CPJ, Betts SM, Booth R, Brown WJ, et al. PLEIADES: a picosecond Compton scattering x-ray source for advanced backlighting and time-resolved material studies. *Phys Plasmas* (2004) 11:2857–64. doi:10.1063/1.1646160

63. Hartemann FV, Tremaine AM, Anderson SG, Barty CPJ, Betts SM, Booth R, et al. Characterization of a bright, tunable, ultrafast Compton scattering x-ray source. *Laser Part Beams* (2004) 22:221–44. doi:10.1017/S0263034604223059

64. Shverdin MY, Jovanovic I, Semenov VA, Betts SM, Brown C, Gibson DJ, et al. High-power picosecond laser pulse recirculation. *Opt Lett* (2010) 35:2224–6. doi:10.1364/OL.35.002224

65. Messerly MJ, Dawson JW, Barty CPJ, Gibson DJ, Prantil MA, Cormier E. Directly driven source of multi-gigahertz, sub-picosecond optical pulses. United States patent US 9166355B2 (2015).

66. Reutershan T, Effarah HH, Lagzda A, Barty CPJ. Numerical evaluation of high-energy, laser-Compton x-ray sources for contrast enhancement and dose reduction in clinical imaging via gadolinium-based k-edge subtraction. *Appl Opt* (2022) 61:C162–C178. doi:10.1364/AO.446189

67. Albert F, Anderson SG, Gibson DJ, Marsh RA, Siders CW, Barty CPJ, et al. Three-dimensional theory of weakly nonlinear Compton scattering. *Phys Plasmas* (2011) 18:013108. doi:10.1063/1.3536457

68. Sun C, Li J, Rusev G, Tonchev AP, Wu YK. Energy and energy spread measurements of an electron beam by Compton scattering method. *Phys Rev Spec Top - Acc Beams* (2009) 12:062801. doi:10.1103/PhysRevSTAB.12.062801

69. Krafft GA, Johnson E, Deitrick K, Terzić B, Kelmar R, Hodges T, et al. Laser pulsing in linear Compton scattering. *Phys Rev Acc Beams* (2016) 19:121302. doi:10.1103/PhysRevAccelBeams.19.121302

70. Hwang Y, Effarah HH, Tajima T, Barty CPJ, Gibson DJ, Marsh RA. Electron beam characterization through K-edge filtering of laser Compton-scattered x rays. *Phys Rev Acc Beams* (2023) 26:072802. doi:10.1103/PhysRevAccelBeams.26.072802

71. Limborg-Deprey C, Adolphsen C, McCormick D, Dunning M, Jobe K, Li H, et al. Performance of a first generation X-band photoelectron rf gun. *Phys Rev Acc Beams* (2016) 19:053401. doi:10.1103/PhysRevAccelBeams.19.053401

72. Marsh RA, Albert F, Anderson SG, Beer G, Chu TS, Cross RR, et al. Modeling and design of an X-band rf photoinjector. *Phys Rev Spec Top - Acc Beams* (2012) 15:102001. doi:10.1103/PhysRevSTAB.15.102001

73. Marsh RA, Anderson GG, Anderson SG, Gibson DJ, Barty CPJ, Hwang Y. Performance of a second generation X-band rf photoinjector. *Phys Rev Acc Beams* (2018) 21:073401. doi:10.1103/PhysRevAccelBeams.21.073401

74. Marsh RA, Anderson SG, Gibson DJ, Hartemann FV, Barty CPJ (2012). Modeling multi-bunch X-band photoinjector challenges. In: *Proc IPAC'12*. JaCoW Publishing p. 658–60.

75. Gibson DJ, Anderson GG, Hwang Y, Marsh RA, Barty CPJ (2016) Multi-bunch operation of a laser-Compton x-ray source based on compact x-band accelerator technology. In: *High-brightness sources and light-driven interactions*. OSA Technical Digest (online), EM1A.3. doi:10.1364/EUVXRAY.2016.EM1A.3

76. Gibson DJ, Hwang Y, Marsh R (2017). Initial performance measurements of multi-GHz electron bunch trains. In: *Proc IPAC'17*. JACOW Publishing. p. 795–7. doi:10.18429/JACoW-IPAC2017-MOPIK111

77. Siders CW, Siders JL, Taylor AJ, Park SG, Weiner AM. Efficient high-energy pulse-train generation using a 2^n-pulse michelson interferometer. *Appl Opt* (1998) 37:5302–5. doi:10.1364/ao.37.005302

78. Adolphsen C. Normal-conducting rf structure test facilities and results. *Proc 2003 Part Accelerator Conf* (2003) 1:668–72. doi:10.1109/PAC.2003.1289005

79. Granados E, Chevallay E, Fedosseev V, Panuganti H. Capabilities and performance of the CLEAR facility photo-injector. *Tech. rep.* (2019). Geneva: CERN.

80. Prantil MA, Cormier E, Dawson JW, Gibson DJ, Messerly MJ, Barty CPJ. Widely tunable 11 GHz femtosecond fiber laser based on a nonmode-locked source. *Opt Lett* (2013) 38:3216–8. doi:10.1364/OL.38.003216

81. Zapata LE, Pergament M, Schust M, Reuter S, Thesinga J, Zapata C, et al. One-joule 500-Hz cryogenic Yb:YAG laser driver of composite thin-disk design. *Opt Lett* (2022) 47:6385–8. doi:10.1364/OL.476964

82. Zapata LE, Ripin DJ, Fan TY. Power scaling of cryogenic Yb:$LiYF_4$ lasers. *Opt Lett* (2010) 35:1854–6. doi:10.1364/OL.35.001854

83. Seggebruch MWL, Amador A, Betts S, Garcia A, Gitlin D, Imeshev G, et al. Multi-GHz photoinjector lasers for high brightness x-ray sources. High-Brightness Sources and Light-Driven Interactions Congress (Optica Publishing Group) (2024). Technical Digest Series, ETu6A.3. doi:10.1364/EUVXRAY.2024.ETu6A.3

84. DesRosiers C, Moskvin V, Cao M, Joshi CJ, Langer M. Laser-plasma generated very high energy electrons in radiation therapy of the prostate. *Commercial and Biomedical Applications of Ultrafast Lasers VIII* (SPIE). *Proc SPIE - Int Soc Opt Eng* (2008) 6881:688109. doi:10.1117/12.761663

85. Breitkreutz DY, Shumail M, Bush KK, Tantawi SG, Maxim PG, Loo BW. Initial steps towards a clinical FLASH radiotherapy system: pediatric whole brain irradiation with 40 MeV electrons at FLASH dose rates. *Radiat Res* (2020) 194:594–9. doi:10.1667/rade-20-00069.1

86. Bourgouin A, Knyziak A, Marinelli M, Kranzer R, Schuller A, Kapsch RP. Characterization of the PTB ultra-high pulse dose rate reference electron beam. *Phys Med Biol* (2022) 67:085013. doi:10.1088/1361-6560/ac5de8

87. Effarah HH, Reutershan T, Nelson EC, Hwang Y, Barty CPJ. X-ray and electron beam considerations for laser-Compton image-guided radiation therapy (2024). High-Brightness Sources and Light-Driven Interactions Congress (Optica Publishing Group). Technical Digest Series, ETu2A.3. doi:10.1364/EUVXRAY.2024.ETu2A.3

frontiers | Frontiers in Physics

TYPE Original Research
PUBLISHED 17 December 2024
DOI 10.3389/fphy.2024.1511830

OPEN ACCESS

EDITED BY
Jiaru Shi,
Tsinghua University, China

REVIEWED BY
Kiki Theodorou,
University of Thessaly, Greece
Lanchun Lu,
The Ohio State University, United States

*CORRESPONDENCE
J. H. Pensavalle,
jakeharold.pensavalle@gmail.com
G. Felici,
giuseppefelici1971@gmail.com

RECEIVED 15 October 2024
ACCEPTED 02 December 2024
PUBLISHED 17 December 2024

CITATION
Pensavalle JH, Di Martino F, Cavalieri A, Celentano M, De Gregorio A, Di Francesco M, Franciosini G, Galluzzo L, Masturzo L, Milluzzo G, Montay-Gruel P, Paiar F, Pantaleoni M, Patera V, Pioli S, Poortmans P, Romano F, Sarti A, Subiel A, Vannozzi A and Felici G (2024) Standard requirements for clinical very high energy electron and ultra high dose rate medical devices.
Front. Phys. 12:1511830.
doi: 10.3389/fphy.2024.1511830

Standard requirements for clinical very high energy electron and ultra high dose rate medical devices

J. H. Pensavalle[1]*, F. Di Martino[1,2,3], A. Cavalieri[4], M. Celentano[1,3], A. De Gregorio[5,6], M. Di Francesco[7], G. Franciosini[6,8], L. Galluzzo[7], L. Masturzo[1,3], G. Milluzzo[9], P. Montay-Gruel[10,11], F. Paiar[2,4,12], M. Pantaleoni[13], V. Patera[6,8], S. Pioli[14], P. Poortmans[15,16], F. Romano[9,17], A. Sarti[6,8], A. Subiel[18,19], A. Vannozzi[14] and G. Felici[7]*

[1]Azienda Ospedaliero Universitaria Pisa (AOUP), Fisica Sanitaria, Pisa, Italy, [2]Centro Pisano Multidisciplinare Sulla Ricerca e Implementazione Clinica Della Flash Radiotherapy (CPFR@CISUP), Pisa, Italy, [3]National Institute of Nuclear Physics (INFN), Section of Pisa, Pisa, Italy, [4]Center for Instrument Sharing University of Pisa (CISUP), University of Pisa, Pisa, Italy, [5]Dipartimento di Fisica, Sapienza Università di Roma, Roma, Italy, [6]Istituto Nazionale di Fisica Nucleare (INFN) Sezione di Roma I, Roma, Italy, [7]SIT Sordina IORT Technologies, Aprilia, Italy, [8]Dipartimento di Scienze di Base e Applicate per l'Ingegneria, Sapienza Università di Roma, Roma, Italy, [9]Istituto Nazionale di Fisica Nucleare (INFN), Sezione di Catania, Catania, Italy, [10]Center for Oncological Research (CORE), Integrated Personalized and Precision Oncology Network (IPPON), Faculty of Medicine and Health Sciences, University of Antwerp, Wilrijk, Belgium, [11]Iridium Netwerk, Radiation Oncology, Antwerp, Belgium, [12]Department of Translational Research and New Technologies in Medicine and Surgery, University of Pisa, Pisa, Italy, [13]Maytal International Ltd – Global Med Dev Expertise, London, United Kingdom, [14]Laboratori Nazionali Frascati-Istituto Nazionale di Fisica Nucleare (LNF-INFN), Frascati, Italy, [15]Department of Radiation Oncology, Iridium Netwerk, Antwerp, Belgium, [16]Faculty of Medicine and Health Sciences, University of Antwerp, Antwerp, Belgium, [17]Particle Therapy Research Center (PARTREC), Department of Radiation Oncology, University Medical Center Groningen, University of Groningen, Groningen, Netherlands, [18]National Physical Laboratory, Teddington, London, United Kingdom, [19]University College London, London, United Kingdom

Very High-Energy Electrons (VHEE) present a promising innovation in radiation therapy (RT), particularly for the treatment of deep-seated tumors using Ultra High Dose Rate (UHDR) within the framework of FLASH-RT. VHEE offers significant advantages, such as improved tumor targeting, reduced treatment times, and potential utilization of the FLASH effect, which may minimize normal tissue toxicity. However, the lack of an international technical standard for VHEE systems, especially for UHDR applications, remains a critical challenge. Current standards for radiation therapy equipment, such as IEC 60601-2-1 and IEC 60601-2-64, do not encompass VHEE technology. This regulatory gap underscores the need for developing a structured international standard to ensure the basic safety and essential performance of VHEE medical devices. Addressing this challenge requires overcoming complex dose delivery issues, such as the interaction of multiple fields and beam conformality and incorporating novel techniques like broad beam or pencil beam scanning. Establishing comprehensive regulatory standards is essential to ensure patient safety, consistent treatment practices, and the successful clinical integration of VHEE systems. These standards must encompass design guidelines, radiation protection protocols, and integration

with existing oncology practices. Collaborative research and development efforts are crucial to formulating evidence-based guidelines, fostering the safe and effective use of VHEE in clinical settings. By addressing these challenges, VHEE technology has the potential to revolutionize cancer therapy, particularly for deep-seated tumors, while enhancing therapeutic outcomes for patients.

KEYWORDS

VHEE radiotherapy, FLASH radiotherapy, UHDR, regulatory standards, IEC (international electrotechnical commission)

Introduction

Very High-Energy Electrons (VHEE) represent a promising advancement in radiation therapy (RT), particularly for treating deep-seated tumors using Ultra High Dose Rate (UHDR) in the context of FLASH-RT. However, the lack of an international technical standard governing VHEE systems, especially for UHDR applications, poses a significant challenge.

To design future VHEE medical devices, it is essential to consider the following current evidence [1–3]:

- UHDR VHEE is a promising and likely alternative to other UHDR External Beam RT (EBRT) modalities for treating deep-seated tumors, as electrons, even at very high energies, offer advantages in terms of easier high-current beam acceleration and potential cost reductions in clinical linear accelerator (linac) implementation.
- Optimizing VHEE dose delivery requires addressing challenges beyond conventional radiation oncology, factoring in beam temporal structure and the interaction of overlapping beams.
- Unlike single-field, lower-energy potential FLASH treatments (e.g., in the framework of Intra Operative RT (IORT) or dermatological treatments), VHEE conformality requires multiple fields, utilizing either broad beam and/or pencil beam scanning techniques.

Current standards, such as IEC 60601-2-1 [4], which covers electron RT equipment up to 50 MeV, and IEC 60601-2-64 [5], which addresses light ions, do not encompass VHEE technology. This regulatory gap underlines the necessity for a structured approach to establish an international technical standard that ensures the basic safety and essential performance of VHEE-capable medical equipment.

The development of such a standard would provide the foundation for safe clinical application of VHEE systems. Given that basic safety and essential performance are already determined for other forms of RT, including electron and proton systems, it becomes clear that the objective is not merely to address technological advancements, but to establish a clear regulatory framework. This would guide the design, manufacturing, and clinical use of VHEE systems in a way that prioritizes patient safety while maximizing therapeutic efficacy.

From a clinical perspective [6], VHEE holds great promise for improving outcomes in several challenging cancer types. Preclinical studies on FLASH-RT delivered with ultra-high high dose rate intermediate energy electrons (4–20 MeV) have shown encouraging results in multiple organs and tumor types. If confirmed with VHEE, this technology could be a game changer for multiple indications in radiation oncology.

For instance, in the treatment of multiple brain metastases or primary brain tumors such as high-grade gliomas, current methods are often limited by the radiosensitivity of healthy brain tissue [7, 8]. These tumors typically require large-volume irradiation [9], yet delivering curative doses is often impossible without damaging surrounding brain structures [10]. FLASH-RT with intermediate energy electrons showed a significant advantage over conventional dose rate RT in the brain tissues, particularly in preserving cognitive function in animal models, suggesting that neurocognitive sparing might be possible with FLASH-RT in adult [11–14] and juvenile animals [15]. If these effects are confirmed in human trials, it could open the door for dose-escalation studies aimed at enhancing local control of intracranial disease and potentially improving overall survival rates.

Locally advanced non-small cell lung cancer (NSCLC) is another area where VHEE could provide a breakthrough. In cases where surgery is not an option, RT plays a critical role, but long-term survival remains low, with only 15%–20% of patients surviving 5 years post-diagnosis [16, 17]. The challenge lies in delivering curative radiation doses while sparing healthy lung tissue, as the limiting toxicities—acute pneumonitis and late fibrosis—are directly related to the volume of lung exposed to radiation [18–20]. Preclinical data suggest that FLASH-RT delivered with intermediate energy electrons induces significantly less lung fibrosis compared to similar doses of conventional dose rate RT [21, 22]. This positions VHEE as a potentially game-changing modality for lung cancer treatment, enabling higher tumoricidal doses with reduced risks of debilitating side effects.

Recent studies in various preclinical models suggest that, compared to conventional dose-rate RT (CONV), FLASH-RT has distinct effects on circulating immune cells, the tumor immune microenvironment, cytokine production, and inflammatory responses [23–25]. Based on these findings, FLASH-RT could be an ideal complement to immunomodulating drugs, potentially enhancing the therapeutic window of current radioimmunotherapy strategies.

Vertebral metastases, which often affect patients requiring palliative RT, represent another potential application for VHEE. The main challenge is protecting the radiosensitive spinal cord while delivering optimal doses to the vertebra [26]. Exceeding the maximum tolerated dose to the spinal cord can lead to irreversible damage, making it difficult to treat metastatic tumors effectively. Although preclinical studies on the FLASH effect in spinal tissues are still needed, VHEE could allow higher therapeutic

doses to be delivered while minimizing spinal cord risk. This makes vertebral metastases an ideal candidate for early clinical trials of VHEE, given the straightforward treatment geometry and high therapeutic potential. For pancreatic cancer, where prognosis remains poor due to local recurrence and early metastasis [27], VHEE could have a profound impact. The proximity of critical organs like the duodenum and small intestine limits RT, making high tumoricidal doses difficult to deliver without severe gastrointestinal complications [28]. While stereotactic ablative RT (SABR) has been explored, complication rates remain high. Emerging data on the protective effects of FLASH-RT on intestinal tissues provide a compelling rationale for investigating VHEE in this context. If validated, this approach could allow higher doses and/or volumes to be delivered safely, without increasing the possible side-effects, and thereby potentially improving local control and survival outcomes in pancreatic cancer patients and other challenging intra-abdominal tumor locations. As we move toward clinical translation, several technological challenges must be addressed. Firstly, there is no clinically certified VHEE linear accelerator available. Moreover, the existing methods of beam delivery for high-energy electrons differ from those for low-energy electrons. Importantly, no pre-clinical study pertaining to the FLASH effect has employed VHEE. Similar to other multiple-beam VHEE applications, understanding the "volume effect" and whether time delays between field transitions could affect the FLASH effect (FE) will be critical for the safe and effective use of VHEE in the clinic.

While FLASH-RT has generated substantial interest in the radiation oncology community, the key to its widespread adoption, together with the technological development and radiobiological knowledge advancement, will be the establishment of a comprehensive international technical standard for VHEE systems. Such a standard would determine the basic safety and essential performance requirements, ensuring that VHEE technology can be implemented safely and effectively in clinical settings.

The complexities associated with VHEE dose delivery, particularly in the context of UHDR modalities, necessitate a thorough understanding of basic safety and essential performance metrics as outlined in IEC standards, specifically IEC 60601-2-1, which governs medical electrical equipment, including electron linacs up to 50 MeV.

Towards a VHEE medical device

VHEE therapy, operating in the range of 50–300 MeV, presents unique challenges that differ significantly from conventional radiation oncology techniques. Traditional methods primarily focus on optimizing conformality—the precision with which the radiation dose conforms to the shape of the tumor. In contrast, VHEE treatments require an integrated approach that considers both the temporal beam structure and the spatial overlap of multiple beams. This dual consideration is particularly critical given that UHDR VHEE modalities can deliver high doses rapidly, which may enhance tumor targeting while minimizing damage to surrounding healthy tissues [3].

TABLE 1 Physical observables for Basic Safety and Essential Performance, conventional RT and VHEE UHDR.

Basic safety and essential performance – physical observables	
Conventional	VHEE UHDR
Ionizing Radiation (X, e, p, …)	TIME (Total Irradiation time, time of pulse, etc.)T, t_p
Beam Energy E	Rates (what rates? Average? Instantaneous?)D/t
Beam Fluence φ	Dose (Total, per fraction, per pulse) D_T, D_F, D_p
Dose (Total, per fraction) D_T, D_F	Beamlet Position and Divergence X, Θ

Temporal and spatial considerations

The temporal dynamics of UHDR VHEE beams, characterized by their ultra-short pulse delivery, can influence the biological effectiveness of the treatment. Research indicates that the FLASH effect—whereby high doses delivered in very short time frames reduce damage to normal tissues while maintaining tumor control—can be particularly useful in VHEE therapies. This necessitates a comprehensive evaluation of how these time dynamics interact with spatial dose distributions, especially in multi-beam configurations.

Safety and performance metrics

Basic Safety and Essential Performance consist in properly setting (via Human Machine Interface–HMI), monitoring (using a monitoring systems in conjunction with HMI) and reporting on the HMI the physical observables involved in the dose delivery and essential for guaranteeing both safety and quality of and during the treatment. For conventional therapy machines, the observables are the type of radiation (X-rays, electrons, protons, etc.), beam energy E, beam fluence φ and dose (total or for each fraction). With UHDR, also the temporal beam structure should be included in the physical observables, and for VHEE, depending on the delivery technology, also beamlet position and/or divergence. In Table 1 the physical observables are summarized.

Additional safety requirements

According to IEC 60601-2-1, basic safety also encompasses the protection of patients and operators from electrical, mechanical, and radiation hazards. Also, for VHEE systems, this should include the following requirements:

- Radiation Leakage: The system must minimize radiation exposure to non-target areas, ensuring compliance with strict limits on leakage radiation.

- Electrical Safety: All electrical components must be designed to prevent electric shock and ensure safe operation under fault conditions.
- Mechanical Integrity: The equipment must maintain structural integrity to prevent accidents or malfunctions during operation.

Performance requirements

Essential performance refers to the equipment's ability to operate as intended without compromising safety. For conventional medical accelerators, this is defined by IEC 60976 [29]. Although much of this standard may be applicable, modifications are necessary to account for the temporal beam structure for VHEE systems. Thus, an analogous standard for VHEE systems should take into consideration the following:

- Dose Delivery Accuracy: The system must accurately deliver the prescribed dose to the target while minimizing exposure to surrounding organs at risk (OARs). This requires accurate calibration and real-time monitoring of dose delivery.
- Conformality and Homogeneity: VHEE treatments should achieve a high degree of dose conformality and homogeneity, particularly when treating complex tumor geometries. Studies have shown that VHEE beams can provide superior dose distribution compared to conventional photon beams, leading to better sparing of OARs and enhanced tumor coverage [3].
- Temporal Control: The ability to modulate the dose rate and timing of beam delivery is crucial for optimizing treatment effectiveness and minimizing side effects. This includes the implementation of advanced treatment planning systems capable of accounting for the unique temporal characteristics of VHEE beams.

Additionally, periodic tests to assure the integrity of essential performance are mandatory. The IEC 60977 standard [30] describes the type tests required for conventional linacs, but adaptations are necessary for the higher energy and unique temporal beam structure.

The integration of basic safety and essential performance metrics, as defined by IEC standards, is vital for the successful implementation of VHEE therapy. As the field of RT advances with modalities like VHEE, establishing comprehensive standards to address these unique challenges posed by these systems will be key to ensuring both patient safety and treatment efficacy. The interplay of temporal and spatial factors in VHEE dose delivery underscores the need for continued research and development to refine treatment protocols and enhance clinical outcomes.

VHEE medical device certification process

In this article, we will only discuss the essential elements of the certification process in the European context (CE marking), although with the entry in force of the EU Medical Device Regulation (MDR) 2017/745 [31], the evidence supporting this process is quite similar to that in other major economic areas (United States, Canada, United Kingdom, Japan, China, etc.).

The certification process for a Medical Device (MD) is based on two conditions that are both necessary: a "technical" verification, whose focus is essentially product safety, and clinical evaluation, which integrates clinical safety and expected clinical performance for the product.

The "technical" verification is essentially based on compliance with technical regulations applicable to the medical device, based on its intended use.

These standards are issued by standardization bodies such as IEC [32].

Dealing with medical accelerators, the reference standard is IEC 60601-1 [33], a general standard that applies to all electro-medical devices, flanked by other collateral standards such as 60601-1-2 [34] for electromagnetic compatibility, 60601-1-6 [35] for usability etc., and particular standards dependent on the type of accelerator (60601-2-8 [36] X ray in the range 10 kV up to 1 MV, 60601-2-1 [4] for electrons between 1 and 50 MeV, 60601-2-64 [5] light ions).

From this it follows that although there will be, in the near future, for VHEE accelerators a particular technical standard, to the analogous IEC 60601-2-1, which is used today for electron accelerators in the class between 1 and 50 MeV, this standard will only be the first necessary step to provide the basis for getting to clinical use of a VHEE system, but it will not be a sufficient condition.

Indeed, it will be necessary for the manufacturer of a MD for VHEE to also demonstrate clinical efficacy for target tumors and areas through a clinical evaluation in compliance with MDR. This pathway will be equally challenging.

Indeed, the clinical evaluation of a medical device, and particularly an innovative medical device such as a device for VHEE, will have to demonstrate the safety and clinical performance of the device, now inferred from various pre-clinical studies in in vitro and/or animal models, on humans.

Without a clinical evaluation according to the requirements of MDR2017/745, demonstrating that what has already been achieved in pre-clinical testing is replicable in humans in a safe and effective manner, there can be no DM on the market that can be authorized for use in humans for VHEE.

In fact, the MD regulatory landscape in Europe, prescribes that the clinical evaluation to be based on clinical data obtained by a scientifically valid method from a critical review of the currently available scientific literature on the issues of safety, performance, design characteristics and intended use of the device, and/or a critical analysis of the results of all available clinical investigations and a review of any alternative treatment options currently available for the same purpose (ref. to Art.61 of the MDR).

All this clinical data must demonstrate that the proposed device, such as the device for VHEE, is capable of providing the intended benefit (e.g., treatment of target tumors) with a benefit-to-risk ratio that is equal to or less than currently commercially available treatment options.

For clinical evaluations to be performed in humans (clinical investigations) the MDR 2017/745, in order to protect the health of the patients involved, prescribes specific authorization pathways by the National Competent Authorities (Italian Healt Ministry in Italy, BfArm in Germany etc.), and due to the very nature of the target diseases to be treated, clinical investigations can only be lengthy, since post-treatment follow-ups will necessary require important, time-consuming and clinically complex observations.

From these considerations, therefore, it is clear that it cannot be overlooked that while there is extremely interesting pre-clinical data on Flash technology today, the need to obtain clinical confirmations on humans will be a major challenge from all parties (manufacturers, scientific community) who would like to confirm the validity of this technology on humans. A challenge as necessary as of defining a particular standard to be used for verification of radiogenic safety, similar to 60601-2-1, and no less complicated, indeed.

Proposed standards for VHEE systems

Future standards for Very High Energy Electron (VHEE) therapy must focus on ensuring optimal Dose Volume Histograms (DVH) and Dose Rate Volume Histograms (DRVH) on a voxel-by-voxel basis [37], specifically tailored to the unique characteristics of each dose delivery mechanism. This approach is essential for accurately assessing treatment plans and improving patient outcomes.

Establishing thresholds

To effectively implement these standards, a double threshold must be established:

- Energy Threshold: The lower threshold should be set at 50 MeV, as this is the point beyond which IEC 60601-2-1 standards do not apply. This regulation ensures that equipment used for VHEE therapy meets stringent safety and performance criteria, which are crucial for high-energy applications.
- Average/Instantaneous Dose Rate and Dose per Pulse Threshold: The second threshold should focus on average/instantaneous dose rates and/or dose per pulse metrics. This is particularly important for UHDR modalities, where the delivery of high doses in short time frames can significantly impact treatment efficacy and normal tissue sparing.

Mathematical definitions of UHDR

Defining precise mathematical parameters for UHDR in the context of VHEE is essential, as current definitions designed for proton therapies may not directly apply. This requires the development of new models and algorithms that consider the unique interactions and physical characteristics of VHEE beams, including their energy deposition patterns and biological effects. The relationship between the quantities measured by the beam monitoring system, those verified through quality assurance, and those calculated by the treatment planning system is particularly complex.

In conventional RT, the physical observable is the delivered dose, monitored by the monitoring system (monitor chamber, electrometer, HMI). However, in the case of UHDR, it is critical to not only define the delivered dose but also account for the temporal characteristics of each beam delivery within the different radiation fields. This ensures:

- Accurate evaluation of radiobiological effects: The treatment planning system must be able to correctly assess the radiobiological impact of the dose delivery.
- Real-time monitoring of quality and conformity: During treatment, the beam monitoring system must verify that the delivery aligns with the calculated plan in terms of quality and dose conformity both spatially and temporally.

In addition, for pencil beam scanning, a new formalism must be developed to manage beamlet penumbra and scanning time, similar to the approach used for protons [38].

Temporal beam structure

There are two conditions which seem to trigger the FLASH effect: average dose rate greater than 40 Gy/s and a total irradiation time less than 0.2 s [39, 40]. Nevertheless, the temporal beam structure is quite complex, and these two parameters are not enough to fully describe it [41–43]. Given the relationship between VHEE and UHDR, it is crucial to establish standard definitions for the beam's temporal structure, along with the mathematical relationships between these parameters:

- Temporal beam structure: The temporal sequence of the beam delivery. It is identified by the entire set of Dose per pulse, Pulse duration, Time between pulses, Pulse Repetition Frequency, Number of Pulses, Irradiation Time, and Delay Time.
- Dose per pulse (D_p): Dose of a single pulse at the Equipment reference point (ERP).
- Pulse duration (t_p): Temporal width of a single pulse.
- Time between pulses (t_r): Time between two pulses in a sequence of pulses of irradiation.
- Pulse repetition frequency (PRF): Frequency of repetition of the pulses in a sequence of pulses of irradiation.
- Number of pulses (n_p): Number of pulses in a sequence of pulses of the irradiation.
- Irradiation time (t_{FL}): Temporal duration of a sequence of pulses of the irradiation.
- Delay time (t_D): Time separation between two subsequent sequences of pulses of the irradiation.
- Delivered dose (DD): Total delivered dose at ERP during t_{FL}.
- Total irradiation time (t_{IRR}): The sum of all irradiation and delay times.
- Total delivered dose (TD): Total delivered dose at ERP during t_{IRR}.
- Average Dose rate (DR): Dose rate during a sequence of pulses of the irradiation at ERP. The ratio of Delivered Dose (DD) and Irradiation Time (t_{FL}).
- Intra-pulse Dose rate (DR_p): Dose rate within the pulse at ERP. The ratio of Dose per Pulse (D_p) and Pulse Duration (t_p).
- Instantaneous Dose rate (IDR): Dose rate value at a specific moment of time within the pulse at ERP.

In general, medical linacs inherently generate pulsed beams; each irradiation event encompasses a sequence of pulses, each pulse of the duration t_p of a few microseconds. The pulses are spaced apart by a time interval denoted as t_r, which typically ranges in the order of tenths of milliseconds. The value of t_r is inversely

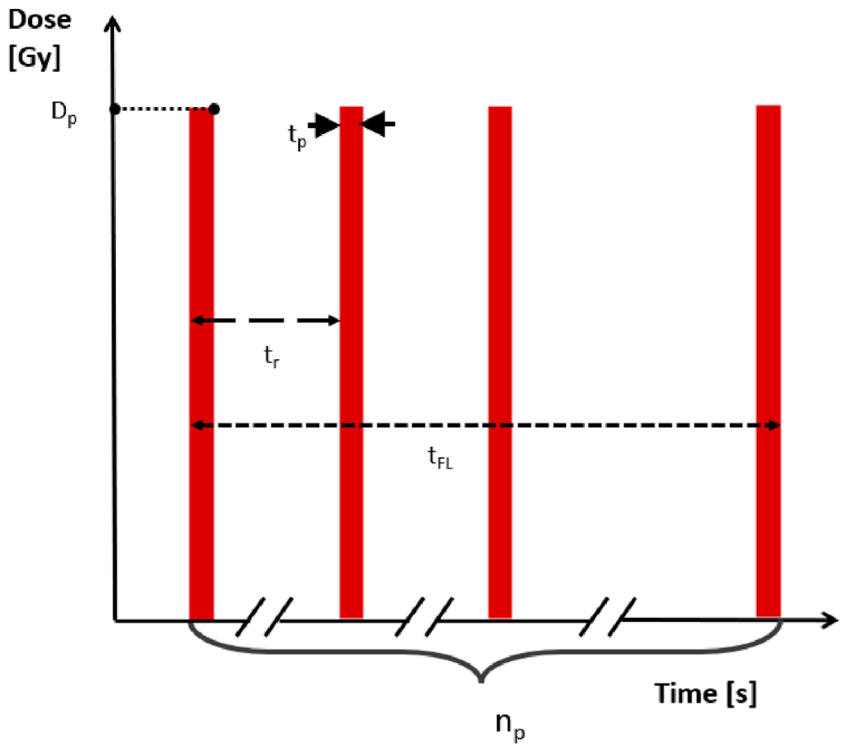

FIGURE 1
Temporal beam structure scheme of a single irradiation.

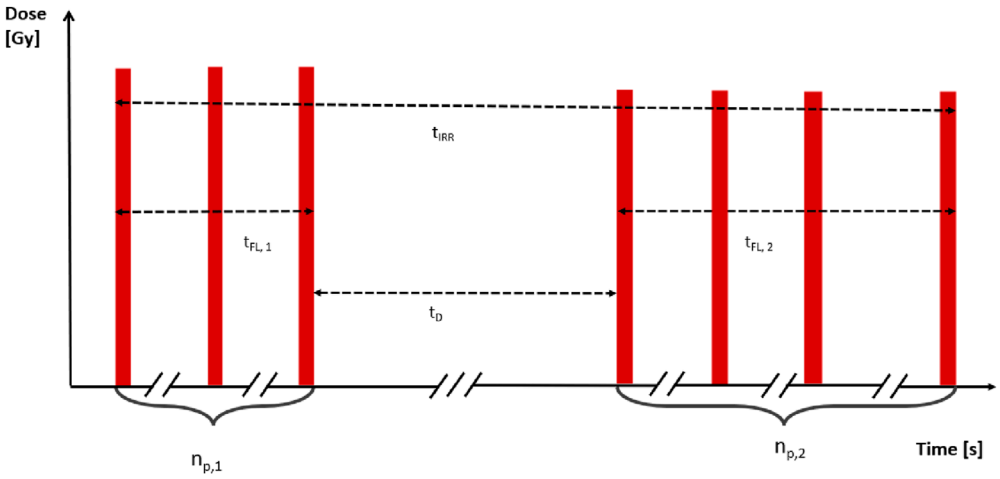

FIGURE 2
Structure of multiple irradiations separated by a delay time t_D.

related to the *Pulse Repetition Frequency* (*PRF*), determining the rate at which pulses are delivered. A representation of this general scheme is depicted in Figure 1. An irradiation can also consist in a series of multiple sub-irradiations separated by a delay time t_D. A representation of this general scheme is depicted in Figure.

Where:

– $D_p^{(n),k}$ dose of n^{th} pulse in the k^{th} irradiation at the ERP [Gy]
– t_p^k time width of a single pulse in the k^{th} irradiation [s]
– t_r^k time between two pulses in the k^{th} irradiation [s]
– PRF^k Pulse Repetition Frequency in the k^{th} irradiation [s^{-1}]
– $n_{p,k}$ Number of pulses of the k^{th} irradiation
– t_{FL}^k irradiation time of the k^{th} irradiation [s]
– t_D^k delay time, time separation between the k^{th} and $(k+1)^{th}$ irradiations [s]
– DD^k delivered dose at ERP during t_{FL}^k [Gy]

– t_{IRR} Total irradiation time [s]
– TD total delivered dose at ERP during t_{IRR} [Gy]
– DR^k Average Dose Rate during the k^{th} irradiation at ERP [Gy s^{-1}]
– $DR_p^{i,k}$ Dose rate within the i^{th} pulse during the k^{th} irradiation at ERP [Gy s^{-1}]
– $IDR^{i,k}$ Instantaneous Dose Rate within the i^{th} pulse during the k^{th} irradiation at ERP [Gy s^{-1}]

In case of a single irradiation (Figure 1), the following relations hold:

$$PRF = \frac{1}{t_r}$$

$$t_{Fl} = \frac{n_p - 1}{PRF} + t_p \cong \frac{n_p - 1}{PRF}$$

$$TD = \sum_{i=1}^{n_p} D_p^i = n_p \cdot \overline{D_p}, \ \ where \ \overline{D_p} = \frac{1}{n_p}\sum_{i=1}^{n_p} D_p^i$$

$$DR = \frac{TD}{t_{FL}} = \frac{1}{t_{FL}}\sum_{i=1}^{n_p} D_p^i \cong PRF \cdot \overline{D_p}$$

$$DR_p = \frac{D_p}{t_p}; DR_p = \frac{t_r}{t_p} DR$$

$$D_p = \int_0^{t_p} IDR(t)dt = DR_p \cdot t_p; DR_p = IDR \leftrightarrow \frac{dIDR(t)}{dt} = 0 \, \forall t \epsilon \left(0, t_p\right)$$

If the irradiation consists of multiple sub-irradiations (Figure 2), the previous equations can be easily generalized and the additional relations hold:

$$t_{IRR} = {t_{FL}}^1 + {t_D}^1 + \ldots + {t_D}^{N-1} + {t_{FL}}^N,$$

being N the total number of sub – irradiations

$$\boldsymbol{TD} = \sum_{i=1}^{N} DD^i$$

Correlation between e-beam current and its kinetic energy

To reach the fluences required in for UHDR mode, electron beam current accelerated is increased respect to the current electron accelerators. In these conditions, the power absorbed by e-beam becomes comparable with the power absorbed by the accelerating waveguide; therefore, any e-beam current variation implies a variation in the kinetic energy [44]. Let be W the power generated by the radiofrequency, it is

$$W_{TOT} = W_{LINAC} + W_{BEAM} + W_{LOSS}$$

The power absorbed by the accelerated waveguide, and thus the electric field, can be calculated as

$$W_{LINAC} = \frac{\left(\int_0^{S_{LINAC}} E_0(s) \cdot ds\right)^2 \cdot T^2}{Z_{LINAC}}$$

where $\boldsymbol{E_0}$ is the on axis electric field inside the accelerating waveguide, $\boldsymbol{S}$ its overall length, $\boldsymbol{T}$ the transit time factor and $\boldsymbol{Z_{LINAC}}$ its shunt impedance.

The power absorbed by the electron beam can be calculated as

$$W_{BEAM} = E(eV) I_{BEAM}(A)$$

In the following example, consider the case of a high current VHEE linac [45]:

- Nominal energy $E_0 = 130\,MeV$
- Beam Current $I_{BEAM} = 0.2\,A$
- Linac length $S_{LINAC} \cong 5\,m$

Assuming a shunt impedance per unit length of 100 MΩ/m, resulting in $Z_{LINAC} \sim 500\,M\Omega$, it follows that:

$$W_{LINAC} = \frac{\left(\int_0^{S_{LINAC}} E_0(s) \cdot ds\right)^2 \cdot T^2}{Z_{LINAC}} \cong \frac{130^2}{500} MW = 34\,MW$$

And

$$W_{BEAM} = E(eV) I_{BEAM}(A) \cong \left(130 \cdot 10^6 eV \cdot 0.2A\right) = 26\,MW$$

Therefore, the two terms are comparable; any variation in the beam current implies a fluctuation in beam energy as well. Hence both beam current and beam energy should be measured independently, and an additional interlock on beam energy could be considered.

Beam monitoring and temporal structure

Importance of beam monitoring

Effective beam monitoring is vital for ensuring treatment accuracy and safety. The **temporal structure** of VHEE beams, along with the potential spatial overlap of individual beamlets in pencil beam scanning delivery, must be meticulously monitored. Therefore, alternatives to conventional ionization chambers and detectors, which are susceptible to saturation at ultra-high dose rates [44] must be considered [46, 47].

Special considerations for beam monitoring

Real-time beam monitoring presents significant challenges, particularly with respect to ultra-high dose rate delivery and the beam's temporal structure of VHEE system. Conventional transmission detectors, such as gas-filled transmission ionization chambers used as golden standard in radiotherapy, encounter issues like ion recombination effect under UHDR exposures [44]. Additionally, these detectors must provide rapid feedback signals to halt the beam once the intended radiation dose has been delivered. However, ionization chambers, which are commonly used as beam monitors in clinical radiotherapy, tend to have slow timing responses with ion collections times on the order of 300 μs in 5 mm air gap separation. As a result, new beam monitoring systems may be required for safe delivery of clinical VHEE RT machines.

Currently, no ideal detector exists for monitoring UHDR VHEE beams. Nonetheless, various approaches are being explored to adapt ionization chambers for this purpose. One promising design is the multi-gap ionization chamber proposed by Giordanengo et al. [48].

This instrument features three parallel-plate ionization chambers, each with a different gap width. The charge collected by each chamber exhibits varying levels of ion recombination depending on the electrode spacing, which can be phenomenologically modeled to facilitate corrections for charge collection efficiency.

Ultra-thin silicon detectors have also been investigated as potential beam monitors due to their high sensitivity, exceptional spatial resolution, and strong radiation hardness [49]. Previous studies have demonstrated excellent linearity with dose rates for both photon [50] and proton beams [51]; however, further evaluation is needed to assess their applicability for pulsed electron beams. As such, the design and development of an optimal geometry for silicon detectors are still in progress.

Silicon carbide (SiC) detectors are gaining traction as a promising alternative for dosimetry and monitoring in UHDR beam applications [52]. These detectors offer significant advantages, including strong radiation resistance, rapid response times, high sensitivity, and stability across varying dose rates [53, 54]. However, extensive research is still required to fully harness the capabilities of this technology.

Beam current transformers (BCTs) are non-intercepting, inductive current monitors that have shown potential for real-time monitoring of UHDR electron beams [55–57]. Commonly used in research electron accelerators, they facilitate non-destructive charge measurements of individual beam pulses with high accuracy and reproducibility [58]. However, a key limitation of BCTs is their inability to provide information on beam cross-section and spatial distribution, rendering them ineffective for determining beam dimensions or flatness [29].

Recently, calorimetric methods have emerged as viable options for monitoring UHDR exposures [59]. A significant advantage of calorimetry is its dose-rate independence due to the physical nature of the phenomena. Furthermore, a transmission calorimeter can be designed with multiple sections to effectively detect beam symmetry and flatness. While further development is needed to fully exploit the capabilities of calorimetric methods, they continue to show promise as a technique for monitoring UHDR beams.

Differentiation of beam types

Additionally, it is important to distinguish between the treatment approaches for broad and pencil beams, as each modality presents unique advantages and challenges. Broad beams offer the advantage of quicker implementation since they are more closely aligned with conventional irradiation techniques and single-field UHDR irradiation. The beam monitoring requirements are less stringent, with the primary distinction from IEC 60601-2-1 being the UHDR component. Monitoring for broad beams must focus on the dose delivered, current and energy variations, temporal beam structure, and gantry rotation, which affects the delay between irradiation trains. However, broad beams face significant challenges, particularly because clinical implementation heavily relies on the tissue-sparing effect of FLASH. This is compounded by the fact that broad beams offer less conformality compared to pencil beams and result in a higher surface dose than protons or light ions. Radiation safety can also be a concern, as beam broadening (whether passive or active) and field collimation introduce additional stray radiation and neutron production due to interactions between high-energy electrons and beamline components.

On the other hand, pencil beams offer greater conformality [60], which reduces the reliance on a stronger FLASH effect and allows for more complex treatments. This approach also minimizes stray radiation through magnetic scanning techniques. However, pencil beam scanning presents a more complex formalism, similar to UHDR protons [38], and necessitates monitoring of the angular divergence of beamlets, as seen in proton therapy (IEC 60601-2–64). Furthermore, pencil beams require a more advanced beam monitoring system to track the position of individual beamlets, necessitating sophisticated technology beyond the integration systems like ACCTs (Alternating-Current Current Transformers) typically used for UHDR delivery [61]. In summary, the development of future standards for VHEE therapy should prioritize the development of comprehensive DVH and DRVH metrics that are energy-specific and dose-rate-focused. By establishing clear thresholds and enhancing beam monitoring capabilities, the treatment planning process can be significantly improved. This approach will ultimately lead to better patient outcomes through optimized dose delivery and reduced risks to healthy surrounding tissues, paving the way for the clinical implementation of VHEE therapies in radiation oncology.

Human-machine interface and radiation protection

The design of the human-machine interface (HMI) and control console for VHEE systems is crucial for ensuring both intuitive operation and robust safety protocols. As VHEE technology advances, it is essential to evaluate how these systems differ from existing standards, particularly concerning radiation protection aspects such as neutron yield and stray radiation.

Human-machine interface design

The HMI for VHEE systems must prioritize user-friendliness to facilitate seamless operation by medical personnel. Key features include:

- Intuitive Controls: The interface should provide clear visual indicators and controls that allow operators to easily adjust settings and monitor system performance in real-time.
- Safety Features: Built-in safety mechanisms, such as emergency shut-off controls and interlocks, are paramount to protect both patients and staff.

Radiation protection considerations

Differences from existing standards

Current regulations, including IEC 60601-2-1, may not adequately encompass the specific safety requirements presented by VHEE systems. Key areas that require attention include:

- Neutron Yield: VHEE systems can produce photoneutrons due to high-energy electron interactions, which poses unique

challenges in radiation protection. Studies indicate that the neutron yield from VHEE systems is comparable to that of conventional proton therapy [62]. However, it is crucial to carefully evaluate the implications for both patient and staff exposure.
- Stray Radiation: The risk of stray radiation from VHEE systems necessitates additional monitoring and shielding strategies to ensure compliance with safety standards. This is particularly important in clinical settings where multiple treatment areas may be in proximity, in addition to UHDR radiation safety requirements [63].

Need for dedicated standards

A simple amalgamation of existing standards, such as IEC 60601-2-1 and IEC 60601-2-64, is insufficient to guarantee the basic safety and essential performance of VHEE systems. Instead, a dedicated set of standards tailored to the unique characteristics of VHEE technology is required. This includes:

- Advanced Beam Monitoring Requirements: Establishing precise standards for real-time beam monitoring systems is critical, especially for UHDR VHEE beams. This includes defining the performance specifications for new detectors, tailored to the ultra-high dose rates and unique temporal structures of VHEE beams. These standards must address rapid feedback mechanisms, accuracy in dose delivery, and spatial beam monitoring to ensure treatment precision and patient safety.
- Integration with Imaging and Treatment Planning: Updates to the broader family of radiation oncology systems must encompass imaging, planning, and positioning technologies to accommodate the new VHEE requirements. This integration will enable comprehensive treatment planning that considers both therapeutic and safety aspects.
- Specific Radiation Protection Guidelines: Developing guidelines that address the unique neutron and radiation profiles of VHEE systems will enhance safety protocols and operational standards.

The design of the human-machine interface and control console for VHEE systems must balance intuitive operation with stringent safety measures. As VHEE technology progresses, it is crucial to develop dedicated standards that address the unique radiation protection challenges associated with high-energy electron therapy. By focusing on specific guidelines for neutron yield, stray radiation, and comprehensive treatment planning, the medical community can ensure the safe and effective implementation of VHEE systems in clinical practice.

Conclusion

The integration of VHEE technology into clinical practice represents a transformative advancement in the treatment of deep-seated tumors, particularly through the application of Ultra-High Dose Rate (UHDR) modalities. While the potential benefits are substantial, the absence regulatory standards poses significant challenges that must be addressed through collaborative research and development efforts.

Promising advances in treatment

VHEE technology offers several advantages for radiation oncology, particularly in the treatment of tumors located deep within the body. Key benefits include:

- Enhanced Tumor Targeting: VHEE beams can deliver high doses of radiation with precision, allowing for effective treatment of complex tumor geometries while minimizing damage to surrounding healthy tissues.
- Potential for FLASH Effect: The ultra-high dose rates associated with VHEE therapy may leverage the FLASH effect, which has been shown to reduce normal tissue toxicity while maintaining tumor control, thus improving patient outcomes.
- Reduced Treatment Times: The UHDR capabilities of VHEE systems enable rapid dose delivery, which can improve patient throughput and enhance overall treatment efficiency.

Challenges of regulatory standards

Despite the promising advances in VHEE technology, the absence of established regulatory standards poses several challenges:

- Safety and Efficacy Concerns: Without comprehensive standards, there is a risk that VHEE systems may not meet the necessary safety and performance benchmarks, potentially compromising patient safety and treatment efficacy.
- Variability in Practice: The lack of standardized protocols can lead to inconsistencies in treatment practices across different institutions, making it challenging to ensure consistent patient care and outcomes.
- Need for Collaborative Research: Addressing these challenges necessitates a collaborative effort among stakeholders - including regulatory bodies, manufacturers, and clinical practitioners -to develop evidence-based guidelines that reflect the unique characteristics of VHEE technology.

Establishing comprehensive standards

To facilitate the successful integration of VHEE systems into clinical practice, it is essential to establish a comprehensive set of standards that encompass:

- Design and Implementation Guidelines: Clear guidelines for the design and operational protocols of VHEE systems will aid manufacturers in creating equipment that meets safety and performance criteria.
- Integration with Existing Oncology Practices: Standards should also consider the integration of VHEE technology with existing imaging, planning, and treatment delivery systems to create a cohesive treatment environment.
- Radiation Protection Protocols: Specific protocols addressing the unique radiation profiles of VHEE systems, including neutron yield and stray radiation, are crucial for ensuring the safety of both patients and healthcare providers.

In conclusion, the future of radiation oncology may significantly depend on the successful integration of VHEE technology, contingent upon the development and adoption of essential regulatory standards. By addressing the current challenges through collaborative research and establishing comprehensive guidelines, the medical community can harness the full potential of VHEE systems to enhance the treatment of deep-seated tumors. This proactive approach will not only ensure patient safety and treatment efficacy but also foster innovative advancements in cancer therapy, ultimately improving patients' outcomes worldwide.

Data availability statement

The original contributions presented in the study are included in the article/supplementary material, further inquiries can be directed to the corresponding authors.

Author contributions

JP: Conceptualization, Investigation, Writing–original draft, Writing–review and editing. FD: Conceptualization, Writing–original draft, Writing–review and editing. AC: Writing–review and editing. MC: Writing–review and editing. AD: Writing–review and editing. MD: Writing–review and editing. GF: Writing–review and editing. LG: Writing–review and editing. LM: Writing–review and editing. GM: Writing–review and editing. PM-G: Writing–review and editing. FP: Writing–review and editing. MP: Writing–original draft, Writing–review and editing. VP: Writing–review and editing. SP: Writing–review and editing. PP: Writing–review and editing. FR: Writing–review and editing. ASa: Writing–review and editing. ASu: Writing–original draft, Writing–review and editing. AV: Writing–review and editing. GF: Conceptualization, Investigation, Writing–original draft, Writing–review and editing.

Funding

The author(s) declare that financial support was received for the research, authorship, and/or publication of this article. We thank Fondazione Pisa for funding CPFR with the grant "prog. n. 134/2021." The research is also partially supported by INFN CSN5 funded project "FRIDA." The research has received funding from the European Union—NextGenerationEU through the Italian Ministry of University and Research under PNRR—M4C2-I1.3 Project PE_00000019 "HEAL ITALIA." This work was supported by United Kingdom Research and Innovation (grant MR/Y018761/1). This work was funded by Piano Nazionale di Ripresa e Resilienza (PNRR), Missione 4, Componente 2, Ecosistemi dell'Innovazione–Tuscany Health Ecosystem (THE), Spoke 1 "Advanced Radiotherapies and Diagnostics in Oncology"—CUP I53C22000780001.

Conflict of interest

Authors MD, LG, and GF were employed by Sordina IORT Technologies S.p.A. Author MP was employed by Maytal International Ltd. – Global Med Dev Expertise.

The remaining authors declare that the research was conducted in the absence of any commercial or financial relationships that could be construed as a potential conflict of interest.

Generative AI statement

The author(s) declare that no Generative AI was used in the creation of this manuscript.

Publisher's note

References

1. Schüler E, Eriksson K, Hynning E, Hancock SL, Hiniker SM, Bazalova-Carter M, et al. Very high-energy electron (VHEE) beams in radiation therapy; Treatment plan comparison between VHEE, VMAT, and PPBS. *Med Phys* (2017) 44(6):2544–55. doi:10.1002/mp.12233

2. Bazalova-Carter M, Qu B, Palma B, Hårdemark B, Hynning E, Jensen C, et al. Treatment planning for radiotherapy with very high-energy electron beams and comparison of VHEE and VMAT plans. *Med Phys* (2015) 42(5):2615–25. doi:10.1118/1.4918923

3. Muscato A, Arsini L, Battistoni G, Campana L, Carlotti D, De Felice F, et al. Treatment planning of intracranial lesions with VHEE: comparing conventional and FLASH irradiation potential with state-of-the-art photon and proton radiotherapy. *Front Phys* (2023) 11:1185598. doi:10.3389/fphy.2023.1185598

4. Webstore. IEC 60601-2-1:2020, Medical electrical equipment - Part 2-1: particular requirements for the basic safety and essential performance of electron accelerators in the range 1 MeV to 50 MeV (2020) Available from: https://webstore.iec.ch/publication/31388. Accessed on 15th of October 2024.

5. Webstore. IEC 60601-2-64:2014. Particular requirements for the basic safety and essential performance of light ion beam medical electrical equipment (2014) Available from: https://webstore.iec.ch/en/publication/2680. Accessed on 15th of October 2024.

6. Ursino S, Gadducci G, Giannini N, Gonnelli A, Fuentes T, Di Martino F, et al. New insights on clinical perspectives of FLASH radiotherapy: from low-to very high electron energy. *Front Oncol* (2023) 13:1254601. doi:10.3389/fonc.2023.1254601

7. Achrol AS, Rennert RC, Anders C, Soffietti R, Ahluwalia MS, Nayak L, et al. Brain metastases. *Nat Rev Dis Primers* (2019) 5(1):5. doi:10.1038/s41572-018-0055-y

8. Rodríguez-Camacho A, Flores Vazquez JG, Moscardini Martelli J, Torres-Rio JA, Olmos-Guzman A, Ortiz-Arce CS, et al. Glioblastoma treatment: state-of-the-art and future perspectives. *Int J Mol Sci* (2022) 23:7207. doi:10.3390/ijms23137207

9. Kruser TJ, Bosch WR, Badiyan SN, Bovi JA, Ghia AJ, Kim MM, et al. NRG brain tumor specialists consensus guidelines for glioblastoma contouring. *J Neurooncol* (2019) 143(1):157–66. doi:10.1007/s11060-019-03152-9

10. Zhong X, Huang B, Feng J, Yang W, Liu H. Delayed leukoencephalopathy of non-small cell lung cancer patients with brain metastases underwent whole brain radiation therapy. *J Neurooncol* (2015) 125(1):177–81. doi:10.1007/s11060-015-1888-9

11. Montay-Gruel P, Petersson K, Jaccard M, Boivin G, Germond JF, Petit B, et al. Irradiation in a flash: unique sparing of memory in mice after whole brain irradiation with dose rates above 100 Gy/s. *Radiother Oncol* (2017) 124(3):365–9. doi:10.1016/j.radonc.2017.05.003

12. Montay-Gruel P, (2019) Long-term neurocognitive benefits of FLASH radiotherapy driven by reduced reactive oxygen species. *Proc Natl Acad Sci U S A* 116, 10943–51. doi:10.1073/pnas.1901777116

13. Montay-Gruel P, Acharya MM, Gonçalves Jorge P, Petit B, Petridis IG, Fuchs P, et al. Hypofractionated FLASH-RT as an effective treatment against glioblastoma that reduces neurocognitive side effects in mice. *Clin Cancer Res* (2021) 27(3):775–84. doi:10.1158/1078-0432.ccr-20-0894

14. Allen BD, Alaghband Y, Kramár EA, Ru N, Petit B, Grilj V, et al. Elucidating the neurological mechanism of the FLASH effect in juvenile mice exposed to hypofractionated radiotherapy. *Neuro-oncology* (2023) 25(5):927–39. doi:10.1093/neuonc/noac248

15. Alaghband Y, Allen BD, Kramár EA, Zhang R, Drayson OG, Ru N, et al. Uncovering the protective neurologic mechanisms of hypofractionated FLASH radiotherapy. *Cancer Res Commun* (2023) 3(4):725–37. doi:10.1158/2767-9764.crc-23-0117

16. Casal-Mouriño A, Ruano-Ravina A, González ML, Rodríguez-Martínez A, Osorio AG, Lema LV, et al. Epidemiology of stage III lung cancer: frequency, diagnostic characteristics, and survival. *Transl Lung Cancer Res* (2021) 10(1):506–18. doi:10.21037/tlcr.2020.03.40

17. Nichols L, Saunders R, Knollmann FD. Causes of death of patients with lung cancer. *Arch Pathol Lab Med* (2012) 136(12):1552–7. doi:10.5858/arpa.2011-0521-OA

18. Käsmann L, Dietrich A, Staab-Weijnitz CA, Manapov F, Behr J, Rimner A, et al. Radiation-induced lung toxicity - cellular and molecular mechanisms of pathogenesis, management, and literature review. *Radiat Oncol* (2020) 15(1):214. doi:10.1186/s13014-020-01654-9

19. Meng J, Li Y, Wan C, Sun Y, Dai X, Huang J, et al. Targeting senescence-like fibroblasts radiosensitizes non-small cell lung cancer and reduces radiation-induced pulmonary fibrosis. *JCI Insight* (2021) 6(23):e146334. doi:10.1172/jci.insight.146334

20. Arroyo-Hernández M, Maldonado F, Ruiz FL, Muñoz-Montaño WM, Nuñez-Baez M, Arrieta O. Radiation-induced lung injury: current evidence. *BMC Pulm Med* (2021) 21:9. doi:10.1186/s12890-020-01376-4

21. Favaudon V, Caplier L, Monceau V, Pouzoulet F, Sayarath M, Fouillade C, et al. Ultrahigh dose-rate FLASH irradiation increases the differential response between normal and tumor tissue in mice. *Sci translational Med* (2014) 6.245. doi:10.1126/scitranslmed.3008973

22. Fouillade C, Curras-Alonso S, Giuranno L, Quelennec E, Heinrich S, Bonnet-Boissinot S, et al. FLASH irradiation spares lung progenitor cells and limits the incidence of radio-induced senescence. *Clin Cancer Res* (2020) 26:1497–506. doi:10.1158/1078-0432.ccr-19-1440

23. Montay-Gruel P, Acharya MM, Petersson K, Alikhani L, Yakkala C, Allen BD, et al. Long-term neurocognitive benefits of FLASH radiotherapy driven by reduced reactive oxygen species. *Proc Natl Acad Sci U S A* (2019) 116(22):10943–51. doi:10.1073/pnas.1901777116

24. Buonanno M, Grilj V, Brenner DJ. Biological effects in normal cells exposed to FLASH dose rate protons. *Radiother Oncol* (2019) 139:51–5. doi:10.1016/j.radonc.2019.02.009

25. Montay-Gruel P, Markarian M, Allen BD, Baddour JD, Giedzinski E, Jorge PG, et al. Ultra-high-dose-rate FLASH irradiation limits reactive gliosis in the brain. *Radiat Res* (2020) 194(6):636–45. doi:10.1667/rade-20-00067.1

26. Peyraga G, Ducassou A, Arnaud F-X, Lizée T, Pouédras J, Moyal E. Radiothérapie et toxicité médullaire: actualités et perspectives [Radiotherapy and spinal toxicity: News and perspectives]. *Cancer Radiother* (2021) 25(1):55–61. doi:10.1016/j.canrad.2020.05.017

27. Park W, Chawla A, Eileen M. O'Reilly pancreatic cancer: a review. *JAMA* (2021) 326(9):851–62. doi:10.1001/jama.2021.13027

28. Goldsmith C, Plowman PN, Melanie M, Green MM, Dale RG, Price PM, et al. Stereotactic ablative radiotherapy (SABR) as primary, adjuvant, consolidation and re-treatment option in pancreatic cancer: scope for dose escalation and lessons for toxicity. *Radiat Oncol* (2018) 19 13(1):204. doi:10.1186/s13014-018-1138-3

29. Webstore. Medical electrical equipment - medical electron accelerators - functional performance characteristics (2007) Available from: https://webstore.iec.ch/en/publication/4088. Accessed on 15th of October 2024.

30. Webstore. IEC TR 60977:2008. Medical electrical equipment - medical electron accelerators - guidelines for functional performance characteristics (2008) Available from: https://webstore.iec.ch/en/publication/4089. Accessed on 15th of October 2024.

31. EU MDR: REGULATION (EU) 2017/745 of the EUROPEAN parliament and of the council of 5 april 2017 on medical devices, amending directive 2001/83/EC, regulation (ec) No 178/2002 and regulation (EC) No 1223/2009 and repealing council directives 90/385/EEC and 93/42/EEC

32. Available from: https://www.iec.ch/homepage. Accessed on 15th of October 2024.

33. Webstore. IEC 60601-1 Consolidated version, Medical electrical equipment - Part 1: general requirements for basic safety and essential performance. Available from: https://webstore.iec.ch/en/publication/67497. Accessed on 15th of October 2024.

34. Webstore. IEC 60601-1-2 Consolidated version, Medical electrical equipment - Part 1-2: general requirements for basic safety and essential performance - collateral Standard: electromagnetic disturbances - requirements and tests. Available from: https://webstore.iec.ch/en/publication/67554. Accessed on 15th of October 2024.

35. Webstore. *IEC 60601-1-6 Consolidated version, Medical electrical equipment - Part 1-6: general requirements for basic safety and essential performance - collateral standard*. Usability. Available from: https://webstore.iec.ch/en/publication/67381. Accessed on 15th of October 2024.

36. Webstore. IEC 60601-2-8 Consolidated version, Medical electrical equipment - Part 2-8: particular requirements forthe basic safety and essential performance of therapeutic X-ray equipment operating in the range 10 kV to 1 MV. Available from: https://webstore.iec.ch/en/publication/23416. Accessed on 15th of October 2024.

37. Folkerts MM, Abel E, Busold S, Perez JR, Krishnamurthi V, Ling CC. A framework for defining FLASH dose rate for pencil beam scanning. *Med Phys* (2020) 47(12):6396–404. doi:10.1002/mp.14456

38. Schwarz M, Traneus E, Safai S, Kolano A, van de Water S. Treatment planning for Flash radiotherapy: general aspects and applications to proton beams. *Med Phys* (2022) 49(4):2861–74. doi:10.1002/mp.15579

39. Limoli CL, Kramár EA, Almeida A, Petit B, Grilj V, Baulch JE, et al. The sparing effect of FLASH-RT on synaptic plasticity is maintained in mice with standard fractionation. *Radiother Oncol* (2023) 2023:109767. doi:10.1016/j.radonc.2023.109767

40. Liljedahl E, Konradsson E, Gustafsson E, Jonsson KF, Olofsson JK, Ceberg C, et al. Long-term anti-tumor effects following both conventional radiotherapy and FLASH in fully immunocompetent animals with glioblastoma. *Scientific Rep* (2022) 12(1):12285. doi:10.1038/s41598-022-16612-6

41. Garibaldi C, Beddar S, Bizzocchi N, Böhlen TT, Iliaskou C, Moeckli R, et al. Minimum and optimal requirements for a safe clinical implementation of ultra-high dose rate radiotherapy: a focus on patient's safety and radiation protection. *Radiother Oncol* (2024) 196:110291. doi:10.1016/j.radonc.2024.110291

42. McGarrigle JM, Long KR, Prezado Y. The FLASH effect—an evaluation of preclinical studies of ultra-high dose rate radiotherapy. *Front Oncol* (2024) 14:1340190. doi:10.3389/fonc.2024.1340190

43. Vozenin M-C, Montay-Gruel P, Limoli C, Germond JF. All irradiations that are ultra-high dose rate may not be FLASH: the critical importance of beam parameter characterization and *in vivo* validation of the FLASH effect. *Radiat Res* (2020) 194(6):571–2. doi:10.1667/rade-20-00141.1

44. Di Martino F, Barca P, Barone S, Bortoli E, Borgheresi R, De Stefano S, et al. FLASH radiotherapy with electrons: issues related to the production, monitoring, and dosimetric characterization of the beam. *Front Phys* (2020) 8:570697. doi:10.3389/fphy.2020.570697

45. Faillace L, Alesini D, Bisogni G, Bosco F, Carillo M, Cirrone P, et al. Perspectives in linear accelerator for FLASH VHEE: study of a compact C-band system. *Physica Med* (2022) 104:149–59. doi:10.1016/j.ejmp.2022.10.018

46. Felici G, Barca P, Barone S, Bortoli E, Borgheresi R, De Stefano S, et al. Transforming an IORT linac into a FLASH research machine: procedure and dosimetric characterization. *Front Phys* (2020) 8:374. doi:10.3389/fphy.2020.00374

47. Romano F, Bailat C, Jorge PG, Lerch MLF, Darafsheh A. Ultra-high dose rate dosimetry: challenges and opportunities for FLASH radiation therapy. *Med Phys* (2022) 49(7):4912–32. doi:10.1002/mp.15649

48. Giordanengo S, Guarachi LF, Braccini S, Cirrone GAP, Donetti M, Fausti F, et al. Fluence beam monitor for high-intensity particle beams based on a multi-gap ionization chamber and a method for ion recombination correction. *Appl Sci* (2022) 12(23):12160. doi:10.3390/app122312160

49. Medina E, Ferro A, Abujami M, Camperi A, Centis Vignali M, Data E, et al. First experimental validation of silicon-based sensors for monitoring ultra-high dose rate electron beams. *Front Phys* (2024) 12:1258832. doi:10.3389/fphy.2024.1258832

50. Vignati A, Giordanengo S, Fausti F, Martì Villarreal OA, Mas Milian F, Mazza G, et al. Beam monitors for tomorrow: the challenges of electron and photon FLASH RT. *Front Phys* (2020) 8:375. doi:10.3389/fphy.2020.00375

51. Wyrsch N, Antognini L, Ballif C, Braccini S, Casolaro P, Dunand S, et al. Amorphous silicon detectors for proton beam monitoring in FLASH radiotherapy. *Radiat Meas* (2024) 177:107230. arXiv preprint arXiv:2401.14300. doi:10.1016/j.radmeas.2024.107230

52. Okpuwe C, Amato A, D'Amico I, De Liso V, De Napoli M, Di Martino F, et al. Silicon carbide detectors for dosimetry and monitoring of ultra-high dose rate beams. *J Instrumentation* (2024) 19(03):C03064. doi:10.1088/1748-0221/19/03/c03064

53. De Napoli M. SiC detectors: a review on the use of silicon carbide as radiation detection material. *Front Phys* (2022) 10:898833. doi:10.3389/fphy.2022.898833

54. Romano F, Milluzzo G, Di Martino F, D'Oca MC, Felici G, Galante F, et al. First characterization of novel silicon carbide detectors with ultra-high dose rate electron beams for FLASH radiotherapy. *Appl Sci* (2023) 13:2986. doi:10.3390/app13052986

55. Gonçalves Jorge P, Grilj V, Bourhis J, Vozenin C-M, Germond JF, Bochud F, et al. Technical note: validation of an ultrahigh dose rate pulsed electron beam monitoring system using a current transformer for FLASH preclinical studies. *Med Phys* (2022) 49:1831–8. doi:10.1002/mp.15474

56. Oesterle R, Gonçalves Jorge P, Grilj V, Bourhis J, Vozenin M-C, Germond J-F, et al. Implementation and validation of a beam current transformer on a medical pulsed electron beam LINAC for FLASH-RT beam monitoring. *J Appl Clin Med Phys* (2021) 22:165–71. doi:10.1002/acm2.13433

57. Vojnovic B, Tullis IDC, Newman RG, Petersson K. Monitoring beam charge during FLASH irradiations. *Front Phys* (2023) 11:1185237. doi:10.3389/fphy.2023.1185237

58. Schüller A, Illemann J, Renner F, Makowski C, Kapsch RP. Traceable charge measurement of the pulses of a 27 MeV electron beam from a linear accelerator. *J Instrumentation* (2017) 12(03):P03003. doi:10.1088/1748-0221/12/03/p03003

59. Flynn SF, Lee ND, Thomas RAS, Palmans H, Duane S. Transmission calorimeter for measuring dose of radiation (2022) Available from: https://worldwide.espacenet.com/patent/search/family/082324167/publication/WO2023227909A1?q=WO2023227909. Accessed on 15th of October 2024.

60. Fischer J, Whitmore L, Desrosiers C, Sheehy S, Bazalova-Carter M. Very high-energy electrons as radiotherapy opportunity. *The Eur Phys J Plus* (2024) 139(8):728. doi:10.1140/epjp/s13360-024-05455-x

61. Di Martino F, Del Sarto D, Bass G, Capaccioli S, Celentano M, Coves D, et al. Architecture, flexibility and performance of a special electron linac dedicated to Flash radiotherapy research: electronFlash with a triode gun of the centro pisano flash radiotherapy (CPFR). *Front Phys* (2023) 11:1268310. doi:10.3389/fphy.2023.1268310

62. Masilela TAM, Delorme R, Prezado Y. Dosimetry and radioprotection evaluations of very high energy electron beams. *Scientific Rep* (2021) 11(1):20184. doi:10.1038/s41598-021-99645-7

63. Præstegaard LH. Radiation safety of ultra-high dose rate electron accelerators for FLASH radiotherapy. *Med Phys* (2024) 51:6206–19. doi:10.1002/mp.17245

frontiers | Frontiers in Physics

TYPE Original Research
PUBLISHED 15 January 2025
DOI 10.3389/fphy.2024.1496272

OPEN ACCESS

EDITED BY
Xun Jia,
Johns Hopkins Medicine, United States

REVIEWED BY
Yan-Fei Li,
Xi'an Jiaotong University, China
Yujie Chi,
University of Texas at Arlington, United States

*CORRESPONDENCE
Jiaru Shi,
shij@tsinghua.edu.cn

RECEIVED 14 September 2024
ACCEPTED 27 December 2024
PUBLISHED 15 January 2025

CITATION
Li H, Zha H, Lin X, Gao Q, Liu F, Shi J and Chen H (2025) Design of a 100-MeV compact VHEE beam line in Tsinghua University. *Front. Phys.* 12:1496272. doi: 10.3389/fphy.2024.1496272

Design of a 100-MeV compact VHEE beam line in Tsinghua University

Hongyu Li[1,2], Hao Zha[1,2], Xiancai Lin[1,2], Qiang Gao[1,2], Focheng Liu[1,2], Jiaru Shi[1,2]* and Huaibi Chen[1,2]

[1]Department of Engineering Physics, Tsinghua University, Beijing, China, [2]Key Laboratory of Particle and Radiation Imaging of Ministry of Education, Tsinghua University, Beijing, China

A 100-MeV Compact Electron Accelerator design has been proposed for Very High Energy Electron (VHEE) radiotherapy research at Tsinghua University. The microwave source for this system is a 50 MW X-band klystron, paired with a pulse compressor featuring a correction cavity chain. During high-power test, the system achieved a flat-top power gain three times the input. The acceleration system consists of three main components: a backward traveling-wave buncher that bunches and accelerates electrons from a thermionic cathode gun to 8 MeV, followed by two 72-cell X-band constant-gradient traveling-wave accelerating structures, which further increase the electron energy to 100 MeV with a gradient of 80 MV/m. The total length of the system is 1.8 m, and its design is detailed in this paper.

KEYWORDS

VHEE, FLASH radiotherapy, linac accelerator, X-band high gradient, beam line

1 Introduction

Radiotherapy is a globally recognized and effective cancer treatment method [1–6]. In 2014, scientists conducted experiments on lung cancer cells in mice using electron beams, observing the FLASH effect *in vivo* [7]. When treating cancer cells with an ultra high dose rate (UHDR) beam, radiotherapy was as efficient as conventional irradiation for tumor inhibition, while dramatically less damaging to healthy tissue. Since then, FLASH radiotherapy has attracted significant interest in the field [8, 9]. Substantial advancements have been made in radiotherapy facilities utilizing various particles, such as photons [10, 11], electrons [12–15], and protons [16–18]. Among these, very high-energy electrons (VHEE) have emerged as a promising candidate for treating deep-seated tumors in the near future.

VHEE radiotherapy, first proposed in 2000 [19], uses electrons with energies ranging from 50 to 250 MeV [20] for tumor treatment. Compared to conventional electron beam radiotherapy, VHEE provides greater penetration depth and a smaller penumbra [21]. Additionally, in comparison to photon therapy, VHEE can reduce skin dosage and can be integrated with Rapid Intensity Modulated Radiation Therapy (Rapid IMRT) to shorten treatment time. While the dose distribution characteristics of protons and heavy ions, which exhibit a Bragg peak, are advantageous for sparing normal tissues, they present challenges when treating organs with significant tissue density inhomogeneities or substantial movement. In contrast, VHEE's relatively uniform dose distribution near the maximum dose is less impacted by tissue inhomogeneity, making it more suitable

TABLE 1 Comparison of the parameters of different VHEE facilities.

Beam parameters	CLEAR	CLARA	AWA	ARES	Tsinghua university
Energy (MeV)	60–220	50 (250)[a]	6–65	50–160	100
Bunch charge (nC/shot)	0.01–1.5	0.02–0.25	0.1–100	10^{-6}-0.28	~ 0.01 [*2000][b]
Bunch length rms (ps)	0.1–10	0.3–5	0.03–10	0.02	~10
Repetition rate (Hz)	0.833–10	10 (100)[a]	0.5–10	1–50	40
Normalized emittance(μm)	3–20	7.5 (<5)[a]	0.5–240	~0.07π	~50

[a]The values in parentheses represent the target values for facility upgrades.
[b]Tsinghua University used multi-bunch acceleration. There are ~2000 bunches in a input microwave pulse.

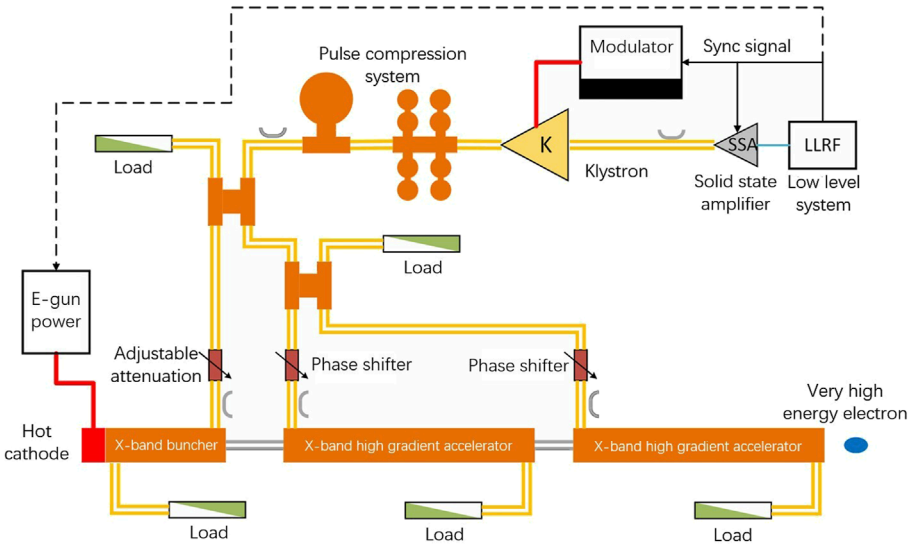

FIGURE 1
The X-band compact VHEE structure layout.

for treating organs with uneven density, such as the lungs, intestines, and cervix [22]. Furthermore, VHEE facilities are more cost-effective compared to proton and heavy ion radiotherapy systems.

In recent years, numerous VHEE experiments have been conducted on various linear accelerator platforms [23–25]. Current operational facilities include CLEAR [26], CLARA [16], AWA [27], ARES [28, 29] and so on. However, in order to achieve high beam quality, most of these facilities have a large footprint, which makes it difficult to VHEE FLASH's clinical translation. The research team at Tsinghua University has proposed a compact VHEE facility based on advanced X-band high-gradient technology, which could produce 100 MeV VHEE within 2 m length. By using a high-voltage direct current (DC) thermionic electron gun, the available charge for UHDR operation is increased at the expense of fundamentally limiting the quality of the electron beam. Table 1 shows the comparison of the parameters of these VHEE facilities.

We employs a commercial klystron with a power output of 50 MW. To minimize the number of klystrons required, a pulse compressor is used to amplify the klystron's output, reducing both costs and the physical footprint of the installation. The electron source is a hot cathode electron gun, and a buncher focuses the emitted electrons. These are then accelerated by a high-gradient accelerator, enabling a compact design while achieving high-energy output. The VHEE beam line is designed to deliver electrons at 40 Hz, with 24 nC per pulse, generating a dose rate of 40 Gy/s over a 6×6 cm^2 field, making it suitable for FLASH radiotherapy research. This article will present the layout and preliminary optimization of the beam line and its components.

TABLE 2 Parameters of the hot cathode electron gun.

Parameters	Value	Parameters	Value
Conductivity	0.347 μP	Geometric emittance	32.7 mm • mrad
Voltage	12.5 kV	Normalized emittance	7.26 mm • mrad
Beam waist radius	0.46 mm		

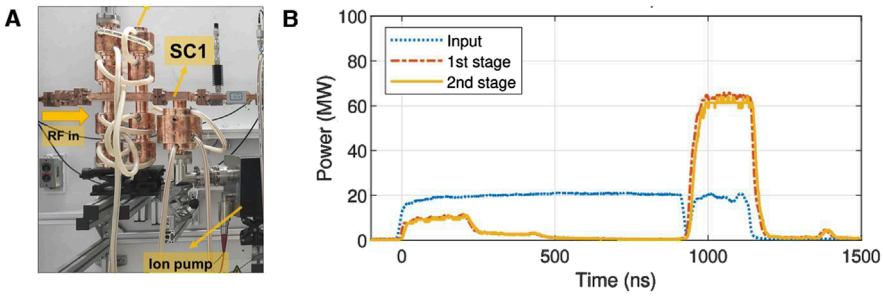

FIGURE 2
The high-power test of the pulse compression system. **(A)** Photograph of the pulse compression system after installation. **(B)** Waveforms of the pulse compressor in high-power test when the second-stage storage cavity was detuned.

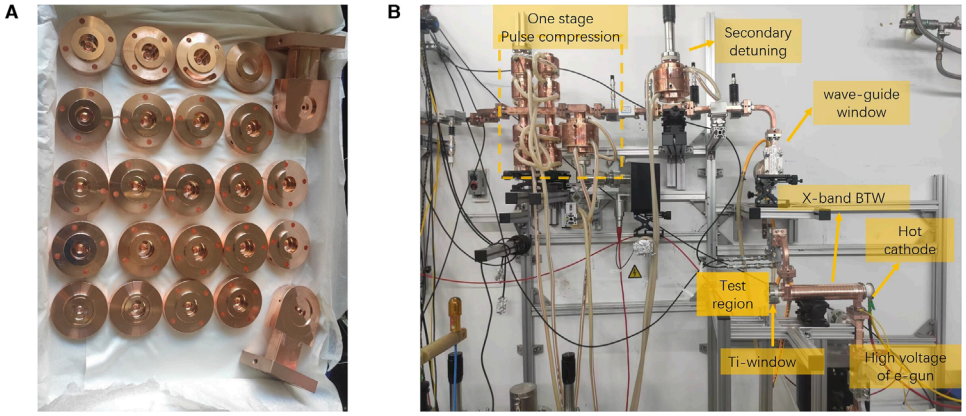

FIGURE 3
Processing and testing of X-band backward traveling wave buncher. **(A)** The processed cells and couplers. **(B)** The high-power beam test of the buncher.

2 Structure layout

Figure 1 presents the schematic diagram of the X-band compact VHEE radiotherapy structure. The power source for the system is a commercial X-band klystron with a 50 MW output, driven by a high-voltage modulator. The microwave signal, originating from the low-level system, is first amplified by a solid-state amplifier before being fed into the klystron.

After amplification, the klystron's microwave output is compressed by a pulse compression system and then distributed to the bunching section and two main accelerating sections via the power transmission system. The transmission system employs two directional couplers as power dividers, which, along with loads, minimize interference between the branches. An adjustable power attenuator is placed at the entrance of the bunching section to optimize electron dynamics.

Ensuring that the electric field phase in the main accelerating sections aligns with the phase of the electrons exiting the bunching section is critical. To achieve this, a phase shifter is installed at the entrance of each accelerating section. The X-band high-power phase shifter has an all-metal structure and consists of a dual-polarization mode coupler and a movable piston. Stainless steel loads are positioned at the exits of both the bunching section and the main accelerating sections to absorb the output power from the accelerating tube.

The electron source for the device is a hot cathode electron gun, with detailed parameters provided in Table 2. The low-level system supplies a synchronization signal to the electron gun, ensuring that the electron pulse is synchronized with the microwave pulse output from the klystron.

The following sections will present the beam line's components, including the power compression system, the backward traveling-wave buncher (BTW), and the constant-gradient traveling-wave accelerator, as well as its preliminary optimization.

3 Components of the beam line

In this section, we will introduce the components of the VHEE beam line, which have been previously studied, including the power compression system, the backward traveling-wave buncher (BTW), and the constant-gradient traveling wave accelerator. These components are critical for achieving the high-gradient acceleration necessary for VHEE radiotherapy applications.

TABLE 3 Comparison of designed and measured values of the BTW structure.

Parameters	Design value	Measured result
Input power [MW]	4.6	5.0
Accelerating gradient [MV/m]	43.6	45.0
Surface eletric field [MV/m]	204	
Surface magnetic field [kA/m]	400	
S_c[MW/mm^2]	4	
Breakdown rate [/pulse]		2×10^{-4}
Capture rate	32%	25%
Current [mA]	155	108
Energy [MeV]	7.8	8.0
r_x(rms) [mm]	0.69	1
r_y(rms) [mm]	0.69	0.95

3.1 The pulse compression system

The proposed VHEE radiotherapy structure comprises a power source section and an accelerator section. The power source section occupies a larger area and incurs higher costs. Calculations indicate that using only a 50 MW klystron would require approximately 4 m to accelerate electrons to 100 MeV, while employing multiple klystrons would significantly increase both the spacial requirements and costs. To address this, we have opted to use a pulse compressor capable of achieving a flat-top power gain of three times [30]. This approach increases the gradient of the acceleration structure, allowing the VHEE radiotherapy system to remain compact while utilizing only one klystron.

Figure 2 illustrates the condition and results of the high-power test for the two-stage pulse compressor when it operates at the first-stage. The X-band amplitude modulation (AM) cavity chain features a novel design, where resonant cavities are connected at both ends of the dual-polarization mode coupler. This design reduces both transmission loss and the length of the AM cavity chain to half of its original size. The length of the first-stage compression part of the X-band pulse compression system is only 0.4 m. In high-power tests, a flat-top power gain of three times was achieved, with the amplitude and phase of the flat-top demonstrating good stability, making multi-bunch acceleration feasible. Thus, the first-stage compression section is well-suited for use in the compact VHEE radiotherapy structure.

3.2 The backward traveling-wave buncher

For the VHEE radiotherapy facility, we developed a prototype of an X-band Backward Traveling Wave (BTW) accelerating structure intended to bunch a DC electron beam and accelerate it to approximately 8 MeV [31]. After optimizing the cavity shape, field distribution, and beam dynamics, the BTW structure was simulated and designed using CST Studio Suite [32]. The simulation results demonstrated a field distribution that closely matches that of the constructed prototype. Additionally, the time-domain circuit model was utilized to analyze the transient beam parameters of the buncher during its unsteady state.

The BTW structure was fabricated at Tsinghua University and underwent high-power test at the Tsinghua X-band High-power Test Stand, as illustrated in Figure 3. The structure was powered by 5 MW microwave pulses from the pulse compressor, operating in one-stage mode (with the second compressor detuned), achieving an average gradient of 45 MV/m. The electron beam was successfully accelerated to 8 MeV, with a pulse current of 108 mA. A comparison between the designed and measured values of the BTW structure is presented in Table 3, where the measured capture rate was calculated by dividing the target current by the gun current. Although some beam parameters did not fully meet the design specifications, the test preliminarily verified the high gradient and large current capabilities of the BTW structure. Future work will focus on addressing fabrication errors in the output coupler to ensure the designed capture rate, and optimizing the magnetic coupling holes between adjacent cells with smooth rounding to improve high-gradient performance.

3.3 The traveling wave accelerator

A constant-impedance traveling-wave structure, consisting of 72 cells operating in the $2\pi/3$ mode, named TTX-XC72 [33], was designed and fabricated for the Very Compact Inverse Compton Scattering Gamma-ray Source (VIGAS) program at Tsinghua University [34]. Although XC72 could reach almost 80 MV/m,its breakdown rate (BDR) is about 10^{-3}/pulse m, which is slightly higher than we required, mostly because the field in the first cell is too high. Therefore, we decided to switch to the constant gradient (CG) approach. Recently, the CG prototype XT72 was developed [35]. This structure is also suitable for use in the main acceleration section of the compact VHEE radiotherapy facility.

The XT72 structure comprises 70 accelerating cavities along with input and output couplers. The fabricated cells are shown in Figure 4. When an 80 MW pulse with top drop from the pulse compressor is introduced into the structure, it achieves an average acceleration gradient of 80 MV/m. With a total length of 0.63 m, the structure provides an energy gain of 50 MeV for electrons. The XT72 prototype underwent high-power test, demonstrating better performance compared to the XC72 structure, with an achieved gradient of 81.0 MV/m *versus* 78.7 MV/m, and a lower breakdown rate (BDR) of 1.5×10^{-4}. Additionally, XT72 exhibited a lower maximum surface electric field and reduced temperature rise from pulse heating. Table 4 shows the parameters of XT72.

4 Preliminary optimization of the beam line

After the technology of each component was verified, we preliminarily calculated the particle dynamics of the whole beam line in steady-state, whose results are shown in Figure 5. The layout

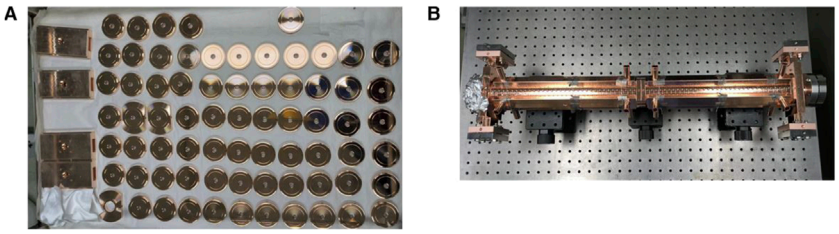

FIGURE 4
Cells of XT72. **(A)** Before brazing. **(B)** After brazing.

TABLE 4 RF properties of the XT72.

Properties	XT72 (CG)
Aperture radius [mm]	3.92 ~ 3.12
Frequency [GHz]	11.424
Quality factor	7056 ~ 6996
v_g/c [%]	3.20 ~ 1.44
Shunt impedance [MΩ/m]	93 ~ 109
Filling time [ns]	98
Working mode	$2\pi/3$

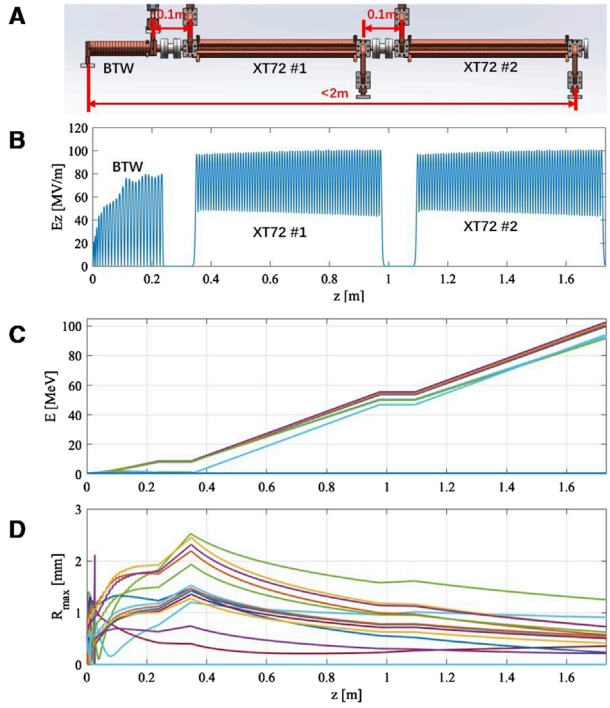

FIGURE 5
Steady-state dynamics calculation results for the entire beamline. **(A)** The beamline layout. **(B)** The electric field along the axis. **(C)** Electron beam energy at different emission phases. **(D)** Electron beam envelopes with different emission phases.

of the entire beam line is depicted in Figure 5A, which includes a bunching section and two main accelerating sections. Its whole length is less than 2 m. Figure 5B illustrates the electric field along the axis, where the amplitude represents the steady-state value, taking into account the beam loading effect. Figures 5C, D show the variations in energy and envelope for electron beams emitted at different phases, which could preliminarily confirm that the beam line could reach the target electron beam output of 100 MeV. These results were calculated using the equivalent circuit model in the time domain [31].

After completing the steady-state calculations, we turned to the optimization of the BTW's parameters, considering the time-domain process within a macro-pulse. The purpose of the optimization is to adjust the filling time of the bunching section to match the time taken by the acceleration section to reach steady-state [36]. The time-domain equivalent circuit model was also applied to this optimization process. Figure 6A shows the transient accelerating voltage in the main accelerating section. Figure 6B illustrates the time-dependent changes of the single-cells' electric fields within the bunching section. Each color line represents a different cell. These cells' electric fields correspond to the order of microwave filling. Specifically, the cell next to the input coupler was excited first, therefore reaching its maximum field first. Noting that the bunching section employs a backward traveling wave structure, the microwave filling order proceeds from the exit to the entrance of the beam, therefore the cell next to the output coupler is at the beam entrance. Since the first 4 cells at the beam entrance are critical for beam capture, it is essential that these cells have nearly reached steady-state when the main acceleration section achieves its steady-state condition.

Due to the complexity of multi-objective optimization, we proposed a single-objective approach, prioritizing the electron charge within a specified energy range at the beam line exit. In the preliminary design, the target energy range was set to 100 ± 2 MeV. During the optimization of the bunching section, we fixed the input frequency, cavity number, input power, and adjusted the BTW's coupling hole size and cavity radius. We also focused on three factors: capture rate, energy spread, and phase spread [31]. While phase spread does not directly affect the application of electron beams in VHEE, it does influence the energy spread of electrons

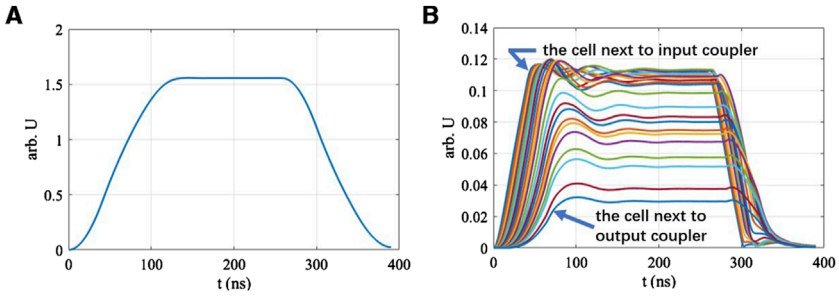

FIGURE 6
Temporal changes of beam parameters. **(A)** Main acceleration section: accelerating voltage. **(B)** Bunching section: single-cell electric fields.

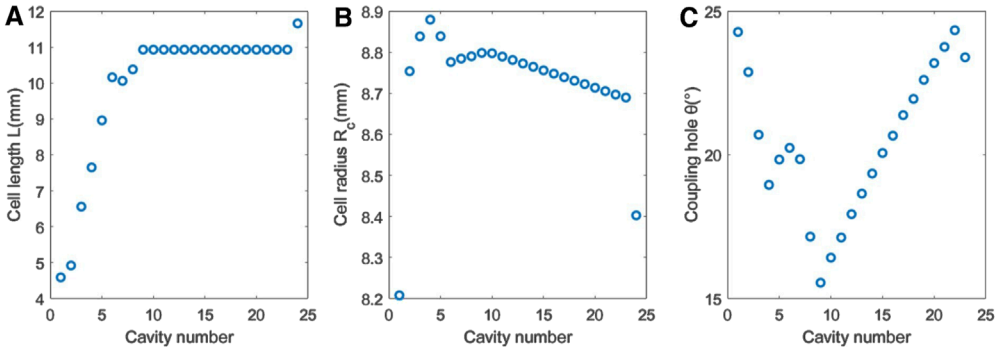

FIGURE 7
Optimization results of the BTW's geometric parameters. **(A)** Cell length. **(B)** Cell radius. **(C)** Coupling hole's angular width.

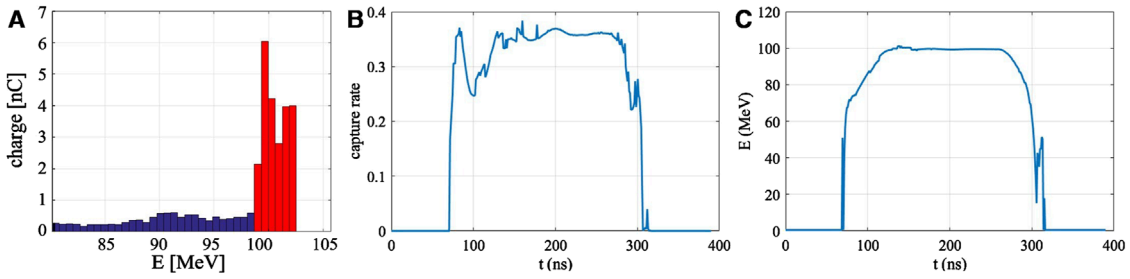

FIGURE 8
Results of the optimization. **(A)** Energy distribution of the electron beam at the exit of the VHEE beam line. **(B)** Transient value of capture rate. **(C)** Temporal changes of electrons' average energy at beam exit.

in the main acceleration section. Results of the optimization will be shown and discussed in the next section.

5 Results and discussion

5.1 Discussion of beam line optimization

The optimization results of the BTW's geometric parameters are shown in Figure 7, where the first eight cells are bunching cells and the rest are accelerating cells.

Figure 8A shows the optimized energy distribution at the beam line exit. Within a macro-pulse, 24 nC of electron charge falls within the 100 ± 2 MeV range, while 11 nC lies outside. A significant proportion of the charge falls outside the specified energy range, which can be attributed not only to the tail generated during the hot cathode bunching process, but also the energy reduction caused by the unsteady state of the acceleration structure. Figure 8B, C illustrate the temporal variations in beam parameters within a macro pulse, highlighting a noticeable drop in capture rate at 100 ns due to field changes in the bunching section. Between 80 and 130 ns, before the main acceleration section reaches steady-state, captured

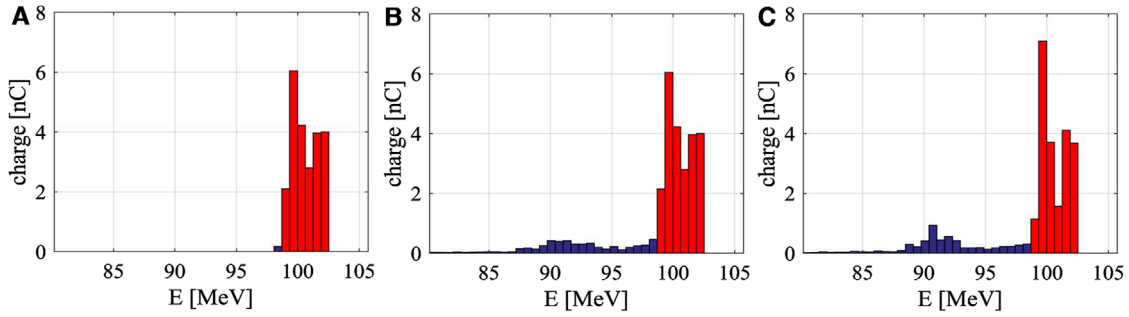

FIGURE 9
Different methods of removing the beam tail. **(A)** Using dipoles and slits at the beam line exit. **(B)** Using dipoles and slits at the bunching section exit. **(C)** Using a grid-controlled pulsed beam electron gun.

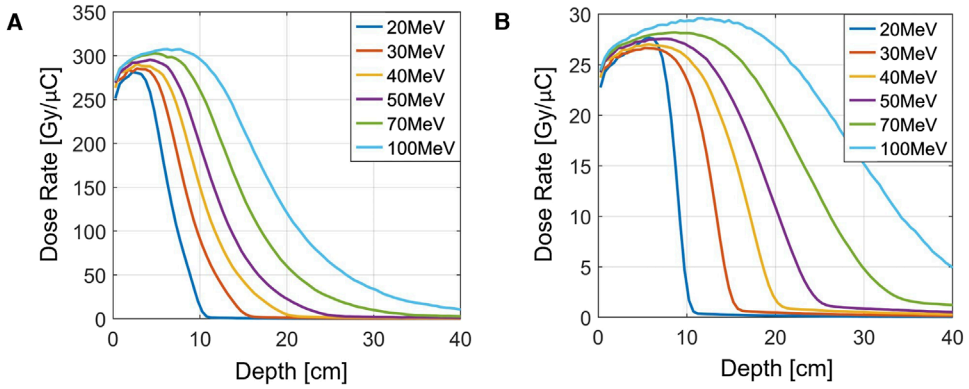

FIGURE 10
Depth-dose distribution of parallel electron beams with different energies. **(A)** 3 × 3 cm^2 parallel electron beam. **(B)** 10 × 10 cm^2 parallel electron beam.

electrons are only accelerated to lower energies. After 270 ns, as the input power decreases and residual electric field remains in the accelerating tube, captured electrons are again accelerated to a lower energies. Calculations show that electrons produced during these unsteady states contribute to 76% of the tail distribution.

Directly using the electron beam of Figure 8A in VHEE radiotherapy experiments would result in significant background, making it necessary to eliminate or suppress the tail. The most straightforward method is to place a dipole and a slit at the beam exit to filter the electrons by energy, as shown in Figure 9A. While effective in removing the tail, this approach requires a large magnet deflection radius which poses shielding challenges.

The second method is to position the dipole and slit at the exit of the bunching section. Since the beam energy is lower at this point, the required deflection radius is smaller, making shielding easier. However, calculations indicate that this method can only filter out 55% of the tail, as shown in Figure 9B. This limitation arises because, while some electrons' energy falls within the specified range upon exiting the bunching section, their large phase deviation causes them to fall outside this range after passing through the acceleration section. Moreover, placing a dipole at the bunching section exit complicates both the microwave and beam systems.

The third method involves using a grid-controlled electron gun with precise beam control, activating the beam when the accelerating structure is nearly filled and deactivating it when input power starts to decline. Since that electrons produced during unsteady states contribute to 76% of the tail distribution, keeping the starting moment of electron emission close to the moment when the accelerator field reaches a steady state may greatly reduce the tail. Considering the beam loading effect, the activating moment is chosen to be when the accelerating structure is nearly filled instead of full filled. The specific activating moment needs to be compared and optimized. Despite this, the unsteady process caused by wakefield effects during beam injection still prevents complete tail removal, as illustrated in Figure 9C.

In summary, while directly screening electrons' energy at the exit of beam line needs a larger dipole, it is more effective. Future work would be necessary to deal with shielding challenges.

5.2 Discussion of preliminary dose estimate

Based on the optimization of the output charge, the Monte Carlo simulation software GEANT4 [37] was employed to preliminarily calculate the depth-dose distribution of the VHEE beam. To simplify the model, the electron beam was assumed to be parallel after expansion. The parallel beam traverses a 50 cm air gap and then interacts with a 40 cm water layer. The depth-dose distributions at the center of the beams, with cross-sections of 3×3 cm^2 and 10×10 cm^2, for various energies, are displayed in Figure 10.

It is clear that higher energy levels allow electrons to penetrate deeper into the material. The designed output energy of the VHEE beam line in this study is 100 MeV. By comparing Figures 10A, B, it can be observed that a smaller beam cross-section results in a more rapid fall-off in the depth dose. This is due to increased scattering experienced by electron beams with smaller cross-sections. The dose at a given depth is approximately inversely proportional to the beam's cross-section area.

For dose estimation, a dose-to-charge ratio of 20 Gy/$\mu C \bullet 10 \times 10$ cm^2 is used. This implies that a 1 μC electron beam expanded to a 10×10 cm^2 area can deliver a 20 Gy dose at the target. This ratio is inversely proportional to the cross-sectional area of the expanded beam and can be applied to estimate the radiation field and dose rate.

Given that the beam line outputs 24 nC per macro pulse and operates at a repetition rate of 40 Hz, the estimated dose rate under a 10×10 cm^2 radiation field is:

$$20\text{Gy}/\mu\text{C} \times 24 \quad \text{nC} \times 40 \quad \text{Hz} = 19.2 \quad \text{Gy/s}$$

When the radiation field is reduced to less than 6×6 cm^2, the dose rate can exceed 40 Gy/s, which is ideal for FLASH radiotherapy research. Future system upgrades, such as increasing the repetition rate of the modulator, could further enhance the dose rate of the entire setup. In addition, it should be noted that this section's dose calculation is only a rough approximation and could only preliminary confirm the beam line's ability to deliver VHEE at UHDR. After the beam line is constructed and tested in the future, detailed dose simulation would be performed to compare the measured results.

6 Summary

A compact electron accelerator design for VHEE radiotherapy has been proposed, utilizing the Tsinghua X-band High Power Test Stand as its foundation. The pulse compression system, backward traveling-wave buncher, and the prototype high-gradient accelerator, XT72, have each successfully undergone high-power test. At present, the design and optimization of the beam line within a single pulse have been finalized. The whole beam line is still under construction. Ongoing work is focused on wakefield calculations to further refine and optimize the structure for enhanced performance.

Data availability statement

The original contributions presented in the study are included in the article/supplementary material, further inquiries can be directed to the corresponding author.

Author contributions

HL: Writing–original draft, Writing–review and editing. HZ: Writing–review and editing. XL: Writing–review and editing, Writing–original draft. QG: Writing–review and editing. FL: Writing–review and editing. JS: Writing–review and editing. HC: Writing–review and editing.

Funding

The author(s) declare that financial support was received for the research, authorship, and/or publication of this article. We gratefully acknowledge the support of the National Natural Science Foundation of China (NSFC Grant No. 12027902).

Conflict of interest

The authors declare that the research was conducted in the absence of any commercial or financial relationships that could be construed as a potential conflict of interest.

Publisher's note

References

1. Vinod SK, Hau E. Radiotherapy treatment for lung cancer: current status and future directions. *Respirology* (2020) 25:61–71. doi:10.1111/resp.13870

2. Zhang Z, Liu X, Chen D, Yu J. Radiotherapy combined with immunotherapy: the dawn of cancer treatment. *Signal Transduction Targeted Ther* (2022) 7:258–34. doi:10.1038/s41392-022-01102-y

3. Petroni G, Cantley LC, Santambrogio L, Formenti SC, Galluzzi L. Radiotherapy as a tool to elicit clinically actionable signalling pathways in cancer. *Nat Rev Clin Oncol* (2022) 19:114–31. doi:10.1038/s41571-021-00579-w

4. De Ruysscher D, Niedermann G, Burnet NG, Siva S, Lee AWM, Hegi-Johnson F. Radiotherapy toxicity. *Nat Rev Dis Primers* (2019) 5:13–20. doi:10.1038/s41572-019-0064-5

5. Atun R, Jaffray DA, Barton MB, Bray F, Baumann M, Vikram B, et al. Expanding global access to radiotherapy. *Lancet Oncol* (2015) 16:1153–86. doi:10.1016/S1470-2045(15)00222-3

6. Schaue D, McBride WH. Opportunities and challenges of radiotherapy for treating cancer. *Nat Rev Clin Oncol* (2015) 12:527–40. doi:10.1038/nrclinonc.2015.120

7. Favaudon V, Caplier L, Monceau V, Pouzoulet F, Sayarath M, Fouillade C, et al. Ultrahigh dose-rate FLASH irradiation increases the differential response between normal and tumor tissue in mice. *Sci Translational Med* (2014) 6:245ra93. doi:10.1126/scitranslmed.3008973

8. Lin B, Gao F, Yang Y, Wu D, Zhang Y, Feng G, et al. FLASH radiotherapy: history and future. *Front Oncol* (2021) 11:644400. doi:10.3389/fonc.2021.644400

9. Bourhis J, Montay-Gruel P, Gonçalves Jorge P, Bailat C, Petit B, Ollivier J, et al. Clinical translation of FLASH radiotherapy: why and how? *Radiother Oncol* (2019) 139:11–7. doi:10.1016/j.radonc.2019.04.008

10. Montay-Gruel P, Bouchet A, Jaccard M, Patin D, Serduc R, Aim W, et al. X-rays can trigger the FLASH effect: ultra-high dose-rate synchrotron light source prevents normal brain injury after whole brain irradiation in mice. *Radiother Oncol* (2018) 129:582–8. doi:10.1016/j.radonc.2018.08.016

11. Gao F, Yang Y, Zhu H, Wang J, Xiao D, Zhou Z, et al. First demonstration of the FLASH effect with ultrahigh dose rate high-energy X-rays. *Radiother Oncol* (2022) 166:44–50. doi:10.1016/j.radonc.2021.11.004

12. Fouillade C, Curras-Alonso S, Giuranno L, Quelennec E, Heinrich S, Bonnet-Boissinot S, et al. FLASH irradiation spares lung progenitor cells and limits the incidence of radio-induced senescence. *Clin Cancer Res* (2020) 26:1497–506. doi:10.1158/1078-0432.CCR-19-1440

13. Chabi S, To THV, Leavitt R, Poglio S, Jorge PG, Jaccard M, et al. Ultra-high-dose-rate FLASH and conventional-dose-rate irradiation differentially affect human acute lymphoblastic leukemia and normal hematopoiesis. *Int J Radiat Oncology* Biology* Physics* (2021) 109:819–29. doi:10.1016/j.ijrobp.2020.10.012

14. Vozenin MC, De Fornel P, Petersson K, Favaudon V, Jaccard M, Germond JF, et al. The advantage of FLASH radiotherapy confirmed in mini-pig and cat-cancer patients. *Clin Cancer Res* (2019) 25:35–42. doi:10.1158/1078-0432.CCR-17-3375

15. Simmons DA, Lartey FM, Schüler E, Rafat M, King G, Kim A, et al. Reduced cognitive deficits after FLASH irradiation of whole mouse brain are associated with less hippocampal dendritic spine loss and neuroinflammation. *Radiother Oncol* (2019) 139:4–10. doi:10.1016/j.radonc.2019.06.006

16. Angal-Kalinin D, Bainbridge A, Brynes AD, Buckley RK, Buckley SR, Burt GC, et al. Design, specifications, and first beam measurements of the compact linear accelerator for research and applications front end. *Phys Rev Acc Beams* (2020) 23:044801. doi:10.1103/PhysRevAccelBeams.23.044801

17. Abel E, Girdhani S, Jackson I, Eley J, Katsis A, Marshall A, et al. Characterization of radiation-induced lung fibrosis and mode of cell death using single and multi-pulsed proton flash irradiation. *Int J Radiat Oncol Biol Phys* (2019) 105:E652–3. doi:10.1016/j.ijrobp.2019.06.1033

18. Mascia AE, Daugherty EC, Zhang Y, Lee E, Xiao Z, Sertorio M, et al. Proton FLASH radiotherapy for the treatment of symptomatic bone metastases: the FAST-01 nonrandomized trial. *JAMA Oncol* (2023) 9:62–9. doi:10.1001/jamaoncol.2022.5843

19. DesRosiers C, Moskvin V, Bielajew AF, Papiez L. 150-250 MeV electron beams in radiation therapy. *Phys Med and Biol* (2000) 45:1781–805. doi:10.1088/0031-9155/45/7/306

20. Papiez L, DesRosiers C, Moskvin V. Very high energy electrons (50 – 250 MeV) and radiation therapy. *Technology Cancer Res and Treat* (2002) 1:105–10. doi:10.1177/153303460200100202

21. Lagzda A. *VHEE radiotherapy studies at CLARA and CLEAR facilities*. United Kingdom), England: The University of Manchester (2019). Ph.D. thesis.

22. Lagzda A, Angal-Kalinin D, Jones J, Aitkenhead A, Kirkby KJ, MacKay R, et al. Influence of heterogeneous media on Very High Energy Electron (VHEE) dose penetration and a Monte Carlo-based comparison with existing radiotherapy modalities. *Nucl Instr Methods Phys Res Section B: Beam Interactions Mater Atoms* (2020) 482:70–81. doi:10.1016/j.nimb.2020.09.008

23. Poppinga D, Kranzer R, Farabolini W, Gilardi A, Corsini R, Wyrwoll V, et al. VHEE beam dosimetry at CERN Linear Electron Accelerator for Research under ultra-high dose rate conditions. *Biomed Phys and Eng Express* (2020) 7:015012. doi:10.1088/2057-1976/abcae5

24. Bazalova-Carter M, Liu M, Palma B, Dunning M, McCormick D, Hemsing E, et al. Comparison of film measurements and Monte Carlo simulations of dose delivered with very high-energy electron beams in a polystyrene phantom. *Med Phys* (2015) 42:1606–13. doi:10.1118/1.4914371

25. Dunning MP, Adolphsen C, Chu TS, Colby ER, Gilevich A, Hast C, et al. Status and upgrades of the NLCTA for studies of advanced beam acceleration, dynamics, and manipulation. In: *Proceedings of 2011 particle accelerator conference*. New York, USA (2011).

26. Gamba D, Corsini R, Curt S, Doebert S, Farabolini W, Mcmonagle G, et al. The CLEAR user facility at CERN. *Nucl Instr Methods Phys Res Section A: Acc Spectrometers, Detectors Associated Equipment* (2018) 909:480–3. doi:10.1016/j.nima.2017.11.080

27. Conde ME, Antipov SP, Doran DS, Gai W, Gao Q, Ha G. Research program and recent results at the argonne wakefield accelerator facility (AWA). In: *Proceedings of the 8th international particle accelerator conference*. Copenhagen, Denmark (2017). doi:10.18429/JACoW-IPAC2017-WEPAB132

28. Burkart F, Assmann R, Dinter H, Jaster-Merz S, Kuropka W, Mayet F, et al. The ares linac at desy. In: *Proceedings of the 31st international linear accelerator conference*. Liverpool, UK (2022). doi:10.18429/JACoW-LINAC2022-THPOJO01

29. Wanstall HC, Burkart F, Dinter H, Kellermeier M, Kuropka W, Mayet F, et al. First *in vitro* measurement of VHEE relative biological effectiveness (RBE) in lung and prostate cancer cells using the ARES linac at DESY. *Scientific Rep* (2024) 14:10957. doi:10.1038/s41598-024-60585-7

30. Lin X, Zha H, Shi J, Jiang Y, Hu F, Gu W, et al. X-band two-stage rf pulse compression system with correction cavity chain. *Phys Rev Acc Beams* (2022) 25:120401. doi:10.1103/PhysRevAccelBeams.25.120401

31. Lin XC, Zha H, Shi JR, Gao Q, Hu FJ, Li QZ, et al. A compact X-band backward traveling-wave accelerating structure. *Nucl Sci Tech* (2024) 35:40. doi:10.1007/s41365-024-01403-7

32. Available from: https://www.cst.com/ (Accessed January 07, 2025).

33. Lin XC, Zha H, Shi JR, Gao Q, Liu JY, Zhou LY, et al. Fabrication, tuning, and high-gradient testing of an X-band traveling-wave accelerating structure for VIGAS. *Nucl Sci Tech* (2022) 33:102. doi:10.1007/s41365-022-01086-y

34. Yingchao D, Han C, Hongze Z, Qiang G, Qili T, Zhijun C, et al. A very compact inverse Compton scattering gamma-ray source. *High Power Laser Part Beams* (2022) 34:104010–9. doi:10.11884/HPLPB202234.220132

35. Gao Q, Zha H, Shi J, Lin X, Du Y, Feng B, et al. Design and test of an X-band constant gradient structure. *Phys Rev Acc Beams* (2024) 27:090401. doi:10.1103/PhysRevAccelBeams.27.090401

36. Liu JY, Shi JR, Zha H, Grudiev A, Wang P, Du YC, et al. Analytic RF design of a linear accelerator with a SLED-I type RF pulse compressor. *Nucl Sci Tech* (2020) 31:107. doi:10.1007/s41365-020-00815-5

37. Available from: https://geant4.web.cern.ch/ (Accessed January 07, 2025).

frontiers | Frontiers in Oncology

TYPE Methods
PUBLISHED 06 March 2025
DOI 10.3389/fonc.2025.1516576

OPEN ACCESS

EDITED BY
James C. L. Chow,
University of Toronto, Canada

REVIEWED BY
Lanchun Lu,
The Ohio State University, United States
Stefano Salvatori,
University Niccolò Cusano, Italy

*CORRESPONDENCE
Mauro Migliorati
mauro.migliorati@uniroma1.it

RECEIVED 06 November 2024
ACCEPTED 10 February 2025
PUBLISHED 06 March 2025

CITATION
Giuliano L, Alesini D, Cardelli F, Carillo M, Chiadroni E, Coppola M, Cuttone G, Curcio A, De Gregorio A, Raddo RD, Faillace L, Farina S, Ficcadenti L, Francescone D, Franciosini G, Franzini G, Gallo A, Magi M, Mauro GS, Mostacci A, Palumbo L, Patera V, Perondi F, Petrarca M, Pioli S, Remetti R, Sarti A, Schiavi A, Spataro B, Torrisi G, Vannozzi A and Migliorati M (2025) A compact C-band FLASH electron linear accelerator prototype for the VHEE SAFEST project.
Front. Oncol. 15:1516576.
doi: 10.3389/fonc.2025.1516576

A compact C-band FLASH electron linear accelerator prototype for the VHEE SAFEST project

Lucia Giuliano[1,2], David Alesini[3], Fabio Cardelli[3], Martina Carillo[3], Enrica Chiadroni[1,3], Massimiliano Coppola[1], Giacomo Cuttone[4], Alessandro Curcio[1,3], Angelica De Gregorio[2,5], Roberto Di Raddo[3], Luigi Faillace[4], Stefano Farina[1,2], Luca Ficcadenti[2], Daniele Francescone[1], Gaia Franciosini[1], Giovanni Franzini[3], Alessandro Gallo[3], Marco Magi[1,2], Giorgio S. Mauro[4], Andrea Mostacci[1,2], Luigi Palumbo[1,2], Vincenzo Patera[1,2], Francesca Perondi[1], Massimo Petrarca[1], Stefano Pioli[3], Romolo Remetti[1], Alessio Sarti[1,2], Angelo Schiavi[1], Bruno Spataro[3], Giuseppe Torrisi[4], Alessandro Vannozzi[3] and Mauro Migliorati[1,2]*

[1]Scienze di Base e Applicate per l'Ingegneria (SBAI) Department, Sapienza University of Rome, Rome, Italy, [2]Sec. Roma1 of Istituto Nazionale di Fisica Nucleare, Rome, Italy, [3]Laboratori Nazionali di Frascati of Istituto Nazionale di Fisica Nucleare (LNF-INFN) Frascati, Frascati, Italy, [4]Laboratori Nazionali del Sud of Istituto Nazionale di Fisica Nucleare Catania, Catania, Italy, [5]Physics Department, Sapienza University of Rome, Rome, Italy

FLASH therapy, a novel cancer treatment technique, aims to control tumor growth, sparing the healthy tissue from radiation damage and thus increasing the therapeutic ratio. Translating FLASH therapy into clinical practice, especially for treating deep-seated tumors, necessitates achieving Very High-Energy Electron (VHEE) levels within the 50-250 MeV range. In 2022 Sapienza University, in collaboration with INFN, launched the SAFEST project, a compact C-band 100 MeV Ultra-High Dose Rate (UHRD) radiation source for the treatment of deep-seated tumors, which was partially funded by Italian PNRR (Next Generation EU). A C-band linac prototype at lower energy, with an electron pulse of 100 nC and repetition frequency <200 Hz, is being developed to test the key choices and technology of a VHEE machine. This paper provides insights into the design strategy of the prototype, discussing the optimization of the main RF and electron beam parameters. The expected dose profiles are also shown and discussed. The progress of this innovative linac represents a step forward in the realization of a C-band compact FLASH VHEE source for cancer treatment.

KEYWORDS

FLASH linac, C-band, FLASH therapy, RF design, beam dynamic analysis

1 Introduction

Radiotherapy (RT) is an effective tool used in more than half of all cancer treatments. Over the past decades, personalized treatment modalities have been developed thanks to technological and biological advancements. However, success in fighting cancer is still constrained by complications in normal tissues and by radiation-induced side effects. These include acute effects, such as inflammation in early-responding tissues (e.g., skin), and late effects, like radiation-induced necrosis and functional loss in late-responding tissues (e.g., brain). Consequently, enhancing the therapeutic ratio, namely the relationship between the probability of tumor control and the likelihood of normal tissue damage, remains the primary goal of modern cancer research.

In the last decade, the investigation of radiobiology at Ultra High Dose Rate (UHDR) has brought a new avenue to the forefront: the so-called "FLASH effect" (1). *In-vivo* experiments under UHDR have shown a significant differential impact on tumors versus normal tissue: healthy tissue toxicity (side effects) is reduced, while tumor damage remains unchanged. If these results are confirmed, the FLASH effect could revolutionize RT. Even if the research in the FLASH regime is still in its early stages, studies involving electron beams [e.g., refs. (2–6)] have demonstrated promising results for clinical application. Early trials in humans (7) and domestic animals (8, 9) are underway, confirming the technique's feasibility while also revealing challenges and the high interest within the medical community.

It remains unclear whether the mechanism behind the FLASH effect lies in differential DNA damage between tumor and healthy cells, in other cellular components (proteins, lipids, membranes, etc.), or if it involves a more complex interaction at the tissue or organ.

Clinical research facilities are too limited to explore this area thoroughly. The parameter space for FLASH therapy is vast, and a systematic investigation is necessary to identify the optimal conditions for future treatments.

A key topic of discussion in electron RT is whether VHEE could facilitate the clinical application of FLASH, as they have the potential to deliver UHDRs while penetrating deep-seated tissues. However, no existing prototypes currently meet hospital requirements because they are based on high-energy accelerators existing in large facilities. Our challenge is developing a compact system that is easy to operate in a hospital and can achieve electron pulses typical of the UHDR for FLASH, as reported in Table 1 (10, 11).

2 VHEE beams for radiotherapy

2.1 FLASH-VHEE therapy potential

The use of electrons in the 50–250 MeV energy range for the treatment of deep-seated tumors has been explored in previous studies demonstrating that VHEE treatments are competitive with conventional radiotherapy and particle therapy (12–15).

TABLE 1 Main parameters for FLASH irradiation.

Symbol	Description	Value
PRF	Pulse repetition frequency	> 100 *Hz*
t_p	Electron pulse width	0.1-4.0 μs
t_i	Total irradiation time	< 100ms
$\overline{\dot{D}}$	Time-averaged dose rate	> 100Gy/s
$\dot{D}_p$	Dose-rate in a single pulse	> 10^6Gy/s
D_p	Dose in a single pulse	> 1Gy

From a physical perspective, electron dose delivery represents a compromise between that of protons and photons. Due to their lower mass compared to protons, electrons exhibit a broader Bragg Peak (BP), as illustrated in Figure 1. However, as charged particles, electrons undergo multiple scattering interactions, unlike photons, leading to less conformal lateral dose deposition.

The broader percentage depth dose curve (PDD) of VHEE does not have the selectivity potential of other RT-charged beams as proton or carbon, but allows to overcome two main limitations of UHDR irradiation with hadrons and photons. There is no need to change the beam energy to cover a large target volume (electrons provide a naturally spread-out BP), and this helps in providing the required high dose rate. There is no need to implement strict safety margins on the patient positioning as the longitudinal absorbed dose distribution does not exhibit any sharp fall.

It is worth mentioning that recent research has shown the additional possibility of tailoring and/or narrowing the PDD of VHEE using suitable magnetic systems to tightly focus the electron beams (19). In fact, an appealing feature of VHEE is the magnetic rigidity smaller than that of protons, which allows easier and faster magnetic bending of the beam when delivered in an active scanning, as in the pencil beams approach.

3 SAFEST Project: a 100 MeV compact C-band linac

3.1 Linac frequency choice

Electron medical accelerators are based on accelerating structures with a resonant frequency in the (S-C-X) band, operating in either Traveling Waves (TW) or Standing Waves (SW) modes. Different technological solutions have been adopted (20) depending on the operating resonant frequency, which represents one of the most RF-relevant parameters to choose when designing a linac. In particular, the scaling laws (21, 22) indicate that, as the frequency of RF cavities increases, it becomes possible to achieve a certain electron beam energy with a shorter accelerator length for a given power. This can be attributed to two main factors: higher shunt impedance per unit length and a higher maximum attainable electric field strength. Moreover, it's known that the maximum accelerating field in RF structures is limited by the RF breakdown effect, which can result in significant damage to

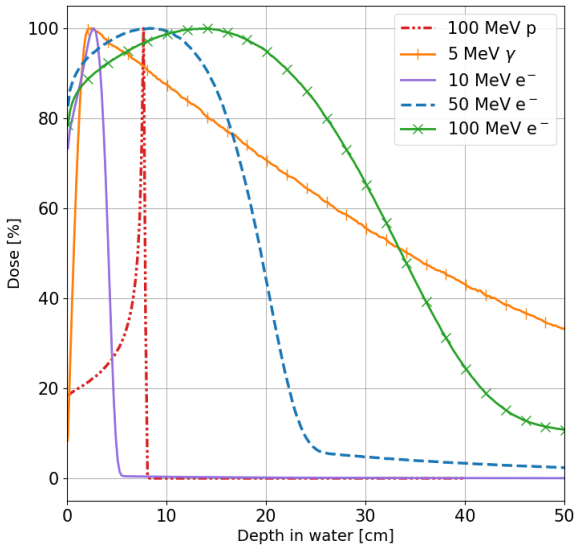

FIGURE 1
Percentage dose profiles along the beam axis for 10 MeV (violet line), 50 MeV (blue line) and 100 MeV (green line) electrons, 5 MeV photons (orange line) and 100 MeV protons (red line) in a water phantom obtained using FRED Monte Carlo software (16–18).

the structure. According to the empirical laws (23–25), a higher frequency of operation allows a higher breakdown limit and a higher accelerating gradient. As a consequence, there are advantages in utilizing higher frequencies. The primary benefit lies in the compactness of the accelerator, resulting in reduced size and weight.

In the past, significant progress was made in developing warm X-band traveling wave (TW) structures, achieving an accelerating gradient of 100 MV/m (26–28). These X-band developments were mainly driven by the need for highly efficient future accelerators for high-energy physics. More recently, C-band warm TW structures achieved a gradient of 50 MV/m (29–33), mainly used in FEL and Compton Sources. Higher gradients, of the order of 100 MV/m, were achieved with C-band structures operating at cryo temperatures (77 K) (34, 35). Also, in industrial and medical applications, there are advantages in utilizing higher frequencies. In this case, SW structures are preferred to accelerate low-energy electrons (20, 36) despite their lower energy efficiency.

For a specific application, the choice of the frequency is crucial to consider certain trade-off factors when going to higher frequencies. Indeed, from the definition of the shunt impedance per unit length:

$$R_{sh} = \frac{V^2}{P_{cav}} \frac{1}{L_{str}}$$

with V the accelerating voltage, P_{cav} the power dissipated in the cavity walls, and L_{str} the linac length, it's apparent that with higher frequency, there is a higher power efficiency.

Nevertheless, other parameters are worsened, such as a lower Q-value and a reduced power dissipation capability of the accelerator structure. Of course, some of these challenges can be overcome through a meticulous design of the cooling system, for example, and high-precision machining and polishing. Finally, in the case of high peak current, the radius of the iris of the accelerating cells plays an important role in the total charge transmission efficiency of the beam (21): a small iris radius typical of high-frequency structures results in a higher number of charges hitting the iris metallic surface, particularly in the structure at low energy where particles are captured.

Taking into account the above considerations, and based on our experience with C-Band technology (31–33), we proposed for the SAFEST Project a compact C-band linac, operating at the frequency of 5.712 GHz, as the best compromise which combines a high shunt impedance R_{sh} with an optimized transmission efficiency allowing a high peak current and UHDR electrons pulses.

3.2 SAFEST linac

In the SAFEST linac (11, 37) electrons are generated by a pulsed DC thermionic gun and injected into a 70 cm long SW structure, bi-periodic, working in $\pi/2$ mode. The beam is accelerated up to the energy of 10 MeV, and with two 1 m long TW structures, it reaches the energy of 100 MeV. A 45 MW klystron powers the accelerating system and foresees the use of a pulse compressor. Beam dynamics studies show that it's possible to accelerate an electron pulse with a charge of 100 nC at the energy of 100 MeV. The accelerating linac is shorter than 3 m, and the system, including vacuum pumps and diagnostic devices, does not exceed 4 m.

The choice of a SW structure as the first accelerating section of the linac is due to several reasons. Indeed, the SW field configuration offers the advantage of maintaining a stable and well-focused particle beam without requiring additional focusing magnets, such as solenoids. This is due to the extra focusing effect of the non-synchronous accelerating field components (backward waves) of a SW structure (38, 39), especially in the low-beta bunching section where electrons are generated with low kinetic

energy. Further, it's possible to feed the structure with a single coupler located far from the cathode cell and the bunching sections, thereby avoiding any distortion of the accelerating field caused by the coupling window. Finally, the fixed phase advance per cell (here $\pi/2$), combined with appropriately designed cell length, optimizes the beam longitudinal capture.

4 C-band prototype @ Sapienza

4.1 Start of the project

The SAFEST project was partially funded in 2023 in the framework of the Italian PNRR plan (EU Next Generation) with a budget limited to the construction of a prototype in which the key components of the system, in particular the hybrid scheme SW and TW, can be tested at lower energy. The construction of the prototype in the Sapienza Campus is expected to be completed at the beginning of 2026. The area where the prototype will be located has, at the moment, a radio-protection constraint limiting the electron energy to 24 MeV. Due to the above limitations, the prototype cannot be used at its potentially extreme performance. Accordingly, we are planning to construct a 24 MeV prototype able to deliver UHDR pulses typical of the FLASH regime, which will allow us to test the combination of SW and TW sections in a compact system. The facility will provide a flexible platform for the development and test of innovative devices for precise measurement, monitoring, and manipulation of electron beam parameters under FLASH conditions and for conducting radiobiology experiments with both *in-vitro* and *in-vivo* samples.

4.2 Prototype description and design

4.2.1 Beam parameters and schematic layout

The layout of the proposed prototype is shown in Figure 2, highlighting the RF power distribution. The accelerating structures are powered by a 5 MW klystron with an RF pulse length of 5 μs. The klystron output feeds a pulse compressor (40) to obtain a shorter pulse length with a peak power of about 25 MW. This pulse enters a power splitter which distributes the available power asymmetrically: the standing wave structure receives 30% of the maximum available power. At the same time, the 70% is directed to the traveling wave structure. The circulator is needed to avoid damage to the klystron due to uncontrolled backward power from the SW cavity. The phase shifter guarantees the proper phase relation between the two structures, while the attenuator allows reducing the accelerating gradient in the TW structure to stay at the nominal energy of 24 MeV. Additionally, the klystron output power can be varied by an input control signal: a small negligible fraction of the klystron output taken from the directional coupler shown in the upper part of the figure (before the circulator) is compared with a reference signal and used to control the klystron input signal.

As shown in Table 2, where the main parameters of the linac prototype are reported, the first SW linac captures and accelerates a 1 μs pulse current of 100 mA, up to the energy of about 11 MeV. The beam reaches then an energy of 24 MeV in the following traveling wave section. The total length of the linac is about one meter and a half.

4.2.2 Pulse compressor

A spherical cavity RF pulse compressor – selected because of its compactness and relative ease of fabrication – is adopted to compress the 5 MW, 5 μs RF pulse coming from the klystron.

The spherical cavity pulse compressor, visible in Figure 3, is composed of a 3 dB coupler (also acting as a circular polarizer, converting the input TE_{10} mode into two, 90-deg shifted, circular TE_{11} output modes) and a single spherical energy storage cavity.

These two subsystems were first designed separately and then assembled to obtain the complete device. For the spherical cavity, two degenerated TE_{114} modes (see Figure 3, center) have been chosen for operation because of their high unloaded quality factor, $Q_0 = 134 \times 10^3$.

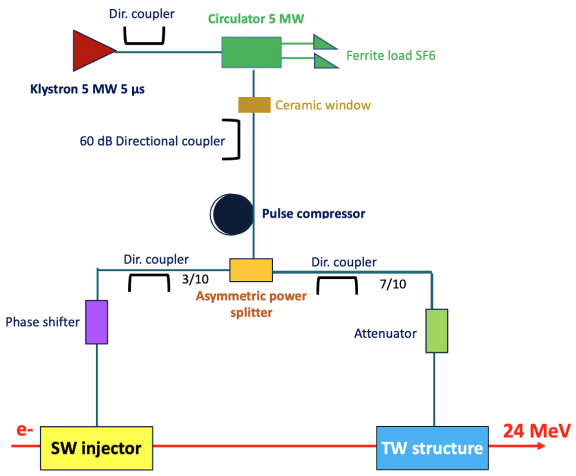

FIGURE 2
Layout of VHEE FLASH linac prototype.

10.3389/fonc.2025.1516576

TABLE 2 Linac prototype main parameters.

Linac parameters	
Frequency	5.712 GHz
Klystron Power	5 MW
Repetition frequency	< 200 Hz
RF pulse width	5 μs
Peak power after compression	24.4 MW
Total linac length	150 cm
Nominal beam energy (loaded)	24 MeV
Current Pulse I_b	100 mA
Pulse current duration	1 μs
Pulse charge	100 nC
Pulse compressor	
Operating mode	TE_{114}
Unloaded Quality Factor Q_0	134000
Coupling coefficient β_{sled}	3
RF input pulse length	5 μs
SW structure	
Structure length L_{SW}	69 cm
Shunt Impedance R_{SW}	116 MΩ/m
Quality factor Q_{SW}	10178
Mode of operation	Bi-periodic π/2
N of accelerating cells N_{SW}	27
Coupling cells length	3 mm
Iris radius	3 mm
Filling time	0.220 μs
Coupling coefficient β_{SW}	1.58
TW structure	
Structure length L_{TW}	43 cm
Number of cells	24
Shunt Impedance R_{TW}	107 MΩ/m
Quality factor Q_{TW}(cell)	10630
Type	Constant Impedance
Operation mode	$\frac{2}{3}\pi$
Iris radius	5 mm
Filling Time	0.143 μs
Group velocity v_g	0.01c*

(*) c = speed of light.

The coupling coefficient β_{sled} of the pulse compressor is calculated to be about 3. The operating frequency can be tuned in two ways: before brazing, by machining a circular ridge placed in the sphere equator (removal of 1 mm in ridge thickness corresponds to a frequency shift of about −2.5 MHz); after brazing, by employing eight push-pull tuners (a penetration of 0.5 mm for the eight tuners corresponds to a frequency shift of about +0.4 MHz). A summary of some main parameters of the pulse compressor is reported in Table 2.

Preliminary COMSOL thermal simulations (41) have been performed on a simplified mechanical model. Considering an input water temperature equal to 20°C and water flux of 20 $\frac{L}{min}$, the temperature distribution visible in the right-hand side of Figure 3 has been obtained. It can be seen that the optimized cooling system allows a temperature distribution close to the input water temperature in the spherical cavity area: further COMSOL structural simulations show that this temperature distribution avoids undesired structure deformations, thus having a negligible effect on resonant frequency value.

4.2.3 Standing wave structure

The C-band SW bi-periodic structure operates in a π/2-mode. It alternates coupling cavities, with no electric field, and accelerating cavities in which the electric field is maximum, as shown in Figure 4. Off-axis magnetic coupling slots are used to connect the accelerating cells with the coupling ones so that the electromagnetic energy can flow through the structure during the pulse generated by the power source.

A detailed analytical and numerical study with CST Microwave Studio Suite (42) has been carried out. The unit cell, which represents the basic device that was optimized, consists of an accelerating cell, two half-coupling cells, and two pairs of slots. The condition of a perfectly conducting surface (PE) at the structure boundaries was imposed to evaluate the resonant frequency and the main RF parameters. The shunt impedance was evaluated considering the copper wall conductivity.

As a first step in the linac design, after fixing the accelerating cell length L according to:

$$L = \frac{\beta\lambda}{2}, \tag{1}$$

with β the relativistic factor and λ the electric field wavelength, we determined the cell's diameters in such a way as to have the right resonance frequency of 5.712 GHz in each cell.

According to Equation 1, the first part of the linac presents a bunching section, composed of three cavities with different lengths, which takes into account the initial non-relativistic speed of the electron beam ($\beta << 1$). In these cells, a higher peak electric field improves the beam capture (43). After the first three cells, the beam becomes relativistic, and the cells maintain the same length because the velocity variation of the particles is negligible. The first cavity of the bunching section is a half-accelerating cell with an end plate where the electron gun is inserted.

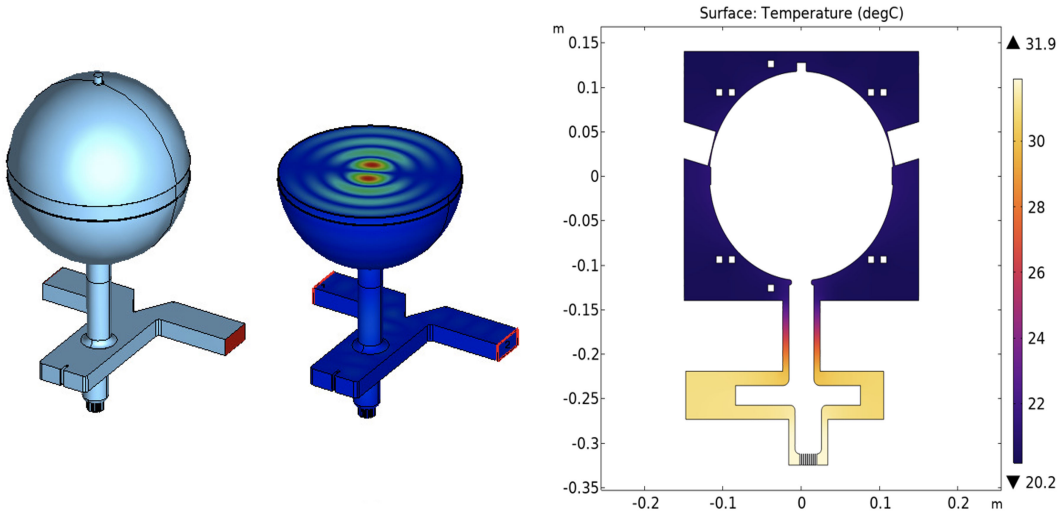

FIGURE 3
Spherical cavity pulse compressor: RF model (left), 2D cut showing the TE_{114} electric field (center), temperature distribution along the cut of the pulse compressor structure (right).

The unit accelerating cell presents a nose-cone structure, visible in the lower part of Figure 4, to maximize the efficiency of the acceleration. Indeed, the nose cone allows the localization of a very high electric field on the axis, creating an efficient beam acceleration. Several iterations have been performed to choose the proper geometry of the two nose cones to achieve high shunt impedance and a high electric field in the center of the cell.

Another important step in the design of the accelerating structure is the optimization of the quality factor (Q_{SW}), which represents the ratio of stored power to the power dissipated at the cavity walls. To this aim, the curvature on the top of the cavity has been varied until reaching an acceptably high value. In general, a higher quality factor and a higher shunt impedance mean higher machine performances.

Finally, the iris radius has been obtained as a compromise between a high shunt impedance per unit length R_{SW} and reasonable particle transmission. A low value of this radius increases R_{SW} but also leads to losses caused by the particles hitting the cavity walls that could activate the copper, creating radioprotection concerns. The chosen values of Q_{SW}, R_{SW}, and R_b are shown in Table 2.

The power feeds the cavities using a tapered RF waveguide through a hole in the wall of the central accelerating cell. This location is chosen because the central coupling, due to the

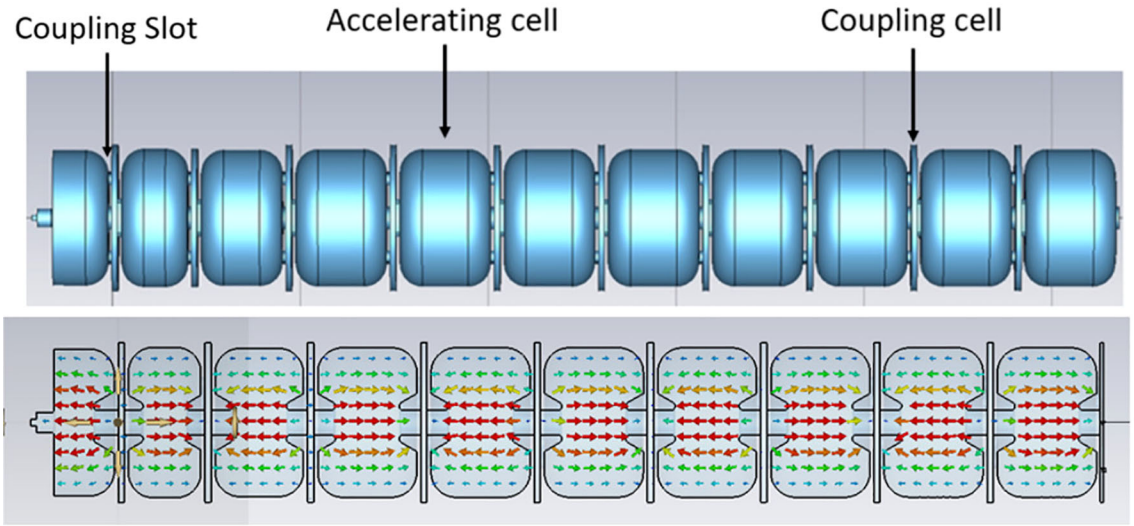

FIGURE 4
RF model of the SW structure with $\pi/2$ accelerating field operation mode. The first 3 low β sections, and 8 (out of 24 of the final design) $\beta = 1$ sections are shown.

symmetry, allows reducing the excitation of half of the linac resonant modes. The dimensions of the coupling hole between the waveguide and the linac have to be suitably chosen to obtain a proper balance between the input and the reflected power, taking into account also the phenomenon of the beam loading (21). Indeed, the waveguide-to-linac coupling coefficient β_{SW} must be optimized to minimize the reflected RF power when the electron beam is accelerated. The formula we used as a reference is the following:

$$\beta_{SW} = 1 + \frac{P_{beam}}{P_{cav}} = 1 + \frac{I_b R_{SW}}{V_{cav}} \quad (2)$$

where P_{beam} is the power delivered to the beam, and V_{cav} is the net cavity voltage (on the crest of the accelerating wave) (21). The value obtained with Equation 2 is shown in Table 2.

Figure 5 shows the amplitude of the longitudinal electric field obtained by CST along the axis and normalized to its maximum value. Of course, the final accelerating gradient depends on the available power. In the first 3 bunching sections, a higher field, which helps the capture process, can be noted (36). Also around the nose cones, the field is higher than in the center of the cells, while it vanishes in the coupling cells.

As already said, the SW field configuration offers the advantage of maintaining a stable and well-focused particle beam without requiring additional focusing magnets, such as solenoids (38, 39), as confirmed by beam dynamics simulations described in the next paragraph.

The simulated reflection coefficient S_{11} of the whole structure, which includes the tapered feeding waveguide, shows that the resonant frequency is 5712.7 MHz, resulting within the tunability range of the klystron (5708-5716 MHz). Additionally, we obtained that there are no longitudinal modes that can be excited inside this frequency range (± 4 MHz).

The main RF parameters of the SW structure are summarized in Table 2.

A small copper prototype, composed of five $\beta = 1$ cells was constructed in collaboration with SIT Sordina IORT Technology Spa and characterized at the Accelerator Laboratory of Sapienza University of Rome (44). In particular, the on-axis accelerating electric field was measured with the bead-pull technique. The tuning procedure provided a nearly uniform electric field distribution across the accelerating cells and, as expected, no field was detected in the coupling cells.

4.2.4 Traveling wave structure

The traveling wave (TW) device is a C-band accelerating structure operating in a TM01-like mode with a $\frac{2}{3}\pi$ phase advance per cell, optimizing the acceleration process's efficiency. Electromagnetic simulations and the design of the structure's cells were carried out using CST Studio Suite, starting with the analysis of a single structure shown on the right-hand side of Figure 6 and consisting of two half cells with proper boundary conditions. The left-hand side of the same figure shows the entire single cell of the TW system.

To simplify the in-house mechanical machining, we opted for the design of a cell geometry with left-right asymmetry. The rounding surface radius R_0 was optimized to maximize the Q-factor, while the ratio between r_1 and r_2 was chosen to maximize the shunt impedance avoiding high-peak electric fields to prevent breakdown phenomena. Further, the size of the iris radius was chosen to achieve a high shunt impedance while maintaining a high group velocity. This ensures that the structure can be filled within a time frame compatible with the duration of the RF pulse.

For the design of the input and output couplers we resorted to the short-circuit method (45), which allowed us to fine-tune the system to minimize the reflection coefficient at the waveguide input port for both the couplers. This approach ensures efficient power transfer into the structure while achieving a high degree of electric field flatness. The constant impedance of the structure inherently leads to some acceptable field attenuation as shown in Figure 7. One key finding during the optimization phase was that, due to the intrinsic asymmetry of the cells, the input and output couplers had

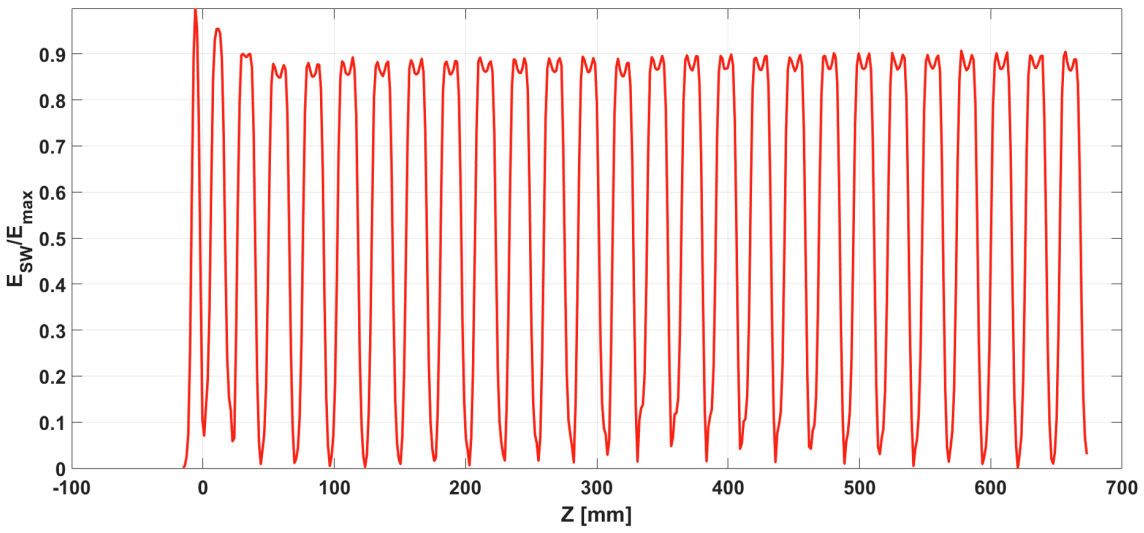

FIGURE 5
On-axis longitudinal electric field of the SW structure normalized to its maximum value.

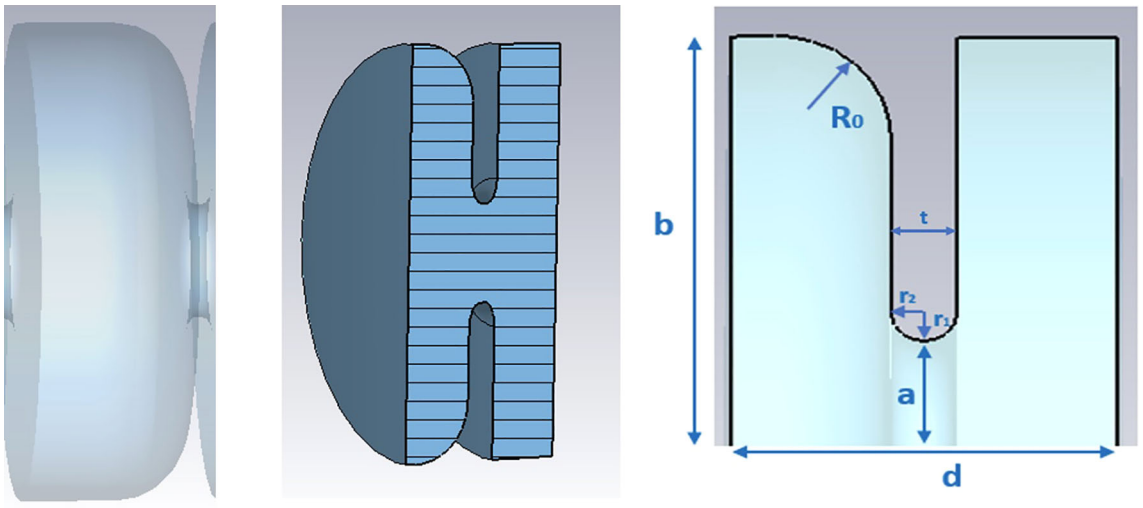

FIGURE 6
Single cell of the TW structure (left), perspective view of the CST simulated single structure (center), CST simulated geometry (right).

to be designed with slightly different dimensions. As a result, the two couplers are not perfectly identical.

Power is fed into the accelerating structure through a splitter as shown in Figure 8, which is integrated into the input coupler. The splitter itself was carefully optimized to ensure maximum power transmission while preventing any mode crosstalk.

The main RF parameters of the TW structure are reported in Table 2

For this TW structure, two prototypes were designed, mechanically engineered and built in collaboration with Roma1 Section of INFN: the first one containing 13 accelerating cells with a maximum length of approximately 30 cm, and the second one with a length of about 50 cm containing 22 cells. The prototypes were useful to verify the mechanical precision of the in-house fabrication and the success of the brazing process performed at the Frascati National Laboratories of INFN. Low-power measurements, field mapping, and tuning process were performed on the prototypes to correct any mechanical errors and ensure the quality of the final structure.

4.3 Beam dynamics studies

The ASTRA (A Space Charge Tracking Algorithm) (46) code has been used to perform single bunch beam dynamics simulations for the C-band linac prototype.

In the following, we show the study of the transport efficiency of the beam current, the particle acceleration and the evolution of relevant beam parameters along the linac.

Furthermore, we present a semi-analytical study of the beam loading in the accelerating structures to determine the correct strategy to compensate for the energy spread along the train of accelerated electron bunches induced by the shape of the compressed RF pulse and by the self-induced electromagnetic fields.

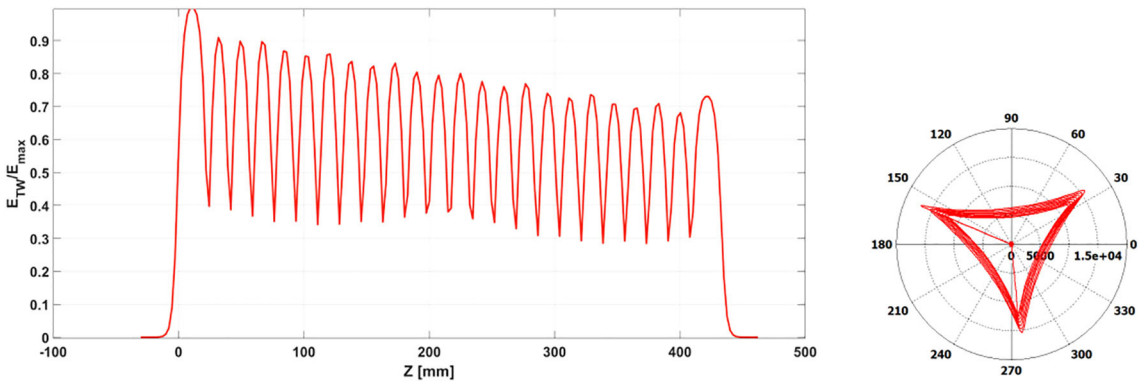

FIGURE 7
TW electric field normalized to its maximum value (left) and phase advance between cells after short circuit method optimization (right).

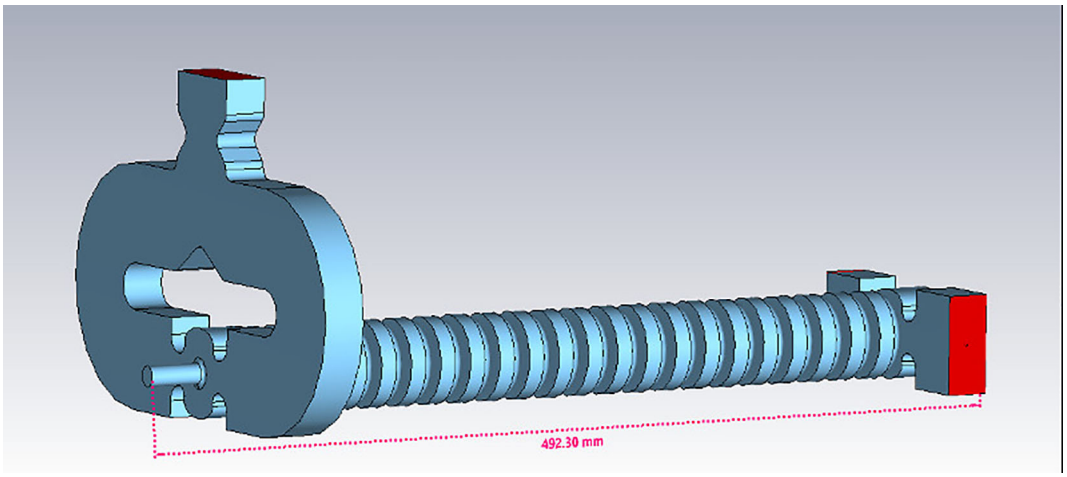

FIGURE 8
3D model of the TW structure. The feeding from the RF waveguide is obtained with a power splitter.

4.3.1 Electron pulse time structure

As already stated, the squared 5 μs pulses exiting the klystron at a repetition rate < 200 Hz are compressed inside the SLED cavity, as depicted in Figure 9. A critical aspect is the synchronization between the RF pulses in the two accelerating structures and the beam current pulse obtained by the DC emission from the thermionic cathode, which is pulsed to 1 μs to obtain a current of 100 mA in 5712 bunches (each carrying about 18 pC). Optimal beam injection times can be found for the two structures, $t_{0,SW}$ and $t_{0,TW}$ respectively. Such a synchronization allows reducing the energy spread along the beam current pulse. In fact, the energy distribution along the current pulse is affected by the combination of beam loading and the shape of the compressed RF pulses, which modulates the accelerating field experienced by the electron bunches in the pulse. The shape of the compressed pulse consists in a prepulse, which is not used for acceleration, and a main pulse that starts in correspondence of a phase inversion imposed on the RF field at low power (see Figure 9). The time of phase inversion occurs T_{RF} seconds before the end of the uncompressed pulse: indeed T_{RF} denotes the length of the baseline of the main compressed pulse. The β_{sled} coefficient determines the filling time of the SLED cavity and has a crucial role for the shape of the compressed pulse, i.e. for the induced energy spread. A lower β_{sled} allows for slower decay of the compressed pulse on the scale of the beam current pulse length (1 μs), at the expense of the maximum attainable peak power after compression.

4.3.2 Beam capture and energy gain

The first object of the simulation study is the transport efficiency from the cathode to the end of the accelerator, which is related to the beam capture at the entrance of the SW accelerating cavity. this transport efficiency has been determined versus the average accelerating electric field (also called accelerating gradient) reached in the SW structure. Figure 10 shows the results of the ASTRA simulations.

A quasi-saturation level of about 44% is reached for an accelerating gradient greater than 15 MV/m. This means that in order to provide 100 mA of beam current for experiments at the end of the accelerator, about 230 mA must be emitted by the cathode.

The desired final energy of the electron beam at the exit of the linac is 24 MeV. According to the simulations' results, we can reach this value by accelerating the beam from a few tens of keV (emitted

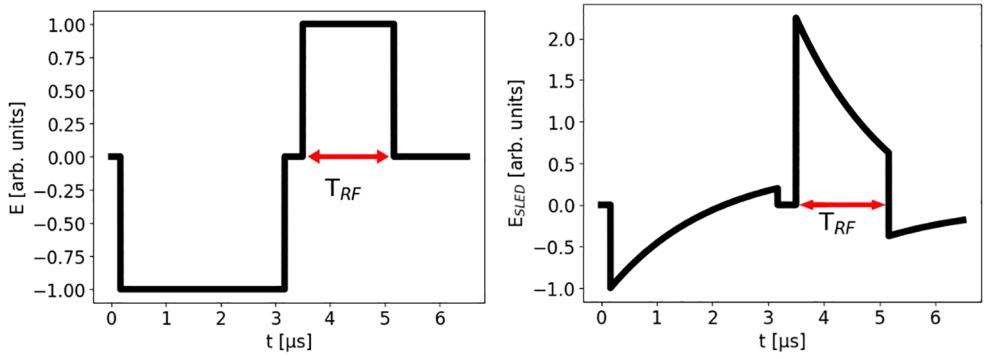

FIGURE 9
RF electric field before (left) and after compression (right).

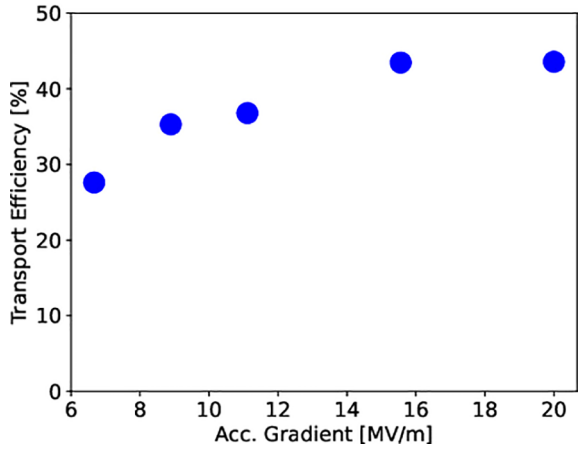

FIGURE 10
Efficiency of beam current transport from the cathode to the end of the SW structure for different average accelerating electric fields (i.e. accelerating gradients).

by the cathode) to ~ 11 MeV in the SW structure, and then gaining an extra 13 MeV in the TW accelerating cavity, as shown in Figure 11.

Analytically, the mean energy gain ΔW_{SW} in the SW cavity can be calculated using the following equation (36):

$$\Delta W_{SW} = \frac{2e\sqrt{R_{SW}L_{SW}\beta_{SW}P_{SW}}}{1+\beta_{SW}} - \frac{eR_{SW}L_{SW}}{1+\beta_{SW}}I_b \tag{3}$$

where e is the elementary charge. The first term in the right-hand side of the equation takes into account the external RF power feeding the structure, while the second term is due to the beam loading. If we consider the relevant parameters of the SW cavity reported in Table 2, in order to obtain an energy gain of about $\Delta W_{SW} \simeq 11$ MeV, and with a pulse current I_b of 100 mA, we need an input cavity peak RF power P_{SW} of 2.8 MW.

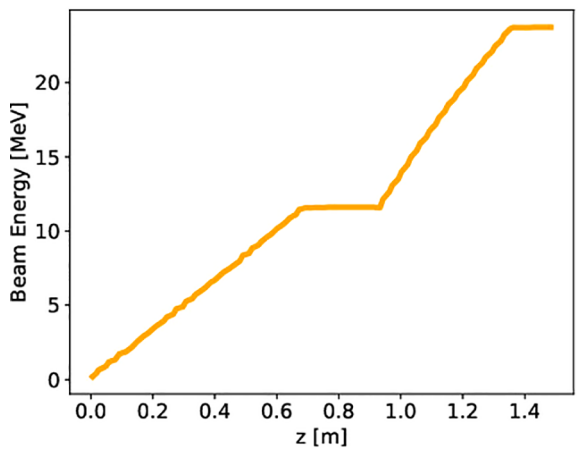

FIGURE 11
Energy gain for a single bunch traveling through the lattice made of an SW and a TW structure. Beam loading is considered for a current of 100 mA, reducing the net gain to ~ 11 MeV in the SW cavity and to ~ 13 MeV in the TW structure.

Moreover, the mean on-crest energy gain ΔW_{TW} in the TW structure of ~ 13 MeV can be calculated through the following equation and by considering an input peak RF Power P_{TW} of 15.5 MW:

$$\Delta W_{TW} = e\sqrt{2R_{TW}L_{TW}P_{TW}}\left(1-e^{-\frac{\pi\nu_{RF}L_{TW}}{v_gQ_{TW}}}\right)\sqrt{\frac{v_gQ_{TW}}{\pi\nu_{RF}L_{TW}}} - \left(1-e^{-\frac{\pi\nu_{RF}L_{TW}}{v_gQ_{TW}}}\right)\frac{v_gQ_{TW}eI_bR_{TW}}{\pi\nu_{RF}} \tag{4}$$

The relevant parameters of the TW structure are reported in Table 2.

The peak electric field value in the SW cavity is 40 MV/m. This choice was made to reduce the energy gain from 14 MeV to 11 MeV, in order to introduce the effect of beam loading in the ASTRA simulations. Therefore, this value should be understood as a loaded value, since the unloaded value of the peak electric field in the SW cavity is $\gtrsim$ 50 MV/m. In other words, a peak electric field of $\gtrsim$ 50 MV/m in the SW cavity can be achieved with the available RF power. However, due to the beam loading induced by the 100 mA beam current, this value will be reduced to 40 MV/m. Furthermore, the average accelerating field in the TW structure is chosen to be 26 MV/m, although the C-band structure can be powered in such a way as to obtain fields up to 40 MV/m. The reason for this choice was due to radiation protection limitations since the prototype linac can be operated with a maximum energy of 24 MeV.

4.3.3 Transverse and longitudinal dynamics

The beam size evolution along the accelerator is determined by two opposite effects: emittance pressure and space-charge, which induce an increase of the beam size in the transverse plane $x - y$ during the beam propagation, and RF focusing acting in the opposite direction. Figure 12 (left) shows the rms transverse beam size evolution along the linac.

The beam is initially overfocused as it exits from the cathode and is captured by the SW cavity. Then the beam size increases for the combined effects of space charge (especially at low energy in the SW structure) and emittance pressure, reaching, toward the end of the machine, an rms value of almost saturation equal to 0.8 mm. In the following drift, the beam size increases linearly due to its natural divergence. Finally, in the TW structure, the RF field refocuses the beam while accelerating it.

The longitudinal dynamics of the beam, i.e. the evolution of the bunch length and relative momentum spread is reported in Figure 12 (right). It is worth specifying that the relative momentum spread, understood as spread of longitudinal momentum, and the relative energy spread, are essentially equivalent concepts for relativistic particles, for the energy is proportional to the momentum via the speed of light in vacuum c. The ASTRA simulations for a single bunch are performed assuming a cathode which thermally emits electrons for 175 ps, corresponding to one period of the C-band RF wave. Therefore the bunch length is "zero" at $z = 0$, since no electron has been emitted yet. While electrons are emitted in front of the cathode, they are injected into the SW cavity and a bunch is formed,

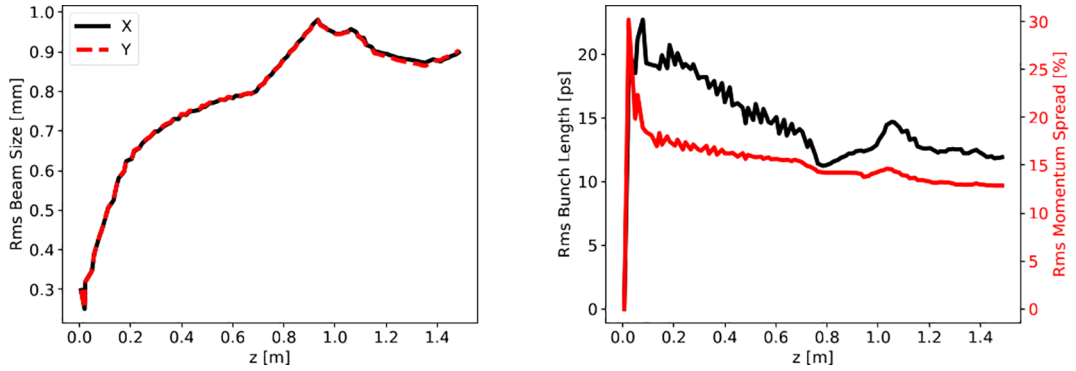

FIGURE 12
Left: beam envelopes of the accelerating beam. The transverse rms beam size is increased by emittance pressure and space-charge effects. No focusing elements are present on the line except for the RF structures. Right: rms bunch length and momentum spread of the accelerating beam. The final value for the bunch length falls around 13 ps, while the momentum spread at the end of the accelerator is around 15%.

with its own length and spread of energies. The rms bunch length is slightly reduced during bunching/capture of the beam in the first cells of the SW structure, then it reaches a constant value as the beam accelerates on-crest at relativistic energies in both SW and TW structures.

The rms relative energy spread is approximately constant below 15% in the SW accelerating structure and it is slightly reduced in the TW structure.

4.3.4 Compensation of the energy spread induced by RF pulse shape and beam loading

The powers in the SW and TW accelerating structures needed to obtain the final nominal design beam energy, as discussed above, can be reached after the RF pulse compression in the dedicated SLED cavity.

Before being compressed and distributed to the SW and TW lines, the RF input pulse to the compressor, as it comes out from the klystron, is a square 5 MW pulse, 5 μs long.

In this section, we present the study of the energy spread along the beam due to the combination of the pulse compressor and the beam loading, corresponding to a compression factor of 3 and with T_{RF} = 1.67 μs. This case is consistent with the pulse compressor design described in Sec. 4.2.2. Such a value for the compression factor has been chosen as a compromise between the compressed length of the RF pulse (to be larger than the current pulse length of 1 μs) and the optimal values of attainable energy gain and spread along the electron current pulse.

Typical shapes for compressed pulses at the exit of the SLED cavity are reported in the left side of Figure 13 (dashed red lines). They are obtained through analytical calculations based on the equations reported in the following. The pulse entering into any of the accelerating structures, say the SW or the TW, is slightly modified by the time constant of the cavities. However, the typical descending slope of the compressed pulses exiting the SLED is also present in the RF pulses feeding the accelerating structures. To obtain the unloaded power $P_{SW}^{unloaded}$ in the SW cavity (black line in top-left plot of Figure 13), the latter can be modeled by a lumped resonant circuit model. We consider a circuit with an inductance $L = 1/(4\pi^2 \nu_{RF}^2 C)$, a capacitance $C = Q_{SW}/(2\pi\nu_{RF} R_{SW} L_{SW})$, and a resistance $R_{SW} L_{SW}$, driven by a current generator that supplies a current $I(t)$ at frequency ν_{RF}. The compressed pulse after the SLED cavity, P_{SLED} can be modeled via equations provided by the work of Farkas et al. (40). The circuit equation to be solved for the SW cavity is (21):

$$\frac{\dot{I}}{C} = \ddot{V} + \frac{\dot{V}}{R_{SW}\ L_{SW} C} + 4\pi^2 \nu_{RF}^2 V \tag{5}$$

where the definition of the generator current is chosen to fit Equation 3, namely:

$$I(t) = \frac{2\sqrt{\beta_{SW} P_{SLED}(t)}}{(1+\beta_{SW})\sqrt{R_{SW} L_{SW}}} \tag{6}$$

It is worth noting that P_{SLED} here denotes only the fraction of compressed power sent to the SW cavity.

Using the method of the Laplace transform, the low-frequency (neglecting oscillations at ν_{RF}) analytical solution of Equation 5, with I(t) given by Equation 6, can be easily found. The obtained voltage allows calculating the unloaded SW power dissipated in the cavity defined as:

$$P_{SW}^{unloaded}(t) = \frac{V^2(t)}{R_{SW} L_{SW}} \tag{7}$$

The power given by Equation 7 is shown in the top-left plot of Figure 13, with a black curve.

The maximum energy gain of the beam due to this power in the SW structure would be 14 MeV. However, this value is reduced by the beam loading term that can be expressed as a function of time as (47):

$$\Delta W_{SW}^{bl}(t) = \frac{\pi e I_b R_{SW} L_{SW}}{Q_{SW}} \left(\frac{1 - e^{-\frac{\pi}{Q_{SW}}(1+\beta_{SW})(\nu_{RF} t+1)}}{1 - e^{-\frac{\pi}{Q_{SW}}(1+\beta_{SW})}} - \frac{1}{2} \right) [\theta(t - t_{0,SW}) - \theta(t - t_{0,SW} - T_b)] \tag{8}$$

Such a beam energy drop is responsible for a reduction of the maximum energy gain in the SW structure to about 11 *MeV* for the last bunch in the beam current pulse. In Equation 8 we have

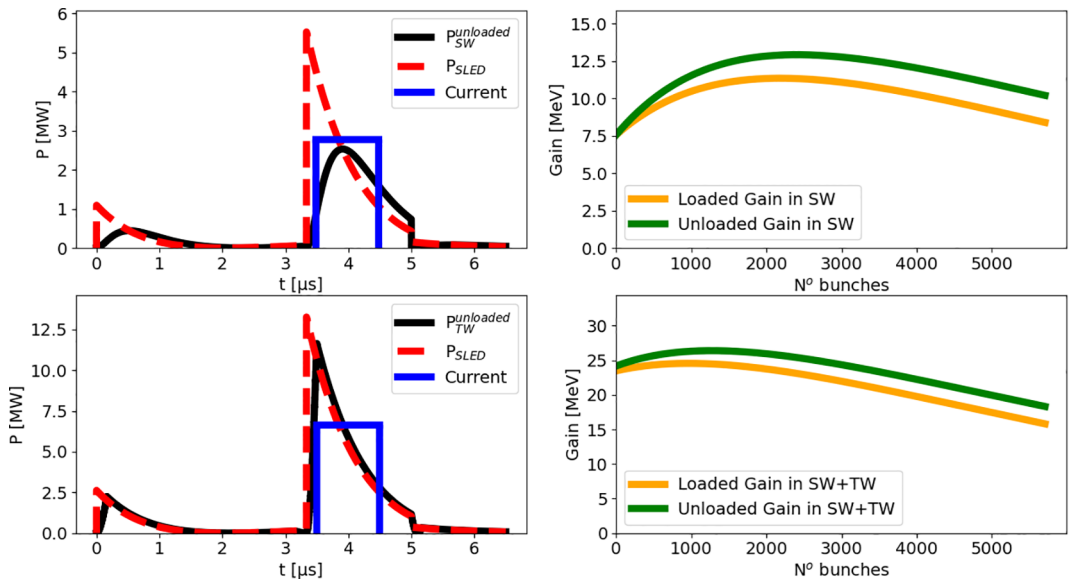

FIGURE 13
Top-left: compressed pulse (dashed red, T_{RF} = 1.67 μs) entering the SW cavity, RF pulse shape in the SW cavity (black), temporal position of the 1 μs train of bunches (blue pulse, arbitrary units). Top-right: Bunch energy along the 1 μs train after the SW cavity. Bottom-left: analog to top-left row but for the TW structure. Bottom-right: Bunch energy along the 1 μs train at the end of the accelerator.

introduced the Heaviside function θ, the injection time of the beam current pulse in the SW structure $t_{0,SW}$ and the duration of the beam current pulse . It is interesting to notice that for $\nu_{RF}t >> 1$, ΔW_{SW}^{bl} tends to the value expressed by the second term in Equation 3, demonstrating the self-consistency of our analytic approach.

A circuital approach may be significantly more complicated for the study of the RF pulse shape in the TW structure. Therefore, to study the in-cavity pulse shape, we use the expression that describes the unloaded power experienced by a bunch of electrons while traversing the whole TW structure (48):

$$P_{TW}^{unloaded}(t) = P_{0,TW}\left[\int_0^{L_{TW}} \frac{dz}{L_{TW}} \frac{E_{SLED}\left(t-\frac{z}{v_g}\right)}{E_0} e^{-\frac{2\pi\nu_{RF}z}{2Q_{TW}v_g}} \theta\left(t-\frac{z}{v_g}\right)\right]^2 \tag{9}$$

where E_{SLED} is the electric field exiting the SLED cavity [calculated by the same model in (40)] and E_0 its maximum. Moreover, $P_{0,TW}$ is the power available for the TW structure after compression and split.

Equation 9 can be derived from the study of the energy flow in a TW structure. The reduction in beam energy gain due to beam loading in the TW structure as function of time is (48):

$$\Delta W_{TW}^{bl}(t) = eI_bR_{TW}\int_0^{L_{TW}}\left[\left(1-e^{-\frac{\pi\nu_{RF}t}{Q_{TW}}}\right)\theta(t) + \left(e^{-\frac{\pi\nu_{RF}t}{Q_{TW}}} - e^{-\frac{\pi\nu_{RF}z}{Q_{TW}v_g}}\right)\theta\left(t-\frac{z}{v_g}\right)\right]dz \tag{10}$$

It is possible to verify that in the limit $\nu_{RF}t >> 1$, and for low attenuation along the structure ($\pi\nu_{RF}L_{TW}/Q_{TW}v_g << 1$), Equation 10 tends exactly to the second term in Equation 4. In Figure 13 the time $t_{0,TW}$ represents the injection time of the beam current pulse in the TW accelerating structure. For the TW structure, the energy drop induced by the beam loading amounts to about 1 MeV, so most of the energy spread distributed along the bunch train is due to the shape of the RF pulse. Synchronizing the start of a T_b = 1 μs long electron current pulse with the RF pulse peak in the TW structure would mean accelerating the first bunches of the train to higher energies and the tail bunches to lower energies (due to the RF pulse slope), i.e. inducing energy spread along the bunch train. Indeed, in 1 μs of the RF pulse oscillating at the RF frequency ν_{RF}= 5.712 GHz, a train of 5712 electron bunches is obtained. Furthermore, another source of energy spread is given by beam loading in the accelerating structures. An optimal injection time of the beam current pulse with respect to the in-cavity RF pulse would flatten to some extent the energy spread induced by the combined action of beam loading and RF pulse shape. The right-hand side of Figure 13 shows the bunch energy along the 1 μs train corresponding to the optimized injection times $t_{0,SW}$ and $t_{0,TW}$, for the case of a compression factor equal to 3. For the calculation of the energy gain along the train of bunches in the SW cavity we have used (47):

$$Gain\ \ in\ \ SW\ \ cavity$$
$$= \frac{2e\sqrt{R_{SW}L_{SW}\beta_{SW}P_{SW}^{unloaded}\left(t=\frac{N}{\nu_{RF}}\right)}}{1+\beta_{SW}} - \Delta W_{SW}^{bl}(N)$$

while for the TW structure, analogously (48):

$$Gain\ \ in\ \ TW\ \ cavity$$
$$= \sqrt{\frac{2\pi\nu_{RF}L_{TW}}{v_gQ_{TW}}R_{TW}L_{TW}P_{TW}^{unloaded}\left(t=\frac{N}{\nu_{RF}}\right)} - \Delta W_{TW}^{bl}(N)$$

We conclude by specifying that the power fractions 30% and 70% in Figure 13 refer to the total available power reduced by 25%,

in order to consider both possible losses along the transmission line and power attenuation, the latter exploited to maintain the average final electron energy to a maximum of 24 MeV.

5 Dose profiles

As a reference for the dose distributions delivered to a patient, we considered the corresponding ones in water produced by a train of bunches with the energy distribution shown in Figure 14 (left), obtained as a histogram of the bottom-right plot in Figure 13 with the SLED compression factor discussed in the previous section. This spectrum represents the distribution of the mean energy of the single bunches contained in the current pulse. For simplicity, the single bunch energy spread (Energy $\simeq p_z c$) of the kind shown in the right-end side of Figure 14 has been neglected since it constitutes only a small correction to the final electron energy distribution.

This energy spectrum directly influences the dose distribution delivered to the patient. As a case study, we analyzed the dose deposition in a water volume, representing patient tissue, using simulations performed with FLUKA. The resulting 2D dose distribution is shown on the left-end side of Figure 15, presented on a logarithmic scale. For comparison, the center of the same figure illustrates the case of a monoenergetic beam with energy equal to the mean energy of the spectrum shown in Figure 14 (left), equal to 21.13 MeV. The small initial transverse size, around 1-2 mm FWHM, is due to the fact that the linac produces a pencil beam at the exit of the TW. However, electron diffusion in water, caused by multiple scattering and photon production by means Bremsstrahlung process, dominates the beam's transverse spread after just a few cm of depth.

The longitudinal integrated dose distributions for the same cases are presented on the right-hand side of the same figure. The green line represents the dose profile from the simulation using the energy spectrum of Figure 14 (left), while the red line corresponds

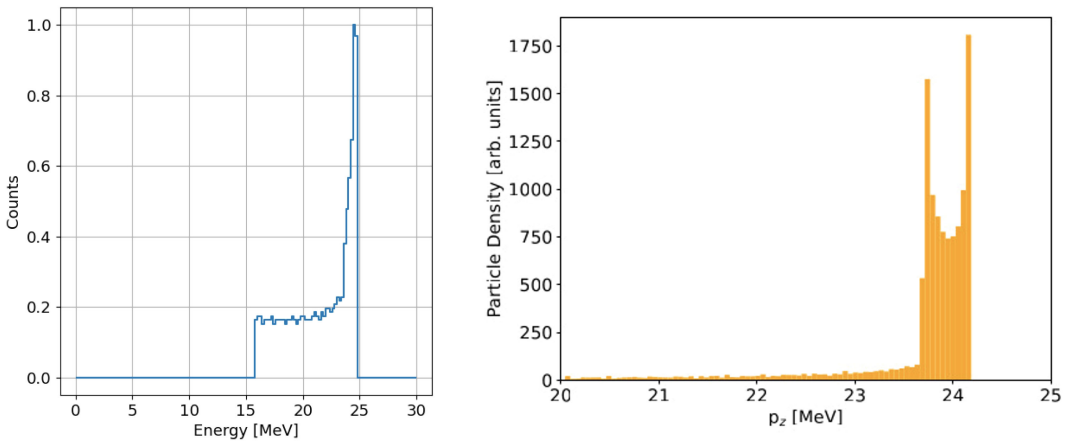

FIGURE 14
Left: energy distribution of a train of bunches with an RF pulse duration of 1.67 μs. The number of counts is normalized to its maximum. Right: energy spectrum of the single bunch simulated by ASTRA at the exit of the accelerator.

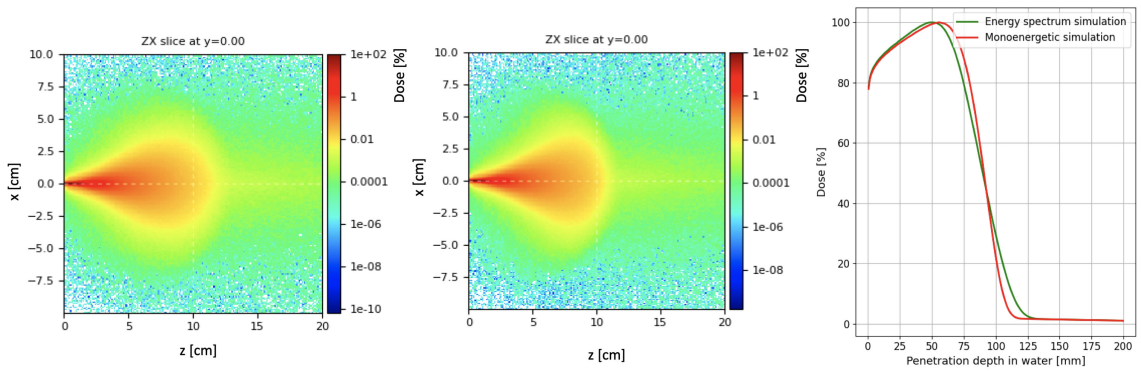

FIGURE 15
Normalized map dose in logarithmic scale considering the energy spectrum reported in Figure 14 (left) and with monoenergetic beam (center). Percentage dose profile as a function of the penetration depth in water (right) for the two energy spectra.

to the dose obtained with the mono-energetic beam. The dose peak, which differs by a few percent compared to the mono-energetic case ($3.69{\cdot}10^8$ and $3.71{\cdot}10^8$ Gy/primary for the energy distribution and mono-energetic beam simulations, respectively), appears in the real case to be shifted a few millimeters backward relative to the mono-energetic beam, due to the contribution of low-energy electrons.

6 Conclusions and future developments

This paper presents the design of a VHEE linac prototype to be built at the University of Rome La Sapienza, with two primary objectives: testing the acceleration scheme and associated technologies (C-band SW structure followed by a C-band TW structure) and providing UHDR electron beams to explore FLASH irradiation techniques and conduct radiobiological experiments. It also represents a foundational step toward the development of a compact VHEE linac capable of reaching 100 MeV energy levels.

Future integration of VHEE linacs into clinical settings will require targeted research and development to address key challenges. These include optimizing treatment planning systems for FLASH delivery, establishing reliable quality assurance protocols, and improving patient positioning and immobilization techniques. Additionally, extensive clinical trials will be crucial to understanding the long-term effects of FLASH radiotherapy with VHEE beams on human health.

Data availability statement

The raw data supporting the conclusions of this article will be made available by the authors, without undue reservation.

Author contributions

LG: Investigation, Visualization, Writing – original draft, Writing – review & editing. MMi: Investigation, Methodology, Validation, Writing – original draft, Writing – review & editing. DA: Writing – review & editing. FC: Writing – review & editing. MCa: Writing – review & editing. EC: Investigation, Writing – review & editing. MCo: Software, Writing – review & editing. GC: Funding acquisition, Writing – review & editing. AC: Writing – original draft, Writing – review & editing. ADG: Writing – original draft. RDR: Conceptualization, Writing – review & editing. LFa: Writing – original draft, Writing – review & editing. SF: Investigation, Writing – original draft, Writing – review & editing. LFi: Conceptualization, Investigation, Writing – review & editing. DF: Writing – original draft. GaF: Writing – original draft, Writing – review & editing. GiF: Writing – review & editing. AG: Writing – review & editing. MMa: Writing – review & editing. GSM: Investigation, Software, Writing – review & editing. AM: Writing – review & editing. LP: Writing – original draft, Writing – review & editing. VP: Writing – review & editing. FP: Writing – review & editing. MP: Writing – review & editing. SP: Writing – review & editing. RR: Writing – review & editing. ASa: Writing – review & editing. ASc: Writing – review & editing. BS: Conceptualization, Supervision, Writing – review & editing. GT: Writing – original draft, Writing – review & editing. AV: Writing – review & editing.

Funding

The author(s) declare that financial support was received for the research, authorship, and/or publication of this article. The research has received funding from the European Union - NextGenerationEU through the Italian Ministry of University and Research under PNRR - M4C2-I1.3 Project PE-00000019 “HEAL ITALIA” to Sapienza University, and from INFN group V - FRIDA experiment.

Conflict of interest

The authors declare that the research was conducted in the absence of any commercial or financial relationships that could be construed as a potential conflict of interest.

The author(s) declared that they were an editorial board member of Frontiers, at the time of submission. This had no impact on the peer review process and the final decision.

Generative AI statement

The author(s) declare that no Generative AI was used in the creation of this manuscript.

Publisher’s note

Author disclaimer

The views and opinions expressed are those of the authors only and do not necessarily reflect those of the European Union or the European Commission. Neither the European Union nor the European Commission.

References

1. Limoli CL, Vozenin MC. Reinventing radiobiology in the light of flash radiotherapy. *Annu Rev Cancer Biol*. (2023) 7:1–21. doi: 10.1016/j.radonc.2019.04.008

2. Montay-Gruel P, Petersson K, Jaccard M, Boivin G, Germond JF, Petit B, et al. Irradiation in a flash: Unique sparing of memory in mice after whole brain irradiation with dose rates above 100gy/s. *Radiotherapy Oncol*. (2017) 124:365–9. doi: 10.1016/j.radonc.2017.05.003

3. Montay-Gruel P. Hypofractionated flash-rt as an effective treatment against glioblastoma that reduces neurocognitive side effects in mice. *Clin Cancer Res*. (2021) 27:75–784. doi: 10.1158/1078-0432.CCR-20-0894

4. Montay-Gruel P. Long-term neurocognitive benefits of flash radiotherapy driven by reduced reactive oxygen species. *Proc Natl Acad Sci U. S. A*. (2019) 166:10943–51. doi: 10.1073/pnas.1901777116

5. Alaghband Y. Neuroprotection of radiosensitive juvenile mice by ultra-high dose rate flash irradiation. *Cancers*. (2020) 12:1–21. doi: 10.3390/cancers12061671

6. Limoli CL. The sparing effect of flash-rt on synaptic plasticity is maintained in mice with standard fractionation. *Radiother. Oncol*. (2023) 186:109767. doi: 10.1016/j.radonc.2023.109767

7. Mascia AE. Proton flash radiotherapy for the treatment of symptomatic bone metastases: The fast-01 nonrandomized trial. *JAMA Oncol*. (2023) 9:62–9. doi: 10.1001/jamaoncol.2022.5843

8. Rohrer Bley C. Dose- and volume-limiting late toxicity of flash radiotherapy in cats with squamous cell carcinoma of the nasal planum and in mini pigs. *Clin Cancer Res*. (2022) 28:3814–23. doi: 10.1158/1078-0432.CCR-22-0262

9. Vozenin MC. The advantage of flash radiotherapy confirmed in mini-pig and cat-cancer patients. *Clin Cancer Res*. (2019) 25:35–42. doi: 10.1158/1078-0432.CCR-17-3375

10. Faillace L, Alesini D, Bisogni G, Bosco F, Carillo M, Cirrone P, et al. Perspectives in linear accelerator for flash vhee: Study of a compact c-band system. *Physica Med*. (2022) 104:149–59. doi: 10.1016/j.ejmp.2022.10.018

11. Palumbo L, Sarti A, Mostacci A, De Gregorio A, De Arcangelis D, Francescone D, et al. Safest. a compact c-band linear accelerator for vhee-flash radiotherapy. *J OF Phys*. (2023) 2687:5079–82. doi: 10.18429/JACoW-IPAC2023-THPM087

12. Bazalova-Carter M, Qu B, Palma B, Hårdemark B, Hynning E, Jensen C, et al. Treatment planning for radiotherapy with very high-energy electron beams and comparison of vhee and vmat plans. *Med Phys*. (2015) 42:2615–25. doi: 10.1118/1.4918923

13. Schüler E, Eriksson K, Hynning E, Hancock SL, Hiniker SM, Bazalova-Carter M, et al. Very high-energy electron (vhee) beams in radiation therapy; treatment plan comparison between vhee, vmat, and ppbs. *Med Phys*. (2017) 44:2544–55. doi: 10.1002/mp.12233

14. Sarti A, De Maria P, Battistoni G, De Simoni M, Di Felice C, Dong Y, et al. Deep seated tumour treatments with electrons of high energy delivered at flash rates: The example of prostate cancer. *Front Oncol*. (2021) 11:777852. doi: 10.3389/fonc.2021.777852

15. Muscato A, Arsini L, Battistoni G, Campana L, Carlotti D, De Felice F, Battistoni G, De Gregorio A, De Maria P, Fischetti M, Franciosini G, et al. Treatment planning of intracranial lesions with vhee: comparing conventional and flash irradiation potential with state-of-the-art photon and proton radiotherapy. *Front Phys*. (2023) 11:1185598. doi: 10.3389/fphy.2023.1185598

16. De Simoni M, Battistoni G, De Gregorio A, De Maria P, Fischetti M, Franciosini G, et al. A data-driven fragmentation model for carbon therapy gpu-accelerated monte-carlo dose recalculation. *Front Oncol*. (2022) 12:780784. doi: 10.3389/fonc.2022.780784

17. Schiavi A, Senzacqua M, Pioli S, Mairani A, Magro G, Molinelli S, et al. Fred: a GPU-accelerated fast-monte carlo code for rapid treatment plan recalculation in ion beam therapy. *Phys Med Biol*. (2017) 62:7482–504. doi: 10.1088/1361-6560/aa8134

18. Franciosini G, Battistoni G, Cerqua A, De Gregorio A, De Maria P, De Simoni M, et al. Gpu-accelerated monte carlo simulation of electron and photon interactions for radiotherapy applications. *Phys Med Biol*. (2023) 68:044001. doi: 10.1088/1361-6560/aca1f2

19. Kokurewicz K, Brunetti E, Curcio A, Gamba D, Garolfi L, Gilardi A, et al. An experimental study of focused very high energy electron beams for radiotherapy. *Commun Phys*. (2021) 4:33. doi: 10.1038/s42005-021-00536-0

20. El-Ashmawy M. Overall quality comparison of c-band and x-band medical linacs, In: *Proceedings of the 14th Symposium on Accelerator Science and Technology*, November 11-13, 2003, Tsukuba, Japan. (2003). pp. 1–3.

21. Wangler T. Rf linear accelerators. *Wiley New York*. (1998). doi: 10.1002/9783527623426

22. Hanna MS. Applications of X-band technology in medical accelerators, In: *Proceedings of the 1999 Particle Accelerator Conference*, New York City, March 29th - April 2nd, 1999. (1999). pp. 2516–8.

23. Kilpatrick WD. Criterion for vacuum sparking designed to include both rf and dc. *Rev Sci Instrum*. (1957) 28:824. doi: 10.1063/1.1715731

24. Tanabe E, Wang JW, Loew GA. Voltage breakdown at x-band and c-band frequencies. *Proc 1986 Int Linac Conf*. (1986) 860602:458–60. Available online at: https://inspirehep.net/literature/240748.

25. Wang J, Loew G. Field emission and rf breakdown in high-gradient room temperature linac structures. *Tech. rep. Stanford Univ. Stanford Linear Accelerator Center CA (US)*. (1997). doi: 10.2172/663321

26. Higo T, Higashi Y, Matsumoto S, Yokoyama K, Doebert S, Grudiev A, et al. Advances in x-band tw accelerator structure operating in the 100 mv/m regime. *Proc IPAC'10 Kyoto Japan*. (2010) 2010:3702–4. Available online at: https://accelconf.web.cern.ch/IPAC10/papers/thpea013.pdf.

27. Simakov EI, Dolgashev VA, Tantawi SG. Advances in high gradient normal conducting accelerator structures. *Nucl Instruments Methods Phys Res Section A: Accelerators Spectrometers Detectors Associated Equip*. (2018) 907:221–30. doi: 10.1016/j.nima.2018.02.085

28. Dolgashev VA, Faillace L, Spataro B, Tantawi S, Bonifazi R. High-gradient rf tests of welded *x*-band accelerating cavities. *Phys Rev Accel. Beams*. (2021) 24:081002. doi: 10.1103/PhysRevAccelBeams

29. Sakurai T, Ego H, Inagaki T, Asaka T, Suzuki D, Miura S, et al. *c*-band disk-loaded-type accelerating structure for a high acceleration gradient and high-repetition-rate operation. *Phys Rev Accel. Beams*. (2017) 20:42003. doi: 10.1103/PhysRevAccelBeams.20.042003

30. Fang W, Gu Q, Zhao Z, Tong D. The c-band traveling-wave accelerating structure for compact x-fel at sinap, In: *Proceedings of the second International Particle Accelerator Conference*, 4 to 9 September, 2011, San Sebastián, Spain (2011). pp. 133–5.

31. Alesini D, Bellaveglia M, Biagini M, Boni R, Brönnimann M, Cardelli F, et al. Design, realization and test of c-band accelerating structures for the sparc lab linac energy upgrade. *Nucl Instruments Methods Phys Res A*. (2016) 837:161–70. doi: 10.1016/j.nima.2016

32. Alesini D, Bellaveglia M, Gallo BSA, Lollo V, Pellegrino L, Piersanti L, et al. Design of high gradient, high repetition rate damped c-band rf structures. *Phys Rev Accelerators Beams*. (2017) 20:032004-1–032004-20. doi: 10.1103/PhysRevAccelBeams.20.032004

33. Alesini D, Boni R, Pirro GD, Raddo RD, Ferrario M, Gallo A, et al. The c-band accelerating structures for sparc photoinjector energy upgrade. *J Instrumentation*. (2013) 8:P05004. doi: 10.1088/1748-0221/8/05/P05004

34. Tantawi S, Nasr M, Li Z, Limborg C, Borchard P. Design and demonstration of a distributedcoupling linear accelerator structure. *Phys Rev Accel. Beams*. (2020) 23:92001. doi: 10.1103/PhysRevAccelBeams.23.092001

35. Nasr M, Nanni E, Breidenbach M, Weathersby S, Oriunno M, Tantawi S. Experimental demonstration of particle acceleration with normal conducting accelerating structure at cryogenic temperature. *Phys Rev Accel. Beams*. (2021) 24:93201. doi: 10.1103/PhysRevAccelBeams.24.093201

36. Miller RH. Comparison of standing-wave and traveling-wave structures. *SLAC-PUB*. (1986) 3935:200–5. Available online at: https://digital.library.unt.edu/ark:/67531/metadc1063921/.

37. Giuliano L, Carillo M, Chiadroni E, De Gregorio A, Ficcadenti L, Francescone D, et al. Safest project, a compact c-band rf linac for vhee flash radiotherapy, In: *Proceedings of the International Particle Accelerator Conference*, 19-24 May 2024, Nashville TN. JACoW Publishing, Proc. IPAC 24. (2024) pp. 3643–6. doi: 10.18429/JACoW-IPAC2024-THPR55

38. Xiang S, Yue Y, Yuzheng L. Rf phase focusing and asymmetric field shape in standing-wave electron linacs, In: *Proceedings of the first Asian Particle Acceleration Conference APAC 1998*, Tsukuba, Japan, March 23 to 27, 1998. (1998). pp. 184–6.

39. Rosenzweig J, Serafini L. Transverse particle motion in radio-frequency linear accelerators. *Phys Rev E*. (1994) 49:1599–602. doi: 10.1103/PhysRevE.49.1599

40. Farkas Z, Hogg H, Loew G, Wilson PB. Sled: A method of doubling slac's energy, In: *Proceedings of 9th International Conference on the High-Energy Accelerators (HEACC 1974)*, Stanford, California, May 2-7, 1974. (1974). p. 576.

41. Multiphysics C. Introduction to comsol multiphysics®. In: *COMSOL Multiphysics*. Burlington, MA: COMSOL. (1998). p. 32.

42. *CST* (2022). Available online at: https://www.3ds.com/products-services/simulia/products/cst-studio-suite/ (Accessed February 25, 2025).

43. Faillace L, Barone S, Battistoni G, Di Francesco M, Felici G, Ficcadenti L, et al. Compact *s*-band linear accelerator system for ultrafast, ultrahigh dose-rate radiotherapy. *Phys Rev Accel. Beams*. (2021) 24:50102. doi: 10.1103/PhysRevAccelBeams.24.050102

44. Giuliano L, Bosco F, Carillo M, Felici G, Ficcadenti L, Mostacci A, et al. Rf design and measurements of a c-band prototype structure for an ultra-high dose rate medical linac. *Microwave Measurements Methods Instruments Science Soc Industry*. (2023) 7:10. doi: 10.3390/instruments7010010

45. Alesini D, Alessandro G, Bruno S, Marinelli A, Palumbo L. Design of couplers for traveling wave rf structures using 3d electromagnetic codes in the frequency domain. *Nucl Instruments Methods Phys Res Section A Accelerators Spectrometers Detectors Associated Equip*. (2007) 580:1176–83. doi: 10.1016/j.nima.2007.06.045

46. Flottmann K. Astra: A space charge tracking algorithm(2022). Available online at: http://www.desy.de/~mpyflo (Accessed February 25, 2025).

47. Boussard D. Beam loading. *CERN-SPS-86-10-ARF*. (1987). Available online at: https://cds.cern.ch/record/167557.

48. Lunin A, Yakovlev V, Grudiev A. Analytical solutions for transient and steady state beam loading in¡? format?¿ arbitrary traveling wave accelerating structures. *Phys Rev Special Topics—Accelerators Beams*. (2011) 14:052001. doi: 10.1103/PhysRevSTAB.14.052001

frontiers | Frontiers in Physics

TYPE Original Research
PUBLISHED 29 April 2025
DOI 10.3389/fphy.2025.1474416

OPEN ACCESS

EDITED BY
Paola Ballesteros Zebadua,
Manuel Velasco Suárez National Institute of Neurology and Neurosurgery, Mexico

REVIEWED BY
Imran Iqbal,
Yale University, United States
Veljko Grilj,
Centre Hospitalier Universitaire Vaudois (CHUV), Switzerland

*CORRESPONDENCE
L. Masturzo,
luigi.note.masturzo@gmail.com

RECEIVED 01 August 2024
ACCEPTED 18 April 2025
PUBLISHED 29 April 2025

CITATION
Del Sarto D, Masturzo L, Cavalieri A, Celentano M, Fuentes T, Gadducci G, Giannini N, Gonnelli A, Milluzzo G, Paiar F, Pensavalle JH, Romano F and Di Martino F (2025) A systematic investigation on the response of EBT-XD gafchromic films to varying dose-per-pulse, average dose-rate and instantaneous dose-rate in electron flash beams.
Front. Phys. 13:1474416.
doi: 10.3389/fphy.2025.1474416

A systematic investigation on the response of EBT-XD gafchromic films to varying dose-per-pulse, average dose-rate and instantaneous dose-rate in electron flash beams

D. Del Sarto[1,2], L. Masturzo[2,3]*, A. Cavalieri[1,2], M. Celentano[2,3], T. Fuentes[2,4], G. Gadducci[2,4], N. Giannini[2,4], A. Gonnelli[2,4], G. Milluzzo[5], F. Paiar[2,4,6], J. H. Pensavalle[2,3], F. Romano[5] and F. Di Martino[2,3]

[1]Center for Instrument Sharing of the University of Pisa (CISUP), University of Pisa, Pisa, Italy, [2]Centro Pisano ricerca e implementazione clinica Flash Radiotheraphy (CPFR), Presidio S. Chiara, Pisa, Italy, [3]U.O. Fisica sanitaria, Azienda Ospedaliero-Universitaria Pisana, Pisa, Italy, [4]Department of Translational Research and New Technologies in Medicine and Surgery, University of Pisa, Pisa, Italy, [5]National Institute of Nuclear Physics (INFN), Section of Catania, Catania, Italy, [6]Department of Radiation Oncology, Azienda Ospedaliero-Universitaria Pisana, University of Pisa, Pisa, Italy

Background: The FLASH effect is a radiobiological phenomena characterized by the reduction of the damage to healthy tissues while maintaining iso-effectiveness on the tumour, obtained by delivering the entire radiation dose in less than 100–200 m and with average dose rate greater than 40–100 Gy/s. Despite the enormous interests of the scientific community, a series of issues must be addressed and overcome to reach its clinical implementation. One of these challenges is related to the dosimetry of ultra-high dose-per-pulse (UHDP) beams, which trigger the effect. The most used dosimeters to date in radiobiological experiments with ultra-high dose rate (UHDR) beams are the radiochromic films. However, a systematic and accurate study of their response by varying dose-per-pulse and dose rate over a wide range has never yet been done.

Purpose: To systematically investigate the response of EBT-XD radiochromic films under UHDR electron beam irradiations by varying different beam parameters independently and over a wide range and using flashDiamond as reference.

Materials and Methods: Thanks to a special research linac, average dose rate (ADR), dose-per-pulse (DP) and instantaneous dose rate (IDR) dependencies on film response have been individually investigated. The reference value of ADR, DP and IDR has been calculated by measuring the dose using a flashDiamond and knowing the temporal beam structure provided by the beam monitoring system of the Linac.

Results: Our results normalized to fD showed an overresponse of the radiochromic films, compared to a conventional irradiation, for ADR values higher than 1000 Gy/s and an IDR higher than 1 MGy/s which could represent a total dose overestimation of about 10%.

Discussion: The gafchromic film EBT-XD have their field of application in UHDP beam dosimetry, considering their excellent spatial resolution; However, particular attention must be paid when using this type of dosimeter for absolute dose measurements at very extreme values of IDR (>1 MGy/s).

KEYWORDS

FLASH radiotherapy, dosimetry, gafchromic films, dose-rate dependence, UHDR regime

1 Introduction

In recent years, the field of radiotherapy has undergone a significant paradigm shift with the emergence of a groundbreaking and promising modality known as FLASH radiotherapy. This innovative approach entails the administration of treatment at ultra high dose-rates (>40 Gy/s), a stark departure from conventional radiotherapy techniques with dose rates of approximately ~ 1–5 Gy/min. The exploration and investigation of FLASH radiotherapy have garnered substantial attention from research teams worldwide, as evidenced by a growing body of literature spanning various studies [1–4]. However, despite the growing body of evidence supporting the existence and potential clinical significance of the FLASH effect, the underlying principles governing this phenomenon remain to be discovered. To design and execute an experiment focusing on the FLASH effect, meticulous attention must be directed towards establishing robust and rigorous dosimetry protocol. This involves a comprehensive consideration of all the fundamental beam parameters associated with the FLASH effect, such as the average dose-rate (ADR), dose-per-pulse (DP), and instantaneous dose-rate (IDR) [5]. Given the extraordinary irradiation conditions requisite for triggering the FLASH effect, conventional reference active dosimeters have proven inadequate [6]. Although corrective methodologies have been proposed [7, 8] they have fallen short in meeting the exacting dosimetry requirements indispensable for radiobiological investigations. In the last years numerous research groups are actively developing specialized FLASH active dosimeters [9–13] and new methods to correct conventional active dosimeters in UHDP conditions. In this context, passive dosimeters, such as radiochromic films, maintain their field of application, considering also their very good spatial resolution [14].

Radiochromic films, widely recognized for their dose rate independence [15–19], have been widely used both in characterizing FLASH sources [5, 20, 21] and in the dosimetry of radiobiological experiments [22–24]. Despite the inconvenience of a delayed dosimetric readout spanning one to 2 days, radiochromic films have enjoyed decades of application in the realm of radiotherapy. Various well-established protocols exist, and their clinical application has undergone comprehensive scrutiny.

Moreover, the advent of deep learning techniques for image classification could speedup and simplify the employment of large batches of films [25]. Determining the response of radiochromic films to UHDR irradiation is a relatively recent development [17, 19]. Several types of radiochromic films, including EBT3, EBT-XD, and OC1, have undergone testing with a range of UHDR sources, including pulsed electrons [17, 26] of varying energies and protons [19]. The collective evidence from these investigations suggests that radiochromic films do not exhibit a pronounced dependency on ADR, within an uncertainty margin of approximately 4% [17, 19]. However, these works have certain limitations due to the use of devices that do not allow for controlled variation of beam parameters independently of one another. Additionally, the findings have not been validated by alternative measurements using accurate dosimeters that are independent of dose rate. The present study aims to provide a comprehensive analysis of Gafchromic EBT-XD films, exploring their sensitivity to the primary beam parameters under UHDR conditions. We compare their response with measurements made using a prototype detector, which has been extensively tested and its dose rate independence verified through comparisons with DP-independent dosimeters [9].

2 Materials and Methods

The irradiations, performed using 9 MeV electron beams, were conducted at the ElectronFlash linac of the Centro Pisano for FLASH Radiotherapy (CPFR) [5], which features a unique triode gun and a dual ACCT monitoring system. Given the ability to maintain consistent irradiation setups while independently varying ADR, DP, and IDR (while preserving the same energy spectrum), this study aims to disentangle the distinct dependencies among these variables and reduce the uncertainties observed in previous studies.

2.1 Radiochromic film preparation

We employed Gafchromic EBT-XD radiochromic films (Ashland ECC), which exhibit an optimal response range when exposed to doses ranging from 0.4 cGy to 40 Gy. The films were cut into 1″ x 1″ squares from multiple 10″ x 8″ sheets, and each piece was assigned a unique number in the upper right corner to ensure consistent orientation during subsequent scans and irradiations. Our film batch was identified by the lot number 05262101. The films were stored in a tight black envelope kept in an environment with no radiation exposure. To acquire the film images, we used an Epson

10000XL flatbed scanner in transmission, whose reading panel was masked with a thick black sheet featuring a $1'' \times 1''$ aperture in the center. This was done to eliminate lateral light contributions and ensure that the same region of the flat panel captured the data, thereby minimizing scanner inhomogeneity. We configured the acquisition software to operate in positive film acquisition mode, resulting in 48-bit color images in lossless TIFF format with a resolution of 127 dpi. The scanner focus was set to 0.

Each film underwent three consecutive scans shortly before and 24 h after irradiation. While the impact of multiple scans on the film is negligible, this procedure enabled us to assess the error σ_{scan} associated with the scanner. We calculated the net optical density (netOD) for each film by analyzing the pixel values (PV) within a circular central ROI of 10 pixel radius (i.e., 2 mm radius). Each image was processed using a Wiener 2D adaptive filter to reduce noise. We calculated the netOD using the following formula (Equation 1):

$$\mathbf{netOD} = \mathbf{log_{10}}\left(\frac{\mathbf{PV_{before}}}{\mathbf{PV_{after}}}\right) \quad (1)$$

Where PV_{before} and PV_{after} the pixel values before and after the exposition of the radiochromic film to the radiation, averaged over the three repeated scans.

Once we characterized the beam output with the flashDiamond dosimeter, we generated a calibration curve by exposing the films to a defined range of doses, from 0.5 Gy to 60 Gy, with an ADR of 0.04 Gy/s and DP of 0.04 Gy (e−gun current of ~4 mA). Films were positioned at the build-up point (13 mm in solid water sheets). The choice of using directly the electron beam rather than a photon beam (from another clinical machine) was made primarly to ensure the same energy spectrum cahracterized with the flashDiamond. This enabled us to establish a functional relationship between the dose and the netOD through data fitting. The relationship can be expressed as:

$$\mathbf{D} = \mathbf{a} \cdot \mathbf{netOD} + \mathbf{b} \cdot \mathbf{netOD^n} \quad (2)$$

For this first set of measurements, we used two films that were uniformly irradiated by a 100 mm diameter flat beam (flatness of 4.03% [5]), and each dose measurement was repeated twice.

2.2 Dosimetric acquisition chain

We utilized a PTW flashDiamond (fD, SN:220,439, REF:TW60025) as an additional monitoring system alongside the beam current transformers (BCTs) integrated into the linac [5]. This detector is known for its capability to function effectively under FLASH irradiation conditions without displaying significant saturation effects and has been employed in UHDR linac commissioning procedures in the past [9, 27, 28]. We also tested the fD dependence of the PRF, and its response was totally indipendent of it in the range of interest (1–245 Hz). The fD was connected to a PTW UNIDOS electrometer. To prevent potential issues, an external box provided by PTW was used between the diamond detector's triaxial cable plug and the electrometer's signal input. This box contained a RC circuit, which helped to smooth the current

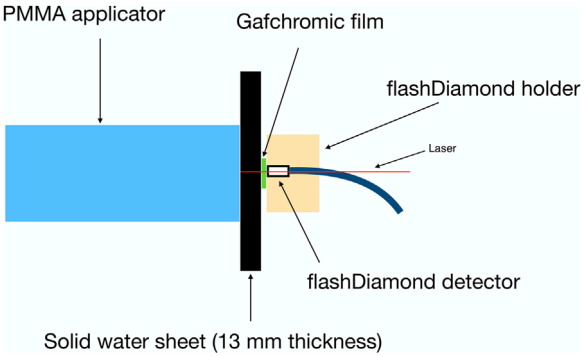

FIGURE 1
Experimental setup used for irradiations, showing the position of the flashDiamond (fD) relative to the GAF measurement position.

pulses from the diamond prototype and prevent excessively high peak currents at the electrometer input [29]. This technique has been demonstrated to not produce any artifacts in the test results [27]. We positioned the EBT-XD films inside a RW3 plastic phantom at a water-equivalent depth corresponding to the R_{100} value (13 mm for a 4 mA e-gun current) obtained from the PDD (Percentage Dose Depth curve). The positioning depth of the films was kept constant, although the R_{100} value changes very slightly (by a total of ~2 mm) when the e-gun current is increased to 100 mA.

The plastic phantom slabs were positioned perpendicular to the beam axis. Using a workbench with adjustable solid water thicknesses, we were able to fix the setup relative to the LINAC and adjust the distance along the beam axis. Centering was achieved by precisely moving the setup closer to or further from the applicator as needed. Additionally, to ensure accurate alignment with the beam center, a laser mounted at the center of the applicator was used to align each component (solid water, GAF film, and fD).

As can be seen in Figure 1, the fD detector was positioned behind the EBT-XD film (with a 1 mm distance of the two points of measurements due to the inherent thickess of the fD(9)), precisely aligned with its center, and enclosed in a 120 mm diameter PMMA cylindrical holder. Using this configuration, we irradiated the Gafchromic films and simultaneously obtained a charge reading from the fD, allowing us to establish an alternative (to the beam monitoring system based on an ACCT signal) correlation between the film response and the beam output. Furthermore, this setup enabled us to account for any output variation from the LINAC.

2.3 Irradiation parameters

The investigation of the film response was studied varying the ADR, the DP and the IDR to assess their individual effect. Throughout the irradiations, we maintained the same amount of total dose delivered to the film and small dose variations were corrected correcting the netOD to the flashDiamond charge reading (see Equation 3). Each measurement point was repeated five times with five different films. A summary of all the irradiation conditions is reported in Table 1. We explored the dependence on the ADR using two different DP values (obtained variying the e-gun current): 3.27 Gy and 13.18 Gy. A total

TABLE 1 Irradiation conditions of the key dosimetric parameters (i.e., Average Dose-Rate (ADR), Dose-per-Pulse (DP) and Instantaneous Dose-Rate (IDR)) along with irradiation parameters (i.e., beam current and pulse duration) explored in this study.

Investigated dependency	Pulse repetition frequency (PRF)	Beam current	Pulse duration	Beam parameters
ADR	Variable intra-set [1, 80, 160, 245 Hz]	Fixed for each set	4μs	Variable ADR [3.64 Gy/s – 4845 Gy/s] Fixed DP [3.27; 13.18 Gy] Fixed IDR [0.82; 3.3 MGy/s]
DP	Variable [adjusted to obtain fixed ADR in the range 3.64–4845 Gy/s]	Variable [100–3.6 mA]	4μs	Fixed ADR [155 Gy/s] Variable DP [0.7–19.3 Gy] Variable IDR [0.18–4.82 MGy/s]
IDR	155 Hz	Variable [adjusted to obtain fixed DP]	Variable [adjusted to obtain fixed DP in the range 1–4 us]	Fixed ADR [3018 Gy/s] Fixed DP [13.0 Gy] Variable IDR [3.5-4-4.8 MGy/s]

number of 12 consecutive pulses were delivered for the lower DP setting while 3 pulses were used for the higher DP. The pulse duration was fixed (4 μs) leading to a constant IDR for each of the two DP settings. The PRF was varied from 1, 80, 160 and 245 Hz and the explored ADR ranged from 3.56 Gy/s to 4845 Gy/s.

On the other hand, the possible dependence of the film response on the DP was investigated keeping the same total dose delivered and varying the PRF to have the same ADR of 155 Gy/s for all the irradiations, by adjusting the number of pulses. We modified the beam current to obtain seven different values of DP ranging from 0.7 Gy to 19.3 Gy. The IDR varied from 0.18 MGy/s to 4.82 MGy/s.

Finally, to investigate the possible effect of the IDR, we fixed a DP value of 13.0 Gy (obtained by changing three different beam currents and respectively adjusting the pulse duration). The pulse repetition frequency was maintained at a fixed value of 155 Hz, and the number of pulses delivered was set to three. Consequently, we obtained three distinct IDR values: 3.5, 4.0, and 4.8 MGy/s at fixed ADR (i.e., 3018 Gy/s) and DP.

3 Results

We obtained the calibration curve by fitting the measured dose as a function of the netOD using the curve presented in Equation 2. The fitting procedure accounted for uncertainties in both the netOD and the dose. The resulting calibration curve is shown in Figure 2, and the fitting parameters are presented in Table 2.

The sensitivity of the film at a given dose level was determined by performing a Taylor expansion of the function and then inverting it. For small differences in dose, we can obtain a corresponding difference in optical density using the Equation 4:

$$\Delta netOD = \frac{\Delta D}{a + b \cdot n \cdot netOD^{n-1}}\Big|_{netOD=netOD_0} \quad (3)$$

Considering that the dose delivered to the film for the netOD dependence study is about 40 Gy, a variation of 2% in dose would lead to a variation of 0.8% of the netOD.

The acquired data and the corresponding fit are presented in Figure 2.

To evaluate the influence of each irradiation parameter to the film response, we first investigated the dependence on ADR. The results of fixed total delivered dose at several ADR values and two different DP settings are shown in Figure 3. In particular, the corrected netOD (which represents the read netOD, corrected to the dose measured with the flashDiamond) as a function of the ADR for DP values of 3.27 Gy and 13.18 Gy is shown. For ADR less than about 1000 Gy/s, the response in terms of netOD (normalized to the fD charge) remained relatively constant for both DP settings, with data points fluctuating randomly. However, as ADR increased, we observed a slight (approximately 2.3%) overresponse normlized against fD, with data points consistently above the average values obtained for ADR lower than 1000 Gy/s. Given the observed slight dependence on the ADR, we conducted subsequent measurements by fixing it and investigate any other possible dependences.

Figure 4 illustrates the normalized response (against fD) of the films to varying DP for an ADR of 155 Gy/s. It is evident from the figure that the normalized netOD increases in a significative way, around 4.5%, starting monotonically from a DP of 5 Gy onward.

The data acquired at a constant DP of 13.0 Gy obtained by varying the IDR are presented in Figure 5, alongside the data obtained by converting the variable DP shown in Figure 4 into the corresponding IDR. It can be observed that there is a good agreement between the two datasets, and the difference between GAF reponse againts fD can be seen even when only the IDR is higher than 2 MGy/s. Moreover, the magnitude of this difference (compared to fD) is consistent with the findings from previous data analysis.

4 Determination of uncertainties

Uncertainties must be determined and appropriately propagated for the following measurements:

- ADR: depends on the dose measured with flashDiamond and total irradiation time.
- DP: depends on the dose measured with flashDiamond.
- IDR: depends on the dose measured with flashDiamond and pulse duration measurement.

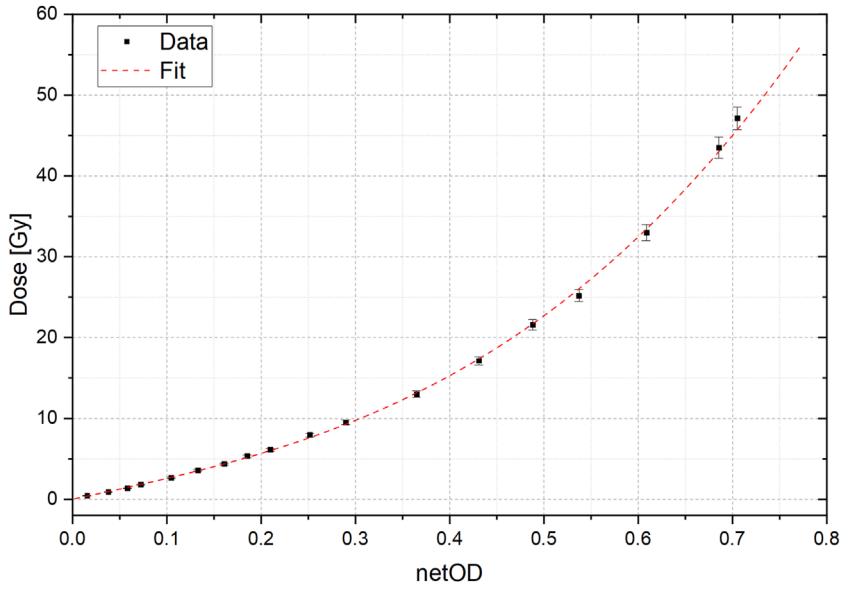

FIGURE 2
Calibration curve obtained comparing netOD values and the dose obtained using the flashDiamond. Error bars result from the uncertainty propagation of two different measurements for single dose value.

TABLE 2 Fit parameters obtained from gafchromic calibration curve.

Parameter	Value
a	25.0 ± 0.6
b	79 ± 7
n	2.9 ± 0.2

- OD: depends on all factors involved in processing radiochromic films.

Regarding dose measurement with the flashDiamond, literature indicates an uncertainty of approximately 3% with this detector [9]. The total irradiation time is related to the PRF, the number of pulses (n_p) and the pulse duration (t_p). Thus, ADR is given by:

$$ADR = \frac{D_p n_p}{t_p + \frac{n_p - 1}{PRF}} \approx D_p \cdot PRF \quad (4)$$

The uncertainty on ADR, if the pulse duration $t_p \ll 1/PRF$, is mainly due to the uncertainty in dose measurement. Nonetheless, if t_p is not negligible with respect to 1/PRF, or in the case of IDR measurements, t_p is measured using on-line measurements of IDR with flashDiamond and an oscilloscope (Rigol DS1074Z Plus). In this case, the uncertainty Δtp on t_p corresponds to the scale on the oscilloscope and can be set so that $\Delta tp \ll t_p$, making it negligible compared to other sources of uncertainty.

Finally, we estimated OD uncertainty following the recommendations of AAPM TG 235 [30] using an estimation of about 5% for dose measurement with radiochromic films, a value consistent with previous literature [31, 32].

5 Discussion

The aim of this study was to assess the response of EBT-XD gafchromic film by independently varying the ADR, the DP and the IDR, by using the fD as reference. We found that, for a total delivered dose of about 40 Gy, there was a significant difference (~2.3%) in the netOD (normalized against the fD reading) response between low (3.56 Gy/s) and high (4845 Gy/s) ADR values. The results also show a dependence of the film response on the IDR, which was investigated up to 4.82 MGy/s. A maximum netOD overresponse (compared to the fD) between 2.5% and 6.5% was found for the extreme IDR of 4.82 MGy/s when compared with IDR of 2 MGy/s. If future studies validate the use of fD as a reference, our finding implies a not negligible corresponding maximum dose overestimation of 7% ± 3.3% for a dose of 40 Gy obtained applying the dose calibration performed at low ADR and IDR conditions. The obtained data suggest that there are two contributing factors to the netOD overestimation. The first factor is linked to the ADR, which was evaluated for two different DP. Though not statistically significant, we observed an increasing trend from an ADR exceeding 1500 Gy/s up to approximately 5,000 Gy/s. The second factor is dependent on the IDR where the effect begins to manifest starting from around 1.5 MGy/s. The study of the IDR dependence was executed at an ADR of 3018 Gy/s, hence higher than the value found with the overresponse linked to the ADR. Given the irradiation conditions the two dependencies can be deemed independent.

The overall uncertainties in the irradiations were minimized thanks to the ElectronFlash linac that enabled us to maintain the same experimental setup and energy spectrum. We also verified, through a calibration curve executed with conventional irradiation parameters, that the selected dose value was within the optimal range of the film's response, excluding phenomena

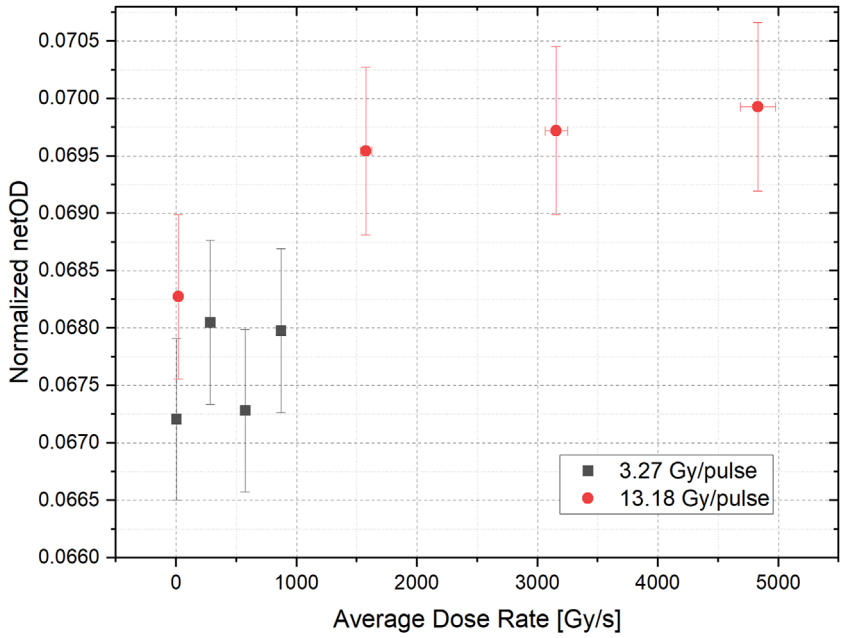

FIGURE 3
Normalized netOD to fD charge for two different dose-per-pulse values (3.27 Gy in black and 13.18 Gy in red) in function of the average dose-rate (ADR). Error bars result from the error proagation of netOD and dose obtained from fD.

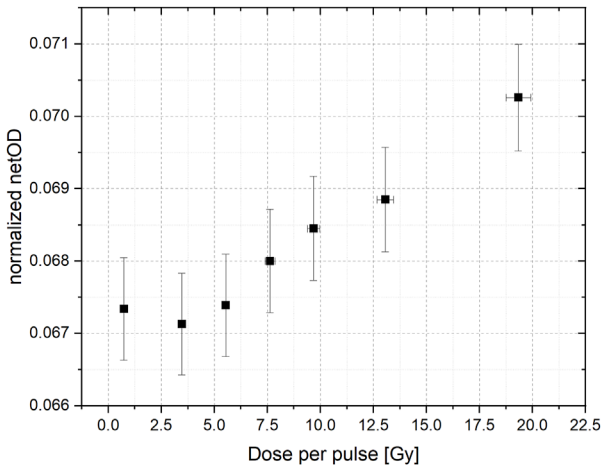

FIGURE 4
Normalized netOD to fD charge in function of the dose-per-pulse. Error bars result from the proagation. Error bars result from the error proagation of netOD and dose obtained from fD.

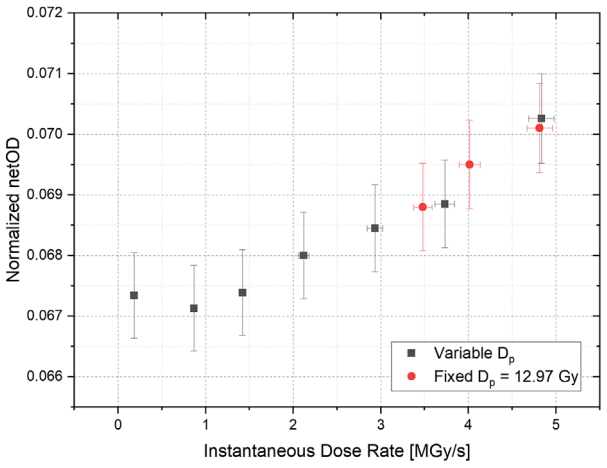

FIGURE 5
Normalized netOD to fD charge in function of the instantaneous dose-rate for a fixed dose-per-pulse (12.97 Gy in red) and variable dose-per-pulse (in black). Error bars result from the error proagation of netOD and dose obtained from fD.

linked to non-standard working conditions. This is consistent with the manufacturer specification and several other studies [33]. Any minor dose variations from the nominal one caused by delivery fluctuations were measured using as monitoring device the same dosimeter used for the reference dosimetry, the flashDiamond, and the resulting netOD was corrected accordingly.

Previous studies have already examined the response of radiochromic films to various beam parameters and concluded that gafchromic films do not exhibit any differences in their response for irradiation conditions. However, in Jaccard et al., the films were irradiated with uneven dose values and compared trough the calibration curve [17]. This approach could mask low entity dependency (below 5%) due to the increased uncertainty associated with the conversion of netOD values to dose values and the inherent uncertainty associated with selecting the appropriate irradiation condition for the calibration curve. As a result, we

conducted our analysis directly on the netOD values to avoid these shortcomings.

More extreme irradiation condition (up to 10^9 Gy/s) were tested in Karsch et al. [15], but again, the comparison was made through the calibration curve (obtained at completely different setup from the one of the study). Meanwhile, a more recent study by Guan et al. [16] asserted that no dose rate dependence was found, but their study was limited to a maximum dose rate of 150 Gy/s. More recently, a study from Villoing et al. [19], started to observe an overresponse of the EBT-XD film to higher ADR and IDR (7500 Gy/s), but they were unable to test the response of the films to individual beam parameters. Our study is subject to certain limitations that warrant consideration.

The study would have been conceptually more precise by reconstructing complete dose-optical density curves across varying beam parameters (ADR, DP, IDP). However, this approach would be overly labor-intensive and practically unfeasible due to the totally different dosimetric steps across different DPs. Instead, we decided to fix the dose level for the irradiations, which allowed us to vary the parameters we wanted to investigate in an extreme manner. We then demonstrated that, for dose variations within 2% (the maximum variation recorded in our data), the resulting change in netOD is negligible and we applied a correction for minor dose variations. While not optimal, since the calibration curve parameters can shift with beam parameters, this correction is certainly more accurate than a linear approximation or no correction at all.

Our decision to focus exclusively on a single type of radiochromic film (EBT-XD) was predicated on its perceived suitability due to its more appropriate dose range response for FLASH irradiation, spanning up to 40 Gy. In contrast, the optimal dose range of EBT-3 (0.2–10 Gy) could potentially prove restrictive in certain extreme FLASH settings necessitating DP values exceeding the 10 Gy threshold. Consequently, opting for EBT-XD enabled us to operate within the optimal range delineated for the film's efficacy (0.4–40 Gy) and conseguently have a superior response compared to the EBT3 film.

In our investigation, a uniform dose of approximately 40 Gy was administered across all films. This was motivated by our goal to create the most extreme irradiation conditions achievable within the operational limits of the linac, while independently manipulating the beam parameters. While existing studies suggest that observable effects may not emerge until doses reach 30 Gy [19], our decision to deliver higher doses was also informed by the potential insights that could be gained at higher values.

Further steps will be made to extend the results of this study to more extreme irradiation conditions and different beam energies. In conclusion, we advise caution when employing these films for absolute dosimetry within FLASH conditions—both in the context of FLASH source commissioning and radiobiological experiments.

Data availability statement

The raw data supporting the conclusions of this article will be made available by the authors, without undue reservation.

Author contributions

DD: Conceptualization, Data curation, Formal Analysis, Investigation, Methodology, Project administration, Resources, Software, Supervision, Validation, Visualization, Writing – original draft. LM: Conceptualization, Data curation, Formal Analysis, Investigation, Methodology, Project administration, Resources, Software, Supervision, Validation, Visualization, Writing – original draft, Writing – review and editing. AC: Data curation, Investigation, Methodology, Software, Validation, Visualization, Writing – original draft. MC: Data curation, Investigation, Methodology, Software, Validation, Visualization, Writing – original draft. TF: Methodology, Validation, Visualization, Writing – review and editing. GG: Methodology, Validation, Visualization, Writing – review and editing. NG: Methodology, Validation, Visualization, Writing – review and editing. AG: Visualization, Writing – review and editing, Methodology, Validation. GM: Data curation, Investigation, Methodology, Software, Validation, Visualization, Writing – review and editing. FP: Funding acquisition, Methodology, Validation, Visualization, Writing – original draft. JP: Data curation, Investigation, Methodology, Software, Validation, Visualization, Writing – original draft, Writing – review and editing. FR: Data curation, Investigation, Methodology, Software, Validation, Visualization, Writing – original draft, Writing – review and editing. FD: Conceptualization, Data curation, Formal Analysis, Funding acquisition, Investigation, Methodology, Project administration, Resources, Software, Supervision, Validation, Visualization, Writing – original draft, Writing – review and editing.

Funding

The author(s) declare that financial support was received for the research and/or publication of this article. This work was funded by European Union - Next Generation EU, Mission 4 Component 2 Inv. 1.5, ECS00000017 "Ecosistema dell'innovazione" Tuscany Health Ecosystem (THE), Spoke 1 "Advanced Radiotherapies and Diagnostics in Oncology"—CUP I53C22000780001.

Acknowledgments

We thank Fondazione Pisa for funding CPFR with the grant "prog. n. 134/2021".

We also thank Minibeam Radiotheraphy (MIRO) INFN project for scientific collaboration.

Conflict of interest

The authors declare that the research was conducted in the absence of any commercial or financial relationships that could be construed as a potential conflict of interest.

The author(s) declared that they were an editorial board member of Frontiers, at the time of submission. This had no impact on the peer review process and the final decision.

Publisher's note

References

1. Bourhis J, Sozzi WJ, Jorge PG, Gaide O, Bailat C, Duclos F, et al. Treatment of a first patient with FLASH-radiotherapy. *Radiother Oncol* (2019) 139:18–22. doi:10.1016/j.radonc.2019.06.019

2. Montay-Gruel P, Petersson K, Jaccard M, Boivin G, Germond JF, Petit B, et al. Irradiation in a flash: unique sparing of memory in mice after whole brain irradiation with dose rates above 100 Gy/s. *Radiother Oncol* (2017) 124(3):365–9. doi:10.1016/j.radonc.2017.05.003

3. Favaudon V, Caplier L, Monceau V, Pouzoulet F, Sayarath M, Fouillade C, et al. Ultrahigh dose-rate FLASH irradiation increases the differential response between normal and tumor tissue in mice. *Sci Transl Med* (2014) 6:245ra93. doi:10.1126/scitranslmed.3008973

4. Durante M, BräUer-Krisch E, Hill M. Faster and safer? FLASH ultra-high dose rate in radiotherapy. *Br J Radiol* (2018) 91:1082. doi:10.1259/bjr.20170628

5. Di Martino F, Del Sarto D, Bass G, Capaccioli S, Celentano M, Coves D, et al. Architecture, flexibility and performance of a special electron linac dedicated to Flash radiotherapy research: electronFlash with a triode gun of the centro pisano flash radiotherapy (CPFR). *Front Phys* (2023) 11:1268310. doi:10.3389/fphy.2023.1268310

6. Di Martino F, Barca P, Barone S, Bortoli E, Borgheresi R, De Stefano S, et al. FLASH radiotherapy with electrons: issues related to the production, monitoring, and dosimetric characterization of the beam. *Front Phys* (2020) 8:570697. doi:10.3389/fphy.2020.570697

7. Di Martino F, Del Sarto D, Barone S, Giuseppina Bisogni M, Capaccioli S, Galante F, et al. A new calculation method for the free electron fraction of an ionization chamber in the ultra-high-dose-per-pulse regimen. *Physica Med* (2022) 103:175–80. doi:10.1016/j.ejmp.2022.11.001

8. Petersson K, Jaccard M, Germond JF, Buchillier T, Bochud F, Bourhis J, et al. High dose-per-pulse electron beam dosimetry - a model to correct for the ion recombination in the Advanced Markus ionization chamber. *Med Phys* (2017) 44(3):1157–67. doi:10.1002/mp.12111

9. Marinelli M, di Martino F, Del Sarto D, Pensavalle JH, Felici G, Giunti L, et al. A diamond detector based dosimetric system for instantaneous dose rate measurements in FLASH electron beams. *Phys Med Biol* (2023) 68(17):175011. doi:10.1088/1361-6560/acead0

10. Di Martino F, Del Sarto D, Giuseppina Bisogni M, Capaccioli S, Galante F, Gasperini A, et al. A new solution for UHDP and UHDR (Flash) measurements: theory and conceptual design of ALLS chamber. *Physica Med* (2022) 102:9–18. doi:10.1016/j.ejmp.2022.08.010

11. Gómez F, Gonzalez-Castaño DM, Fernández NG, Pardo-Montero J, Schüller A, Gasparini A, et al. Development of an ultra-thin parallel plate ionization chamber for dosimetry in FLASH radiotherapy. *Med Phys* (2022) 49(7):4705–14. doi:10.1002/mp.15668

12. Romano F, Milluzzo G, Di Martino F, D'Oca MC, Felici G, Galante F, et al. First characterization of novel silicon carbide detectors with ultra-high dose rate electron beams for FLASH radiotherapy. *Appl Sci* (2023) 13(5):2986. doi:10.3390/app13052986

13. Medina E, Ferro A, Abujami M, Camperi A, Centis Vignali M, Data E, et al. First experimental validation of silicon-based sensors for monitoring ultra-high dose rate electron beams. *Front Phys* (2024) 12:1258832. doi:10.3389/fphy.2024.1258832

14. Pensavalle JH, Romano F, Celentano M, Sarto DD, Felici G, Franciosini G, et al. Realization and dosimetric characterization of a mini-beam/flash electron beam. *Front Phys* (2023) 16(11):1269495. doi:10.3389/fphy.2023.1269495

15. Karsch L, Beyreuther E, Burris-Mog T, Kraft S, Richter C, Zeil K, et al. Dose rate dependence for different dosimeters and detectors: TLD, OSL, EBT films, and diamond detectors. *Med Phys* (2012) 39(5):2447–55. doi:10.1118/1.3700400

16. Guan F, Wang X, Yang M, Draeger E, Han D, Iga K, et al. Dosimetric response of Gafchromic™ EBT-XD film to therapeutic protons. *Precision Radiat Oncol* (2023) 7(1):15–26. doi:10.1002/pro6.1187

17. Jaccard M, Petersson K, Buchillier T, Germond J, Durán MT, Vozenin M, et al. High dose-per-pulse electron beam dosimetry: usability and dose-rate independence of EBT3 Gafchromic films. *Med Phys* (2017) 44(2):725–35. doi:10.1002/mp.12066

18. Togno M, Nesteruk K, Schäfer R, Psoroulas S, Meer D, Grossmann M, et al. Ultra-high dose rate dosimetry for pre-clinical experiments with mm-small proton fields. *Physica Med* (2022) 104:101–11. doi:10.1016/j.ejmp.2022.10.019

19. Villoing D, Koumeir C, Bongrand A, Guertin A, Haddad F, Métivier V. Technical note: proton beam dosimetry at ultra-high dose rates (FLASH): evaluation of GAFchromic™ (EBT3, EBT-XD) and OrthoChromic (OC-1) film performances. *Med Phys* (2022) 49:2732–45. doi:10.1002/mp.15526

20. Oh K, Gallagher KJ, Hyun M, Schott D, Wisnoskie S, Lei Y, et al. Initial experience with an electron FLASH research extension (FLEX) for the Clinac system. *J Appl Clin Med Phys* (2024) 25(2):14159. doi:10.1002/acm2.14159

21. Felici G, Barca P, Barone S, Bortoli E, Borgheresi R, De Stefano S, et al. Transforming an IORT linac into a FLASH research machine: procedure and dosimetric characterization. *Front Phys* (2020) 8:569691. doi:10.3389/fphy.2020.00374

22. Byrne KE, Poirier Y, Xu J, Gerry A, Foley MJ, Lauren Jackson I, et al. Technical note: a small animal irradiation platform for investigating the dependence of the FLASH effect on electron beam parameters. *Med Phys* (2024) 51:1421–32. doi:10.1002/mp.16909

23. Patriarca A, Fouillade C, Auger M, Martin F, Pouzoulet F, Nauraye C, et al. Experimental set-up for FLASH proton irradiation of small animals using a clinical system. *Int J Radiat Oncol Biol Phys* (2018) 102:619–26. doi:10.1016/j.ijrobp.2018.06.403

24. Schüler E, Trovati S, King G, Lartey F, Rafat M, Villegas M, et al. Experimental platform for ultra-high dose rate FLASH irradiation of small animals using a clinical linear accelerator. *Int J Radiat Oncol Biol Phys* (2017) 97:195–203. doi:10.1016/j.ijrobp.2016.09.018

25. Imran I, Younus M, Walayat K, Kakar MU, Ma J. Automated multi-class classification of skin lesions through deep convolutional neural network with dermoscopic images. *Comput Med Imaging graphics* (2021) 88:101843. doi:10.1016/j.compmedimag.2020.101843

26. Jorge PG, Jaccard M, Petersson K, Gondré M, Durán MT, Desorgher L, et al. Dosimetric and preparation procedures for irradiating biological models with pulsed electron beam at ultra-high dose-rate. *Radiother Oncol* (2019) 139:34–9. doi:10.1016/j.radonc.2019.05.004

27. Marinelli M, Felici G, Galante F, Gasparini A, Giuliano L, Heinrich S, et al. Design, realization, and characterization of a novel diamond detector prototype for FLASH radiotherapy dosimetry. *Med Phys* (2022) 49:1902–10. doi:10.1002/mp.15473

28. Verona RG, Felici G, Galante F, Gasparini A, Kranzer R, Mariani G, et al. Application of a novel diamond detector for commissioning of FLASH radiotherapy electron beams. *Med Phys* (2022) 49:5513–22. doi:10.1002/mp.15782

29. Kranzer R, Schüller A, Bourgouin A, Hackel T, Poppinga D, Lapp M, et al. Response of diamond detectors in ultra-high dose-per-pulse electron beams for dosimetry at FLASH radiotherapy. *Phys Med & Biol* (2022) 67(7):075002. doi:10.1088/1361-6560/ac594e

30. Niroomand-Rad A, Chiu-Tsao ST, Grams MP, Lewis DF, Soares CG, Van Battum LJ, et al. Report of AAPM Task Group 235 radiochromic film dosimetry: an update to TG-55. *Med Phys* (2020) 47:5986–6025. doi:10.1002/mp.14497

31. Sorriaux J, Kacperek A, Rossomme S, Lee JA, Bertrand D, Vynckier S, et al. Evaluation of Gafchromic® EBT3 films characteristics in therapy photon, electron and proton beams. *Phys Med* (2013) 29:599–606. doi:10.1016/j.ejmp.2012.10.001

32. Akdeniz Y. Comparative analysis of dosimetric uncertainty using Gafchromic™ EBT4 and EBT3 films in radiochromic film dosimetry. *Radiat Phys Chem* (2024) 20:111723. doi:10.1016/j.radphyschem.2024.111723

33. Miura H, Ozawa S, Hosono F, Sumida N, Okazue T, Yamada K, et al. Gafchromic EBT-XD film: dosimetry characterization in high-dose, volumetric-modulated arc therapy. *J Appl Clin Med Phys* (2016) 17:312–22. doi:10.1120/jacmp.v17i6.6281

frontiers | Frontiers in Physics

TYPE Methods
PUBLISHED 28 October 2025
DOI 10.3389/fphy.2025.1597079

OPEN ACCESS

EDITED BY
Jiaru Shi,
Tsinghua University, China

REVIEWED BY
Tatsuhiro Gotanda,
Kawasaki University of Medical Welfare, Japan
Leo Van Battum,
VU Medical Center, Netherlands

*CORRESPONDENCE
Vilde F. Rieker,
vilde.rieker@cern.ch
Joseph J. Bateman,
joe.bateman@ucl.ac.uk

RECEIVED 20 March 2025
ACCEPTED 15 September 2025
PUBLISHED 28 October 2025

CITATION
Rieker VF, Bateman JJ, Wroe L, Caloz M, Grilj V, Aguiar YQ, Schüller A, Bailat C, Farabolini W, Gilardi A, Robertson C, Korysko P, Malyzhenkov A, Stapnes S, Vozenin M-C, Dosanjh M and Corsini R (2025) Radiochromic film dosimetry for VHEE and UHDR: protocol adaptation and verification at the CLEAR facility.
Front. Phys. 13:1597079.
doi: 10.3389/fphy.2025.1597079

Radiochromic film dosimetry for VHEE and UHDR: protocol adaptation and verification at the CLEAR facility

Vilde F. Rieker[1,2]*, Joseph J. Bateman[3]*, Laurence Wroe[1], Misael Caloz[4], Veljko Grilj[5], Ygor Q. Aguiar[1], Andreas Schüller[6], Claude Bailat[5], Wilfrid Farabolini[1], Antonio Gilardi[1], Cameron Robertson[3], Pierre Korysko[1,3], Alexander Malyzhenkov[1], Steinar Stapnes[1,2], Marie-Catherine Vozenin[4], Manjit Dosanjh[1,3] and Roberto Corsini[1]

[1]European Organization for Nuclear Research (CERN), Geneva, Switzerland, [2]Department of Physics, University of Oslo, Oslo, Norway, [3]Department of Physics, University of Oxford, Oxford, United Kingdom, [4]University Hospital of Geneva (HUG), Geneva, Switzerland, [5]Institute of Radiation Physics, Lausanne University Hospital (CHUV), Lausanne, Switzerland, [6]Physikalisch-Technische Bundesanstalt (PTB), Braunschweig, Germany

Radiochromic films (RCFs) offer effective two-dimensional dosimetry with a simple, low-cost operating principle, making them suitable for very high-energy electron (VHEE) and ultra-high dose rate (UHDR) applications, where dosimetry standards are lacking. However, achieving high-accuracy measurements with RCFs presents significant challenges, especially in the absence of standardised protocols. To ensure reliable and comparable outcomes, adapted protocols based on a thorough understanding of RCF behaviour are essential. Despite over 6,000 publications addressing RCF protocols, comprehensive guides for high-throughput research machines with small, non-uniform beams are scarce. This paper aims to be a comprehensive guide for non-expert users of RCFs, particularly in VHEE and UHDR research. We identify common errors in RCF preparation, scanning, and processing, proposing strategies to enhance accuracy and efficiency. Using our optimised RCF protocol at the CLEAR facility, we demonstrate a 5% agreement compared to alanine dosimeters irradiated with Gaussian VHEE beams, establishing this protocol as a solid foundation for reliable dosimetry in advanced radiotherapy research.

KEYWORDS

VHEE, FLASH, radiochromic films, UHDR, alanine, TLD, RPL

1 Introduction

FLASH radiotherapy (FLASH-RT) has emerged as a promising cancer treatment modality, whereby the radiation that delivers radiation at ultra-high dose rates (UHDRs) of $\geq$ 40 Gy s^{-1}, eliciting a biological phenomenon known as the FLASH effect. This effect enhances the sparing of healthy tissue while maintaining equivalent

tumour control compared to conventional dose rates (CDR) of ≤ 0.03 Gy s^{-1} [1]. Preclinical evidence has demonstrated the FLASH effect across various radiation types, including X-rays, protons, and low-energy electrons of ≲ 20 MeV [2–6]. However, very high-energy electron (VHEE) beams of energies ≳ 100 MeV offer a particularly promising approach due to their superior penetration depth compared to clinical energy electrons [7, 8] and their technological ease of production at the required intensities and energies compared to alternatives such as protons and MV photons [9]. This makes FLASH-RT a promising modality for treating deep-seated tumours [10–13].

One of the critical challenges impeding the clinical translation of FLASH-RT, especially for pulsed modalities like VHEE, is developing accurate and reliable active dosimetry. Several studies have demonstrated that ionisation chambers—the standard for active dosimetry in conventional radiotherapy—saturate under the UHDR conditions required for FLASH-RT [14–16]. This dosimetry issue has spurred an area of research alongside the radiobiological studies of FLASH-RT.

The CERN Linear Electron Accelerator for Research (CLEAR) is one of the very few particle accelerators capable of providing VHEE beams at UHDR. CLEAR is a stand-alone user facility located at CERN's Meyrin site that has been engaged in research related to VHEE FLASH-RT since 2019. The accelerator offers a flexible range of beam parameters in the VHEE regime, including a wide range of mean and instantaneous dose rates, making it a suitable testbed for both FLASH-RT and active UHDR dosimetry research. For example, radiobiologists have utilised the facility to study the onset of the FLASH effect in plasmids, zebra fish embryos and *Drosophila* larvae [17–19], while physicists have investigated novel methods for active UHDR dosimetry using scintillating fibres, screens and fluorescing solutions [20–23]. All these experiments rely on passive dosimetry for benchmarking and dose assessment.

At CLEAR the standard choice for passive dosimetry has been radiochromic films (RCFs) because they provide information about the transverse beam distribution—an essential capability when working with small and/or inhomogeneous beams. Considerable effort has been dedicated to optimising procedures for preparing, scanning and processing RCFs to ensure the highest possible accuracy in dosimetry for facility users. However, achieving this accuracy often requires trading off some efficiency—and finding the optimal balance between accuracy and efficiency is highly dependent on the number of samples and the time frame of the experiment. This can pose a major challenge for research facilities, such as CLEAR, that both rely on and operate with a high throughput of RCFs, particularly when combined with a dynamic experimental program.

This paper aims to serve as a comprehensive guide for adapting RCF protocols in research settings, discussing all considerations and potential pitfalls based on our experience. The goal is for scientists at similar facilities to leverage our efforts in protocol optimisation for to adapt a protocol compatible with their setups. Section 2 provides a detailed overview of the various effects that influence RCF accuracy, along with mitigation strategies an particular considerations for CLEAR and similar facilities. The four main parts of the RCF protocol—namely preparation, scanning, calibration and processing—are described in separate subsections, each summarised by the step-by-step procedure used at CLEAR. Section 3 focuses on the validation of the RCF protocol adapted at CLEAR, comparing our RCF analysis to measurements from radiophotoluminescence dosimeters (RPLDs), dosimetry phantoms (DPs) and alanine dosimeters (ADs). It also investigates potential discrepancies in these dosimeters' responses to different energies and dose rates.

2 Radiochromic film dosimetry

RCFs are a type of passive dosimeter commonly used in radiation oncology to assess spatial dose distributions and verify treatment plans [24]. They consist of a self-developing active layer that polymerises and darkens upon radiation exposure. Most RCF models have this active layer—a few tens of microns thick—sandwiched between two polyester substrates, each around 100 microns thick. These substrates exhibit near tissue and water equivalence, which limits discrepancies in dose-to-water calibration [25]. An RCF dosimetry system (RFDS) consists of a calibration curve that relates the level of RCF darkening to a known dose for a given production lot, a digitiser (such as a commercial flatbed photo scanner) for scanning the RCFs, and an RCF processing protocol. However, several sources of uncertainty in an RFDS can lead to significant errors in dose evaluation if procedural consistency is not maintained between calibration and application RCFs. The works by Devic and Bouchard et al. thoroughly demonstrate the various factors that influence accuracy in RCF dosimetry [24, 26]. Most of these uncertainties arise from the handling and processing of the RCFs, and these can, to varying degrees, be minimised at the cost of a more rigorous and time-consuming dosimetry protocol.

A protocol that is both feasible and sufficiently accurate must be independently established by different research facilities, as they typically have varied use cases and time constraints. Adapting an RCF protocol requires an understanding of the uncertainties associated with each part of the process. At CLEAR, we have adapted a protocol that specifically supports high throughput—irradiating up to 100 separate RCF pieces in a single day—and small Gaussian beams. In the following sections, we will outline the protocol currently in use and elaborate on the lessons learned, considerations, and trade-offs encountered along the way.

2.1 RCF models

At the CLEAR facility, RCF dosimetry for VHEE and UHDR studies involves the use of a variety of Gafchromic™ RCF models which are manufactured by Ashland™. EBT3—and more recently EBT4—RCFs are used for doses up to 10 Gy, EBT-XD for the range 10–40 Gy, MD-V3 for 40–100 Gy, and HD-V2 to cover the 100–1,000 Gy range. At CLEAR, all of these RCF models are used for measurements in water, except for HD-V2, which are exclusively used for measurements above 100 Gy in air, typically for small, minimally scattered beams. Ashland states that all these RCF models exhibit a near energy-independent response with <5% difference in net optical density when exposed at 100 keV, 1 MeV and 18 MeV, and it has been shown experimentally that there is a good agreement between simulations and RCF measurements up to 200 MeV [8, 27, 28]. Moreover, Ashland states that the RCFs

TABLE 1 Properties of the different models of Gafchromic™ RCFs used at CLEAR.

CF model	Scanned sample	Cross section	Optimal (dynamic) range/Gy	CLEAR usage
EBT3 [29]		125 p.m. matte polyester 28 p.m. active layer 125 p.m. matte polyester	0.2–10 (0.1–20)	1–10 Gy in water
EBT4 [30]		125 p.m. matte polyester 28 um active layer 125 p.m. matte polyester	0.2–10	1–10 Gy in water
EBT-XD [31]		125 jim matte polyester 25 um active layer 125 jim matte polyester	0.4–40 (0.1–60)	10–40 Gy in water
MD-V3 [32]		125 jim matte polyester 10 jim active layer 125 p.m. matte polyester	1–100	40–100 Gy in water
HD-V2 [33]		12 p.m. active layer 97 p.m. clear polyester	10–1,000	100–1,000 Gy in air

are independent of dose-rate with <5% difference in net optical density for 10 Gy accumulated at 3.4 Gy min^{-1} and 0.034 Gy min^{-1} [29–33]. Studies have found that the dose-rate independence can be extended up to instantaneous dose-rates in the order of 10^9 Gy s^{-1} [10, 34, 35].

The atomic composition of the active layer responsible for darkening is similar across the different RCF models. The key differences between the models are related to the crystalline structure of this layer, which results in different radiosensitivity [36]. An overview of the RCF models used at CLEAR is provided in Table 1.

2.2 RCF handling and preparation

Due to the physical nature of the RCFs and the method of data retrieval, caution is necessary in their storage, preparation and handling to minimise potential uncertainties. In particular, it is essential to limit the splitting of the polyester substrates protecting the active layer, as well as light exposure, the presence of impurities such as dirt, dust and grease, and the formation of scratches, to ensure reliable dosimetry with RCFs. This section will detail good practices for RCF handling and outline strategies for mitigating such effects within the RCF protocol.

2.2.1 RCF handling

The EBT3, EBT4, EBT-XD, and MD-V3 models gain robustness by sandwiching the active layer between two polyester sheets. The design allows them to be irradiated in a water phantom for short periods and handled with bare hands. However, handling with bare hands can transfer fingerprints and impurities, which distort the dose distribution. While it is possible to wipe the RCF pieces clean with an alcohol swab or to handle them by the edges, at CLEAR we prefer to use gloves to ensure consistency when managing large numbers of RCFs.

Despite the sandwich construction, we have observed that water diffuses a few millimetres into the active layer during irradiations in liquid water phantoms. The study by Aldelaijan et. al demonstrates that water not only diffuses from the edges but also penetrates through the RCF faces to some degree. They conclude that short submersions of around 30 min yield negligible impact, whereas longer immersion periods should be corrected for [37] As for the HD-V2 model, which have the humidity sensitive active layer fully exposed, water must be completely avoided and it must in general be handled with more care.

The Gafchromic^{TM} RCF models are relatively insensitive to indoor artificial light and can be left exposed for short periods without noticeable effects. However, they are very sensitive to UV light—even to artificial light containing UV components—which can cause darkening with prolonged exposure [38, 39]. Therefore, it is crucial that the RCFs are stored in an opaque envelope or container when not in use to avoid unnecessary uncertainties. At CLEAR we have purchased small, black antistatic bags—intended for storing electronic components—for the storage of cut RCF pieces.

Another factor to consider is the temperature stability of the RCFs. According to Ashland, EBT3 RCFs are stable up to 60 °C, but they recommend storing them below 25 °C [29]. A study by Trivedi et al. showed that storing RCFs in varying temperatures can lead to self-development, effectively shifting their sensitivity [40]. Therefore, it is good practice to store RCFs not only below 25 °C, but ideally in a temperature-controlled environment.

2.2.2 Cutting and labelling

Gafchromic^{TM} RCFs are manufactured in sheets measuring 203 mm × 254 mm. At the CLEAR facility, a laser machine (Epilog Fusion Maker 12) has been acquired to systematically cut these sheets into 35 mm × 40.5 mm pieces—a suitable size to capture most of the electron beam after scattering through approximately 15 cm of water, including an extra margin for water diffusion [37]. These dimensions are also tailored to fit the 3D-printed sample holders used for irradiations at CLEAR.

The laser cutting system is additionally used to engrave and uniquely label the cut RCF pieces. This ensures easy identification and maintenance of RCF orientation during irradiation, scanning, and processing. Examples of a template used for cutting and engraving the RCF sheets, as well as a prepared RCF sample, can be seen in Supplementary Figure S1.

The templates are vector graphics (SVG) files in which the cutting and engraving paths are differentiated by colour. The Epilog software includes a colour mapping feature that enables the assignment of separate laser attributes to the different colours in the SVG file, allowing for cutting and engraving to be performed in the same process. To prevent damage to the RCFs and achieve satisfactory engraving resolution, it is important to adjust the laser machine's speed, power, and frequency carefully. Although there is currently no literature detailing the specific considerations for laser cutting RCFs, Niroomand-Rad et al. state that, if done 'carefully', all but a 1 mm margin around the edge can be used for dosimetry [36].

The optimal laser settings depend on the specific laser machine being used. With the Epilog Fusion Maker 12, we have observed that cutting at low speeds severely damages the RCF, even at low power. Increasing the speed generally allows for an increase in power, and the least visual damage is achieved at high speed and high power. It is important to flatten the naturally curved RCF sheets in the laser machine using adhesive tape (applied along the edges outside the engraving area) to maintain the laser's focus during engraving.

We also explored the possibility of sealing the edges of the RCFs during the laser cutting process to prevent humidity from entering between the two substrates and diffusing into the active layer. When comparing the non-damaging laser settings, no significant difference in water resistance was observed, despite visual differences in the degree of melting at the edges. All cutting settings resulted in a persistent diffusion of 3–4 mm into the edges after 10 min of submersion in water. However, this effect was most pronounced on the three edges in contact with the sample holder. As this result also contrasts with findings presented by Aldelaijan et al., it indicates that the contact between RCFs and sample holders at CLEAR negatively affects the water diffusion and penetration behaviour [37].

As a final remark, it is important to note that Gafchromic^{TM} RCF models contain trace amounts of chlorine, as reported by Niiroomand et al. [36]. As a safety precaution, it is crucial to cut the RCF sheets in a well-ventilated area using a laser machine connected to a fume extraction system.

2.2.3 The RCF preparation protocol at CLEAR

Based on the considerations in Sections 2.2.1 and 2.2.2, the following procedure for RCF preparation has been established at CLEAR:

1. RCFs are stored in opaque envelopes at room temperature to prevent excess darkening due to UV and ageing.
2. Gloves are used when handling the RCFs to avoid fingerprints and scratches.
3. RCF sheets are cut and engraved using a laser machine at high power and high speed, to avoid damage and ensure reproducibility and traceability.

2.3 RCF scanning

RCFs are most commonly processed using commercially available 48-bit flatbed photo scanners in transmission mode. These scanners measure the red, green, and blue (RGB) colour components of light transmitted by the RCF at a colour depth of 16 bits per channel. This process yields the fraction of incident light transmitted through the sample, I_t/I_0, which is mapped to a range of 2^{16} pixel values (PV) per colour channel, from 0 (opaque) to 65535 (transparent). Several scanning-related factors can affect the accuracy of RCF dosimetry, and this section outlines the existing effects and the mitigation techniques considered at CLEAR.

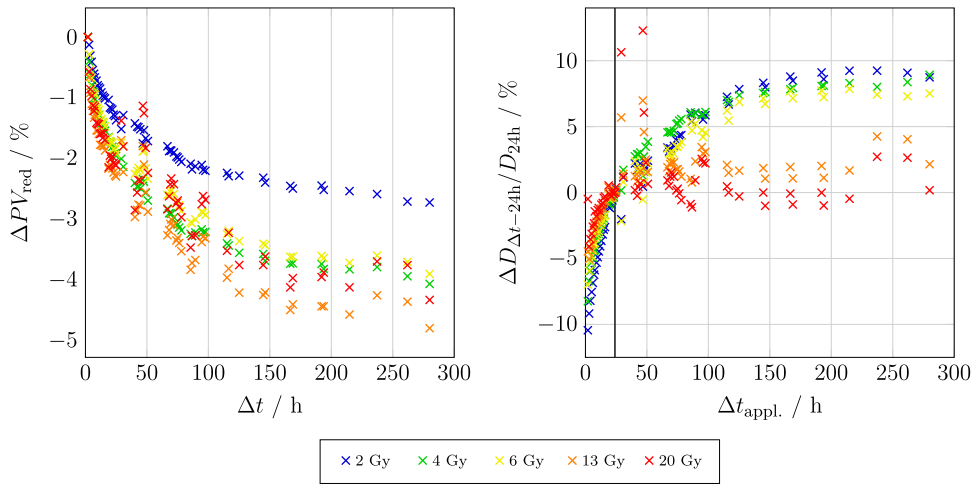

FIGURE 1
Left: The relative change in PV for the red channel of an EBT3 RCF as a function of time after exposure Δt. Right: The dose deviation of the RCFs scanned at different times after exposure, relative to an RCF scanned at $\Delta t_{\mathrm{appl.}} \simeq \Delta t_{\mathrm{calib.}} = 24$ h, indicated by the vertical line.

2.3.1 Timing the scans

RCFs begin to self-develop immediately upon radiation exposure, and the polymerisation process never fully ends; it continues at increasingly slower rates. Therefore, it is important to maintain consistency in the timing of RCF scanning after exposure. The post-exposure self-development of a set of EBT3 RCFs is shown in Figure 1.

The left-hand plot shows that stabilisation appears to occur more rapidly for RCFs exposed to doses at the higher end of the RCF's dynamic range. Moreover, the steepness of these curves dictates the acceptable time window for scanning; the shorter the chosen $\Delta t_{\mathrm{calib.}}$ for the calibration RCFs, the smaller the acceptable absolute deviation of $\Delta t_{\mathrm{appl.}}$ for the application RCFs without introducing significant dose errors. The right-hand plot underscores this point by showing the induced error as a function of scanning time $\Delta t_{\mathrm{appl.}}$ relative to $\Delta t_{\mathrm{appl.}} = \Delta t_{\mathrm{calib.}} = 24$ h. A $\Delta t_{\mathrm{appl.}}$ that is sufficiently different from $\Delta t_{\mathrm{calib.}}$ may result in dose evaluation errors of up to 10%.

Literature therefore often suggests waiting for at least 24 h post-irradiation before scanning, as the polymerisation process is more stable at this point. Beyond 24 h and up to 14 days post exposure, the change is about 2.5% [36]. In summary, the crucial point is ensuring that the post-exposure scanning timing for the application RCFs ($\Delta t_{\mathrm{appl.}}$) relative to that of the calibration RCFs ($\Delta t_{\mathrm{calib.}}$) is minimised according to Equation 1:

$$\left|1 - \frac{\Delta t_{\mathrm{appl.}}}{\Delta t_{\mathrm{calib.}}}\right| \ll 1. \tag{1}$$

There is a technical possibility of mitigating this timing uncertainty by applying the 'one-scan protocol', which also compensates for inter-scan variabilities [41]. However, this approach relies on a recalibration by irradiating a reference RCF to a known dose that is similar to the maximum expected dose on the application RCF. This is not feasible at CLEAR because we depend on external calibration facilities.

In practice, particularly at CLEAR, where we typically scan numerous RCFs one-by-one, maintaining a consistent scanning window is challenging. Based on the aforementioned considerations, it is considered best practice to strictly adhere to $\Delta t \simeq 24$ h, as this offers a reasonable scanning time-window without risking significant error. This protocol offers a good compromise between post-exposure stabilisation and acceptable delay for most experiments at CLEAR. In research settings where the urgency of retrieving dose information is low, it may be advisable to establish a longer Δt, both to further reduce the risk of timing errors and, in the case of water irradiation, to mitigate the impact of water-induced darkening [37].

2.3.2 Sample and scanner preparation

Epson photo scanners are widely used and recommended for RCF dosimetry. It is typically advised to warm up the scanner's electronics before starting the scanning process to ensure reproducible results. If the scanner has not been used in the last hour, turning it on at least 30 min prior to scanning is sufficient. Ashland and most studies suggest performing at least 5 'preview' scans in the Epson Scan software, to warm up the light source and stabilise the response, thereby limiting inter-scan variabilities [36, 39, 42]. It is important to noted that this general recommendation is more critical for cold cathode fluorescent lamp (CCFL) scanners than for LED scanners, as shown in the study by Lárraga-Gutiérrez et al. [43]. While the typically recommended scanner model (Epson Expression 11000XL) is CCFL-based, the model used at CLEAR (Epson Perfection V800 Photo) is LED based and should thus be less susceptible to warm-up effects. Nevertheless, scanner response stability is of particular importance in the CLEAR protocol because the RCFs are scanned one by one. Due to the scarcity of literature documenting the irrelevance of scanner warm-up for the V800 model, we have included five preview scans in the CLEAR protocol as a low-effort precaution.

Before starting the scanning process, it is essential to ensure that both the scanner plate and the RCFs are free from impurities. Both the scanner plate and RCF can be wiped clean with alcohol, and gloves or a vacuum suction pen should be used to position the RCFs

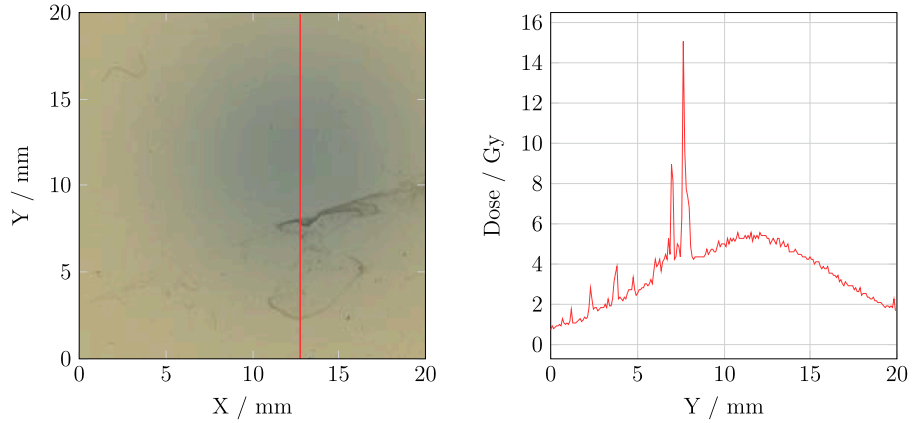

FIGURE 2
Left: An example of an RCF with water residues. Right: The corresponding vertical dose profile.

on the scanner. At CLEAR, where the RCFs are often irradiated in a water phantom, water stains frequently appear on the RCFs, and these must be removed before scanning. As illustrated in Figure 2, such artefacts can significantly affect the pixel value and eventually the dose calculation.

2.3.3 Positioning RCFs on the scanner

The positioning of RCFs on the scanner may significantly impact the results due to the orientation of the RCF polymers and lateral response artifacts (LRA)—which refer to the systematic dependency of measured PVs on the lateral position of the RCF relative to the centre of the scanner. LRA is primarily attributed to the polarisation of light transmitted through the RCF by the polymers in the active layer. The scanner light passes via a set of mirrors and a lens before reaching the image sensor, but the angle of incidence increases with the distance from the centre of the scanner [29]. As a result, RCFs scanned closer to the edges of the scanner appear darker, and the deviation also increases with decreasing PV (i.e., for darker RCFs) [36, 44]. At CLEAR, we have previously found that dose evaluation errors of up to 10% can arise from a lateral offset of the application RCF relative to the calibration RCF during scanning with the V800 model [42].

For RCFs that are large relative to the scanner, the LRA can be mitigated using techniques such as multi-channel processing—which is discussed in section 2.5—and LRA correction matrices, particularly for higher-precision measurements and/or for larger RCFs or multiple RCFs scanned simultaneously [45]. However, using a scanner that is large relative to the RCF is the easiest way to limit the LRA, and Ashland specifically recommends the 11000XL model due to its large scanning area of 310×437 mm^2.

In addition to the lamp, the smaller scanning area (216×297 mm^2) of the V800 model used at CLEAR is a significant difference compared to the 11000XL model [43]. However, this is considered acceptable due to the small dimensions of the RCF pieces used at CLEAR (40×35 mm^2) relative to the scanner surface—which are scanned one by one, centred on the scanner to limit the LRA. Consistent positioning of the RCFs on the scanner is ensured by a custom-made scanner mask with different inserts for different RCF sizes, as shown in Figure 3.

It is essential that the mask itself is positioned consistently on the scanner surface and that the 'calibration region' closest to the starting point of the scan is left blank to ensure proper scanner response calibration.

In addition to ensuring consistent RCF positioning, the scanner mask aids in maintaining a consistent orientation of the RCFs throughout the scanning process. It is a well-known fact that RCF scans are orientation dependent due to the alignment of the polymers in the active layer [39, 46–48]. We have previously reported that increasing relative orientation differences between calibration and application RCFs can yield dose evaluation errors reaching 27% at 90° for an EBT3 RCF exposed to 5 Gy [49]. The choice scanning orientation—e.g. landscape or portrait orientation relative to the uncut sheet—is unimportant; however, it is crucial that the chosen orientation remains consistent between calibration and application RCFs. At CLEAR, we consistently scan in landscape orientation due to the design of the cutting templates.

As a remark, the natural curvature of Gafchromic^{TM} RCF sheets may also affect the scanner response. For a full sheet on a flat surface, the maximum distance between the surface and the RCF is typically in the range of 1–2 mm, depending on the model and production lot. Therefore, particularly for large samples, it is recommended to flatten the RCF on the scanner using a clear glass plate that is 3–4 mm thick to mitigate the potential error in pixel value reading of 1.2% per millimetre offset from the light source [36, 39]. If using a flattening plate, it is important to use it consistently for both calibration and application RCFs. However, at CLEAR, we typically cut RCF sheets into small enough pieces (less than 20% of the height of the full sheet) to largely mitigate this effect, making the consistent use of a glass plate an unnecessary complication.

Lastly, it is crucial to remember that a calibration curve is only valid for a given RFDS, which includes the scanner. This may pose challenges for inter-facility collaborations because using RCFs from an external RFDS might be desired for consistency and comparability during experiments at CLEAR. However, even if the scanner of the external RFDS is the same model as the scanner at CLEAR, the results may differ significantly. An example of the potential error that can arise from using a different scanner

FIGURE 3
Left: The scanner mask used for reproducible positioning of the RCFs. Right: The Epson Perfection V800 Photo scanner with positioning of the mask in the scanner relative to the scanning direction.

is illustrated in Supplementary Figure S2. Moreover, since CLEAR lacks calibration capability, users cannot easily establish a new RFDS for their RCFs using the scanner at CLEAR. Additionally, unless the established Δt of the RFDS is sufficiently long and/or the corresponding scanner is in close proximity to the irradiation facility, timing the scans within a reasonable margin can be challenging. Equally, re-establishing the RFDS by re-scanning the external calibration set at CLEAR will impose a shift of the Δt which may not be compatible with experimental time constraints. The simplest way to mitigate this is for users to either fully rely on the RFDS at CLEAR, or to construct multiple calibration curves (for various Δt), which allows for greater flexibility in post-experimental scanning times.

2.3.4 Scanning software settings

It is important to use appropriate settings in the scanning software when digitising RCFs. According to common practice and literature recommendations, transmission mode is used for RCF scanning, with all image corrections features turned off, and the image type set to '48-bit color' [50]. Ashland provides detailed instructions for the Epson Scan software, which detail the settings used for scanning at CLEAR [39]. Scanned images are stored as TIFF files to maintain adequate bit depth and ensure lossless compression.

Regarding scanner resolution, Gafchromic^{TM} RCF models have a spatial resolution of 25 µm or smaller, with the achievable resolution limited by the scanning system [29]. For applications involving large and uniform radiation fields, a resolution of 72 dpi (0.36 mm pixel size) is sufficient; higher resolutions can increase measurement noise [51]. However, for smaller and/or non-uniform fields, it may be necessary to increase the resolution to better capture the dose distribution [36]. This adjustment comes at the cost of increased scanning time, image size and processing time. Above all, it is crucial to maintain identical scanner settings between calibration and application RCFs. Given that the typical VHEE beam at CLEAR has a Gaussian distribution with 1σ beam sizes down to approximately 1 mm in air, the RCFs are consistently scanned at a resolution of 300 dpi (0.085 mm pixel size), to ensure accurate capture of the distribution for all beams.

2.3.5 Scanning repetitions

Unless the one-scan protocol mentioned in section 2.3.1 is employed—which has the added benefit of avoiding inter-scan variabilities [41]—it is recommended to mitigate these variabilities by performing repeat scans of each RCF and using the average for evaluation [51]. However, this approach can be time-consuming for large batches of RCFs, as is typically the case at CLEAR.

Lewis and Devic proposed mitigating this by including a piece of unexposed RCF in every scan to serve as a reference for scanner response [52]. This strategy is straightforward to implement, and can be used simultaneously for background evaluation and eventual subtraction, as discussed in section 2.4. Provided that the reference is properly aligned with the application RCF in the scanning direction, there should be no LRA difference to compensate for. Additionally, studies have shown that repeated scans of an unexposed RCF do not cause any permanent darkening, indicating that using such a reference repeatedly should not induce artificial offsets [41, 52].

2.3.6 Summary: The CLEAR scanning procedure

Taking into account all the considerations concerning RCF scanning, we have developed a procedure that optimises accuracy while maintaining the necessary efficiency for use at CLEAR:

1. Ensure all calibration and application RCFs are scanned at the same time $\Delta t \geq 24$ h post-irradiation.

2. Switch on the scanner 30 min before starting the scanning to warm up the scanner electronics.
3. Clean the scanner surface and RCFs if they are dirty.
4. Perform five preview scans to warm up the scanner lamp and stabilise the scanner response.
5. Position the RCFs at the centre of the scanner and with consistent orientation using the scanner mask.
6. Ensure the scanner settings are according to protocol, without colour corrections.

2.4 RCF calibration

Each production lot of RCFs must be calibrated to establish a relationship between level of darkening and absorbed dose. Since there are no established VHEE reference beams, external clinical low-energy electron beams are used for RCF calibration in the CLEAR protocol. Previous VHEE dosimetry studies have reported agreement between RCF dose measurements and Monte Carlo simulations, where the RCFs were calibrated to clinical 15–20 MeV electron beams [8, 27, 28]. This indicates that a low-energy RCF calibration is valid for VHEE applications.

RCFs used at CLEAR are typically calibrated using the Oriatron eRT6 linac at Lausanne University Hospital (CHUV) [53], or a Varian TrueBeam medical linac at the Geneva University Hospitals (HUG). Both calibration setups provide a 6 MeV electron beam and calibrate the RCFs to a secondary standard ionisation chamber placed behind a 1 cm slab of solid water. It is important to note that for applications where the experimental submersion time is well-defined, calibration in liquid water should be considered if feasible, as it may better represent the RCF response, including diffusion and penetration effects [37]. The ionisation chambers are calibrated to measure dose to water and are traceable to the primary standard at the Swiss Federal Institute of Metrology (METAS). There are differences in the type of ionisation chamber, the field shape and size, and the temporal beam structure between the two setups. For example, the eRT6 has a circular field while the TrueBeam features a square field. A comparison of the remaining parameters for the two facilities is presented in Table 2, and an illustration of the calibration setups is presented in Figure 4.

RCF calibration involves exposing samples to a sufficient number of known doses within the dynamic range of the RCF model to establish a relationship between dose and darkening level. The required number of dose-points depends on the type of fitting function and the desired range of the calibration curve. According to Ashland, six to eight dose-points $D_{\text{calib.},n}$ arranged in geometric progression are sufficient when using a rational calibration function, such as the one in Equation 4, because this function captures the physical nature of the RCF development [29, 31]. The dose points are determined according to $D_{\text{calib.},n} = D_{\text{calib.},1} r^{n-1}$, where the common ratio r is selected based on the dose range of interest and and the desired number of calibration points. This approach ensures a higher density of dose points in the low end of the range, where the RCF response is more non-linear. Importantly, multiple film pieces should be calibrated to the same dose in order to enable meaningful uncertainty estimations.

The RCF calibrations of the RFDS at CLEAR typically include a few additional dose points (8–12 in total) to cover the entire dynamic range of the RCF. For each dose point, two samples are calibrated simultaneously by stacking them within the solid water phantom. This approach adds statistical robustness without increasing calibration time through separate irradiations and without imposing notable gradients between the two RCFs. If feasible, a higher number of samples per dose point can be utilised to improve statistics and uncertainty estimates. Additionally, including extra dose points for accuracy evaluation of the calibration curve is good practice.

TABLE 2 The beam parameters used for RCF calibration at eRT6 at CHUV and the Varian TrueBeam medical linac at HUG.

Parameter	eRT6 (CHUV)	Varian TrueBeam (HUG)
Energy/MeV	6	6
SSD/cm	60	100
Beam size/mm	46 (1σ)	150 (FWHM)
Dose rate/Gy s^{-1}	0.14	0.16
Pulse width/ms	1	4–6
Pulse frequency/Hz	10	~367
Ionisation chamber	Adv. Markus	Roos
$U_{95,D_{\text{IC}}}$/%	3.0	2.7
Solid water	PTW RW3	PTW RW3

2.4.1 Establishing the calibration curves

To establish a calibration curve, a response variable that describes the dose dependency of the RCF lot must be selected. From the TIFF files of the scanned calibration RCFs, a stack of three 2D arrays corresponding to the responses of the red, green and blue channels is extracted. A curve relating dose to the chosen response variable is established separately for each colour.

There are three response variables that recur in literature: PV, optical density (OD), and net optical density (nOD). PV is often preferred for its simplicity, since the values are obtained directly from the 2D images from each colour channel x. The more widely used choice is OD, which is related to PV according to Equation 2:

$$OD_x = -\ln\left(\frac{PV_x}{65535}\right), \tag{2}$$

where 65535 represents the RGB colour space of the scanner, as described in section 2.3. The conversion to OD is preferred because this quantity exhibits a more linear relationship behaviour with dose compared to PV and requires fewer non-linear terms to fit the inherently non-linear dose-response of RCFs [24]. This can be further extended to nOD by subtracting the mean OD of an unexposed RCF $\langle OD_{x,0}\rangle$ from the OD of an exposed RCF OD_x according to Equation 3:

$$nOD_x = OD_x - \langle OD_{x,0}\rangle. \tag{3}$$

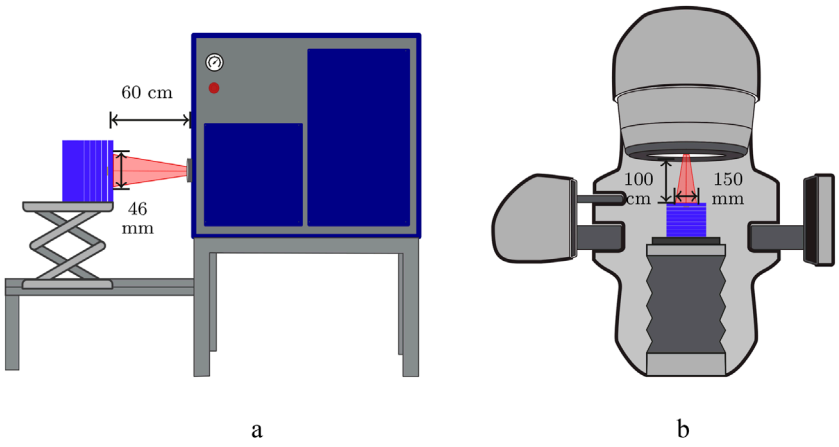

FIGURE 4
RCF calibration setups in solid water using low-energy electrons and ionisation chambers. **(a)** eRT6 linac at CHUV. **(b)** Varian TrueBeam at HUG.

Since there is no pixel-to-pixel correspondence between the unexposed and exposed RCFs, the mean OD across a region of interest (ROI) of the unexposed RCF is subtracted from the OD maps of the exposed RCFs to generate the corresponding nOD maps. This method accounts for the ageing of the RCF lot and is therefore recommended [50]. Ideally, the background should be obtained from the same RCF piece before irradiation. However, due to the number of samples used at CLEAR and the fact that the films are scanned individually, one RCF piece is typically kept from each sheet to serve as background for all irradiated RCFs from that sheet. In the context of irradiation in water, it may be beneficial to establish a background using an unexposed RCF that has been submerged in water in the same configuration as the irradiated RCFs to account for water diffusion effects [37].

A calibration set consists of RCF samples that have been exposed to a uniform field of known doses provided by the ionisation chamber at the calibration facility. To establish the calibration curve, an ROI must be determined that omits the edges and engravings of the RCF, is fully covered by the uniform field, and is large enough for a histogram of all PVs to result in a normal distribution with a measurable standard deviation [36]. At CLEAR, an ROI of 150×150 pixels—corresponding to $12.75 \times 12.75\,\mathrm{mm}^2$ at 300 dpi—centred on the RCF is selected. An example of an EBT3 calibration set is shown in Supplementary Figure S3. For each RCF in the calibration set, the mean nOD within the ROI is calculated, and the response of each dose point is the mean response between the RCF pieces exposed to the same dose.

There are numerous variants of fitting functions in literature; however it is essential to choose a function that most accurately represents the RCF's physical dose-response and fits the calibration points. The darkening of RCFs increases with exposure but approaches a near-constant value towards the end of the dynamic range (saturation). To this end, there are generally three families of functions that express this behaviour: rational, polynomial and exponential functions. Devic et al. showed that the choice may depend on the specific RFDS [54]. More generally, the performance of each function will depend on the number of calibration dose points D_{IC} and the dose-range.

Ashland recommends rational functions of the form in Equation 4, as proposed by Micke et al. [55]:

$$nOD_x(D) = -\ln\left(\frac{a_x + b_x D}{c_x + D}\right), \tag{4}$$

where a_x, b_x and c_x are fitting parameters for colour channel x. Such functions align more closely with the inherent nature of the RCF, as opposed to polynomial functions, which do not necessarily reflect the physical properties of the RCFs outside the range of the fitted data points [33].

At CLEAR, we apply the fitting function in Equation 4, and Figure 5 shows the calibration curves for the different RCF models used. Visually, it is evident that Equation 4 fits the calibration points of the EBT3, EBT-XD, and MD-V3 models well, with the fit lying within 0.2% of the ionisation chamber measurement D_{IC}, which is less than the uncertainty $U_{95,D_{\mathrm{IC}}}$. The exception is HD-V2, for which we speculate that the large uncertainty is due to environmental exposure or handling—factors to which it is more sensitive, as mentioned in Section 2.1. However, since HD-V2 are used less frequently, we do not currently have enough data to verify this.

The uncertainties in calculated doses from RCFs result from a convolution of various factors, which—together with inherent RCF imperfections, inconsistent handling, and scanner response—also include uncertainties from the calibration process, such as those associated with the calibration dose D_{IC} and the fitting procedure. Estimating the uncertainty for a given calibration curve has been discussed by Devic et al., where the error in dose response, σ_{nOD_x}, is expressed via error propagation from σ_{PV_x} via σ_{OD_x} [54, 56]. These steps are also outlined in Section S5. To estimate the overall calibration uncertainty, we use orthogonal distance regression (ODR) for curve fitting, which calculates the perpendicular distance from the data points to the fitted line. This approach takes into account uncertainties in both the calibration dose ($\sigma_{D_{\mathrm{IC}}}$) and nOD (σ_{nOD}) to construct the calibration curve [57]. The related uncertainty may be estimated by error propagation, as outlined in section Section S5.

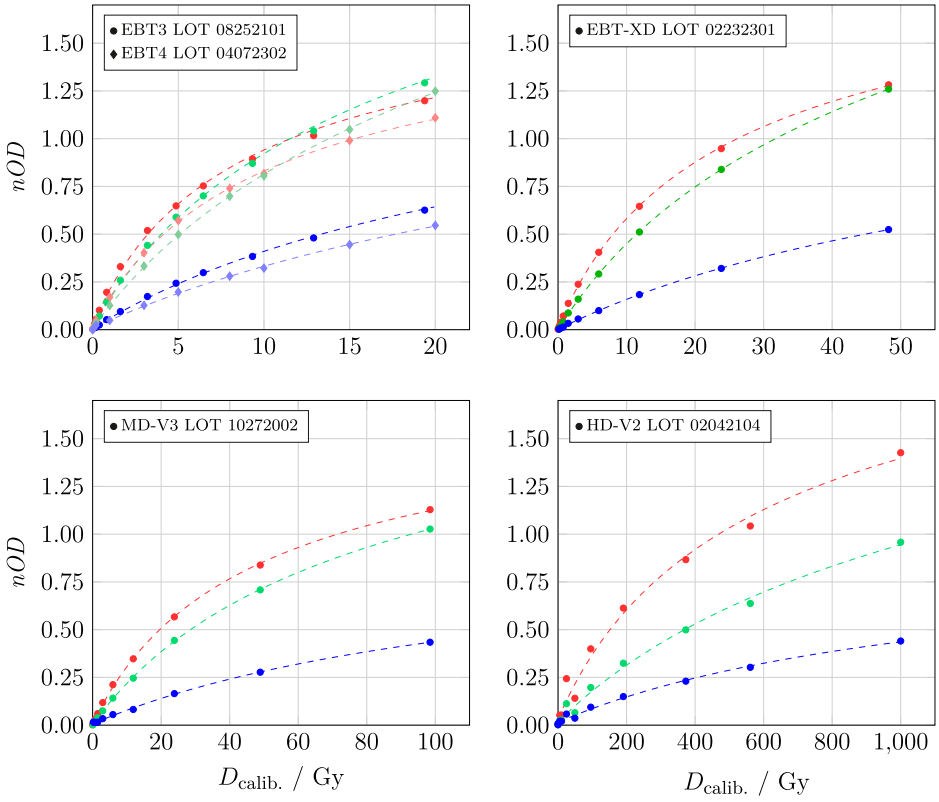

FIGURE 5
Calibration curves for different RCF models. The colours correspond to the respective colour channels, with circles representing the measurements, and the dashed lines indicating the fitted values.

2.4.2 Calibration validity

As stated in Section 2.4, calibrating each lot of RCFs—even if they are of the same model—is crucial to account for inter-lot variability. Supplementary Figure S4 shows an example of the calibration offset between different lots of EBT3 RCFs. Applying a calibration curve from a different lot may lead to dose estimation errors in the order of 20%.

Moreover, as discussed in Section 2.3.1, it is important to maintain consistency in the post-exposure scanning timing Δt for calibration and application RCFs to minimise errors arising from the continuous post-irradiation development of the RCFs.

There is a misconception that RCF ageing can be compensated for by re-scanning the calibration set simultaneously with scanning the application RCFs and updating the calibration curve. This practice can introduce significant errors in the calculated dose due to the considerable time discrepancy in Δt between calibration and application RCFs. Supplementary Figure S5 displays an example of an application RCF exposed to a known dose—scanned at $\Delta t_{\text{appl.}} = 24$ h—and evaluated using calibration curves scanned at a $\Delta t_{\text{calib.}}$ of 24 h and 233 days post-irradiation. The 'updated' calibration imposed more than a doubling of the dose error of the application RCF compared to the scenario where $\Delta t_{\text{calib.}} = \Delta t_{\text{appl.}} = 24$ h.

The rate of post-irradiation development is significantly higher than the natural self-development caused by other environmental factors, which are collectively referred to as ageing. For high accuracy, it is advised to update the calibration curve regularly by re-calibrating the lot. However, due to the lack of calibration capabilities at CLEAR, it is challenging to schedule systematic re-calibrations. Typically, a given production lot will be used at CLEAR for up to a year after calibration. To mitigate the effects of RCF ageing, it is recommended to ensure stable storage conditions, as outlined in Section 2.2.1, and to use nOD as response variable, as it effectively accounts for the drift of the unexposed RCFs [50].

2.4.3 Summary: The CLEAR calibration procedure

Based on the considerations discussed in Section 2.4, the following procedure for RCF calibration has been established at CLEAR:

1. Net optical density *nOD* is used as the response variable to account for ageing.
2. RCFs are calibrated against a secondary standard ionisation chamber using a low-energy electron linac that provides a sufficiently large and uniform field at a conventional dose-rate.
3. 8 to 12 dose points arranged in geometric progression are used to calibrate the full dynamic range of a given RCF model. This includes two to three dose points for calibration verification.
4. The calibration RCFs are scanned at a time $\Delta t \simeq 24$ h post irradiation.

5. The calibration points $nOD_x(D_{IC})$ for each colour channel x are fitted to the rational function in Equation 4, which reflects the physical nature of RCFs.

2.5 RCF processing and analysis

To retrieve dose distributions from application RCFs, calibration curves are applied to the digitised images. RCF processing can be performed using dedicated, commercial programs, such as FilmQAPro (Ashland) and radiochromic.com, which are accessible to some facilities, particularly clinics. Alternatively, open-source image processing software such as ImageJ—which has its own macro language for customisation and task automation—is commonly used among researchers. At CLEAR, a toolkit based on the scientific Python stack has been developed in-house for RCF processing and is under continuous improvement [58].

A key difference in RCF processing arises from whether the dose is calculated using information from one or multiple of the three (RGB) calibration curves. This section details and compares these two approaches—single-channel and multi-channel processing—which have both been utilised at CLEAR.

2.5.1 Single-channel RCF dosimetry

For accurate dosimetry using a single colour channel, it is essential to select the channel that exhibits the highest sensitivity, defined according to Equation 5:

$$S = \frac{\partial nOD_x}{\partial D}. \tag{5}$$

Literature reviews indicate that the red channel is the most commonly used channel for single channel dosimetry, based on the fact that Gafchromic^{TM} RCFs have maximum absorption in the red band (at approximately 633 nm). However, as shown in Figure 5 in Section 2.4, the red channel is not necessarily the most sensitive channel for all dose ranges and RCF models. The sensitivities of the calibration curves are displayed in Figure 6 and illustrate, for example, that beyond 3–4 Gy, the green channel is more sensitive than the red for EBT3. It is also evident why the blue channel is hardly used for single-channel dosimetry; nevertheless, it should be noted that it has been shown to be useful for extending the dynamic range of the RCFs [59].

Using a single colour channel x, the dose is calculated directly from the inverse of the calibration function in Equation 4 according to Equation 6:

$$D = \frac{a_x - c_x e^{-nOD_x}}{e^{-nOD_x} - b_x}. \tag{6}$$

The corresponding uncertainty, σ_D, is calculated by error propagation, outlined in Supplementary Equation S5.

The single-channel processing method has been employed at CLEAR since 2019. However, when determining the dose on the RCF using a single colour channel, the entire response is converted to dose. Due to the numerous potential uncertainties arising from RCF handling and scanning, this approach may lead to potentially significant errors in dose estimation, particularly as certain artefacts yield larger responses in specific channels. This motivated the transition to multi-channel dosimetry, which weighs the responses from the three channels channels to minimise the influence of non-dose-dependent artefacts.

2.5.2 Multi-channel RCF dosimetry

Dedicated commercial tools such as FilmQAPro and radiochromic.com offer multi-channel processing capabilities, utilising information from all three colour channels for dose evaluation. Multi-channel processing separates the RCF response into a dose-dependent component and a dose-independent perturbation [36]. By estimating the perturbation that minimises the difference between doses calculated from each individual colour channel, the noise from the dose-distribution is reduced.

The multi-channel method can mitigate issues such as variations in thickness across the active layer and scanner artefacts—including LRA, noise, and, to some extent, impurities—by optimising the dose value to the most probable value using information from all three calibration curves. The multi-channel method was first proposed by Micke et al. [55], followed by Mayer et al., who proposed an implementable solution to the optimisation problem [60]. This solution expresses the dose as a Taylor expansion with a perturbation, and minimises the cost function, which represents the difference between the true (common) dose D and the channel-dependent responses, encompassing both the dose and the perturbation.

As of 2025, multi-channel processing has been integrated into the RCF processing software at CLEAR [58]. The dose on the RCF is evaluated according to Equation 7, which was introduced by Mayer et al.:

$$D = \frac{\langle D \rangle - RS \cdot \frac{\sum_x D_x \cdot D'_x}{\sum_x D'_x}}{1 - RS}. \tag{7}$$

Here, $\langle D \rangle$ is the average dose estimated using all colour channels, according to Equation 8:

$$\langle D \rangle = \frac{1}{3} \sum_x D_x, \tag{8}$$

and D'_x is the derivative of the dose function w.r.t. the response variable nOD_x, expressed according to Equation 9:

$$D'_x = \frac{\partial D(nOD_x)}{\partial nOD_x} = e^{nOD_x} \cdot \frac{a_x - b_x c_x}{\left(b_x e^{nOD_x} - 1\right)^2}, \tag{9}$$

while RS is the relative slope of the colour channels, given by Equation 10:

$$RS = \frac{1}{3} \frac{\left(\sum_x D'_x\right)^2}{\sum_x D'^2_x}. \tag{10}$$

The corresponding uncertainty is calculated by further propagating the single channel dose uncertainty σ_D as outlined in Equation S5. The accuracy of this method within the context of the CLEAR protocol is currently under evaluation. Examples of relative errors using red, green and multi-channel can be seen in Supplementary Figure S6.

2.5.3 Summary: The CLEAR RCF processing procedure

Based on the considerations described in Section 2.5, the following procedure is followed for RCF processing at CLEAR:

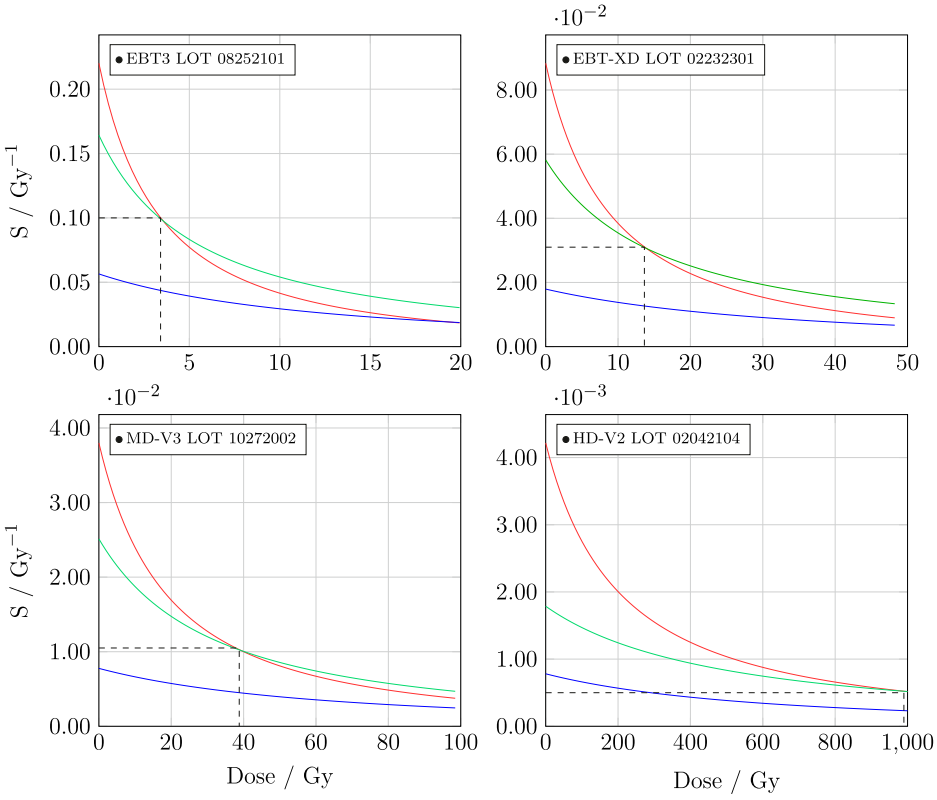

FIGURE 6
Sensitvity of the different calibration functions in Figure 5.

1. Application RCFs are scanned at $\Delta t_{\text{appl.}} \simeq \Delta t_{\text{calib.}} \simeq 24\,\text{h}$.
2. Between 2019–2024 the single-channel method was the sole approach used to convert RCF response to dose, selecting the colour channel with the highest sensitivity for the relevant the dose-regime.
3. Since 2025, the multi-channel method has been implemented to achieve noise reduction and higher accuracy. Its performance is currently being evaluated, and it is used alongside the single-processing method.

3 Protocol validation with passive dosimeters

To evaluate both the accuracy of our RCF dosimetry for typical CLEAR experiments and the robustness of the described RCF dosimetry protocol, we conducted a series of experiments comparing our RCF dosimetry with three other passive dosimeters: alanine dosimeters (ADs), radiophotoluminescence dosimeters (RPLDs), and dosimetry phantoms (DPs). These comparative measurements were performed using a geometry similar to that of a typical irradiation at CLEAR, where the ADs, RPLDs, and DPs were positioned relative to the RCFs in the same manner as typical samples.

3.1 Irradiation setup at CLEAR

CLEAR features a Cartesian robot capable of positioning custom 3D-printed sample holders into and out of the beam without manual intervention [61]. This robot offers significant advantages in many irradiation experiments by ensuring both reproducible sample positioning and the ability to irradiate multiple samples in a relatively short time. This capability is particularly crucial, as a 30-min cool-down period is required to access CLEAR after the beam has been switched off, complicating manual interventions between irradiations[1].

An illustration of the irradiation setup, including the robot, is shown in Figure 7. The robot employs a sample grabber to pick up sample holders from a storage area outside of the beam and place them in front of the beam. The sample storage area has a capacity of up to 32 sample holders and features optional temperature control. Additionally, a water phantom mounted on a vertical stage is positioned within the robot's boundaries along the beam path, enabling sample irradiations in water.

Typical irradiation experiments at CLEAR are conducted inside the water phantom using a Gaussian beam. The chosen irradiation depth varies and depends on the sample geometry and dose requirements of each experiment. Effectively, this

1 This is a radioprotection requirement at CLEAR, linked to its capability for material activation.

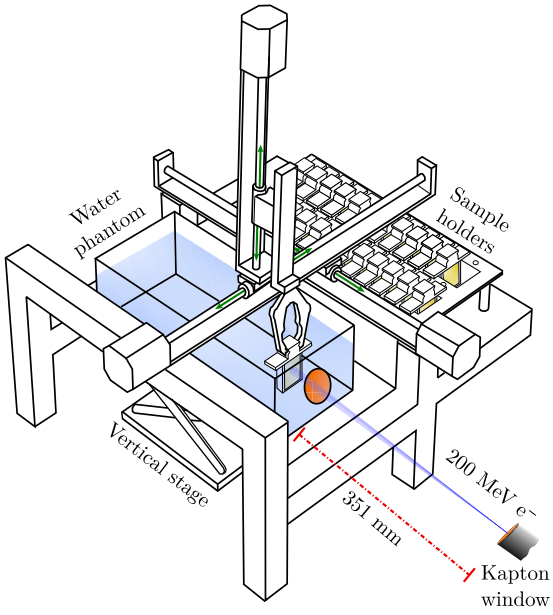

FIGURE 7
A drawing of the robot holding a sample holder inside the water phantom, with the path of the beam indicated in blue. The illustration is adapted from [22].

represents an optimisation between increasing the beam size and improving uniformity across the sample, while also reaching the required dose—particularly at UHDR, which is a single-pulse modality. It is important to note that varying the irradiation depth alters the particle spectra, also known as beam quality, which introduces additional challenges regarding the comparability of experiments.

Figure 8 illustrates the typical evolution of peak dose and beam size throughout the water phantom for a Gaussian beam at CLEAR [62]. The initial phase space of the beam—defined by its Twiss parameters—affects the steepness of the curves, indicating that the irradiation depth for a given beam size depends on the initial beam conditions. The overall evolution aligns with expectations for a Gaussian VHEE beam, contrasting with the flatter build-up for uniform beams as demonstrated by Böhlen et al. [8]. Similar simulations have been experimentally confirmed to be representative of the beam at CLEAR [63].

For the comparative measurements between the RCFs and the RPLDs and DPs, different mean dose rates were employed to study the relative agreement at both CDR and UHDR. The CDR irradiation conditions at the CLEAR facility utilise one bunch per pulse, with a bunch charge on the order of 100 pC and a bunch length of approximately 1–5 ps, delivered at a pulse repetition rate of 0.833 Hz. In contrast, UHDR irradiation conditions deliver a single pulse consisting of a train of bunches spaced at a frequency of 1.5 GHz. The charge per pulse (and thus dose per pulse) is determined by the number of bunches within the train and hence the pulse width, which can be up to ~50 ns.

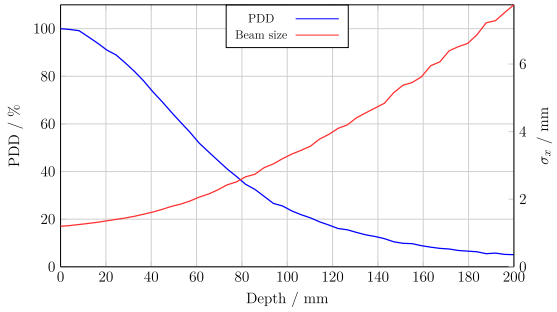

FIGURE 8
A typical percentage-depth-dose (PDD) curve and beam size evolution for the CLEAR beam in water. These curves were obtained from Monte Carlo simulations using TOPAS, as outlined in Section S6.

3.2 Comparison with alanine dosimeters

As part of our efforts to validate the RCF protocol, we collaborated with Physikalisch-Technische Bundesanstalt (PTB) in Germany to compare the agreement between RCF dosimetry at CLEAR and alanine dosimeter (AD) measurements from PTB. Additionally, the goal was to determine if the agreement varied across different energies. The RCFs and ADs were irradiated simultaneously at CLEAR and analysed at CLEAR and PTB, respectively.

Twenty samples—each consisting of a stack of four ADs, shrink-wrapped in polythene foil—were provided by PTB. Each sample was positioned on the downstream side of an EBT-XD RCF and mounted in a robot holder. The setup and dimensions of the samples and ADs are illustrated in Figure 9.

To investigate the energy dependence, four different beam energies of 50, 100, 150, and 200 MeV were targeted. Five samples were irradiated for each energy, with three targeted at 15 Gy and the remaining two were targeted at 10 and 20 Gy to cover the dose range relevant to the majority of experiments at CLEAR. The beam was delivered at CDR. For each energy, the beam size was optimised to approximately $\sigma_{x,y} = 5.5$ mm, minimising dose gradients across the stacks while keeping it consistent for all energies. This required adjustments to the irradiation depth at the different energies.

Both the single green channel—as the overall most sensitive channel for EBT-XD in the range of 10–20 Gy—and multi-channel processing methods were employed to evaluate the dose response of the RCFs. The mean RCF doses and standard deviations were obtained from the ROI corresponding to the positions of the two central ADs (AD two and AD 3), optimising for symmetry and uniformity. The absorbed doses to the ADs were subsequently determined at PTB by measuring the concentration of free radicals produced by ionising radiation using electron spin resonance (ESR) spectroscopy [64–66].

The dose responses of the RCFs and ADs are compared in Figure 10.

The left-hand plot in Figure 10 shows that the dose values obtained from both the single green channel and multi-channel processing of the RCFs agree with the AD values within a single standard deviation for each sample. The right-hand plot

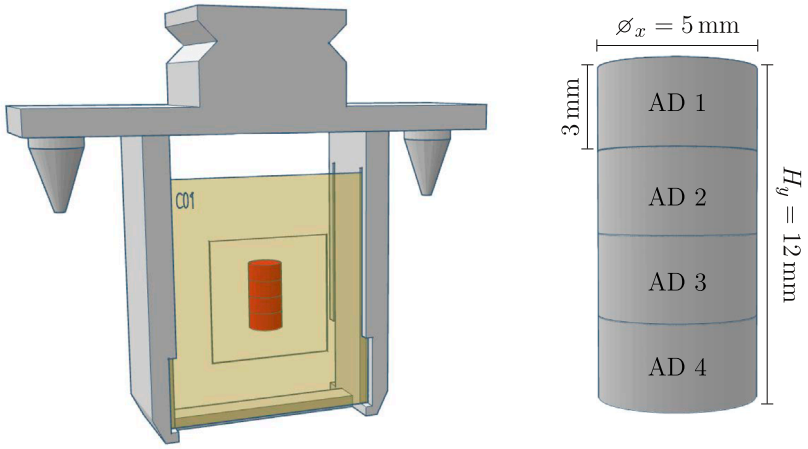

FIGURE 9
Left: The robot holder with a stack of four alanine pellets (indicated in red) packed in plastic and attached on the back of an RCF. Right: The stack of ADs with dimensions.

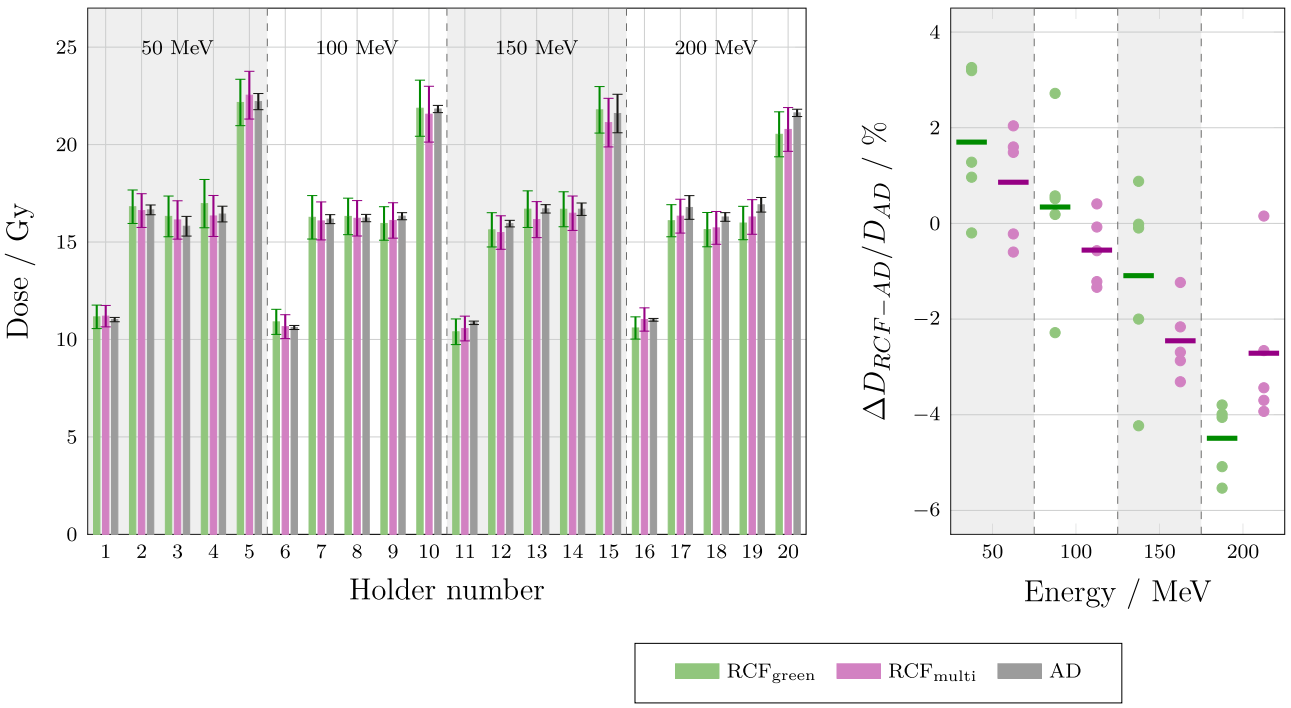

FIGURE 10
Left: Bar chart showing dose measurements from each sample holder of the ADs and EBT-XD RCFs, analysed using both the single green channel and the multi-channel method. The AD doses represent the averages of the two central pellets in each stack (AD two and AD 3) and are compared for 50, 100, 150 and 200 MeV. Right: Deviations between RCF and AD measurements for each beam energy.

demonstrates that both the single green channel and multi-channel RCF processing methods yield average absolute percentage deviations of less than 5% for all beam energies when compared to the AD measurements. Overall, the multi-channel method appears to perform better relative to the AD values. The observed dose overestimation of RCFs compared to ADs at lower energies, and underestimation at higher energies, is not fully understood, and additional statistics under improved irradiation conditions would be necessary to evaluate its significance.

The mean standard deviation of the RCF measurements (5.8%) is larger than of the AD measurements (1.7%) for several reasons. The dominant factor is that the small Gaussian beam ($\sigma_{x,y}$ = 5.5 mm) is inhomogeneous across the area occupied by the ADs (5 mm × 3 mm), whereas the AD calibration refers to a homogeneous

reference field of 10×10 cm^2. Small differences in lateral positioning of the ADs relative to the beam axis in small fields can lead to large deviations in the dose that are challenging to assess. Moreover, the effect of the inhomogeneous distribution of the free radicals on the ESR signal is not easily quantifiable.

Another source of uncertainty arises from deviations from reference conditions. The ADs were positioned in a small Gaussian field at considerable depths in water (62 mm–180 mm), while the AD calibration is based on ^{60}Co irradiations under reference conditions—a homogeneous field of 10×10 cm^2 at a depth of 50 mm in water. This calibration accounts for a radiation quality factor (1.012) that corrects for the AD response to electron radiation under reference conditions—a homogeneous field of 10×10 cm^2 at reference depths of 10 mm–60 mm. For small electron fields, such as those at CLEAR, a reference depth is not even defined.

Lastly, the validity of the AD calibration is only verified for electron energies ranging from 6 to 20 MeV [67]. Although no significant energy dependence has been observed in the range 15 MeV–50 MeV when compared with RCF and ionisation chamber measurements [68], the energy range of 50 MeV–200 MeV used for irradiation at CLEAR could also introduce a source of uncertainty.

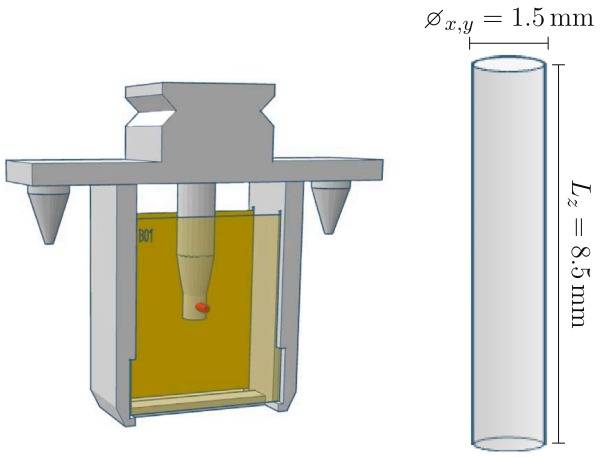

FIGURE 11
Left: The robot holder with an RPLD (indicated in red) positioned between two RCFs. Right: The RPLD with its dimensions.

3.3 Comparison with radiophotoluminescence dosimeters

The RCF dosimetry at CLEAR has also been compared to measurements from radiophotoluminescence dosimeters (RPLDs) in collaboration with the CERN radiation working group (RADWG). An additional aim of this study was to investigate the relative agreement between the responses of the dosimeters to irradiation under both CDR and UHDR conditions. To this end, the RCFs and RPLDs were irradiated simultaneously at CLEAR and analysed at CLEAR and by the RADWG, respectively.

RPLDs are passive dosimeters made from silver-doped phosphate glass. Under radiation exposure, electron-hole pairs generated within the glass are trapped, leading to the formation of two types of optical centres: luminescence centres (RPL centres), and colour centres. When exposed to UV light, the RPL centres emit luminescence light that can be measured to estimate the absorbed dose in the glass dosimeter [69]. While this dosimetry technology is currently less commonly used in medical applications, it is widely used in environmental monitoring. At CERN, their sensitive range extends beyond traditional applications, reaching the MGy-range [70]. RPLDs offer advantages of being robust, exhibiting minimal fading effects, and allowing for repeated readouts without signal loss.

In a previous study, we compared the agreement between RPLDs and HD-V2 RCFs in air within the dose range of 30–300 Gy, finding an agreement within 10% [49]. However, the question remained whether a better agreement could be achieved in water for clinical doses and whether there was a clear dose-rate dependency.

A total of 16 RPLDs were provided by the RADWG and were irradiated alongside both EBT-XD and MD-V3 RCFs under CDR and UHDR conditions. Doses of 10, 15 and 20 Gy were targeted, which are typical for medical application experiments at CLEAR. Whereas the ADs were fixed directly downstream of an RCF, the cylindrical RPLDs were positioned between two RCFs due to their larger longitudinal (z) size, as shown in Figure 11.

Both the single green channel and the multi-channel processing methods were utilised to evaluate the dose response of the RCFs. The mean doses and standard deviations were obtained from an ROI corresponding to the cross-sections of the RPLDs. These results and are presented in Figure 12 along with the RPLD measurements.

The left-hand plot shows that the dose values obtained from both the single green channel and multi-channel processing of the RCFs are generally lower and fall outside the standard deviations of the RPLD measurements. Overall, the mean standard deviation for the RCF measurements is lower than for the RPLDs, with values of 2.9% and 3.3% for the multi-channel and green-channel, respectively, compared to 4.9% for the RPLDs. The left-hand plot also shows that the relative difference between RPLD and RCF measurements is more variable than the differences observed for the ADs *versus* RCFs.

The right-hand plot shows that the single green channel and multi-channel processing methods yield average absolute percentage deviations of more than 5% at UHDR and more than 10% at CDR, with spreads of up to 30% relative to the RPLD measurements.

The significant and variable discrepancies observed between the RCFs and RPLDs can be attributed to multiple factors. While the wide spread in relative measurements complicates the ability to draw definitive conclusions, several known issues need to be addressed in future experiments. First, the RPLDs were firmly inserted into a hole in a resin-printed sample holder, raising the possibility that some resin may have rubbed off onto the RPLDs. Although an ultrasonic bath cleaning procedure of the RPLDs was performed before readout—resulting in a somewhat improved agreement with the RCF measurements—it is still possible that residues remain, potentially affecting the measurements.

Secondly, although RPLDs are thought to exhibit minimal dose rate effects, recent studies have indicated that exposure to dose rates differing from the calibration conditions can impact the formation of both RPL and colour centres within the dosimeter [71].

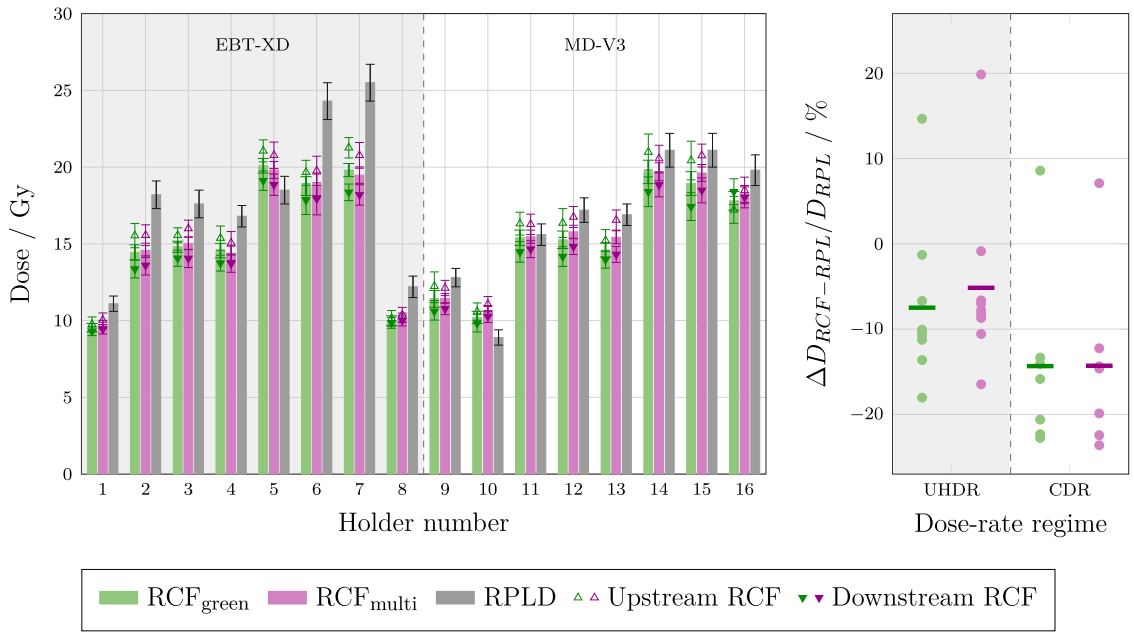

FIGURE 12
Left: Bar chart of the individual dose measurements of the RPLDs and various RCF types analysed using both the single green channel and the multi-channel method. The chart display the average between upstream and downstream RCFs, as well as the upstream and downstream RCF measurements. The irradiations were performed at UHDR (holders 1–7) and CDR dose-rates (holders 8–16). Right: The deviations between RCF and RPLD measurements for each dose-rate regime.

Lastly, and most importantly, the calculation of the relative dose between the RCFs and RPLDs is susceptible to misalignment errors. A slight offset between the region of the Gaussian beam intercepted by the RPLD and the ROI analysed on the RCF can contribute to the relative dose uncertainty. Given that the cross-sectional area of the RPLDs is smaller than that of the ADs, alignment inaccuracies can have a more pronounced impact on the dose recorded by the RPLDs.

3.4 Comparison with dosimetry phantoms

Finally, we compared our RCF dosimetry with measurements from 'dosimetry phantoms' (DPs) in collaboration with Institiut de Radiophysique (IRA) at CHUV in Switzerland. Similar to the RPLDs, we simultaneously investigated the relative responses under UHDR and CDR conditions. Upon irradiation at CLEAR, the RCFs were analysed using the described protocol, while the DPs were analysed by IRA.

The DPs are 3D-printed from ONYX® —a composite material of micro carbon fibre filled nylon with a density of 1.2 g cm^{-3} [72]—and each contains three LiF-100 thermoluminescent dosimeters (TLD) interleaved with approcimately 10 small (⌀ = 3 mm)EBT3 RCFs. The remaining volume of the DP is filled with rubber to prevent large air gaps. This configuration is inspired by the multi-centre UHDR dosimetry cross validation conducted at CHUV and Stanford University, which utilised a cuboid DP filled with TLDs, ADs and RCFs to compare the measurements of 8 MeV UHDR electron beams [73].

A total of 10 DPs were provided by IRA. For irradiation, each DP was positioned in a custom sample holder, between two RCFs, as illustrated in Figure 13.

The setup is similar to that used in radiobiology experiments at CLEAR, where there is particular interest in validating the dosimetry. In these experiments, an Eppendorf tube is typically positioned between two RCFs to evaluate the dose delivered to the samples in the tube. However, because the DPs are relatively large compared to these tubes, the separation between the two RCFs was increased from 12 mm to 20 mm to accommodate their length. We targeted 10 Gy for all holders, which is a typical dose for biological irradiations at CLEAR. The agreement among different RCF models were simultaneously investigated by interchanging between EBT3, EBT-XD and MD-V3 in the different sample holders.

For each DP, the dose and uncertainty were calculated as the mean and standard deviation across the constituent dosimeters. Both the single green channel and the multi-channel processing methods were employed to evaluate the dose response of the upstream and downstream RCFs. The RCF doses and standard deviations were obtained from an ROI corresponding to the cross-sections of the sensitive volumes of the DPs. These results are presented in Figure 14.

The left-hand plot shows that, for most of the holders, the dose obtained from the DP is within the uncertainty range of the mean RCF response. The magnitude of the individual standard deviations can be attributed to the small beam size relative to the cross-section of the DPs, resulting in a significant transverse variation in dose. Furthermore, notable differences in doses measured by the upstream and downstream RCFs can be attributed to significant beam scattering between the two RCFs. This scattering

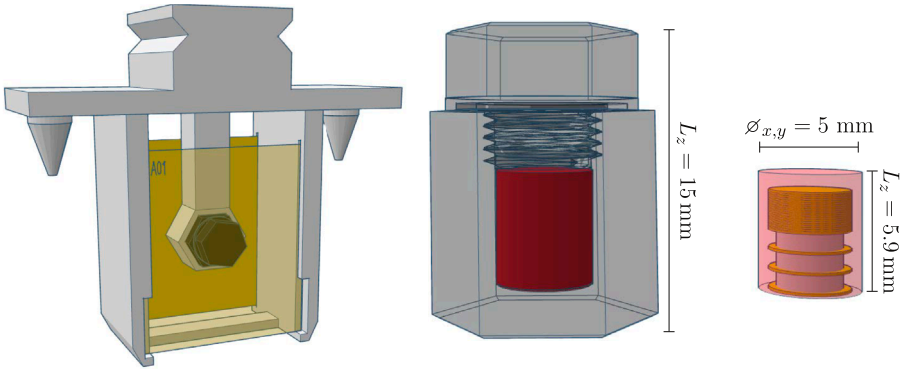

FIGURE 13
Left: The robot holder with the DP positioned between two RCFs. Right: The structure of the DP, highlighting its sensitive volume (in red) and dimensions.

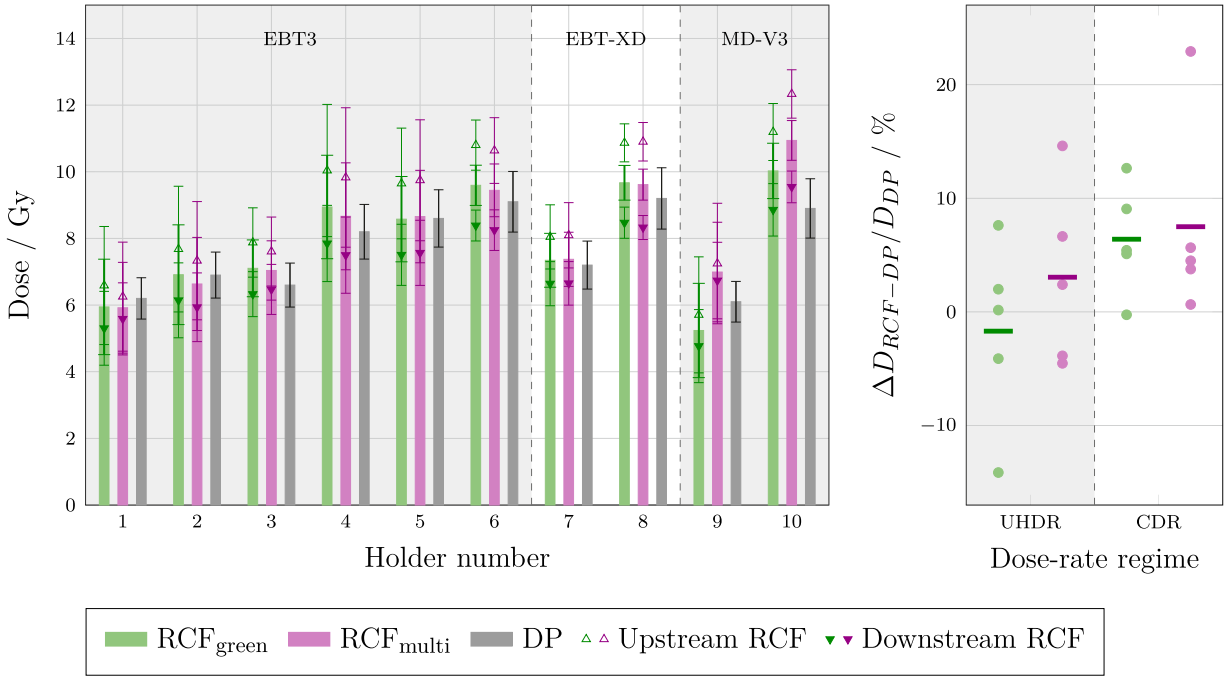

FIGURE 14
Left: Bar chart of dose measurements from each sample holder, displaying the dose from the DPs and the RCFs analysed using both the single green channel and the multi-channel methods. The RCF doses represent the averages between upstream and downstream films, as well as the individual upstream and downstream measurements. Holders 1–3, seven and nine were irradiated at UHDR, while holders 4–6, 8 and 10 were irradiated at CDR. Right: The deviations between RCF and DP measurements for each dose-rate regime.

may also contribute to the discrepancies observed between the doses determined by the RCFs and the DPs. Additionally, it is evident that the relative difference between the upstream and downstream RCFs is variable, which could indicate inconsistent beam divergence between irradiations, complicating the evaluation of measurement accuracy.

The right-hand plot shows the relative deviation between RCFs and DPs irradiated at UHDR and CDR. There seems is a larger spread in measurements at UHDR *versus* CDR. This discrepancy may be attributed to pulse-to-pulse position jitter, which is often more pronounced (≃ 1 mm) for UHDR irradiations than for CDR (where several pulses are accumulated). This alignment error between the sample and the centre of the beam increases the dose gradients across the DPs, significantly raising the uncertainty. In addition to the factors discussed above, several known uncertainties may help explain the discrepancies in the results. One issue is that, due to a problem with the accelerator, half of the DPs were irradiated 13 days after the other half. At IRA, the protocol involves irradiating reference TLDs in a ^{60}Co beam to a known reference dose on the same day as the irradiation of the TLDs being

tested. This practice allows for correction of the daily sensitivity of the dosimetric system, thereby avoiding the need for additional fading corrections [34]. Since the TLD reference irradiation was performed simultaneously with half of the DP irradiations, this may imply that the measurement uncertainties for the other half are higher.

4 Conclusion

In this paper we presented a comprehensive overview and discussion of the various factors that impact the accuracy of RCF dosimetry. This evaluation was used to motivate the RCF dosimetry protocol that has been adapted for CLEAR—a research facility that relies heavily on RCFs for VHEE and UHDR studies.

With the aim of serving as a guide for similar facilities needing to adapt RCF protocols for high throughput and small or non-uniform beams, we highlighted the key principles, pitfalls and lessons learned at CLEAR. This enables informed decisions to achieve adequate accuracy while optimising time and resources for compatibility with a research setting. Strict adherence to a protocol is imperative for reliable RCF dosimetry; particularly in maintaining complete consistency in the handling of calibration and application RCFs. The scanning time Δt often presents challenges in a research setting, especially during inter-facility collaborations. We demonstrated that inconsistent post-irradiation scanning timing between calibration and application RCFs can lead to dose errors exceeding 5%.

We have identified areas for improvement in the current RCF protocol that are feasible to implement at CLEAR. Most importantly, consistently scanning the background (unirradiated) RCF simultaneously with each application RCF is a straightforward approach to mitigating inter-scan variability, as well as offsetting the ageing of the RCF lot. For RCF irradiations in water, using a background that has been submerged in the same manner and for the same duration as the application RCFs will also help offset water penetration effects.

We have verified the RCF protocol at CLEAR by comparing RCF measurements with alanine dosimeters (ADs), radiophotoluminescence dosimeters (RPLDs), and dosimetry phantoms (DPs). We achieved relative agreement between RCFs and ADs within 5% using a Gaussian beam, whilst the agreement was lower between RCFs and RPLDs and DPs. We explained that the latter inconsistencies were likely due to experimental uncertainties, such as alignment inaccuracies, which pose challenges for irradiations with small and non-uniform beams. By leveraging the experience gained from these outcomes, along with recent advancements in irradiation procedures at CLEAR, we foresee future optimised experiments yielding better agreement.

First and foremost, the development of VHEE dual scattering systems capable of generating larger and more uniform beams would significantly enhance the assessment of the RCF dosimetry accuracy relative to other dosimeters [74]. For Gaussian beams, minimising the distance between the RCF and sample, along with improving alignment and ROI selection procedures for the RCFs, would help reducing uncertainties. Lastly, particularly for UHDR irradiations, improved control of pulse-to-pulse beam position is likely to improve the results.

Data availability statement

The raw data supporting the conclusions of this article will be made available by the authors, without undue reservation. The software developed for RCF processing and analysis is available from the BeamDosimetry repository https://gitlab.cern.ch/CLEAR/dosimetry/.

Author contributions

VR: Conceptualization, Data curation, Formal Analysis, Investigation, Methodology, Software, Visualization, Writing - original draft, Writing - review and editing. JB: Conceptualization, Data curation, Formal Analysis, Investigation, Methodology, Software, Visualization, Writing - original draft, Writing - review and editing. LW: Methodology, Writing - review and editing, Investigation. MC: Investigation, Methodology, Resources, Writing - review and editing. VG: Methodology, Writing - review and editing, Resources. YA: Investigation, Writing - review and editing, Formal Analysis, Methodology, Resources, AS: Investigation, Methodology, Writing - review and editing, Formal Analysis, Resources. CB: Formal Analysis, Investigation, Methodology, Resources, Writing - review and editing. WF: Investigation, Methodology, Resources, Writing - review and editing. AG: Formal Analysis, Investigation, Writing - review and editing, Data curation, Writing - original draft. CR: Investigation, Writing - review and editing, Software. PK: Writing - review and editing, Investigation, Methodology. AM: Writing - review and editing, Investigation. SS: Supervision, Writing - review and editing, Funding acquisition. M-CV: Conceptualization, Resources, Supervision, Writing - review and editing, Methodology. MD: Conceptualization, Funding acquisition, Resources, Supervision, Writing - review and editing. RC: Conceptualization, Funding acquisition, Methodology, Project administration, Resources, Supervision, Writing - review and editing.

Funding

The author(s) declare that financial support was received for the research and/or publication of this article. This work was partly supported by the Research Council of Norway (NFR grant no. 310713) and the Science and Technology Facilities Council (STFC grant no. 2432490).

Acknowledgments

This work has to a great extent been based on the comprehensive compilation of best-practices for RCF dosimetry by Niroomand-Rad et al. in the Report of AAPM Task Group 235 [36], the numerous papers of S. Devic et al. which thoroughly describe various aspects of RCF dosimetry [24, 54, 56, 59, 75], and the literature on multichannel dosimetry by Micke et al. [55] and Mayer et al. [60]. Moreover, we have to extend our gratitude towards CHUV, HUG, PTB, and the CERN radiation working group (RADWG), for their

support and useful input in calibrations and dosimetry cross-correlation experiments, which has been instrumental in this work.

Conflict of interest

The authors declare that the research was conducted in the absence of any commercial or financial relationships that could be construed as a potential conflict of interest.

Generative AI statement

The author(s) declare that no Generative AI was used in the creation of this manuscript.

Any alternative text (alt text) provided alongside figures in this article has been generated by Frontiers with the support of artificial intelligence and reasonable efforts have been made to ensure accuracy, including review by the authors wherever possible. If you identify any issues, please contact us.

Publisher's note

Supplementary material

The Supplementary Material for this article can be found online at: https://www.frontiersin.org/articles/10.3389/fphy.2025.1597079/full#supplementary-material

References

1. Vozenin MC, Bourhis J, Durante M. Towards clinical translation of FLASH radiotherapy. *Nat Rev Clin Oncol* (2022) 19(12):791–803. doi:10.1038/s41571-022-00697-z

2. Gao F, Yang Y, Zhu H, Wang J, Xiao D, Zhou Z, et al. First demonstration of the FLASH effect with ultrahigh dose rate high-energy X-rays. *Radiother Oncol* (2022) 166:44–50. doi:10.1016/J.RADONC.2021.11.004

3. Miles D, Sforza D, Wong JW, Gabrielson K, Aziz K, Mahesh M, et al. FLASH effects induced by orthovoltage X-rays. *Int J Radiat Oncology∗Biology∗Physics* (2023) 117:1018–27. doi:10.1016/j.ijrobp.2023.06.006

4. Diffenderfer ES, Verginadis II, Kim MM, Shoniyozov K, Velalopoulou A, Goia D, et al. Design, implementation, and *in vivo* validation of a novel proton FLASH radiation therapy system. *Int J Radiat Oncol Biol Phys* (2020) 106:440–8. doi:10.1016/J.IJROBP.2019.10.049

5. Favaudon V, Caplier L, Monceau V, Pouzoulet F, Sayarath M, Fouillade C, et al. Ultrahigh dose-rate FLASH irradiation increases the differential response between normal and tumor tissue in mice. *Sci Translational Med* (2014) 6:245ra93. doi:10.1126/scitranslmed.3008973

6. Vozenin MC, De Fornel P, Petersson K, Favaudon V, Jaccard M, Germond JF, et al. The advantage of FLASH radiotherapy confirmed in Mini-pig and Cat-cancer Patients. *Clin Cancer Res : official J Am Assoc Cancer Res* (2019) 25:35–42. doi:10.1158/1078-0432.CCR-17-3375

7. DesRosiers C, Moskvin V, Bielajew AF, Papiez L. 150-250 MeV electron beams in radiation therapy. *Phys Med and Biol* (2000) 45:1781–805. doi:10.1088/0031-9155/45/7/306

8. Böhlen TT, Germond JF, Traneus E, Bourhis J, Vozenin MC, Bailat C, et al. Characteristics of very high-energy electron beams for the irradiation of deep-seated targets. *Med Phys* (2021) 48:3958–67. doi:10.1002/MP.14891

9. Montay-Gruel P, Corde S, Laissue JA, Bazalova-Carter M. FLASH radiotherapy with photon beams. *Med Phys* (2022) 49:2055–67. doi:10.1002/MP.15222

10. Bazalova-Carter M, Liu M, Palma B, Dunning M, McCormick D, Hemsing E, et al. Comparison of film measurements and Monte Carlo simulations of dose delivered with very high-energy electron beams in a polystyrene phantom. *Med Phys* (2015) 42:1606–13. doi:10.1118/1.4914371

11. Schuler E, Eriksson K, Hynning E, Hancock SL, Hiniker SM, Bazalova-Carter M, et al. Very high-energy electron (VHEE) beams in radiation therapy; Treatment plan comparison between VHEE, VMAT, and PPBS. *Med Phys* (2017) 44:2544–55. doi:10.1002/MP.12233

12. Böhlen TT, Germond JF, Traneus E, Vallet V, Desorgher L, Ozsahin EM, et al. 3D-conformal very-high energy electron therapy as candidate modality for FLASH-RT: a treatment planning study for glioblastoma and lung cancer. *Med Phys* (2023) 50:5745–56. doi:10.1002/MP.16586

13. Böhlen TT, Germond JF, Desorgher L, Veres I, Bratel A, Landström E, et al. Very high-energy electron therapy as light-particle alternative to transmission proton FLASH therapy – an evaluation of dosimetric performances. *Radiother Oncol* (2024) 194:110177. doi:10.1016/J.RADONC.2024.110177

14. McManus M, Romano F, Lee ND, Farabolini W, Gilardi A, Royle G, et al. The challenge of ionisation chamber dosimetry in ultra-short pulsed high dose-rate Very High Energy Electron beams. *Scientific Rep* (2020) 10:9089. doi:10.1038/s41598-020-65819-y

15. Di Martino F, Barca P, Barone S, Bortoli E, Borgheresi R, De Stefano S, et al. FLASH radiotherapy with electrons: issues related to the production, Monitoring, and dosimetric characterization of the beam. *Front Phys* (2020) 8:570697. doi:10.3389/fphy.2020.570697

16. Poppinga D, Kranzer R, Farabolini W, Gilardi A, Corsini R, Wyrwoll V, et al. VHEE beam dosimetry at CERN Linear Electron Accelerator for Research under ultra-high dose rate conditions. *Biomed Phys and Eng Express* (2020) 7:015012. doi:10.1088/2057-1976/ABCAE5

17. Wanstall HC, Korysko P, Farabolini W, Corsini R, Bateman JJ, Rieker V, et al. VHEE FLASH sparing effect measured at CLEAR, CERN with DNA damage of pBR322 plasmid as a biological endpoint. *Scientific Rep* (2024) 14(1):14803–13. doi:10.1038/s41598-024-65055-8

18. Kacem H, Kunz L, Korysko P, Ollivier J, Tsoutsou P, Martinotti A, et al. Modification of the microstructure of the CERN- CLEAR-VHEE beam at the picosecond scale modifies ZFE morphogenesis but has no impact on hydrogen peroxide production. *Radiother Oncol* (2025) 209:110942. doi:10.1016/J.RADONC.2025.110942

19. Hart A. *Dosimetry and radiobiology of ultrahigh dose-rate radiotherapy delivered with low-energy x-rays and very high-energy electrons*. Victoria: University of Victoria (2024).

20. Bateman JJ, Buchanan E, Corsini R, Farabolini W, Korysko P, Garbrecht Larsen R, et al. Development of a novel fibre optic beam profile and dose Monitor for very high energy electron radiotherapy at ultrahigh dose rates. *Phys Med and Biol* (2024) 69:085006. doi:10.1088/1361-6560/AD33A0

21. Hart A, Giguère C, Bateman J, Korysko P, Farabolini W, Rieker V, et al. Plastic scintillator dosimetry of ultrahigh dose-rate 200 MeV electrons at CLEAR. *IEEE Sensors J* (2024) 24:14229–37. doi:10.1109/JSEN.2024.3353190

22. Rieker VF, Corsini R, Stapnes S, Adli E, Farabolini W, Grilj V, et al. Active dosimetry for VHEE FLASH radiotherapy using beam profile monitors and charge measurements. *Nucl Instr Methods Phys Res Section A: Acc Spectrometers, Detectors Associated Equipment* (2024) 1069:169845. doi:10.1016/J.NIMA.2024.169845

23. Mill J, Jaroszynski D, Maitrallain A, Baldacchino G. Real-time dosimetry of very high energy electrons using fluorescence spectroscopy, 125. *Elsevier BV* (2024). doi:10.1016/j.ejmp.2024.103883

24. Devic S. Radiochromic film dosimetry: Past, present, and future. *Physica Med* (2011) 27:122–34. doi:10.1016/J.EJMP.2010.10.001

25. Sutherland JG, Rogers DW. Monte Carlo calculated absorbed-dose energy dependence of EBT and EBT2 film. *Med Phys* (2010) 37:1110–6. doi:10.1118/1.3301574

26. Bouchard H, Lacroix F, Beaudoin G, Carrier JF, Kawrakow I. On the characterization and uncertainty analysis of radiochromic film dosimetry. *Med Phys* (2009) 36:1931–46. doi:10.1118/1.3121488

27. Subiel A, Moskvin V, Welsh GH, Cipiccia S, Reboredo D, Evans P, et al. Dosimetry of very high energy electrons (VHEE) for radiotherapy applications: using radiochromic film measurements and Monte Carlo simulations. *Phys Med and Biol* (2014) 59:5811–29. doi:10.1088/0031-9155/59/19/5811

28. Lagzda A, Angal-Kalinin D, Jones J, Aitkenhead A, Kirkby KJ, MacKay R, et al. Influence of heterogeneous media on Very High Energy Electron (VHEE) dose penetration and a Monte Carlo-based comparison with existing radiotherapy modalities. *Nucl Instr Methods Phys Res Section B: Beam Interactions Mater Atoms* (2020) 482:70–81. doi:10.1016/J.NIMB.2020.09.008

29. Gafchromic. EBT3 dosimetry film (2016).

30. Ashland. Gafchromic™ EBT4 films (2022).

31. Ashland. Gafchromic™ EBT-XD films (2021).

32. Ashland. *Gafchromic™ MD-V3 films* (2021).

33. Ashland. Gafchromic™ HD-V2 films (2021).

34. Jaccard M, Petersson K, Buchillier T, Germond JF, Durán MT, Vozenin MC, et al. High dose-per-pulse electron beam dosimetry: Usability and dose-rate independence of EBT3 Gafchromic films. *Med Phys* (2017) 44:725–35. doi:10.1002/MP.12066

35. Karsch L, Beyreuther E, Burris-Mog T, Kraft S, Richter C, Zeil K, et al. Dose rate dependence for different dosimeters and detectors: TLD, OSL, EBT films, and diamond detectors. *Med Phys* (2012) 39:2447–55. doi:10.1118/1.3700400

36. Niroomand-Rad A, Chiu-Tsao ST, Grams MP, Lewis DF, Soares CG, Van Battum LJ, et al. Report of AAPM task group 235 radiochromic film dosimetry: an update to TG-55. *Med Phys* (2020) 47:5986–6025. doi:10.1002/mp.14497

37. Aldelaijan S, Devic S, Mohammed H, Tomic N, Liang LH, DeBlois F, et al. Evaluation of EBT-2 model GAFCHROMIC™ film performance in water. *Med Phys* (2010) 37:3687–93. doi:10.1118/1.3455713

38. Butson MJ, Yu PK, Metcalfe PE. Effects of read-out light sources and ambient light on radiochromic film. *Phys Med and Biol* (1998) 43:2407–12. doi:10.1088/0031-9155/43/8/031

39. Ashland™. Efficient protocols for accurate radiochromic film calibration and dosimetry. *Tech Rep* (2016).

40. Trivedi G, Singh PP, Oinam AS. EBT3 Radiochromic film response in time-dependent thermal environment and water submersion conditions: its clinical relevance and uncertainty estimation. *Radiat Phys Chem* (2025) 227:112403. doi:10.1016/J.RADPHYSCHEM.2024.112403

41. Lewis D, Micke A, Yu X, Chan MF. An efficient protocol for radiochromic film dosimetry combining calibration and measurement in a single scan. *Med Phys* (2012) 39:6339–50. doi:10.1118/1.4754797

42. Rieker V, Bateman JJ, Farabolini W, Korysko P. Development of reliable VHEE/FLASH passive dosimetry methods and procedures at CLEAR. In: *Proceedings of the 14th International particle accelerator Conference*. Venice, Italy (2023). p. 5028–31. doi:10.18429/JACoW-IPAC2023-THPM059

43. Lárraga-Gutiérrez JM, García-Garduño OA, Treviño-Palacios C, Herrera-González JA. Evaluation of a LED-based flatbed document scanner for radiochromic film dosimetry in transmission mode. *Physica Med* (2018) 47:86–91. doi:10.1016/J.EJMP.2018.02.010

44. Van Battum LJ, Huizenga H, Verdaasdonk RM, Heukelom S. How flatbed scanners upset accurate film dosimetry. *Phys Med and Biol* (2015) 61:625–49. doi:10.1088/0031-9155/61/2/625

45. Lewis D, Chan MF. Correcting lateral response artifacts from flatbed scanners for radiochromic film dosimetry. *Med Phys* (2015) 42:416–29. doi:10.1118/1.4903758

46. Zeidan OA, Stephenson SAL, Meeks SL, Wagner TH, Willoughby TR, Kupelian PA, et al. Characterization and use of EBT radiochromic film for IMRT dose verification. *Med Phys* (2006) 33:4064–72. doi:10.1118/1.2360012

47. Sipilä P, Ojala J, Kaijaluoto S, Jokelainen I, Kosunen A. Gafchromic EBT3 film dosimetry in electron beams - energy dependence and improved film read-out. *J Appl Clin Med Phys* (2016) 17:360–73. doi:10.1120/JACMP.V17I1.5970

48. Lynch BD, Kozelka J, Ranade MK, Li JG, Simon WE, Dempsey JF. Important considerations for radiochromic film dosimetry with flatbed CCD scanners and EBT GAFCHROMIC film. *Med Phys* (2006) 33:4551–6. doi:10.1118/1.2370505

49. Rieker V, Bateman JJ, Corsini R, Dyks LA, Farabolini W, Korysko P. VHEE high dose rate dosimetry studies in CLEAR. In: *13th Int. Particle Acc. Conf.ticle accelerator Conference Bangkok, Thailand: JACoW publishing, Geneva, Switzerland*. International Particle Accelerator Conference (2022). p. 3026–9. doi:10.18429/.JACoW-IPAC2022-THPOMS031

50. Aldelaijan S, Devic S. Comparison of dose response functions for EBT3 model GafChromic™ film dosimetry system. *Physica Med* (2018) 49:112–8. doi:10.1016/J.EJMP.2018.05.014

51. Martišíková M, Ackermann B, Jäkel O. Analysis of uncertainties in Gafchromic® EBT film dosimetry of photon beams. *Phys Med and Biol* (2008) 53:7013–27. doi:10.1088/0031-9155/53/24/001

52. Lewis D, Devic S. Correcting scan-to-scan response variability for a radiochromic film-based reference dosimetry system. *Med Phys* (2015) 42:5692–701. doi:10.1118/1.4929563

53. Jaccard M, Durán MT, Petersson K, Germond JF, Liger P, Vozenin MC, et al. High dose-per-pulse electron beam dosimetry: Commissioning of the Oriatron eRT6 prototype linear accelerator for preclinical use. *Med Phys* (2018) 45:863–74. doi:10.1002/MP.12713

54. Devic S, Seuntjens J, Hegyi G, Podgorsak EB, Soares CG, Kirov AS, et al. Dosimetric properties of improved GafChromic films for seven different digitizers. *Med Phys* (2004) 31:2392–401. doi:10.1118/1.1776691

55. Micke A, Lewis DF, Yu X. Multichannel film dosimetry with nonuniformity correction. *Med Phys* (2011) 38:2523–34. doi:10.1118/1.3576105

56. Devic S, Seuntjens J, Sham E, Podgorsak EB, Schmidtlein CR, Kirov AS, et al. Precise radiochromic film dosimetry using a flat-bed document scanner. *Med Phys* (2005) 32:2245–53. doi:10.1118/1.1929253

57. Virtanen P, Gommers R, Oliphant TE, Haberland M, Reddy T, Cournapeau D, et al. SciPy 1.0: fundamental algorithms for scientific computing in Python. *Nat Methods* (2020) 17(3):261–72. doi:10.1038/s41592-019-0686-2

58. Rieker V. BeamDosimetry (2025).

59. Devic S, Tomic N, Soares CG, Podgorsak EB. Optimizing the dynamic range extension of a radiochromic film dosimetry system. *Med Phys* (2009) 36:429–37. doi:10.1118/1.3049597

60. Mayer RR, Ma F, Chen Y, Miller RI, Belard A, McDonough J, et al. Enhanced dosimetry procedures and assessment for EBT2 radiochromic film. *Med Phys* (2012) 39:2147–55. doi:10.1118/1.3694100

61. Korysko P, Dosanjh M, Dyks L, Bateman J, Robertson C, Corsini R, et al. Updates, Status and experiments of CLEAR, the CERN linear electron accelerator for research. In: *13th Int. Particle Acc. Conf.* Bangkok, Thailand (2022). p. 3022–5. doi:10.18429/JACoW-IPAC2022-THPOMS030

62. Perl J, Shin J, Schümann J, Faddegon B, Paganetti H. TOPAS: an innovative proton Monte Carlo platform for research and clinical applications. *Med Phys* (2012) 39:6818–37. doi:10.1118/1.4758060

63. Rieker VF, Aksoy A, Malyzhenkov A, Wroe L, Corsini R, Farabolini W, et al. Beam Instrumentation for real time FLASH dosimetry: experimental studies in the CLEAR facility. In: *Proceedings of the 14th International particle accelerator Conference*. Venice, Italy (2023). p. 5032–5. doi:10.18429/JACoW-IPAC2023-THPM060

64. Bourgouin A, Hackel T, Marinelli M, Kranzer R, Schüller A, Kapsch RP. Absorbed-dose-to-water measurement using alanine in ultra-high-pulse-dose-rate electron beams. *Phys Med Biol* (2022) 67:205011. doi:10.1088/1361-6560/.AC950B

65. Anton M, Allisy-Roberts PJ, Kessler C, Burns DT. A blind test of the alanine dosimetry secondary standard of the PTB conducted by the BIPM. *Metrologia* (2014) 51:06001. doi:10.1088/0026-1394/51/1A/06001

66. Anton M. Uncertainties in alanine/ESR dosimetry at the Physikalisch-Technische Bundesanstalt. *Phys Med and Biol* (2006) 51:5419–40. doi:10.1088/0031-9155/51/21/003

67. Vörös S, Anton M, Boillat B. Relative response of alanine dosemeters for high-energy electrons determined using a Fricke primary standard. *Phys Med Biol* (2012) 57:1413–32. doi:10.1088/0031-9155/57/5/1413

68. Kokurewicz K, Brunetti E, Curcio A, Gamba D, Garolfi L, Gilardi A, et al. An experimental study of focused very high energy electron beams for radiotherapy. *Commun Phys* (2021) 4(1):33–7. doi:10.1038/s42005-021-00536-0

69. Yamamoto T, Rosenfeld A, Kron T, d'Errico F, Moscovitch M. RPL dosimetry: principles and applications. *AIP Conf Proc* (2011) 217–30. doi:10.1063/1.3576169

70. Pramberger D, Aguiar YQ, Trummer J, Vincke H. Characterization of radio-photo-luminescence (RPL) dosimeters as radiation monitors in the CERN accelerator Complex. *IEEE Trans Nucl Sci* (2022) 69:1618–24. doi:10.1109/TNS.2022.3174784

71. Aguiar Y, Garcia R, Kranjcevic M, Ferrari M, Soderstrom D, Mandal AR, et al. Dose rate effects in Ag-doped metaphosphate glass RPL dosimeters up to MGy range Maspalomas, Spain. In: *IEEE Radecs 2024* (2024). doi:10.34894/.VQ1DJA

72. Markforged Inc. Material Datasheet: Composites REV 5.3 (2023).

73. Jorge PG, Melemenidis S, Grilj V, Buchillier T, Manjappa R, Viswanathan V, et al. Design and validation of a dosimetric comparison scheme tailored for ultra-high dose-rate electron beams to support multicenter FLASH preclinical studies. *Radiother Oncol* (2022) 175:203–9. doi:10.1016/J.RADONC.2022.08.023

74. Robertson C, Bateman JJ, Dosanjh M, Korysko P, Corsini R, Farabolini W, et al. Dual-scattering foil Installation at CLEAR. In: *Proceedings of the 14th International particle accelerator Conference* (2023). p. 5059–62. doi:10.18429/.JACoW-IPAC2023-THPM073

75. Devic S, Wang YZ, Tomic N, Podgorsak EB. Sensitivity of linear CCD array based film scanners used for film dosimetry. *Med Phys* (2006) 33:3993–6. doi:10.1118/1.2357836

Frontiers in Physics

Investigates complex questions in physics to understand the nature of the physical world

Addresses the biggest questions in physics, from macro to micro, and from theoretical to experimental and applied physics.

Discover the latest Research Topics

See more →

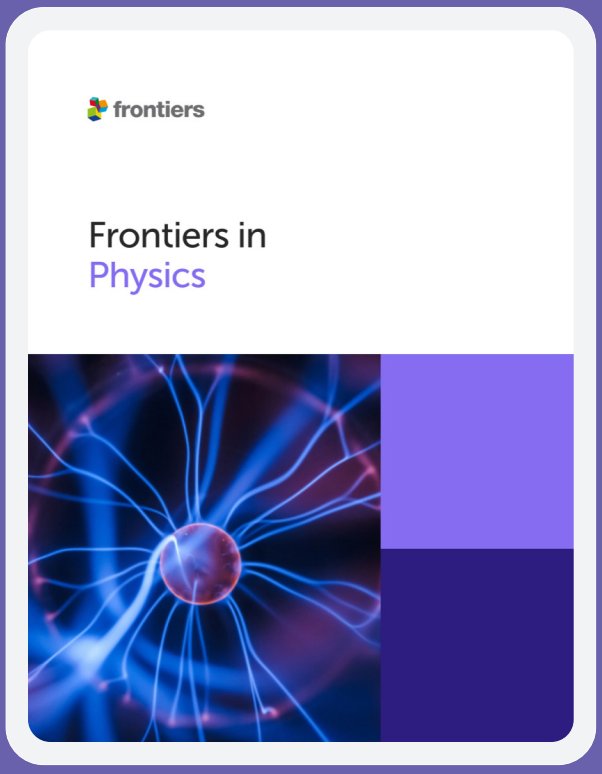

Frontiers

Avenue du Tribunal-Fédéral 34
1005 Lausanne, Switzerland
frontiersin.org

Contact us

+41 (0)21 510 17 00
frontiersin.org/about/contact